

---

# Single-molecule mechanics and regulatory conformational transitions of the force-sensing protein von Willebrand factor

Achim Löff

---



München 2019



---

**Single-molecule mechanics and  
regulatory conformational transitions  
of the force-sensing protein  
von Willebrand factor**

Achim Löff

---

Dissertation  
an der Fakultät für Physik  
der Ludwig-Maximilians-Universität  
München

vorgelegt von  
Achim Löff  
aus München

München, den 21.03.2019

Erstgutachter: Prof. Dr. Hermann Gaub  
Zweitgutachter: Prof. Dr. Joachim Rädler  
Tag der mündlichen Prüfung: 30.04.2019





# Zusammenfassung

Die Bildung eines hämostatischen Pfropfs aus Blutplättchen im Falle einer Gefäßverletzung stellt einen ersten essentiellen Schritt der Blutgerinnungskaskade dar. Dieser Prozess beruht auf der Funktion des Plasmaproteins Von Willebrand Faktor (VWF), welches in Form großer, linearer Multimere vorliegt und in der Lage ist, Blutplättchen zu binden und selbst unter hoher Scherspannung an die verletzte Gefäßwand anzuheften. Bemerkenswerterweise wird die Aktivität des VWF durch Kraft reguliert. Die auf den VWF wirkenden mechanischen Kräfte entstehen aus dem Zusammenspiel der äußerst langen (bis zu  $\approx 15 \mu\text{m}$ ) Multimere mit dem hydrodynamischen Fluss im Blutkreislauf. Im Falle normalen Blutflusses ist der VWF inaktiv, wohingegen er durch erhöhte hydrodynamische Kräfte, die infolge von Veränderungen des Flussprofils in Verbindung mit Gefäßverletzungen auftreten, aktiviert wird. Hierbei ist eine erhöhte Elongationsströmung, eine Teilkomponente der Scherströmung, von besonderer Bedeutung. Diese Kraft-Regulation der hämostatischen Funktion des VWF ist nicht nur aus biophysikalischer Sicht faszinierend, sondern auch physiologisch äußerst wichtig. Sie verhindert einerseits eine unerwünschte Aktivität des VWF in intakten Blutgefäßen, die zu thromboembolischen Komplikationen führen kann, und ermöglicht andererseits eine effiziente Aktivierung der Blutplättchenaggregation genau dort, wo sie benötigt wird.

Voraussetzung für die Aktivierung eines VWF Multimers ist der Kraft-induzierte, abrupte Übergang von einer kompakten, insgesamt annähernd globulären Konformation zu einer elongierten, gestreckten Konformation. Das Elongationsverhalten unter Kraft wird insbesondere durch eine Reihe spezifischer, intramolekularer Interaktionen sowie Kraft-induzierter Konformationsübergänge innerhalb der dimerischen Untereinheiten des VWF bestimmt. Indem sie die effektive Multimerlänge beeinflussen, regulieren diese intramolekularen Interaktionen zudem die anfängliche Kraft-Sensitivität des VWF, da hydrodynamische Kräfte stark mit der Länge skalieren. Allerdings sind diese regulatorischen intramolekularen Interaktionen und Kraft-induzierten Konformationsübergänge – trotz ihrer zentralen Rolle für die Kraft-Regulation der hämostatischen Funktion des VWF – größtenteils noch nicht ausreichend untersucht und verstanden.

Um diesen regulatorischen Mechanismen, die die hämostatische Aktivität des VWF bestimmen, auf den Grund zu gehen, wurden im Rahmen dieser Dissertation sowohl die Mechanik als auch das Ensemble verschiedener Konformationen von VWF Dimeren – den kleinsten sich wiederholenden Untereinheiten in VWF Multimeren – auf Einzelmolekülebene eingehend untersucht.

Mithilfe einer Kombination aus Rasterkraftmikroskopie (AFM)-basierter Bildgebung und AFM-basierter Einzelmolekülkraftmessungen war es möglich zu zeigen, dass schon geringe Abweichungen des pH-Werts vom physiologischen Wert von 7,4, insbesondere hin zu sauren Bedingungen, eine deutlich verringerte mechanische Widerstandskraft der VWF Dimere zur Folge haben, welche auf die Destabilisierung einer spezifischen und starken, durch die D4 Domänen vermittelten Interaktion in Dimeren zurückzuführen ist. Dieser Effekt könnte einen Mechanismus zur gezielten Aktivierung des VWF als Reaktion auf lokale Veränderungen des pH-

Werts darstellen, die potentiell in Verbindung mit Gefäßverletzungen auftreten. Darüber hinaus konnte aus den Ergebnissen der AFM-Bildgebung auf die Existenz weiterer pH-abhängiger, mechanisch sehr schwacher Interaktionen in der C-terminalen Stammregion der VWF Dimere geschlossen werden.

Um auch intramolekulare Interaktionen im VWF direkt untersuchen zu können, deren Dissoziation sich schon bei extrem niedrigen, aber physiologisch hochrelevanten Kräften bis hinunter zu  $< 1$  pN ereignet, wurde ein neuartiger Ansatz für Einzelmolekülkraftspektroskopie an Proteinen, basierend auf magnetischen Pinzetten (MT), entwickelt, der hochparallele und stabile Messungen bei konstanter Kraft ermöglicht. Dieser Ansatz wurde validiert durch Messungen an der bereits eingehend charakterisierten Proteindomäne ddFLN4. Im Kontext dieser Validierung wurde auch die Lebensdauer einzelner Streptavidin–Biotin Bindungen untersucht und es konnte mithilfe von Messungen an Streptavidin-Mutanten mit unterschiedlicher Valenz gezeigt werden, dass die Lebensdauer der Bindung stark von der Zuggeometrie abhängt.

Die Verwendung des neuen MT-Ansatzes für Messungen an VWF Dimeren ermöglichte die Charakterisierung verschiedener Kraft-induzierter Übergänge im VWF. Beispielsweise konnte der Einfluss der Bindung von Calcium-Ionen auf die Kinetik der Entfaltung und Rückfaltung der A2 Domäne des VWF aufgeklärt werden, ein Prozess, der sowohl für die Aktivierung als auch für die Herunterregelung der hämostatischen Funktion des VWF von Bedeutung ist. Darüber hinaus konnten mechanisch sehr schwache Interaktionen in der C-terminalen Stammregion von VWF Dimeren, auf welche zuvor nur indirekt geschlossen werden konnte, bei Kräften von  $\approx 1$  pN direkt beobachtet werden. Es ist anzunehmen, dass diese Interaktionen wichtige physiologische Konsequenzen nach sich ziehen, da ihre Dissoziation aller Wahrscheinlichkeit nach den ersten spezifischen Schritt der Elongation des VWF unter Kraft darstellt. Überdies wurde ein zuvor unbekannter Konformationsübergang in der N-terminalen D'D3 Domäne des VWF entdeckt, der vermutlich eine regulatorische Funktion während der Biosynthese des VWF erfüllt.

Schließlich wurde AFM-basierte Bildgebung auf Einzelmolekülebene als Methode zur Bestimmung der Größenverteilung von VWF Multimeren eingeführt. Diese Größenverteilung ist aufgrund des positiven Zusammenhangs zwischen Multimerlänge und hydrodynamischer Kraft von herausragender Bedeutung für die Gesamtaktivität des VWF. Diese Herangehensweise bestätigte die schon zuvor berichtete exponentielle Größenverteilung des VWF und lieferte Einsichten in klinisch relevante Multimerisierungsdefekte, die nicht durch etablierte Methoden der Multimeranalyse gewonnen werden können.

Zusammengenommen liefern die in dieser Arbeit präsentierten Ergebnisse einen wichtigen Beitrag zum tieferen Verständnis des komplexen Zusammenspiels der verschiedenen Interaktionen und Konformationsveränderungen, welche die molekulare Basis der Kraft-Regulation des VWF, und somit der primären Hämostase, darstellen.

# Abstract

The formation of hemostatic plugs at sites of vascular injury represents a first essential step in the blood coagulation cascade. This process crucially relies on the large, linear multimeric glycoprotein von Willebrand factor (VWF) and its ability to stably bind and recruit platelets to the damaged vessel wall even under conditions of high shear stress. Remarkably, VWF's hemostatic activity is regulated by force. Forces on VWF multimers in the bloodstream result from the interplay of their immense lengths (up to  $\approx 15 \mu\text{m}$ ) with the hydrodynamic flow they encounter. While being inactive under normal blood flow conditions, VWF is activated for its hemostatic function by increased hydrodynamic forces that result from changes in the blood flow profile in the wake of vascular injury, especially due to an elevated elongational flow component. This force-regulation of VWF's hemostatic activity is not only highly intriguing from a biophysical perspective, but also of eminent physiological importance. On the one hand, it prevents undesired activity of VWF in intact vessels that could lead to thromboembolic complications. On the other hand, it provides a mechanism to facilitate efficient VWF-mediated platelet aggregation exactly where needed.

Prerequisite for activation of a VWF multimer is the force-induced, abrupt transition from a rather compact, overall globular conformation to an elongated, string-like conformation. Importantly, VWF's elongation behavior is governed by several specific intramolecular interactions and force-induced conformational transitions within VWF's dimeric subunits. By regulating the effective multimer length, these intramolecular interactions also govern VWF's initial force sensitivity, as hydrodynamic forces strongly scale with dimension. However, despite their central role in the mechano-regulation of VWF's hemostatic function, these intramolecular interactions and further regulatory force-induced conformational transitions are for the most part not well understood and characterized.

In the framework of this thesis, in order to dissect regulatory conformational transitions governing VWF's hemostatic activity, the mechanical response and the conformational ensemble of VWF dimers –the smallest repeating subunits of multimers– were investigated at the single-molecule level.

Using a combination of atomic force microscopy (AFM) imaging and AFM-based single-molecule force measurements, it was shown that even minor pH changes from the physiologic pH of 7.4, especially acidification, result in a markedly decreased mechanical resistance of VWF's dimeric subunits. This effect could be traced back to destabilization of a specific, strong intermonomer interaction mediated by VWF's D4 domains. This pH dependence might represent a mechanism to promote activation of VWF in response to local pH changes, which may occur at sites of vascular injury. In addition, further pH-dependent, but mechanically very weak interactions in the C-terminal stem region of VWF dimers could be inferred from the imaging results.

To enable direct investigation of interactions in VWF that dissociate at very low, but physiologically highly relevant forces down to  $< 1 \text{ pN}$ , a novel approach for single-molecule protein force spectroscopy based on magnetic tweezers (MT) was developed. This approach, which enables highly parallel and stable measurements at constant forces, was validated using the

well-characterized protein domain ddFLN4 as a model system. In this context, also the lifetime of single biotin–streptavidin bonds was investigated and, by measurements with streptavidin variants of different valencies, it was shown that the bond lifetime strongly depends on the pulling geometry.

Applying the MT assay to dimeric VWF constructs, several force-induced conformational transitions in VWF could be characterized. For instance, the impact of calcium binding on the kinetics of unfolding and refolding of the VWF A2 domain, a process relevant both for VWF's activation and down-regulation, was elucidated. Furthermore, mechanically very weak interactions in the C-terminal stem region of VWF dimers, which had previously only been inferred indirectly, were observed directly at a force of  $\approx 1$  pN. These interactions can be expected to have important physiological implications, as their dissociation likely represents the first specific step of force-induced elongation of VWF. Moreover, a previously unknown transition within VWF's N-terminal D'D3 assembly was discovered that likely plays a regulatory role in VWF's biosynthesis.

Finally, single-molecule AFM imaging was introduced as a tool to determine the multimer size distribution of VWF, which, due to the positive relation between multimer length and hydrodynamic force, is highly important for VWF's overall activity. This approach confirmed the previously described exponential size distribution of VWF and, in particular, yielded insights into clinically relevant multimerization defects that could not be gained by established methods of multimer analysis.

Taken together, the findings presented in this thesis help to gain a deeper understanding of the complex interplay of interactions and conformational transitions underlying the force-regulation of VWF's hemostatic function.

# Contents

<b>Zusammenfassung</b>	<b>vii</b>
<b>Abstract</b>	<b>ix</b>
<b>Introduction</b>	<b>1</b>
<b>1 Biophysics and physiology of von Willebrand factor (VWF)</b>	<b>5</b>
1.1 Physiological roles and von Willebrand disease . . . . .	5
1.2 Domain organization, structure and biosynthesis . . . . .	6
1.3 VWF as a force-sensing polymer in hydrodynamic flow . . . . .	11
1.4 Force-induced activation and down-regulation of VWF . . . . .	14
1.5 Interim conclusion: regulation of VWF's force sensing and force response by interactions in dimers . . . . .	20
<b>2 Experimental methods and materials</b>	<b>23</b>
2.1 Atomic Force Microscopy (AFM) imaging . . . . .	23
2.2 Magnetic tweezers (MT) . . . . .	28
2.2.1 Fundamentals of single-molecule force spectroscopy . . . . .	28
2.2.2 MT working principle and setup . . . . .	31
2.2.3 Protein force spectroscopy in MT using Elastin-like polypeptide linkers	35
2.3 Recombinant protein constructs and protein purification . . . . .	38
2.4 Buffers . . . . .	41
<b>3 Role of pH-dependent interactions in dimers for regulating the mechanics and structure of VWF</b>	<b>43</b>
3.1 Force response of VWF dimers under varied pH conditions . . . . .	43
3.2 Static conformation of VWF dimers under varied pH and ionic conditions . . .	47
3.3 Obstruction of the strong D4-mediated intermonomer interaction by imidazole	50
3.4 Discussion and Conclusion . . . . .	51
<b>4 Modular, ultra-stable and highly parallel protein force spectroscopy in MT</b>	<b>57</b>
4.1 Protein force spectroscopy in MT: state of the art and challenges . . . . .	58
4.2 Protein attachment <i>via</i> Elastin-like polypeptides . . . . .	59
4.3 Three-state unfolding and folding of ddFLN4 at constant force . . . . .	61
4.4 Lifetime of single biotin-streptavidin bonds under constant load . . . . .	67
4.5 Distinct lifetimes of biotin unbinding owing to streptavidin's multivalency . .	69
<b>5 Single-molecule constant force measurements on VWF dimers</b>	<b>75</b>
5.1 Impact of calcium binding on A2 domain unfolding and folding . . . . .	75
5.2 Dissociation of the D4-mediated strong intermonomer interaction . . . . .	80

---

5.3	VWF stem zipping and unzipping at low forces . . . . .	83
5.4	Fast transitions of an intra-domain interaction within the D'D3 assembly . . . . .	86
<b>6</b>	<b>Advancing multimer analysis of VWF by single-molecule AFM imaging</b>	<b>101</b>
6.1	VWF multimer size distribution and multimerization defects . . . . .	101
6.2	Quantitative analysis of VWF multimer size distributions by AFM imaging . . . . .	103
6.3	Insights into processing defects beyond conventional multimer analysis . . . . .	105
6.4	Discussion and conclusion . . . . .	109
<b>7</b>	<b>Summary, conclusions, and outlook</b>	<b>113</b>
	<b>Bibliography</b>	<b>119</b>
	<b>List of Figures</b>	<b>135</b>
	<b>List of Tables</b>	<b>137</b>
	<b>List of Publications</b>	<b>139</b>
	<b>Acknowledgements</b>	<b>141</b>

# Introduction

Mechanical forces acting on biomolecules, in particular proteins, are an integral part of many biological processes and often critically regulate the physiological functions of a protein [1, 2]. A remarkable example is the large, multimeric protein von Willebrand factor (VWF), which is activated for its vital function in primary hemostasis upon sensing elevated hydrodynamic forces in the bloodstream that emerge due to alterations in the blood flow in the wake of vascular injuries [3, 4].

This force sensing of VWF –*i.e.* the conversion of changes in the hydrodynamic flow into a physiological response– is highly remarkable from a biophysical point of view, as the forces acting on VWF are not governed externally, but result from the interplay of its structure with hydrodynamic flow encountered in blood vessels. In other words, the forces that VWF can experience in the vasculature are “built-in” into its molecular architecture. Here, the linear multimeric nature of VWF, allowing for immense lengths of multimers of up to several  $\mu\text{m}$  [5], is key to the sensitivity of VWF to hydrodynamic forces, since hydrodynamic forces strongly scale with dimension [4, 6, 7].

VWF’s physiological role in primary hemostasis is to bind and recruit platelets to the damaged subendothelium in order to form a platelet plug sealing the site of vessel injury [8, 9]. To fulfill this function, VWF needs to overcome rather high hydrodynamic lift forces acting on platelets under high shear rates that counteract the adhesion of platelets to the vessel wall [5], therefore requiring stable binding of VWF both to subendothelial collagen and to platelet receptors. At the same time, inactivity of VWF under normal blood flow conditions has to be ensured, as otherwise formation of platelet plugs could rapidly lead to thrombotic occlusions, as for instance occurring in pathologically stenosed vessels [10]. Accomplishing these opposing requirements warrants a strict regulation of VWF’s activity. The physiological relevance of VWF, and the importance of its tight regulation, are demonstrated by a variety of mutations in VWF that lead to different forms of the bleeding disorder von Willebrand disease [11, 12], and by VWF’s role in thrombotic complications such as myocardial infarction or stroke [13–16]. Prerequisite for activation of VWF multimers is their force-induced transition from a rather compact conformation to an elongated, string-like conformation [5, 17], which is thought to result in an increased accessibility of previously shielded binding sites, thus facilitating multivalent binding [4, 5]. In addition, due to the positive feedback between multimer length and force, this large-scale elongation increases the force acting on the multimer sufficiently to induce further small-scale conformational changes within the main platelet-binding domain of VWF under high tension, which markedly increase the affinity for platelet binding [17–19].

Importantly, recent findings have indicated that the elongation of VWF, which has been observed as a rather sharp and seemingly cooperative transition [5], is not just a simple uncoiling of a coiled polymer, but involves the dissociation of specific intramolecular interactions and reversible domain unfolding [7, 20]. Since recently identified intramolecular interactions within VWF shield and “hide” a significant fraction of the length of its dimeric subunits, they can be expected to significantly reduce the initial force sensitivity of VWF by reducing the effective

multimer length, thus likely promoting the initial compact, inactive conformation of VWF [20]. Once sufficient force is reached to provide a first significant length gain by dissociation of the weaker interactions, dissociation also of stronger interactions and thus further elongation can be expected to be triggered in a cascade-like fashion due to the positive feedback between length and force, unless rapid relaxation of the multimer can occur. In this context, the flow profile encountered in the blood stream plays an important role. Elevated elongational flow components, as found at sites of vascular injury [3, 4, 7], are especially effective in promoting elongation of VWF, as they allow for alignment of the multimer with the direction of flow and thus prolonged exposure to force [21, 22]. Undisturbed blood flow, in contrast, which resembles simple shear flow [23], possesses a significant rotational flow component, resulting in tumbling of the molecule and thus facilitating more efficient relaxation [4, 21, 24].

To fully comprehend how intramolecular interactions and transitions regulate VWF's force sensing and force-induced activation at the molecular level, a comprehensive characterization of their stability, in particular of the kinetics of both dissociation and re-association under physiologically relevant forces, is of outstanding interest. Moreover, it should be studied to which degree the stability and kinetics can be tuned by external parameters. This may have far-reaching physiological implications, since activation of VWF may not be purely force-induced, but also supported by changes of the local environment occurring in connection with vascular injury, such as for instance local pH changes [25, 26].

With the work presented in this thesis, motivated by the above considerations, I primarily aimed at investigating the mechanical response and the conformational ensemble of VWF's dimeric subunits at the single-molecule level, under varied pH and ionic conditions, to elucidate and thoroughly characterize regulatory conformational transitions that govern VWF's hemostatic activity.

I will first give background on the physiological roles of VWF and on the unique, close interplay between multimer structure, force, and function, which have to be considered in unison to allow for a thorough comprehension of VWF's force-regulation. In this context, I will briefly discuss general considerations about the behavior of polymers in hydrodynamic flow and, in particular, review the current state of knowledge on the molecular basis of the mechano-regulation of VWF's hemostatic activity. An interim conclusion will be drawn to point out open questions and to motivate the research I conducted.

After introducing the employed experimental methods and materials (chapter 2), I will present the results of my studies and discuss them in detail, in particular with regard to their implications for VWF's physiological roles. Here, I will first describe a marked impact of the pH on the conformation and mechanical resistance of VWF, as inferred from a combination of atomic force microscopy (AFM)-based single-molecule force spectroscopy and AFM imaging (chapter 3). Next, I will present and validate a novel approach for protein force spectroscopy based on magnetic tweezers (MT), which allows for parallel measurements at constant and low forces (chapter 4). Application of this approach to VWF's dimeric subunits allowed for directly probing several interactions and force-induced transitions within VWF (chapter 5), including observation of a previously predicted interaction at very low forces on the order of only 1 pN, and discovery of a previously unknown transition within an individual domain of VWF. In the last results chapter (chapter 6), I will present the use of single-molecule AFM imaging for determining the multimer size distribution of VWF, which is of utmost importance for VWF's

activity, and for gaining insights into pathological processing defects of VWF. Finally, I will summarize the insights gained from my work in a brief conclusion and point out possible future lines of research that could help to further deepen the understanding of the molecular mechanisms underlying VWF's intricate mechano-regulation.



# Chapter 1

## Biophysics and physiology of von Willebrand factor (VWF)

In this chapter, I briefly want to give a background on the physiological importance and the extraordinary biophysical properties of von Willebrand factor. First, physiological functions and pathological dysfunctions of VWF will shortly be described. Key to VWF's functional diversity are its highly complex multi-domain and multimeric structure and its remarkable responsiveness to hydrodynamic forces in the vasculature, and these aspects will be addressed in detail. In particular, the force-induced activation and down-regulation of VWF's hemostatic function, which make VWF a highly fascinating system from a biophysical point of view, will be discussed. Finally, I will summarize to which extent the molecular mechanisms that underlie VWF's mechano-regulation are understood, and will draw an interim conclusion to motivate the research I conducted within the framework of this thesis.<sup>1,2</sup>

### 1.1 Physiological roles and von Willebrand disease

The central and best-described function of the plasma glycoprotein VWF is its role in primary hemostasis. At sites of vascular injury, where conditions of elevated hydrodynamic forces are present, VWF recruits platelets to the damaged endothelium, thereby inducing formation of a platelet plug and initiating wound closure. Efficient binding of VWF to platelets and sub-endothelial collagen correlates with the force-induced transition of VWF molecules from a rather globular to an elongated "string"-like conformation [5, 27]. The string-like structure of VWF results from its linear multimeric nature, and the extraordinary length of multimers (up to several  $\mu\text{m}$ ) is key to VWF's sensitivity to hydrodynamic forces. The structure and biosynthesis

---

<sup>1</sup>Section 1.1 and the summary of previous AFM-based force spectroscopy measurements on page 16 in section 1.4 are adapted from a review article that I authored and that was published in *Advances in Biological Regulation*, vol. 63, pp. 81-91, 2017, as *Biophysical approaches promote advances in the understanding of von Willebrand factor processing and function* by Achim Löff, Jochen P. Müller, Martin Benoit, and Maria A. Brehm.

<sup>2</sup>Section 1.4 closely follows a review article that I authored and that was published in the *Journal of Cellular Physiology*, vol. 233, pp. 799-810, 2018, as *A biophysical view on von Willebrand factor activation* by Achim Löff, Jochen P. Müller, and Maria A. Brehm.

of VWF multimers will be described in the next section, and the force-activation of VWF for its hemostatic function will be discussed in detail in section 1.4.

A second vital, yet likely force-independent, function of VWF related to hemostasis is to act as a transporter of coagulation factor VIII, which circulates in the bloodstream bound to VWF and is thereby protected from otherwise rapid degradation [28].

In addition to its functions in hemostasis, VWF has been described to be involved in a remarkably wide variety of other processes. For instance, VWF has been reported to act as a negative regulator of angiogenesis [29], to be able to stimulate smooth muscle cell proliferation [30, 31], to contribute to platelet and tumor cell apoptosis [32] as well as to inflammatory processes [33–35], to directly interact with neutrophil extracellular traps [36], and to influence physiological bone remodeling via its interaction with osteoprotegerin [37]. In the work performed in the framework of this thesis, however, I focused on VWF's central role in primary hemostasis.

The importance of VWF for primary hemostasis is illustrated by von Willebrand Disease (VWD), the most common hereditary bleeding disorder, which arises from a variety of mutations in the VWF gene (reviewed *e.g.* in [12]). Three types of VWD have been defined: While type 1 is characterized by low levels of functional VWF, patients with type 3 have virtually no VWF in their plasma and platelets. In VWD type 2, VWF exhibits structural and functional defects [11]. Type 2 is further divided into subtypes 2A, 2B, 2M and 2N. VWD 2A is associated with a significant reduction of high molecular weight multimers (HMWM), resulting in deficits in platelet-dependent function of VWF. 2M shows a similar phenotype, although HMWM are present at almost normal levels. 2B exhibits lack of HMWM due to enhanced VWF proteolysis or due to increased platelet binding. The latter often leads to strongly reduced platelets counts (thrombocytopenia). In subtype 2N, mutations diminish factor VIII binding, leading to a phenotype similar to hemophilia A [38]. Furthermore, VWF is also involved in arterial [39] and venous thrombosis [14] as well as stroke [15, 16, 40].

## 1.2 Domain organization, structure and biosynthesis

### General structure and domain organization

VWF circulates in the bloodstream in the form of linear multimers that can reach immense lengths above 15  $\mu\text{m}$  [5]. In these linear multimers, large multi-domain monomers are C-terminally connected in a tail-to-tail fashion via three disulfide bonds [43–45], and the resulting dimers are N-terminally linked in a head-to-head fashion via two disulfide bonds [46] (Fig. 1.1B). Consequently, dimers are the smallest repeating subunits of VWF multimers.

The domain organization of a VWF monomer, following the domain annotation introduced by Zhou *et al.* [41], is depicted in Fig. 1.1A. Monomers are synthesized as a preproprotein including a short signal peptide sequence (amino acids 1-25) and a propeptide sequence comprising the two domains D1 and D2 (aa 26-763) in addition to mature VWF (aa 764-2813), which comprises domains D'D3, A1, A2, A3, D4, C1 to C6, and the so-called C-terminal cystine knot domain (CK) [12, 43]. While the full preproVWF monomer has a mass of  $\approx 309$  kDa, the mature monomer is reduced to approximately  $\approx 226$  kDa. The static length of a mature monomer is roughly 70 nm [47] (see Figs. 1.1 and 1.2).

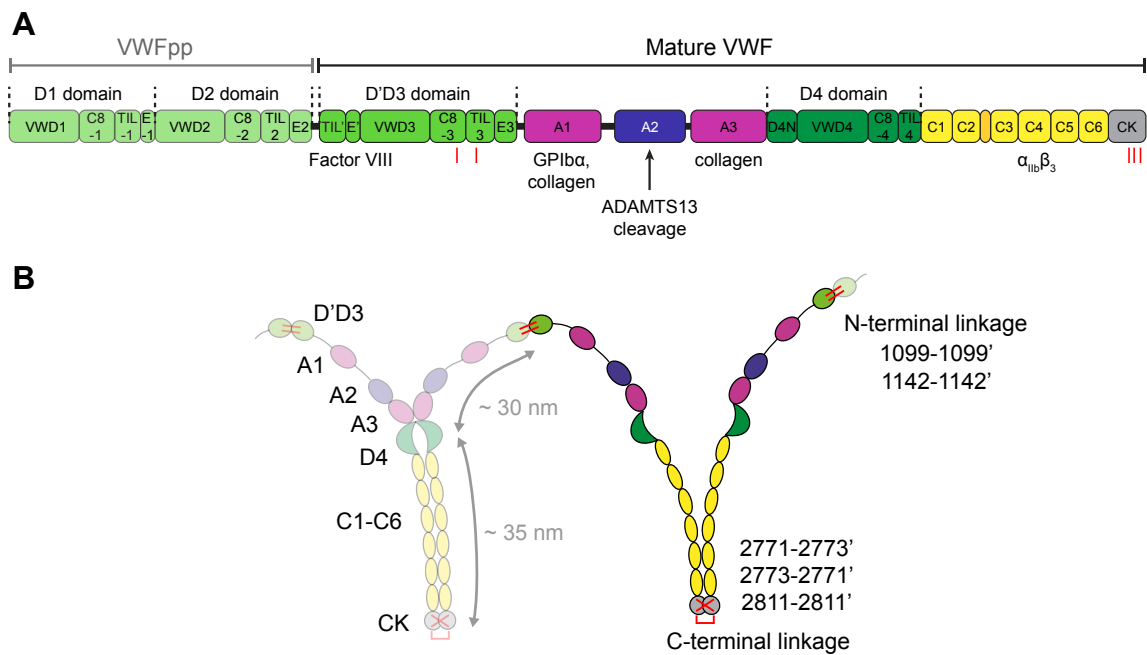


**Figure 1.1: Structure and domain organization of VWF.** (A) Domains of the VWF propeptide (pp) and of mature VWF, following the annotation introduced in [41], with locations of binding sites for specific binding partners. Red lines beneath the CK and the D'D3 domain indicate cysteine residues that form disulfide bonds during dimerization and multimerization, respectively. (B) Linear VWF multimers are built from dimers as smallest repeating subunits, which are linked in a head-to-head fashion via the disulfide bonds Cys1099-Cys1099' and Cys1142-Cys1142' between their N-terminal D'D3 domains. Dimers consist of two monomers that are linked in a tail-to-tail fashion via the disulfide bonds Cys2771-Cys2773', Cys2773-Cys2771', and Cys2811-Cys2811' between their C-terminal CK domains. The C-terminal C domains can zip up into a compact "stem" with a length of approximately 35 nm. Panel B adapted from [42].

The N-terminal D and A domains of VWF are significantly larger than the C-terminal domains C1 to C6 and CK. All domains except the D domains, which are assemblies of several distinct submodules, were reported or predicted to adopt an approximately globular structure [47]. D4 was shown to exhibit an overall crescent-like shape in transmission electron microscopy [41], but no high-resolution structure of D4 is currently available. In D'D3, which has very recently been crystallized, submodules VWD3, C8-3, TIL3, and E3 form a compact entity with the latter three modules being wrapped around VWD3, whereas submodules TIL' and E', which contain the binding site for factor VIII, protrude from the rest of the assembly [48]. High-resolution structures are further available for the three A domains [49–52] as well as for domains C4 [53] and CK [44].

With exception of domains A1, A2, and A3, which possess a hydrophobic core, domains in VWF are mainly stabilized by a remarkably large number of intradomain disulfide bonds [4, 12]. Importantly, all domains except A2 have been predicted to be protected against force-induced unfolding by long-range (in sequence) disulfides connecting residues close to their termini [41]. Furthermore, VWF is heavily glycosylated with both O- and N-linked glycans. Glycosylation is most abundant in two flexible linker regions flanking the A1 domain [4, 41].

## Domain functions

Special functions have been assigned to most domains. The propeptide domains D1 and D2 are essential for multimerization, as they mediate orderly association of dimers [54], as will be described below.

D'D3 can form two disulfide bonds with another D'D3 domain via its cysteines Cys1099 and Cys1142, thereby facilitating N-terminal multimerization [46]. Furthermore, D'D3 contains the binding site for coagulation factor VIII, located primarily in submodules TIL' and E' [12, 48, 55]. A1 possesses binding sites for collagen and, importantly, for platelet glycoprotein GPIb $\alpha$  [4, 8]. The A1–GPIb $\alpha$  interaction is central for the hemostatic function of VWF, as it is crucial for recruitment of platelets to the injured vessel wall and formation of platelet plugs [4, 8, 27].

A2 is the only domain in VWF not stabilized against domain unfolding by disulfide bonds [41], and reversible force-induced unfolding of A2 has been demonstrated at forces relevant for VWF multimers in the blood flow [7, 56]. Since a cryptic cleavage site for the protease ADAMTS13 (a disintegrin and metalloprotease with a thrombospondin type 1 motif, member 13) buried in A2 becomes accessible only upon A2 unfolding [7, 50, 57, 58], the force-induced unfolding of A2 is a prerequisite for the enzymatic control of multimer size and consequently for the down-regulation of VWF's hemostatic activity, as the activity of a VWF multimer depends on the multimer size, as will be discussed in the following sections. Furthermore, A2 unfolding has implications for the elongation behaviour of VWF in the bloodstream under elevated flow conditions, as will also be discussed in the following sections.

A3 is the main collagen binding domain of VWF [59–61] and thus mediates binding of VWF to the damaged subendothelium at sites of vascular injury.

In work that I was involved in, D4 was recently shown to critically influence the structure and force response of VWF by formation of a strong intermonomer interaction that markedly decreases the effective multimer length [20], as will be described in more detail in section 1.4. Domains C1 to C6 allow for a "zipping" of the C-terminal segments of the two VWF monomers within a dimer into a compact stem under acidic conditions [47], which is important during the biosynthesis of VWF, as described below. Recently, it was furthermore shown that also at physiological, neutral pH, intermonomer interactions between the C domains influence the compactness of dimers and thus may tune the effective length of a multimer. This aspect will also be discussed in section 1.4.

C4 additionally comprises the binding site for the platelet integrin GP2b3a, also known as  $\alpha_{IIb}\beta_3$  [41, 43].

CK is responsible for C-terminal dimerization of VWF monomers *via* disulfide bonds involving its three cysteines Cys2771, Cys2773, and Cys2811 [44].

## pH-guided biosynthesis and multimerization

The rather complex biosynthesis of VWF multimers, which takes place only in megakaryocytes (the precursor cells of platelets) and vascular endothelial cells [43], can be divided into different steps that are spatially separated and exhibit different pH requirements. As will be outlined in the following, the pH changes that VWF encounters in different cell compartments critically guide its correct biosynthesis and multimerization by inducing structural transitions.

After synthesis as preproteins, VWF monomers are transported to the endoplasmatic reticulum (ER) (Fig. 1.2A), which possesses an approximately neutral pH [12, 43]. Here, the

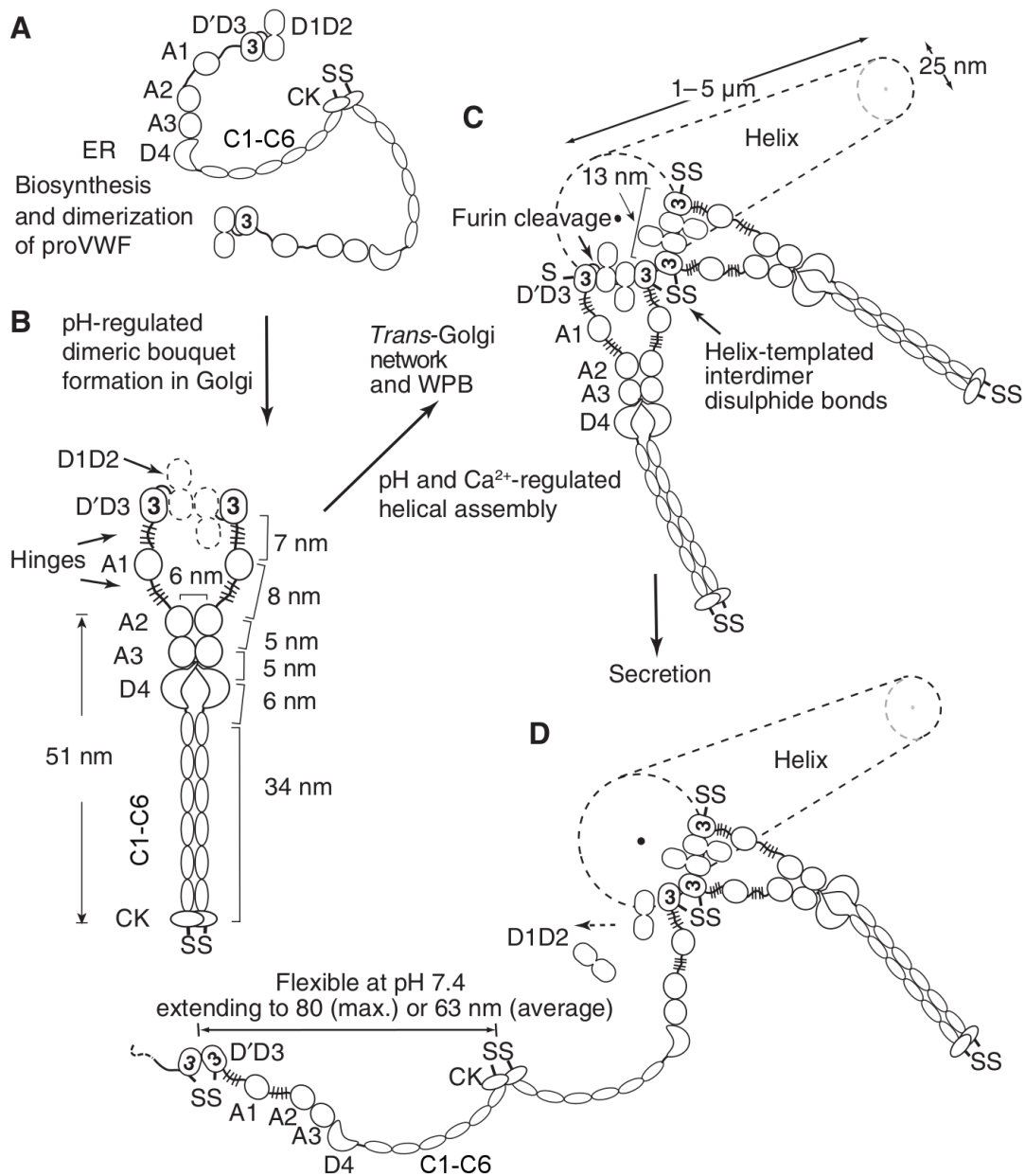


**Figure 1.2: Biosynthesis of VWF.** (A) In the ER, at an approximately neutral pH of 7.4, proVWF monomers are N-glycosylated and most of the disulfide bonds present in mature VWF are formed. Monomers are dimerized by C-terminal linkage *via* formation of disulfide bonds between their CK domains. (B) At the slightly acidic pH of the Golgi (pH  $\approx$  6.2), dimers adopt a more compact conformation due to formation of C-terminal stems. In addition, further O-glycans are added. (C) Triggered by the acidic pH of the trans-Golgi network and WPB (pH  $\approx$  5.5), dimers self-assemble into tightly packed helical tubules and are multimerized *via* disulfide bond formation between their D'D3 domains. The propeptide, comprising domains D1 and D2, is cleaved by furin. (D) The resulting mature VWF multimers are stored in WPB until stimulated secretion into the bloodstream. At the physiologic blood pH of 7.4, the constituent dimers adopt a more flexible conformation. Figure adapted with permission from [47].

signal peptide is cleaved and the resulting proVWF monomers are equipped with N-linked glycans. Furthermore, the majority of disulfide bonds present in mature VWF are formed [3, 12], and monomers are dimerized *via* C-terminal linkage. Dimerization involves formation of the three disulfide bonds Cys2771-Cys2773', Cys2773-Cys2771', and Cys2811-Cys2811' between the two CK domains [44, 45] (see also chapter 6). Recently, in work that I was involved in, it was shown that dimerization is catalyzed by protein disulfide isomerase (PDI) [45].

The next step of processing, addition of O-linked glycans, occurs in the Golgi [43] (Fig. 1.2B), where VWF dimers encounter a slightly acidic pH of approximately 6.2. Electron microscopy (EM) performed on VWF dimers immobilized onto an EM grid at this pH revealed that most dimers adopted a compact conformation, with the C-terminal portions of two monomers –from the CK domain up to A2– within the dimer being zipped up to form a compact "stem" [47] (Fig. 1.2B). This conformation was termed "dimeric bouquet" [47]. Such compact stems were also observed for truncated dimers only comprising domains A3-CK or D4-CK, indicating that domains N-terminal of D4 are not essential for stem formation. In contrast, addition of a specific protease that targets a cleavage site within the D4 domain to the D4-CK constructs resulted in mostly unzipped dimers, suggesting a central role of D4 for stem formation under acidic conditions.

Regarding the potential mechanism underlying the pH-dependent stem formation, an involvement of protonation of histidine sidechains was proposed [47]. This assumption was based on a pH titration curve of the fraction of flexible dimers observed in EM, obtained at pH values between 4.4 and 8.6, which reached its half-maximum at a pH value around 6.5, close to the  $pK_a$  value of histidines. Furthermore, stem formation was not inhibited by high salt concentrations of up to 2 M NaCl, which suggested that stem formation does not rely on simple electrostatic interactions, but on more specific interactions such as hydrogen bonds involving histidine sidechains.

After processing in the Golgi, VWF dimers are transported further on through the trans-Golgi network and to Weibel-Palade bodies (WPB) (Fig. 1.2C), which is accompanied by a further decrease of the pH to a value of approximately 5.5 [43, 54, 62]. WPB are secretory granules that are uniquely found in vascular endothelial cells. Triggered by the low pH and the high  $Ca^{2+}$  concentration of the trans-Golgi, dimers self-assemble into tightly packed helical tubules and are multimerized by formation of disulfide bonds Cys1099-Cys1099' and Cys1142-Cys1142' between their N-terminal D'D3 domains [46, 54]. The formation of helical tubules is thought to ensure orderly association of the D'D3 domains of neighbouring dimers, thereby enabling correct multimerization, yielding linear multimers.

It has been demonstrated by EM that individual D'D3 domains form dimers under acidic, but not under neutral pH conditions [47], and that D'D3 dimers together with the VWF propeptide domains D1 and D2 are sufficient for the self-assembly of helical tubules very similar to the tightly packed tubules of full-length VWF observed in WPB. This tubule formation only occurred under acidic pH conditions and in the presence of  $Ca^{2+}$ . The pH dependence of tubule formation is in all probability mediated by histidine residues. Phylogenetic analyses allowed to identify 13 highly conserved histidine residues in domains D1, D2 and D'D3 [63]. In particular, the two histidine residues His395 and His460 in the D2 domain were found to be essential for correct multimerization.

Importantly, a prerequisite for the formation of tightly packed tubules of full-length VWF appears to be the above-mentioned pH-regulated compactness of dimers with their C-terminal portions forming a rigid stem. Tight packing of VWF in WPB is further thought to be supported by the fact that the pH of mature WPB is close the isoelectric point of VWF [62, 64], which minimizes electrostatic repulsion.

Helical assembly further goes along with cleavage of the propeptide domains D1 and D2 by the enzyme furin, which however remain associated to the mature part of VWF until secretion [3, 12, 47].

In WPB, VWF multimers are stored in the highly compact, tubular form until secretion into the bloodstream [43] (Fig. 1.2D). For the sake of completeness it should be mentioned that in addition to a stimulated pathway of secretion, VWF is also secreted constitutively [65]. After secretion, multimers encounter the approximately neutral pH 7.4 of the vasculature. Efficient secretion by exocytosis of WPB likely is promoted by an increasing flexibility of dimers at this pH as compared to acidic conditions, and by electrostatic repulsion resulting from the rise in pH. Based on EM images obtained at the physiological pH of 7.4, which did exhibit only flexible or loosely associated dimers [47], it was claimed that the constituent dimers of VWF multimers adopt a nearly fully flexible conformation in the blood [3, 4, 47]. However, these experiments as well as earlier EM studies [66] were performed in the absence of divalent ions or even in the presence of EDTA. In contrast, in recent work that I was involved in, a prominent and mechanically stable intermonomer interaction mediated by VWF's D4 domain was identified that crucially depends on divalent ions and that under near-physiological conditions is present in roughly one-half of all dimers [20]. This interaction and its implications, as well as further C-domain interactions present at physiologic pH, will be described in more detail in section 1.4.

### 1.3 VWF as a force-sensing polymer in hydrodynamic flow

The prerequisite for VWF's sensitivity to hydrodynamic forces in the bloodstream is the extraordinary length of its linear multimers. Importantly, the peak force acting on an extended linear polymer in a flow gradient scales strongly –roughly quadratically– with multimer length [4, 6, 7]. This can be intuitively rationalized considering that, first, larger multimers experience a larger flow gradient than smaller ones as they cross more shear lamina, and that, second, larger multimers possess more subunits and the forces acting on all subunits of the multimer add up. More formally, one may for instance model the extended polymer as a bead–rod chain and apply Stoke's law to obtain the peak forces on the polymer, which act on the center of the polymer [6].

The situation before elongation of the linear polymer is however more complex and strongly depends on the flow profile. Therefore, to gain an understanding of the forces acting on VWF multimers in the bloodstream, an understanding of the flow profiles found in the circulation obviously is of great importance. However, blood –containing a variety of cells, proteins, ions *etc.*– is a complex non-Newtonian fluid and flow conditions vary significantly between different parts of the circulatory system [23]. Effects of crowding and margination effects, resulting from cell depletion close to the vessel walls due to hydrodynamic lift forces [67–69], further complicate the matter. Thus, a comprehensive treatment of the interplay of VWF with the hydrodynamic flow profiles encountered in the vasculature is beyond the scope of this thesis. Still,

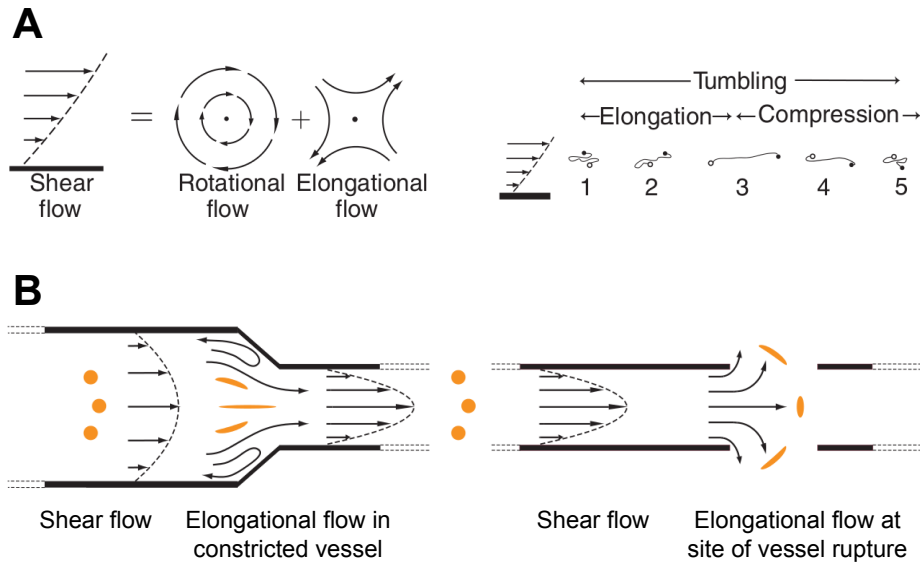


**Figure 1.3: VWF as a linear polymer in shear and elongational flow.** (A) Linear polymers subjected to steady shear flow. Simple shear flow can be conceptualized as superposition of a rotational and an elongational flow component with equal magnitudes (left). Consequently, a linear polymer will in shear flow undergo a tumbling motion with alternating periods of higher and lower extension (right). (B) Elevated elongational flow at sites of vessel rupture and vasoconstriction. The simple shear flow profile assumed for an idealized vessel is distorted e.g. at sites of vasoconstriction (left) or vessel rupture (right), resulting in an elevated elongational flow component. Elongational flow facilitates alignment and more efficient elongation of linear polymers. Orange shapes schematically indicate the expected elongation of VWF subjected to the respective flow profiles. Figure adapted with permission from [3].

a few very simple considerations already can provide important insights for comprehension of VWF's force sensing ability.

In healthy arteries, blood can usually be described as a Newtonian fluid, and laminar shear flow with a parabolic velocity profile can be assumed [23]. Under the assumption of non-slip boundary conditions at the vessel wall, such a flow profile is characterized by the flow velocity  $u(r)$  and the shear rate  $\dot{\gamma}$ , which simply is the velocity gradient in direction of  $r$ , i.e. perpendicular to the flow direction [24]:

$$\dot{\gamma} = \frac{\partial u(r)}{\partial r}. \quad (1.1)$$

The wall shear stress resulting from the blood flow across the vessel wall is given by

$$\tau = \eta \cdot \frac{\partial u(r)}{\partial r} = \eta \cdot \dot{\gamma}, \quad (1.2)$$

where  $\eta$  is the dynamic viscosity of blood, which is approximately four times as high as the dynamic viscosity of water [23].

Importantly, simple shear flow can be conceptualized as superposition of an elongational and a rotational flow component with equal magnitudes [24] (Fig. 1.3A). As a consequence of the rotational flow component, a linear polymer subjected to steady shear flow will undergo a

tumbling motion and exhibit periodic fluctuations in its extension (Fig. 1.3A), as observed both in simulation and experiment [24, 70]. This implicates that VWF under conditions of normal blood flow can be expected to hardly stay in an elongated conformation for an extended period of time due to the rapid relaxation associated with tumbling.

In contrast, much more efficient elongation of a linear polymer is facilitated when the elongational flow component is elevated. The extreme case of steady elongational flow, for which the rotational flow component is absent, is defined by a linear velocity gradient along the direction  $x$  of flow and therefore can be described by the strain rate  $\dot{\epsilon}$  [22]:

$$\dot{\epsilon} = \frac{\partial u(x)}{\partial x}. \quad (1.3)$$

In such a purely elongational flow profile, significant stretching of a linear polymer in the flow direction sets in at markedly lower rates as compared to simple shear flow, as the polymer will align with the direction of elongational strain and maintain this alignment over time [22, 24, 70]. Consequently, elongational flow should be especially effective for elongation and activation of VWF, as multimers are subjected to higher forces and experience these forces for a longer period of time [4, 21].

Importantly, flow profiles with an elevated elongational component are indeed found in the circulation at sites of vascular injury –*i.e.* where VWF needs to be activated–, resulting from constriction of vessels in the wake of injury or from outflow at vessel rupture sites [3, 4] (Fig. 1.3B). Moreover, conditions of elevated elongational flow also occur in pathologically stenosed vessels, where VWF can provoke thrombotic occlusions [4, 10].

To allow for connecting the elongation of VWF to underlying force-induced molecular transitions, estimates of the forces that VWF multimers experience in the bloodstream are of interest. Based on a simple model describing VWF as a rigid chain of beads connected by rods [71], Zhang *et al.* estimated the maximum force reached for a fully extended 200-mer subjected to a relatively high shear stress of  $100 \text{ dyn/cm}^{-2}$  to be on the order of 100 pN [7]. However, in this picture VWF was modeled as rigid and fully extended, so that tumbling due to rotational flow components –as present in shear flow–, which is accompanied by alternating extension and relaxation, was not taken into account. As the tumbling timescale depends both on the multimer length and the shear rate, and as VWF may only reach its highest extension for a short period of time during a tumbling cycle, it is not trivial to determine at which point during tumbling VWF will experience the highest force [7, 24].

In order to obtain a more realistic estimate of the maximum force acting on a flexible VWF multimer in shear flow, Zhang *et al.* aimed at considering the point of maximum elongation during a tumbling cycle. They assumed this maximum elongation to be reached under an angle of  $\theta = 3^\circ$  relative to the direction of flow, as had been suggested by coarse-grained simulations modeling polymers as chains of beads connected by springs and interacting according to a Lennard-Jones potential [72]. Multiplying the maximum force of 100 pN obtained for the rigid case by  $\sin(2\theta)$  thus yielded an estimate of  $\approx 10$  pN for the maximum force reached in the center of a 200-mer subjected to a shear stress of  $100 \text{ dyn/cm}^{-2}$  [7], in quantitative agreement with another computational study [21].

These estimates are further in line with the range of forces at which physiologically relevant

molecular transitions in VWF, such as unfolding of A2 domains and dissociation of inter-monomer interactions, have been observed experimentally, as will be described in the following section.

## 1.4 Force-induced activation and down-regulation of VWF

Platelet adhesion to subendothelial matrix proteins and platelet aggregation are crucial initial steps for the formation of hemostatic plugs at sites of vascular injury. These processes are highly complex and dynamic and involve a variety of specific adhesion receptors and ligands, as reviewed for example in [8, 9]. As mentioned above, a key player in platelet adhesion and aggregation is the large, multi-domain and multimeric plasma protein VWF. Via its domains A1 and A3, VWF can bind to constituents of the extracellular matrix of the subendothelium, for instance to different types of collagen (reviewed in [73]). VWF can further directly interact with platelets, as it exhibits binding sites for the N-terminal domain of GPIb $\alpha$  [74], which is part of the platelet membrane receptor complex GPIb-IX-V, and for the platelet integrin  $\alpha_{\text{IIb}}\beta_3$ , located in its A1 [75] and C4 domain [76], respectively.

VWF circulates in the plasma in the form of multimers that comprise a varying number of linearly connected monomeric subunits (*cf.* section 1.2 and Fig. 1.1) [43]. VWF multimers can reach an immense length, in the order of several micrometers, but adopt a loosely collapsed, globular conformation under normal blood flow conditions [5]. In this form, VWF can bind coagulation factor VIII [77], while exhibiting only a very low affinity to platelets [8, 9].

The prerequisite for an increase in the affinity, and thus, binding of the VWF A1 domain to platelet GPIb $\alpha$ , is that VWF experiences increased hydrodynamic forces [78] due to alterations from the normal blood flow profile, in particular as a result of increased elongational flow [4, 7, 21]. Such conditions can for instance be found at sites of vascular injury where vasoconstriction reduces the vessel diameter, thereby increasing hydrodynamic forces enough for VWF multimers to be elongated, resulting in efficient binding of VWF to subendothelial collagen [5]. When immobilized, a VWF multimer experiences further increased tensile force along its contour, which promotes activation of binding to platelet GPIb $\alpha$  [17]. The latter also holds for VWF multimers still bound to the surface of endothelial cells after stimulated secretion [79–81]. Furthermore, pathologically high shear rates can occur in stenosed vessels or at prosthesis. In this case, the A1-GPIb $\alpha$  interaction can even mediate adhesion and aggregation of non-activated platelets without involvement of integrins [27].

Remarkably, also the down-regulation of VWF's hemostatic activity is induced by force, as it relies on enzymatic cleavage of VWF at a cryptic cleavage site buried within VWF's A2 domain. This site is only accessible for cleavage by the enzyme ADAMTS13 upon force-induced unfolding of A2 [7, 50, 57, 58], which in single-molecule force measurements on isolated A2 domains using optical tweezers (OT) has been demonstrated to occur at forces of approximately 10 pN [7]. As such forces can be expected to be readily reached only for larger multimers [7], this force-dependent cleavage mechanism provides a means to preferably cleave the largest and hemostatically most active multimers. Refolding of A2 against force was observed to be relatively slow, so that it can stay in the unfolded state long enough to allow for cleavage by ADAMTS13 [7], if the multimer experiences force for an extended period of time. In the absence of force, in contrast, fast and reliable refolding of A2 was observed, which very likely

is important to prevent excessive cleavage. The importance of this mechano-enzymatic down-regulation of VWF's hemostatic potential is underlined both by VWD-related mutations that cause enhanced ADAMTS13 cleavage, for instance by destabilizing the A2 domain [82], and by pathological disorders resulting from deficient cleavage, such as thrombotic thrombocytopenic purpura [83].

The regulation of VWF's hemostatic activity by hydrodynamic forces is not only highly intriguing from a biophysical perspective, but also of eminent physiological importance. While VWF-mediated platelet aggregation is necessary at sites of vascular injury, it would rapidly induce thrombotic occlusions if activated under normal blood flow conditions. However, whereas the molecular mechanism of VWF's down-regulation appears to be quite well understood, the current picture of the force-induced conformational changes that lead to activation of VWF is less complete.

Especially in the last decade, tremendous efforts have been made to apprehend the molecular basis of the complex mechano-regulation of the VWF A1-GPIb $\alpha$  interaction. In the following, I will give a brief overview on different regulatory mechanisms that likely are involved in VWF's force-induced activation. For a more extensive discussion, the reader is referred to a recent review I authored [84]. The mechanisms regulating the A1-GPIb $\alpha$  interaction can roughly be grouped into two main pictures. First, the A1 domain likely is initially "shielded" and only accessible for GPIb $\alpha$  binding upon force-induced elongation of VWF and opening of intramolecular interactions under elevated flow conditions. Second, the A1-GPIb $\alpha$  bond *per se* may possess an intrinsic force dependence and exhibit an enhanced affinity upon loading with force, resulting from force-induced conformational changes within A1 and/or GPIb $\alpha$ .

### The globule–stretch transition of VWF

It has been shown that VWF multimers adopt a loosely collapsed, globular conformation in solution [5], but the precise nature of the interactions that promote this conformation is not yet well understood. However, it can be assumed that recently discovered specific intermonomer interactions contribute by promoting a compact conformation of the individual dimers within a multimer [20]. Very likely, also additional interactions between the different dimers of a multimer are involved. Such inter-dimer interactions might be of a more unspecific nature, for example based on electrostatic or van der Waals interactions or on hydrophobic effects.

When subjected to hydrodynamic forces above a certain threshold, globular multimers undergo an abrupt transition into an elongated, "stretched" form [5, 72], and this elongation of VWF was shown to correlate with efficient binding to subendothelial collagen [5], and to be a prerequisite for binding to platelet GPIb $\alpha$  [17]. In the vasculature, this conformational change likely occurs primarily at sites of vascular injury or in stenosed vessels, where alterations from the normal blood flow profile can be expected to result in increased elongational forces acting on VWF multimers [4, 7, 21]. A key aspect to comprehend the abruptness of VWF's elongation is the positive feedback between the effective length of a multimer and the hydrodynamic force it experiences in flow [4, 7, 20]. In other words, initial partial stretching of a multimer leads to higher forces acting on the multimer, which in turn promote further elongation. Here, elongational flow is particularly effective, as the relaxation of a multimer is suppressed compared to simple shear flow [7, 21, 22]. Also due to the relation between multimer length and force, larger

multimers –comprising more dimeric subunits– will experience higher forces in the blood flow than smaller ones. Indeed, the latter have been reported to be the hemostatically less active multimers, since in VWD patients the reduction of high-molecular-weight multimers leads to bleeding symptoms (reviewed in [11, 13]). Although trivial, it is important to note that force acting along the contour of a multimer also impacts each domain within the multimer, unless the domains are shielded by intramolecular interactions within VWF [20].

Recent work that I was involved in suggests that force-induced elongation of VWF is not simply an uncoiling of a more or less randomly coiled polymer, but also involves dissociation of a hierarchy of specific interactions within dimeric subunits with different mechanical stabilities. In brief, atomic force microscopy (AFM)-based single-molecule force measurements (*cf.* section 2.2.1) were conducted to pull VWF dimers specifically and in their native force-sensing direction [20]. Specific force–extension traces were identified by using the appearance of two A2 domain unfolding peaks as a positive fingerprint. Under near-physiologic buffer conditions, *i.e.* at pH 7.4 and in the presence of divalent ions, two types of characteristic force–extension traces were obtained at roughly the same ratios: Traces of type II only showed the two A2 unfolding signals, whereas traces of type I additionally exhibited a peak at comparably high forces above  $\approx 50$  pN (*cf.* Fig. 3.1). This peak was shown to result from the dissociation of a strong intermonomer interaction that is mediated by VWF’s D4 domain and crucially relies on divalent ions. As this strong intermonomer interaction, which is present in roughly half of the dimers, initially shields  $\approx 80$  nm of the length of a dimer (see Fig. 1.4), it will significantly decrease the effective length of VWF multimers (up to  $\approx 30\%$ ). Consequently, as the forces acting on a multimer in hydrodynamic flow strongly correlate with multimer length, the strong intermonomer interaction can be expected to considerably affect VWF’s force-sensing ability. Complementarily to the force measurements, AFM imaging was employed to investigate the conformation of VWF dimers. In addition to corroborating the existence of the D4-mediated intermonomer interaction, the AFM imaging data further suggested the existence of interactions between C domains that promote a more compact conformation of the C-terminal stem region in VWF dimers, even at physiologic pH. However, the mechanical resistance of these C-domain interactions was too low to directly observe their dissociation in the AFM-based force measurements, and from AFM imaging data the force required for their dissociation was estimated to be in the range of only 1 pN. Since AFM imaging of VWF multimers did not show prominent interactions between their individual dimeric subunits, it may be assumed that the force response of multimers can be mainly tracked back to the force response of dimers.

Taken together, these findings suggest elongation of VWF to occur in a cascade-like fashion (see Fig. 1.4): weak interactions in the C-terminal stem region of dimers that are not firmly closed by the strong intermonomer interaction are likely the first to open up at low forces. As a consequence of the length increase by unzipping of these stems, the VWF multimer will experience a higher force. If the force becomes high enough and acts for a sufficiently long period of time, unfolding of A2 domains can occur, which will markedly increase the effective multimer length and thus also the force on the multimer. Opening of dimers exhibiting the strong D4-mediated intermonomer interaction may then be the final step of VWF’s elongation. However, it should be noted that the mechanical stability of the strong D4-mediated interaction was probed in measurements with very likely unphysiologically high force-loading rates, and it

appears plausible that *in vivo* dissociation of this interaction may occur already at lower forces. Indeed, as will be described in section 5.2, in magnetic tweezers (MT)-based measurements at constant force I observed dissociation of the strong D4-mediated intermonomer interaction in the same force range as A2 unfolding.

Elongation of VWF presumably leads to increased exposure and accessibility of A1 domains containing the binding site for GPIIb $\alpha$ , thus in principle facilitating multivalent binding events. However, such a simple correlation between elongation of VWF and binding to GPIIb $\alpha$ , as shown for collagen binding [5], has not been observed experimentally. In fact, a recent study showed in microfluidic experiments that force-induced elongation of VWF preceded activation of A1 for GPIIb $\alpha$  binding, and that binding of GPIIb $\alpha$  required higher tension acting on the multimer than necessary for elongation [17]. In line with this, a markedly higher shear rate threshold has been observed for VWF-mediated aggregation of non-activated platelets than for activation of VWF for collagen binding [27]. These observations suggest that at least one force-dependent regulatory mechanism is present within VWF that tunes the affinity of the A1 domain for the platelet receptor GPIIb-IX-V. This hypothesis is supported by the fact that the A1-GPIIb $\alpha$  interaction can be induced even in the absence of force by certain modulators that interact with the A1 domain, for example, the bacterial glycoprotein ristocetin [85–87] or the snake venom protein botrocetin [88, 89].

Mechanisms that have been found to directly regulate the A1-GPIIb $\alpha$  binding will briefly be treated in the following; first, interdomain interactions between the A1 domain (aa 1260-1479) and its neighboring peptide sequences that inhibit its binding activity, and second, an intrinsic regulation of the A1-GPIIb $\alpha$  binding based on a force-induced conformational change of A1.

### Shielding of A1 by neighboring peptide sequences

First indication that A1 domain-neighboring amino acid sequences are involved in the regulation of the A1-GPIIb $\alpha$  interaction has been provided already 30 years ago by experiments that showed that isolated peptides comprising the sequence N-terminal of the A1 domain (aa1232–1261) inhibited binding of purified VWF to platelets [90], and that stepwise deletion of the amino acid segment aa1204–1270 increased binding of the remaining A1 peptide to GPIIb $\alpha$  [91]. A series of studies, as reviewed in [84], confirmed the regulatory effect of the peptide sequence N-terminal of A1, and further established a role also of the sequence C-terminal of A1. Intriguingly, these findings are in line with the location of certain VWD-related VWF mutants. Certain mutations primarily localized in the A1 flanking regions result in VWD type 2B, which is characterized by an increased affinity of VWF for GPIIb $\alpha$  even without prior activation (see *e.g.* [11, 13]). In contrast, type 2M mutations that cause a decreased affinity for platelet GPIIb $\alpha$  are localized primarily in the A1 domain.

It should be noted that the majority of above-mentioned studies relied on assays performed under static conditions and often required the use of modulators such as ristocetin to induce binding of A1 domain variants to GPIIb $\alpha$ . Thus, the implications of the described observations for the physiologically relevant case of binding of A1 to GPIIb $\alpha$  under flow and in the absence of modulators are not entirely clear. However, a handful of studies that also performed experiments under shear flow yielded similar results. In particular, A domain constructs lacking the A1 N-terminal flanking peptide exhibited enhanced binding to isolated GPIIb $\alpha$  as well as to platelets

under flow [92–94].

In addition to the linker regions directly adjacent to A1, also the D'D3 assembly likely inhibits the A1–GPIb $\alpha$  interaction by binding to A1, as indicated by the finding that both addition of antibodies specifically blocking an epitope in D'D3 [95] and deletion of D'D3 [94, 95] resulted in enhanced binding of A1 to GPIb $\alpha$ . Moreover, addition of isolated D'D3 domains led to re-inhibition of GPIb $\alpha$  binding to the VWF construct with a deletion of D'D3 [95].

Finally, also the A2 domain might be able to inhibit binding of GPIb $\alpha$  to A1. A possible inhibitory interaction between A1 and A2 was suggested by the observations that deletion of A1 drastically increased the cleavage of VWF by ADAMTS13 [96] and that a VWF construct with an A2 domain deletion exhibited a slightly increased ristocetin-induced binding to GPIb $\alpha$  [97], and direct interaction of isolated A1 and A2 domains in pull-down experiments was reported [98]. Recently, microfluidic experiments indicated that deletion of the A2 domain yielded a gain-of-function VWF variant with enhanced binding to GPIb $\alpha$  under flow [99], and MD simulations suggested that A1 and A2 may be able to directly interact in the context of the full-length protein [99]. However, to my knowledge, so far an interaction of A1 and A2 in the full-length protein, *i.e.* in the presence of all other domains of VWF, has not been shown experimentally. A further wrinkle is added by a recent study that reported that binding of A2 to A1 depends on the redox state of a disulfide bond between two neighboring cysteines in A2 [100]. Force-spectroscopic approaches that aimed to investigate the potential effect of the A1–A2 interaction using AFM [99] or a biomembrane force probe [100] unfortunately did not provide sufficient controls that single-molecular interactions were probed, and it has to be assumed that also multiple and unspecific interactions have been taken into account. Summarizing, these data suggest that an intramolecular interaction between the domains A1 and A2 exists, but if this interaction in context of the full-length protein has an inhibitory effect on A1–GPIb $\alpha$  binding or rather plays a role in regulation of A2 cleavage by ADAMTS13 requires further experimental investigation.

Taken together, it appears well-substantiated that intramolecular interactions of A1 with its N- and C-terminal flanking peptides, with D'D3, and possibly with A2 shield the GPIb $\alpha$  binding site, at least as long as VWF adopts a globular conformation. Increased hydrodynamic forces may induce translocation of the interacting peptide sequences or domains from A1, thus lifting their inhibitory effects. However, it has so far not been determined which forces are required for dissociation of these interactions. Since their dissociation has not been observed in the AFM-based force measurements described above, it appears well possible that dissociation occurs already at very low forces, and that these interactions may primarily serve to prevent binding of VWF to platelets under normal blood flow conditions. This assumption is further supported by MT-based measurements on dimers over a wide force range, as will be described in chapter 5, that also did not show dissociation of intramonomer interactions involving the A1 domain.

### **Intrinsic force-regulation of the A1–GPIb-IX-V interaction**

The above-described mechanisms for regulating VWF's hemostatic activity are based on initial shielding of the A1 domain by intramolecular interactions and an increased exposure of A1 domains under elevated flow conditions. However, already two decades ago it has been proposed

that A1 also possesses an intrinsic regulatory mechanism, as studies on a series of fragments of the A1 domain had suggested the existence of two different conformations of A1 exhibiting markedly distinct kinetics of binding to GPIIb $\alpha$  [101, 102]. Force acting on A1 may induce the transition from its low-affinity state to a distinct high-affinity conformation. It is important to note here again that A1 is protected from full unfolding by a disulfide bond connecting residues close to its two termini. In recent years, strong experimental evidence for a force-induced conformational transition of A1 to a high-affinity state has been put forward, as reviewed in [84].

The most detailed insights into how the application of force modulates the interaction between A1 and GPIIb $\alpha$  at the single-molecule level have been gained recently by two force spectroscopic studies by Kim *et al.* employing optical tweezers [18, 19]. A protein construct comprising both A1 and the N-terminal domain of GPIIb $\alpha$ , connected by a flexible polypeptide linker, was used to investigate the force dependence of the binding and unbinding kinetics of the A1–GPIIb $\alpha$  bond. Force-induced switching of the bond to a distinct second state was observed at forces above  $\approx 10$  pN [18, 19], in the physiologically relevant force range [7]. This second bond state exhibited a greater force resistance, a markedly longer lifetime due to a lower off-rate [18], and a higher on-rate [19]. Thus, the observed mechanism of force-induced switching to a second high-affinity bond state provides an explanation for the enhanced binding of A1 to GPIIb $\alpha$  under elevated flow conditions. This catch bond-like behavior of A1 can be assumed to markedly stabilize binding under high force, while at the same time allowing for reversibility of binding when force decreases again, as supported by simulations [103]. Importantly, the existence of two distinct bond states –which were observed not only for unbinding, but also for rebinding– again suggests the existence of two different conformational states of A1 already before binding to GPIIb $\alpha$ . This idea is in line with the observation that the modulator ristocetin, which is thought to activate A1 in a manner closely resembling force-dependent activation [86], selectively stabilizes the second bond state [18]. In contrast, for the modulator botrocetin, which induces activation by a different mechanism not resembling force-induced activation [85, 86, 88], only a single bond state was observed [18]. Presumably, binding of ristocetin to the A1 domain induces or stabilizes a configuration of A1 corresponding to its force-induced active conformation. Although due to the artificial connection between the two proteins in this experimental setup also GPIIb $\alpha$  might in principle undergo relevant force-induced conformational changes, it seems reasonable to assume that the observed changes of the affinity of A1 and GPIIb $\alpha$  for each other primarily traces back to conformational changes of A1, since in the physiological case of platelet binding to VWF only A1, but not GPIIb $\alpha$ , is expected to experience significant forces prior to binding [7, 19].

Interestingly, Kim *et al.* further investigated the effect of two gain-of-function mutations in A1 (p.Arg1306Gln) or in GPIIb $\alpha$  (p.Met239Val) that lead to a higher affinity of A1 and GPIIb $\alpha$  for each other and cause type 2B VWD and platelet-type VWD, respectively [19]. Force-induced switching between two different bond association/dissociation pathways was still observed for both of these mutants, at forces similar to the wildtype. In the first bond state at low force, binding kinetics exhibited only modest changes compared with the wt – counterintuitive to the fact that VWF mutants associated with type 2B VWD exhibit enhanced binding to platelets also under static conditions [11]. The second bond state at higher forces, however, showed markedly faster bond association and slower bond dissociation than observed for the wildtype, indicating that type 2B VWD mutations enhance the impact of force on the modulation of the

A1-GPIb $\alpha$  interaction.

The picture of a force-induced transition of A1 to a conformation distinct from its native structure –occurring after autoinhibitory interactions of A1 with other domains are lifted– is fully in line with the very recent observation from microfluidic experiments that elongation of VWF precedes binding of GPIb $\alpha$  [17], implicating that efficient binding requires even higher forces than elongation of VWF. Indeed, the forces required for switching to the second bond state in the OT experiments were above the forces for A2 unfolding –which very likely represents a critical step of VWF’s elongation– observed in other OT studies.

A series of studies have investigated the possible nature of the force-induced conformational change of A1. The conformational transition of A1 to its high-affinity state likely includes local conformational changes in the main binding interface region –for example local unfolding of A1’s  $\alpha$ 2 helix– but possibly also further large-scale structural rearrangements that release strain and allow for enlarging the contact area with GPIb $\alpha$ . However, an extensive discussion of the proposed structural changes is beyond the scope of this brief background chapter, and the reader is again referred to a recent review I authored [84].

## 1.5 Interim conclusion: regulation of VWF’s force sensing and force response by interactions in dimers

The insights into the force-induced activation of VWF from the previous section are summarized in Fig. 1.4: Under normal blood flow conditions, VWF multimers adopt a compact globular conformation that presumably markedly reduces the accessibility of binding sites for subendothelial collagen and platelet receptor GPIb $\alpha$  located in the A3 and A1 domain, respectively. In addition, A1 is shielded by specific, inhibitory intramolecular interactions (Fig. 1.4A). Under elevated flow conditions, as found at sites of vascular injury, multimers experience higher hydrodynamic forces, which above a certain threshold lead to a rather abrupt elongation that correlates with enhanced binding to subendothelial collagen (Fig. 1.4B). Elongation likely also goes along with dissociation of the autoinhibitory interactions of the A1 domain. Efficient binding of A1 to GPIb $\alpha$  is however thought to further require a small-scale conformational change of A1 occurring at forces higher than the ones required for elongation (Fig. 1.4B).

Importantly, regulation of VWF’s initial sensitivity to hydrodynamic forces as well as its elongation behavior can be assumed to be critically influenced by intermonomer interactions –mediated by VWF’s C domains and D4 domain– that initially promote a compact conformation of dimeric subunits and release significant length upon dissociation (Fig. 1.4C). In addition, also unfolding of A2 domains provides a marked increase of the effective multimer length and represents a central step in VWF’s elongation.

There are however a number of open questions regarding these regulatory interactions and transitions within dimers:

First, as explained in section 1.2, it is known that low pH affects the conformation of dimers, but it is not clear to what extent pH changes may influence the force response of VWF. It is important to note that the overall pH in the vasculature is precisely regulated, so that small deviations of 0.1 from the physiological value of 7.4 already represent pathophysiological conditions. Still, it appears well possible that the pH can locally vary, *e.g.* at sites of injury

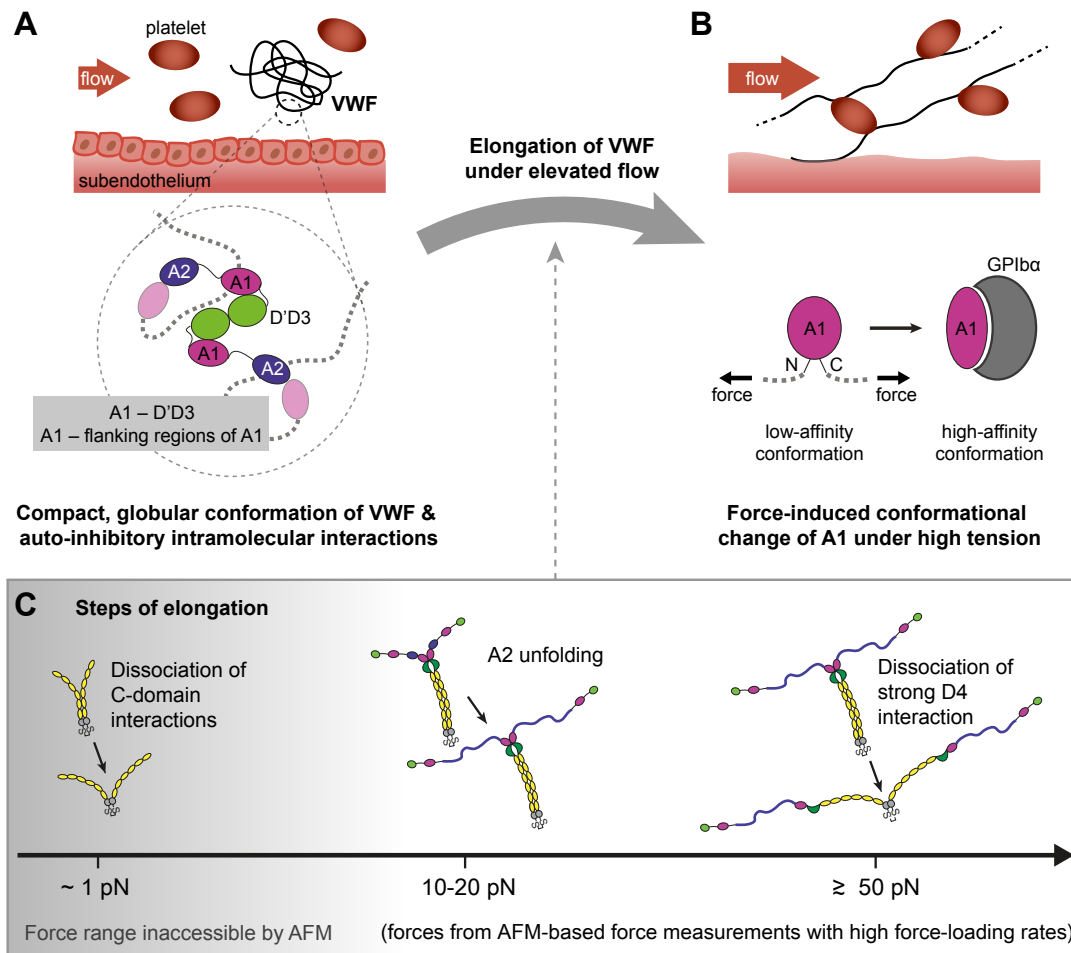


**Figure 1.4: Force-induced transitions during elongation and activation of VWF.** (A) Inactive conformation of VWF under normal blood flow conditions. In healthy vessels, VWF multimers adopt a compact globular conformation that presumably markedly reduces the accessibility of binding sites for subendothelial collagen and platelet receptor GPIIb/IIIa located in the A3 and A1 domain, respectively. In addition, A1 is shielded by specific, inhibitory intramolecular interactions. (B) Force-induced activation of VWF. Under elevated flow conditions, as found at sites of vascular injury, VWF multimers experience higher hydrodynamic forces, which above a certain threshold lead to a rather abrupt elongation that correlates with enhanced binding to subendothelial collagen. Elongation likely primarily relies on dissociation of intermonomer interactions that promoted a compact conformation of dimeric subunits (see panel C), as well as on A2 unfolding, and can be assumed to go along with dissociation of autoinhibitory interactions of the A1 domain. Efficient binding of A1 to GPIIb/IIIa is further thought to require a small-scale conformational change of A1 occurring under high force. (C) Transitions in VWF dimers that likely contribute significantly to elongation of VWF multimers under force. Schematically depicted are intermonomer interactions within VWF dimers, as identified by AFM-based force measurements and AFM imaging at near-physiologic conditions (pH 7.4 and in the presence of divalent ions), and the observed or estimated forces needed for dissociation of the respective interactions. In addition, A2 unfolding is depicted. The stated forces correspond to the ones observed in AFM-based force measurements conducted with high loading rates. The respective forces *in vivo* can be expected to be lower. Importantly, the weak interactions involved in formation of C-terminal stems could not directly be probed by AFM force measurements. Panels A and B adapted with permission from [84].

or inflammation [26, 104–107], and it has been proposed that pH variations could play an important role for activation of VWF by affecting critical flow rates that need to be reached for multimer elongation [25].

Second, C-domain interactions in the stem region of VWF dimers were inferred from AFM images, but could not directly be probed in AFM-based force measurements due to their low mechanical resistance. To fully characterize these interactions and dissect the contributions of individual C domains, force measurements at markedly lower forces in the physiologically relevant force range of down to  $< 1$  pN would be of great interest. However, reliably probing single proteins at such low forces will require novel force spectroscopy approaches.

Third, previous AFM-based force spectroscopy measurements were conducted at high, very likely unphysiological, force-loading rates, implicating that the observed forces required for, *e.g.*, dissociation of the strong D4-mediated intermonomer interaction may be markedly higher than the forces required *in vivo* in the vasculature. Indeed, in OT experiments with much lower loading rates, A2 unfolding was observed at significantly lower forces as compared to AFM-based force measurements. Measurements at constant force would likely more closely resemble the way force acts on a multimer in the bloodstream, and could thus provide more realistic values of critical forces *in vivo* and help to gain a better understanding of the order of events involved in elongation and activation of VWF. Moreover, force-clamp measurements allow to measure rates of different processes more straightforwardly and precisely than in force experiments with variable force, and could thus provide a tool to detect even small alterations in the mechanical stability of an interaction, *e.g.* due to changes of the environment.

Motivated by above considerations, in the framework of my PhD thesis I aimed at gaining a thorough understanding of the interactions and transitions that govern the force-sensing ability of VWF and its extraordinary elongation behavior under force. In the following chapters, I will present a detailed investigation of both the static conformation of VWF dimers as well as of their force response under varied pH and ionic conditions, at the single-molecule level. In particular, I will present a novel approach for MT-based force spectroscopy that allowed for highly parallel force-clamp measurements on VWF dimers under a wide force range, which enabled direct observation of weak interactions in dimeric stems, a thorough characterization of the kinetics of A2 unfolding and folding, and identification of a previously unknown intradomain interaction within VWF's D'D3 assembly. Furthermore, motivated by the importance of multimer size for force sensing, I will present the use of AFM imaging for analysis of VWF multimer size distributions and for characterization of VWF variants with dimerization and multimerization defects.

# Experimental methods and materials

In this chapter, the experimental techniques that I employed within the framework of this thesis –primarily atomic force microscopy imaging and magnetic tweezers-based single-molecule force spectroscopy– will briefly be introduced, and experimental protocols, materials, and data analysis procedures will be described in detail.

## 2.1 Atomic Force Microscopy (AFM) imaging

### Basics of AFM imaging

Since its introduction in the 1980s [109], the atomic force microscope has become one of the most versatile tools for visualization of surface topographies, providing high resolution at the nano- and even atomic scale [108, 110]. For biological applications, *e.g.* for imaging of single biological macromolecules, as conducted also in the framework of this thesis, a major advantage of AFM is the possibility to perform imaging in liquid and thus close to the native environment of biological molecules [111, 112], in contrast to other imaging techniques with similar resolution such as transmission electron microscopy. However, as the molecules of interest have to be adsorbed onto a substrate for imaging, surface effects may play a role. A commonly used substrate is muscovite mica, a sheet silicate that can readily be cleaved to obtain atomically flat surfaces [113]. Moreover, AFM imaging provides information on the sample height in addition to the lateral dimensions. This facilitates, for instance, to identify and distinguish different domains within a protein, as exploited also for work on VWF presented in this thesis (see *e.g.* Figs. 2.2 and 6.3), or to detect ligands bound to the molecule of interest, as I could demonstrate for example for binding of protein disulfide isomerase to VWF [45].

AFM utilizes a sharp tip (tips with an apex radius of a few nanometers are commercially available) on a flexible cantilever beam, which serves as a soft spring to measure force interactions between the sample surface and the tip. These forces can be detected by monitoring the deflection of the cantilever beam. Under the assumption that the cantilever can be described as a simple Hookean spring, a force  $F$  acting on it will lead to a deflection  $s$  determined by its spring constant  $k$ :  $F = k \cdot s$ . Typically, the cantilever deflection is detected by using a laser beam

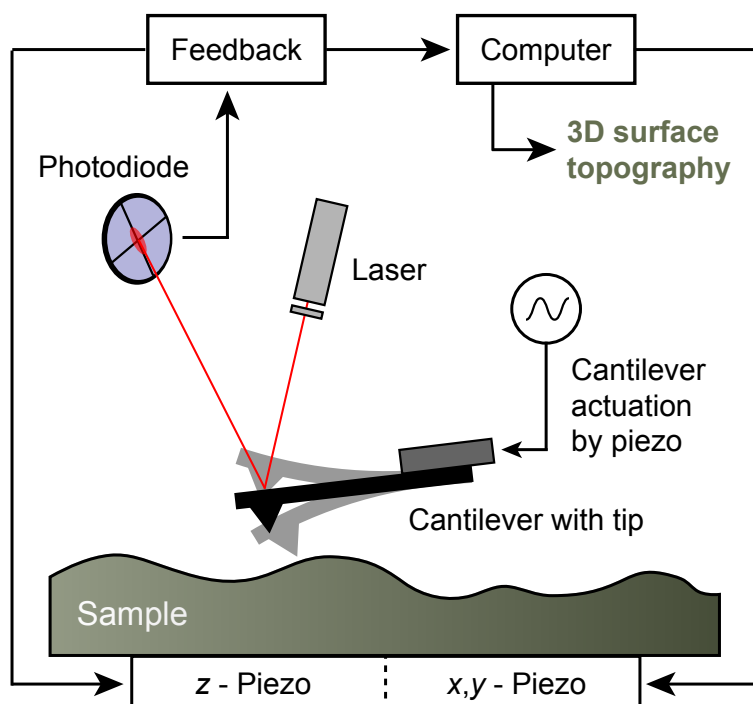


**Figure 2.1: Schematic of AFM imaging in tapping mode.** During a line-wise scan of the sample surface, the AFM cantilever is excited at a constant frequency near its resonance, and its tip intermittently taps the sample surface during the oscillation cycle. The cantilever resonance frequency shifts with changing tip–surface interaction, resulting in a change of the oscillation amplitude and phase. The amplitude is monitored and kept constant by a feedback loop regulating the  $z$ -position of the sample, allowing for reconstruction of the sample surface topography. Graphical representation inspired by Fig. 22.10 in [108].

that is reflected by the cantilever onto a segmented photodiode. A deflection of the cantilever then results in a change in the differential voltage signal recorded by the photodiode. With spring constants of commercially available cantilevers ranging from roughly 10 pN/nm to tens of nN/nm, a sensitivity of 0.1 nm in the deflection measurement allows for the detection of forces from the pN to nN regime.

In order to obtain a three-dimensional topography image of the sample surface, the sample is scanned by a piezo-electric scanner against the tip in the sample plane ( $x,y$ -plane) in a line-by-line pattern, while monitoring the cantilever deflection. Usually, a feedback loop is implemented to regulate the distance between tip and sample surface by also moving the sample in the  $z$ -direction.

AFM imaging can be conducted in a static, so-called contact mode [109], or in a dynamic mode [114] that involves external excitation of the cantilever. In contact mode, the tip is brought into contact with the surface, and the resulting repulsive force is detected as a deflection of the cantilever. During scanning, differences in the height profile of the sample surface will change the force acting on the tip and thus the cantilever deflection. Usually, a feedback loop is implemented to keep the cantilever deflection and thereby the force between tip and surface constant, by adjusting the  $z$ -position of the sample. While this mode of operation in principle allows for fast scanning and very high resolution, it is suitable only to a limited extent for delicate and soft samples –such as most biomolecules–, as the tip exerts high lateral forces on the sample during scanning [115]. For this reason, the dynamic modes of operation are of

special importance for biological samples. Here, the cantilever is actively excited to oscillations close to its resonance frequency, *e.g.* by a piezo-electric element, and the effects of a shift of the resonance frequency due to tip–surface interactions are monitored instead of the cantilever deflection.

The most frequently employed dynamic mode is the so-called tapping mode (also termed intermittent contact or force modulation mode), as it drastically decreases the lateral forces exerted on the sample [116]. In tapping mode, as schematically depicted in Fig. 2.1, the cantilever is excited at a constant frequency near its resonance and approached to the surface so that the tip only intermittently makes contact with the sample surface during each oscillation cycle. Amplitude and phase, the other two degrees of freedom of the oscillation, are monitored. Typical cantilever resonance frequencies range from a few kHz to hundreds of kHz, and typical amplitudes lie in the range of a few nm to tens of nm. The oscillation amplitude (which is detected as an alternating current signal recorded by the segmented photodiode using the laser beam method described above) is kept constant by a feedback loop regulating the *z*-position of the sample, ensuring a constant average force normal to the surface and allowing for reconstruction of the sample surface topography.

### Single-molecule imaging of VWF

Samples for AFM imaging experiments on VWF constructs were prepared by adsorption of overall negatively charged VWF to substrates functionalized with positively charged poly-L-lysine (PLL). To this end, first freshly cleaved mica sheets (grade I; SPI Supplies) were incubated with 20  $\mu\text{l}$  of a 0.01 % (w/v) PLL solution (molecular weight 500–2000, in ultrapure water; Sigma-Aldrich) for 30 s. Afterwards, they were thoroughly rinsed with 25 ml of ultrapure water and gently dried in a stream of nitrogen. Then, 20  $\mu\text{l}$  of buffer solution containing  $\approx 5 \mu\text{g/ml}$  of the respective VWF construct was deposited on the functionalized mica substrates and incubated for 30 s. Finally, the substrates were rinsed with 20 ml of ultrapure water and dried in a stream of nitrogen. It should be noted that immobilization of VWF onto the PLL-coated mica substrate might not proceed identically for varying pH conditions, as VWF's net charge changes with pH. Low pH conditions near VWF's pI may allow dimers to more effectively equilibrate than at higher pH values [64], at which the higher negative net charge of VWF molecules might lead to slightly faster trapping on the surface.

AFM images of  $1 \mu\text{m} \times 1 \mu\text{m}$  (for dimeric VWF constructs) or  $2 \mu\text{m} \times 2 \mu\text{m}$  (for multimeric VWF constructs) and  $1024 \times 1024$  pixels were recorded in tapping mode in air using an MFP-3D atomic force microscope (Asylum Research). Cantilevers with silicon tips, possessing a nominal spring constant of 26 N/m and a resonance frequency of  $\approx 300$  kHz (AC160TS; Olympus, Japan), were used. Raw image data were processed and analyzed using SPIP software (v6.4.4; Image Metrology, Denmark). Image processing involved plane correction (third-order polynomial plane-fitting and flattening according to the histogram alignment routine) and Gaussian filtering.

Dimer conformations were analyzed by tracing dimers individually along their contour, following local maxima in height, employing poly-line profiling (Fig. 2.2). As a measure to quantify the compactness of a dimer, I introduced the stem length, which is the distance along the contour between the CK domain and the position at which the two constituent monomers

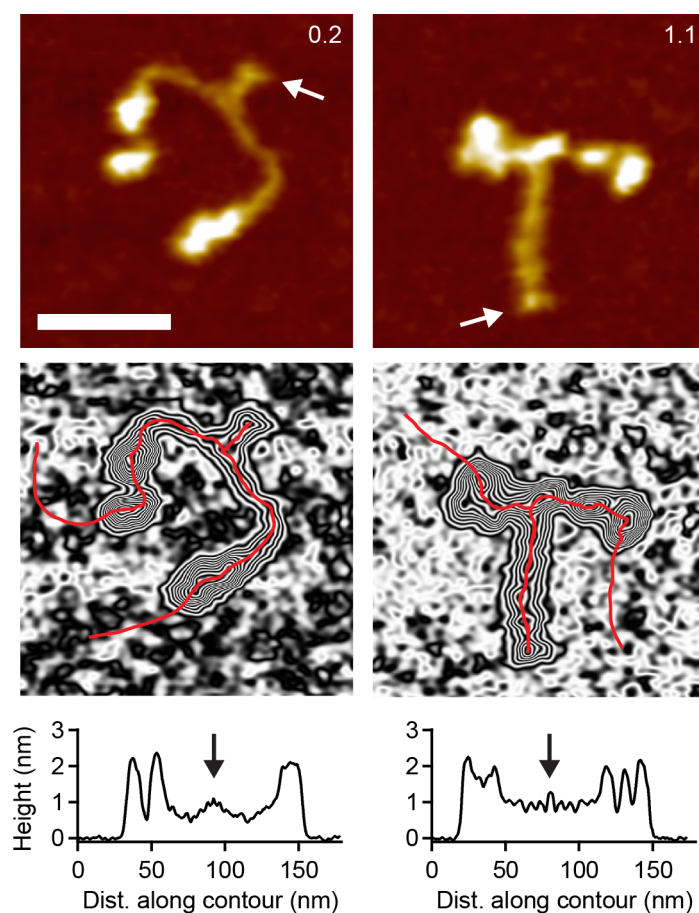


**Figure 2.2: Height profiling of VWF dimers in AFM images.** Characteristic lengths within VWF dimers were determined from height profiles of individual molecules. Height profiles were obtained by tracing each dimer in AFM images individually along its contour, following local maxima in height. Arrows indicate the position of the dimerized CK domains, which were identified with the last C-terminal local maximum in height in the VWF "stem". The boundary between the stem region and the higher N-terminal "head" domains was defined as the position where the first large height increase N-terminal of the CK domains reached its half-maximum value. Numbers in images indicate values of the normalized stem length, as explained in the text. A value above 1 corresponds to a fully closed stem. Scale bar is 30 nm, range of color scale is 2.4 nm. Figure adapted from [20].

separate from each other. In addition, the distance from the CK domain to the beginning of higher N-terminal domains was determined for the two constituent monomers and the mean of these distances was used to normalize the stem length.

The size distributions of multimeric VWF samples were analyzed by directly counting VWF molecules and determining the number of dimeric and monomeric subunits for each molecule. Poisson noise (1 SD) was assumed to estimate statistical uncertainties in counting. Reliable identification of VWF molecules and their subunits was enabled by their large size and their characteristic structure, exhibiting a higher "head" portion comprising the larger N-terminal domains, and a rather uniform "tail" region of markedly lower height (see Fig. 6.3). The CK domain of a monomer typically exhibits a slightly larger height than the rest of the "tail". Paired CK domains within a dimer show a markedly increased height compared to CK domains in individual monomers. Thus, linear VWF multimers exhibit a characteristic alternating pattern

of larger and higher, and thinner and lower portions. Occasional VWF molecules that could not be analyzed unambiguously, *e.g.* owing to colocalization with other VWF or contaminant molecules, were discarded from analysis.

In order to quantify the severity of dimerization defects in different VWF variants, I defined the dimerization abolishment (DA) as the overall fraction of monomers –both isolated and as constituents of multimers– that are not C-terminally linked to another monomer. Thus, the DA is obtained by dividing the number of monomeric building blocks incorporated into all observed VWF molecules (including isolated monomers) by the sum of monomeric building blocks and two times the number of dimeric building blocks.

VWF size distributions obtained by AFM imaging were compared with results obtained by the established method of electrophoretic multimer analysis. Electrophoretic multimer analysis was performed by Sonja Schneppenheim and Ulrich Budde, affiliated with the MEDILYS Laborgesellschaft mbH at the Asklepios Klinik Altona, Hamburg, as previously reported [117–119]. In brief, VWF multimers were separated by SDS-agarose electrophoresis, transferred onto a nitrocellulose membrane, detected with anti-human VWF antibody-HRP linked (DAKO) and visualized by luminescence. Frequencies of multimers of size  $i$  ( $i = 1$  corresponds to a dimer) were extracted quantitatively from each blot lane by analyzing the luminescence intensity profile along a cross-section through the lane. Intensity profiles exhibited clear peaks at the positions of bands visible in the blot, and were fitted with a multi-Gaussian function. Areas of fitted Gauss peaks were normalized by the respective multimer size  $i$  in order to obtain relative frequencies. This quantitative analysis of luminescence intensity profile was performed by Jochen P. Müller (LMU Munich).

### Imaging of streptavidin constructs of different valencies

Streptavidin (SA) constructs possessing a single C-terminal cysteine (see section 2.3) were reduced using 50 mM of dithiothreitol and mixed with biotinylated 250 basepairs (bp) double-stranded DNA in phosphate-buffered saline, with DNA being in large excess to ensure that SA molecules with the maximum number of bound DNA strands can be observed. A  $\approx 1:10$  SA:DNA stoichiometry was chosen for the 4SA and 3SA variants, and a  $\approx 1:4$  stoichiometry for 1SA and 0SA, with a final DNA concentration of approximately 4 nM.

After at least 15 min of incubation, the SA-DNA mix was immobilized onto a PLL-functionalized mica substrate, analogous to the protocol described in the previous section. The positively charged PLL allows for stable attachment of negatively charged DNA and of DNA-SA complexes. Free SA without bound DNA strands, however, does not stably attach to the substrate. AFM images of  $1 \mu\text{m} \times 1 \mu\text{m}$  or  $2 \mu\text{m} \times 2 \mu\text{m}$  and  $1024 \times 1024$  pixels were recorded as described in the previous section, and processed using SPIP software (v6.5.1; Image Metrology, Denmark). Image processing involved plane correction (third order polynomial plane-fitting), line-wise flattening (according to the histogram alignment routine), and Gaussian smoothing (for zoom-ins only).

## 2.2 Magnetic tweezers (MT)

### 2.2.1 Fundamentals of single-molecule force spectroscopy

Single-molecule force spectroscopy (SMFS) techniques have provided unprecedented insights into a variety of fundamental biomolecular processes and interactions, such as protein folding, the mechanical stability of receptor–ligand bonds, or the mechano-activation of enzymes [1, 2, 120]. More generally, SMFS enables to study the kinetics and thermodynamics of single biomolecules without ensemble averaging, thus allowing to extract intrinsic properties and to detect heterogeneity at the single-molecule level that is missed in bulk studies, as for instance multiple binding modes or different unfolding pathways of a protein.

For SMFS, as *e.g.* reviewed in [121], the molecule of interest is usually tethered between a surface and a sensitive force probe allowing to exert a force on the molecule and detect its response. In AFM-based SMFS for instance, the force probe is a cantilever acting as a soft spring with a sharp tip (apex radius typically on the order of 10 nm) at its end for attaching the molecule of interest. By increasing the distance between cantilever and surface, the force on the molecule is increased. The resulting deflection of the cantilever spring is detected to precisely determine the force. While AFM provides excellent spatial and temporal resolution, it is limited to higher forces as compared to other techniques and can hardly resolve forces below  $\approx 10$  pN.

Optical tweezers (OT) provide excellent spatial and temporal resolution even at forces as low as  $\approx 1$  pN. In OT, a dielectric bead trapped in the optical gradient of a highly focused laser beam serves as force probe, with the optical trap acting like a spring so that a displacement of the bead from its equilibrium position is proportional to the exerted force. OT are likely the most versatile SMFS technique, as they enable to manipulate the molecule of interest non-invasively in solution in all three dimensions. However, limitations of OT are their low throughput, as usually only one molecule at a time can be measured, and local heating and photo-damage of the sample due to the high laser intensity required for optical trapping.

A third common technique, especially for studying nucleic acids, are magnetic tweezers (MT), which not only allow to exert and measure force, but also torque. In MT, the molecule of interest is tethered to a superparamagnetic bead so that a force can be exerted by applying a suitable external magnetic field. While AFM and OT intrinsically control the position of the force probe and thus need feedback to regulate the force, MT directly control the force. In addition, MT provide the ability to measure many molecules in parallel, and offer a wide force range, including very low forces below 1 pN. The principle of MT, and their strengths and limitations, are discussed in more detail in section 2.2.2.

Centrifugal force spectroscopy [122, 123] and acoustic force spectroscopy [124] should be mentioned as further, however less commonly used, SMFS techniques allowing for parallel measurements.

Importantly, a vital prerequisite for meaningful force spectroscopy experiments is that single molecules can be pulled specifically and in a well-defined geometry. Therefore, it is desirable to attach the molecules of interests *via* handles that allow for stable and highly specific linkage. In the case of protein force spectroscopy, such handles may be small peptide tags

that can easily be introduced by standard cloning methods and are unlikely to interfere with protein folding and function [125]. In addition, the use of linker molecules is advantageous to minimize unspecific surface interactions [125, 126]. Finally, in order to facilitate identification of specific, single-molecule events in SMFS measurements, the use of so-called fingerprint domains is highly advisable, *i.e.* of protein domains that exhibit well-known, characteristic unfolding signatures. The fingerprint domain can either be recombinantly expressed together with the protein of interest as a fusion protein or attached post-translationally *via* specific enzymatic reactions [125, 127].

### Polymer elasticity and the Worm-like chain model

In SMFS experiments, the extension of the investigated molecule as a function of the applied force is of interest to extract structural information. For instance, in the MT force-clamp measurements on proteins that I performed within the framework of this thesis (see chapters 4 and 5), traces of the tether extension *vs.* time were recorded, and protein unfolding and folding events are observed as positive or negative steps in the traces, respectively. From the height of these steps as a function of the clamped force one can extract the contour length and stiffness of the portion of the protein that has unfolded or folded, provided one has a suitable polymer elasticity model describing the non-linear force response of the unfolded polypeptide chain. It should be stressed here that, importantly, in measurements at constant force the force response of additional molecular linkers is not relevant, in contrast to measurements with variable force as usually performed in AFM- and OT-based SMFS.

Typical simple models of polymer elasticity treat the polymer's force response as purely entropic, which has proven to be a valid approximation for unfolded polypeptide chains, but usually is not a sufficient description of a folded protein, as in the latter case enthalpic contributions are likely to play a non-negligible role. A very common polymer elasticity model, which I also employed within the framework of this thesis, is the so-called Worm-like chain (WLC) model [128–130]. The WLC model assumes a continuous, flexible, and isotropic rod that is subjected to thermal fluctuations. The rod is characterized by its length, the so-called contour length  $L_C$ , and by the persistence length  $P$ , which is a measure for the rod's bending stiffness. Formally, the persistence length is the length over which correlations with respect to direction of tangent vectors to the rod are lost.

A simple approximation for the relation between the extension  $x$  of a Worm-like chain and the force, with a relative error of  $\approx 15\%$ , has been reported [128, 130]:

$$\frac{FP}{k_B T} = \frac{1}{4} \left(1 - \frac{x}{L_C}\right)^{-2} - \frac{1}{4} + \frac{x}{L_C} \quad (2.1)$$

A more accurate expression, with only  $\approx 1\%$  relative error, has also been reported [131]:

$$\frac{FP}{k_B T} = \frac{1}{4} \left(1 - \frac{x}{L_C}\right)^{-2} - \frac{1}{4} + \frac{x}{L_C} - 0.8 \left(\frac{x}{L_C}\right)^{2.15} \quad (2.2)$$

Enthalpic contributions to the force response are taken into account in the extensible WLC model [132], which introduces the stretch modulus as an additional parameter. Two further commonly used purely entropic polymer elasticity models are the freely-jointed chain model

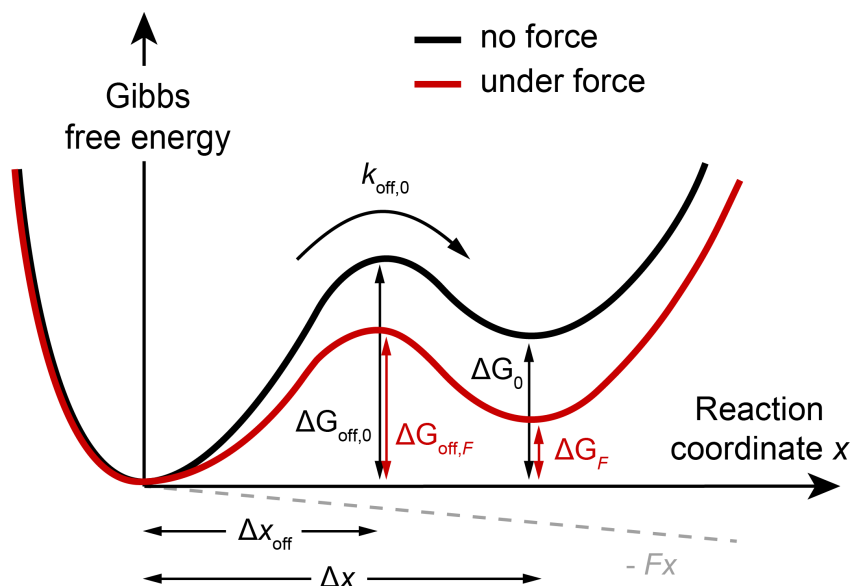


**Figure 2.3: Two-state, single-barrier kinetic model.** Schematically depicted is the one-dimensional Gibbs-free energy landscape along a reaction coordinate  $x$  of a system with two states separated by an energy barrier, in the absence (black) and in the presence (red) of an external force  $F$ . The external force tilts the energy landscape due to an additional energy term  $-Fx$  and thereby shifts the thermodynamic equilibrium towards the second state by decreasing the energy difference  $\Delta G$  between the states. It further influences the transition rates by changing the respective energy differences between the states and the barrier, as exemplarily depicted for the off-rate  $k_{\text{off}}$ , which depends on the energy difference  $\Delta G_{\text{off}}$  to the transition state.

[133, 134], which describes the polymer as a chain of rigid segments of fixed length with equiprobable bond and torsion angles, and thus essentially as a random walk, and the freely-rotating chain model [135], which extends the freely-jointed chain model by assuming fixed bond angles between neighbouring segments to mimic specific chemical bonding. Finally, more complicated models take into account excluded volume to avoid self-overlapping of the polymer.

### Two-state, single-barrier kinetic model of protein unfolding and refolding

SMFS experiments not only yield structural information, but in particular also provide insights into the kinetics of processes such as protein unfolding and folding or dissociation of a receptor–ligand interaction. In force-clamp experiments, one can directly infer the lifetime  $\tau$  of the folded/unfolded or bound state at the clamped force from the distribution of observed dwell times in the respective state, and the inverse of this lifetime  $\tau$  is the rate  $k$  of unfolding/folding or dissociation.

The process of protein unfolding and folding can be modeled as a two-state system. In the simplest, one-dimensional model, such a two-state system is described by a Gibbs free energy landscape along a reaction coordinate  $x$  with two local minima, which are separated by a single barrier (Fig. 2.3). If the energy difference between the two states in the absence of an external force is  $\Delta G_0$ , the two states will in thermal equilibrium be populated with a ratio of  $e^{\Delta G_0/k_B T}$ . The rate of transition from one state to the other depends exponentially on the respective energy difference to the transition state, *i.e.* to the barrier; for example the rate  $k_{\text{off},0}$

from the state with lower energy to the state with higher energy, as sketched in Fig. 2.3, is proportional to  $e^{-\Delta G_{\text{off},0}/k_{\text{B}}T}$ .

Application of an external force  $F$  along the direction coordinate  $x$  will shift the thermodynamic equilibrium towards the second state, as it tilts the energy landscape due to an additional energy term  $-Fx$ . The extent of the effect this has on the system depends on the distance  $\Delta x$  between the two states. Under the assumption that this distance stays approximately constant even when force is applied, the two states will be populated with an altered ratio of  $e^{(\Delta G_0 - F\Delta x)/k_{\text{B}}T}$ . Similarly, also the transition rates will be affected by the external force, as the height of the energy barrier is changed. These considerations are central to the Bell model [136, 137]. With  $\Delta x_{\text{off}}$  being the distance between the first state and the energy barrier, and again assuming that this distance does not significantly change due to the force, the rate  $k_{\text{off}}$  as a function of the force is given by

$$k_{\text{off}}(F) = \nu_0 \cdot e^{-\frac{\Delta G_{\text{off},0} - F\Delta x_{\text{off}}}{k_{\text{B}}T}} = k_{\text{off},0} \cdot e^{\frac{F\Delta x_{\text{off}}}{k_{\text{B}}T}}. \quad (2.3)$$

Here,  $\nu_0$  is a system-specific attempt frequency, which is on the order of the oscillation frequency of atoms in solids, but can for simplicity be absorbed into the intrinsic rate at zero force  $k_{\text{off},0}$  [136].

Taken together, in the simple model above, application of an external force exponentially increases the rate of protein unfolding. Conversely, the refolding rate is exponentially decreased. Similarly, with the above considerations, also the rate of dissociation of a receptor–ligand complex increases exponentially with force. Measuring rates at different forces in force-clamp experiments hence permits to extract values for the respective zero-force rates as well as for the distances to the transition state.

### 2.2.2 MT working principle and setup

Magnetic tweezers (MT) are a force spectroscopy technique that stands out from other methods by its wide accessible force range, including very low forces, and its ability for highly parallel measurements [121].

In MT, the molecules of interest are tethered between the bottom surface of a flow cell and superparamagnetic beads of  $\approx \mu\text{m}$  diameter [121, 134, 139]. In an external magnetic field, the superparamagnetic beads are magnetized, and in sufficiently strong field gradients they experience significant forces. The simplest way of applying a suitable external magnetic field is the use of permanent magnets positioned above the flow cell. In conventional MT, a pair of magnets is used in a usually vertical, anti-parallel configuration [121, 140], *i.e.* with the north pole of one magnet and the south pole of the other one facing the flow cell, with a small  $\approx \text{mm}$  gap between the magnets, as schematically depicted in Fig. 2.4. Different magnet configurations have been described for different applications [140]. By adjusting the distance between magnets and flow cell, the force acting on the bead –and therefore on the molecule of interest– can be controlled very precisely in the range of roughly 0.01-100 pN [121, 141]. If the molecule of interest is tethered in a way such that it is rotationally constrained, not only force, but also torque can be applied and controlled by rotation of the magnets [121, 140]. A second possibility is to utilize electromagnets, which allow for faster and more flexible adjustment of the force as compared to mechanical movement of permanent magnets, but require a more complicated experimental setup. In addition, they generate significant heat by the high current needed to

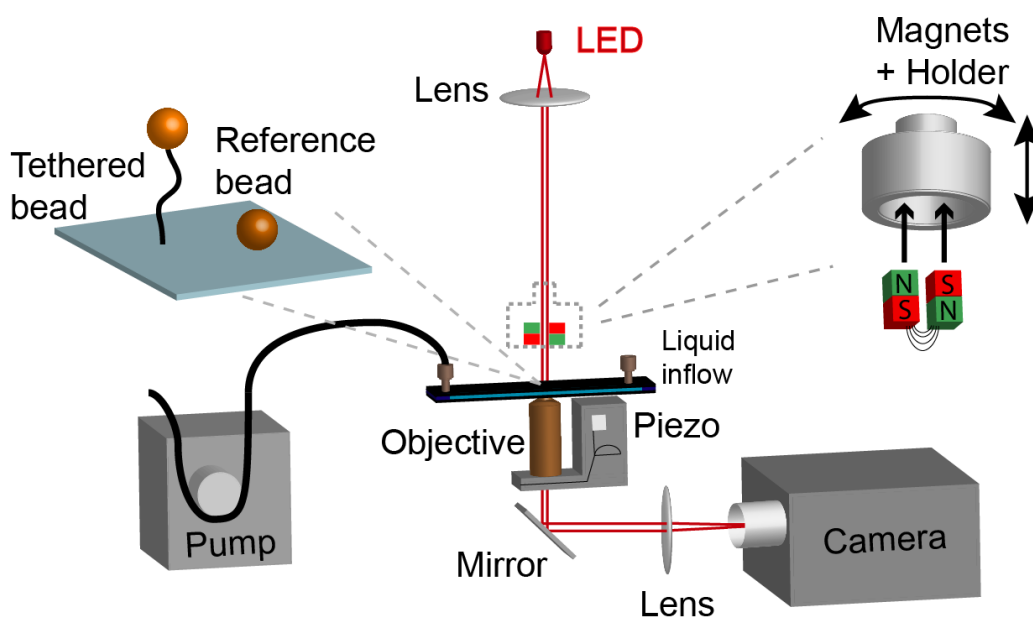


**Figure 2.4: Schematic of a conventional MT setup.** In MT, the molecules of interest are tethered between a superparamagnetic bead and the bottom surface of a flow cell. In the setup used within the framework of this thesis, the flow cell is illuminated using an LED, and a large field of view is imaged using an oil-immersion objective and a CMOS sensor camera. For creating the look-up table necessary to track the  $z$  position of the beads, the objective is mounted on a piezo stage. A set of two cubic permanent magnets is positioned above the flow cell. The distance between magnets and flow cell can be adjusted using a DC-motor in order to adjust the force applied to the magnetic beads. A peristaltic pump allows for flushing the flow cell. For technical details of the different components of the custom MT setup used within this thesis, see the description on page 33. Figure adapted with permission from [138].

create sufficiently strong magnetic fields, and, since usually pole pieces in the electromagnetic coils are needed, electromagnetic tweezers can suffer from hysteresis effects [121].

MT naturally operate in constant force mode [121], *i.e.* the applied force is constant during the measurement (to within  $\approx 0.01\%$ ; *cf.* Fig. 2.5), as long as the external magnetic field is not actively changed, with excellent sensitivity in particular at low forces.

The extension of a tether, *i.e.* of a protein of interest, is determined by camera-based tracking of the  $(x,y,z)$ -position of the attached bead. To this end, the bead is imaged slightly out of focus (see Fig. 4.1B), and determining the center of its diffraction ring pattern yields the  $(x,y)$ -position with sub-nanometer resolution [142]. The  $z$ -position can be obtained with  $\approx$  nm resolution by comparing the bead's current diffraction ring pattern with a look-up table of its diffraction ring pattern at different  $z$  heights, which is created by moving the objective used for imaging in defined steps using a piezo [142]. Correction of sample drift is enabled by subtracting the signal of a reference bead that is firmly bound to the flow cell surface [121]. Camera-based tracking for  $\approx 10$ s-100s of  $\gamma$ -nucleic acid-tethered- beads simultaneously has been demonstrated [142–144].

A disadvantage of MT has been the lower temporal resolution compared to other techniques [121], limiting its ability to detect very fast processes and measure lifetimes of short-lived states. However, in recent years, MT measurements with  $\leq$  ms temporal resolution have been demonstrated [145–147]. Furthermore, MT do not suffer from local heating or photo-damage, as is for instance the case in OT [121].

In summary, MT allow for long-term, stable measurements at constant force and on many molecules in parallel, which permits to obtain statistics in a single measurement run and to observe rare or conditional events. However, while these strengths of MT have impressively been demonstrated in studies on nucleic acid tethers, MT have so far only rarely been used for investigating proteins, and, in particular, there have been no reports of parallel measurements of protein unfolding and folding, as will be discussed in more detail in section 4.1.

### Custom MT setup

The MT force spectroscopy measurements presented in this work were performed on a custom MT setup built by Dr. Philipp U. Walker (LMU Munich). Its specifications are described in detail in Dr. Philipp U. Walker's PhD thesis [138]. The setup uses a pair of permanent magnets ( $5 \times 5 \times 5 \text{ mm}^3$  each; W-05-N50-G, Supermagnete, Switzerland) in conventional, vertical configuration. The distance between magnets and flow cell (and, therefore, the force acting on magnetic beads) is controlled by a DC-motor (M-126.PD2; PI Physikinstrumente, Germany). For illumination, an LED (69647, Lumitronix LED Technik GmbH, Germany) is used. Using a  $40\times$  oil immersion objective (UPLFLN  $40\times$ , Olympus, Japan) and a CMOS sensor camera with  $4096 \times 3072$  pixels (12M Falcon2, Teledyne Dalsa, Canada), a large field of view of approximately  $440 \times 330 \mu\text{m}^2$  can be imaged at a frame rate of 58 Hz. For measurements with an acquisition rate of 1 kHz, a reduced field of view of  $1792 \times 280$  pixels was used. Images are transferred to a frame grabber (PCIe 1433; National Instruments) and analyzed with an open-source tracking software [142]. The bead tracking accuracy was determined to be  $\approx 0.6 \text{ nm}$  in  $(x,y)$  and  $\approx 1.5 \text{ nm}$  in  $z$  direction, as determined by tracking non-magnetic polystyrene beads, with a diameter comparable to the magnetic beads used in experiments ( $3 \mu\text{m}$ ), after baking them onto the flow cell surface. For creating the look-up table required for tracking the bead positions in  $z$ , the objective is mounted on a piezo stage (Pifoc P-726.1CD, PI Physikinstrumente, Germany).

Force calibration was performed by Dr. Philipp U. Walker as described by te Velthuis et al., based on the fluctuations of long DNA tethers [138, 148]. The final force calibration, *i.e.* the dependence of the force applied to a bead on the distance between magnets and flow cell, is shown in Fig. 2.5A, together with an example trace showing the DNA B-S overstretching transition at the expected force of  $\approx 65 \text{ pN}$  (Fig. 2.5B), confirming the force calibration from the analysis of transverse fluctuations. Importantly, for the small extension changes on the length scales of the protein tethers investigated in the framework of this thesis, the force stays constant to very good approximation, with the relative change in force due to tether stretching or protein (un-)folding being  $< 10^{-4}$  (Fig. 2.5C). Further, the uniformity of the magnetic field across the field of view was verified and the change in force across the full range of the field of view was found to be  $< 3 \%$  (Fig. 2.5E). The largest source of force uncertainty is the bead-to-bead variation, which was found to be on the order of  $\leq 10 \%$  for the beads used in this study (Fig. 2.5D), in line with several previous reports [149–151].

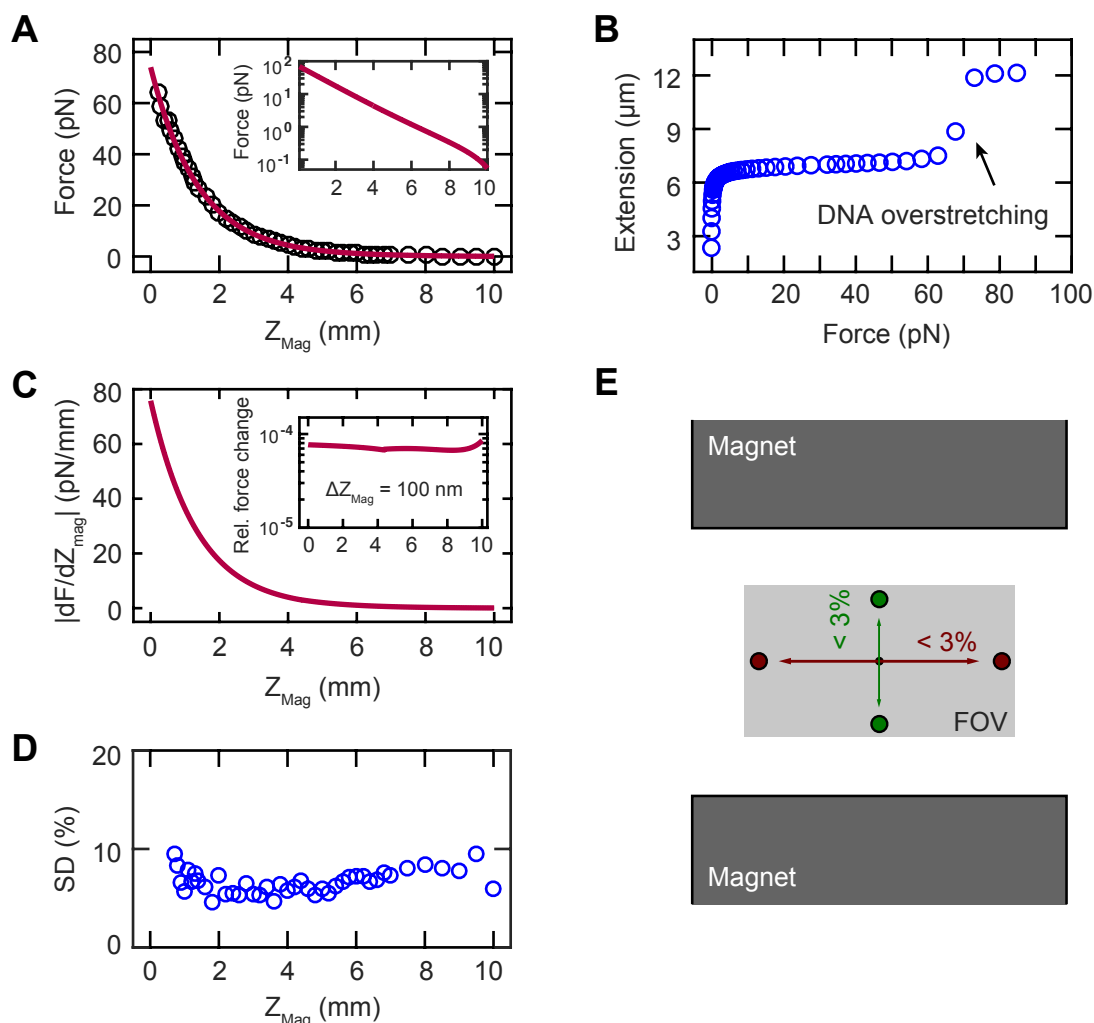


**Figure 2.5: Force calibration of the custom MT setup.** (A) Force acting on the magnetic beads used in the framework of this thesis (Dynabeads M270) as a function of the distance  $Z_{\text{Mag}}$  between the magnets and the flow cell. Forces were calibrated based on the Brownian fluctuations of 21 kbp double-stranded (ds) DNA tethers. Data points are mean forces determined from 16 DNA tethers. The red line is the final fit of the dependence of force on the magnet distance. (B) Exemplary trace of a 21 kbp dsDNA tether, showing the B-S overstretching transition at the expected force of  $\approx 65$  pN. (C) Absolute value of the derivative of the force with respect to  $Z_{\text{Mag}}$ . The inset shows the relative force change for extension changes in  $z$  direction of 100 nm —larger than any (un-)folding steps in the proteins investigated in this thesis—, which was found to be  $< 10^{-4}$  for all forces, as calculated from the expression for  $|dF/dZ_{\text{Mag}}|$ . (D) Bead-to-bead force variation. Independently performing the calibration procedure for 16 different DNA tethers, the standard deviation of the force from the mean value was found to be  $\leq 10\%$  over the whole range of magnet distances, indicating a bead-to-bead force variation of  $\leq 10\%$ . (E) Force uniformity across the field of view (FOV). The force calibration procedure for the same DNA tether was performed repeatedly at different positions at the edges of the FOV, as schematically indicated by circles, and in the middle of the FOV. For each of four independently measured DNA tethers, changes in force were found to be  $< 3\%$  both along the axis parallel to and the axis perpendicular to the gap between the magnets (not drawn to scale). Force calibration was performed by Dr. Philipp U. Walker. Figure adapted with permission from [138].

### 2.2.3 Protein force spectroscopy in MT using Elastin-like polypeptide linkers

#### Site-specific, covalent protein attachment and flow cell preparation

Functionalization of glass slides with Elastin-like polypeptide (ELP) linkers followed the protocol by Ott et al. [126]. Glass slides were first silanized with 3-(aminopropyl)dimethylethoxysilane (APDMES, ABCR GmbH, Germany), and then coated with 10 mM of a sulfosuccinimidyl 4-(N-maleimidomethyl)cyclohexane-1-carboxylate cross-linker with a negligible contour length of 0.83 nm (Sulfo-SMCC, Thermo Fisher Scientific), dissolved in 50 mM Hepes, pH 7.5. Subsequently, ELP linkers were linked to the thiol-reactive maleimide groups via a single cysteine at their N-terminus in coupling buffer consisting of 50 mM sodium phosphate, 50 mM NaCl, 10 mM EDTA, pH 7.2. Afterwards, 10 mM L-cysteine dissolved in coupling buffer were added to saturate potentially remaining unreacted maleimide groups. Finally, non-magnetic polystyrene beads (Polybead Microspheres 3  $\mu\text{m}$ ; Polysciences GmbH, Germany) dissolved in ethanol were baked onto the slides at  $\approx 70^\circ\text{C}$  for 5 min for use as reference beads. After each step, slides were extensively rinsed with ultrapure water. Flow cells were assembled from an ELP-functionalized cover slip as the bottom surface and a non-functionalized cover slip with two small holes for inlet and outlet as the top, with a layer of cut-out parafilm (Pechiney Plastic Packaging, USA) as a spacer to form a ( $\approx 4$  mm wide and 50 mm long) flow channel. Flow cells were assembled by heating on a hot plate to  $\approx 70^\circ\text{C}$  for  $\approx 2$  min. Assembled flow cells can be stored under ambient conditions for weeks.

Prior to experiments, the flow cells were incubated with 1 % casein solution (Sigma-Aldrich) for 1 h and afterwards flushed with 1 ml (approximately 20 flow cell volumes) of buffer (20 mM Hepes, 150 mM NaCl, 1 mM  $\text{MgCl}_2$ , 1 mM  $\text{CaCl}_2$ , pH 7.4). CoA-biotin (New England Biolabs) was coupled to the ybbR-tag on the protein of interest in a bulk reaction in the presence of 5  $\mu\text{M}$  sfp phosphopantetheinyl transferase and 10 mM  $\text{MgCl}_2$  at  $37^\circ\text{C}$  for 60 min. In the case of VWF, subsequently TEV protease was added to a final concentration of approximately 25  $\mu\text{M}$  and incubated for 30-60 min. Dithiothreitol (DTT) present in the storage buffer of TEV protease was removed beforehand using desalting columns (Zeba Spin 40 K MWCO, Thermo Fisher Scientific). Afterwards, the protein was diluted to a final concentration of approximately 10 nM (VWF dimers) or 25 nM (ddFLN4) in 20 mM Hepes, 150 mM NaCl, 1 mM  $\text{MgCl}_2$ , 1 mM  $\text{CaCl}_2$ , pH 7.4, and incubated in the flow cell in the presence of 1-2  $\mu\text{M}$  sortase A for 30 min. Subsequently, the flow cell was flushed with 1 ml of buffer.

Magnetic beads –either Dynabeads M-270 streptavidin (diameter of 2.8  $\mu\text{m}$ ; Thermo Fisher Scientific) or custom beads functionalized with different streptavidin variants (see the following paragraph)– in measurement buffer containing 0.1 % (v/v) Tween-20 (Sigma-Aldrich) were incubated in the flow cell for 60 s, and unbound beads were flushed out with 2 ml of measurement buffer. All measurements were performed at room temperature ( $\approx 22^\circ\text{C}$ ).

Starting with silanized glass slides, complete flow cell preparation takes less than 7 h. In addition, flow cells functionalized with ELP linkers, but not yet incubated with casein and protein, can be prepared in advance and stored at room temperature for weeks without loss of functionality. Starting with ELP-functionalized flow cells, measurements can be started within 120 min.

### Functionalization of magnetic beads with streptavidin variants

Most of the MT experiments presented in this thesis were performed using commercially available superparamagnetic beads functionalized with streptavidin (Dynabeads M-270 Streptavidin, Invitrogen/Thermo Fisher). However, for measurements investigating the lifetime of the biotin–streptavidin bond under constant force, custom beads functionalized with different streptavidin variants, immobilized site-specifically and covalently, were used. For preparation of these beads, first 5  $\mu\text{M}$  of different SA variants possessing a single C-terminal cysteine (1SA, 3SA, or 4SA, see page 41) were supplemented with 5 mM Bond-Breaker TCEP Solution (Thermo Fisher Scientific). After one hour, the mixture was purified using Zeba Spin Desalting Columns (Thermo Fisher Scientific) with a molecular weight cut-off of 40 kDa, equilibrated with coupling buffer, according to the manufacturer's instruction. Bifunctional polyethylene glycol of 5 kDa having an N-hydroxysuccinimide group at one end and a maleimide group at the other (Rapp Polymere, Germany) was dissolved in 50 mM Hepes, pH 7.5, to a final concentration of 25 mM and immediately used to incubate superparamagnetic beads with amine groups (Dynabeads M-270 Amine, with a diameter of 2.8  $\mu\text{m}$ ; Thermo Fisher Scientific). After 45 min, beads were washed extensively with DMSO and water. Beads were then incubated with the respective SA construct in coupling buffer for 90 min and extensively washed with measurement buffer.

### Data analysis

MT data analysis was carried out using custom-written Matlab scripts (Matlab v.R2015b; The MathWorks Inc., Natick, MA), most of which are incorporated into a custom Matlab GUI written by Dr. Philipp U. Walker and described in his PhD thesis [138]. Matlab scripts for analysis of the data presented in section 5.4 were written by me. Tether extension *vs.* time traces were obtained by subtracting the *z*-position of the reference bead from the *z*-position of the protein-tethered bead. All traces shown and analyzed are the raw extension *vs.* time traces recorded at 58 Hz, used without any filtering or smoothing, unless stated otherwise. For ddFLN4 measurements, only beads that in unfolding force plateaus repeatedly showed a double-step with a short-lived intermediate state were taken into account for further analysis. Similarly, for VWF measurements, only beads repeatedly exhibiting two steps of equal height corresponding to unfolding of the A2 domains in unfolding force plateaus were analyzed, unless otherwise noted.

To determine the position of (un)folding steps of ddFLN4 or the VWF A2 domains, a step-finding algorithm by Kerssemakers et al. was employed [152], and the corresponding change in extension was determined as the difference between the average extensions of the adjacent 1000 frames recorded before and after the step, respectively (fewer frames were used if the 1000-frame interval contained another step). Extensions of folding and unfolding (sub)steps were histogrammed for each clamped force (1 nm binning for ddFLN4, and 3 nm and 2 nm binning for VWF A2 unfolding and refolding, respectively), and fitted with Gaussians. Error bars in figures report the FWHM of the fits, divided by the square root of the respective counts. The resulting force–extension profiles were fitted to the WLC model of polymer elasticity (an approximation to this model with less than 1 % relative error was used for fitting [131], see equation 2.2). In the case of ddFLN4, a fixed persistence length of 0.5 nm was used to enable direct comparison with results from an AFM study by Schwaiger et al. [153]. In the case of VWF A2, both persistence length and contour length were free fit parameters.

To determine the unfolding or refolding rates  $k(F)$  at a given constant force  $F$ , the respective fraction of observed unfolding or refolding events as a function of time was fitted with the exponential expression  $1 - a \exp(-kt) + b$  (cf. section 4.3 and Fig. 4.4), where the free parameters  $a$  and  $b$  can compensate for events that were missed due to the finite measurement time or due to the finite time of motor movement when setting the force. However, such missed events were rare and parameters  $a$  and  $b$  were close to 1 and 0, respectively. Error bars on rates in figures indicate 95 % confidence bounds of fits. In the case of VWF, only events corresponding to steps with extensions  $\leq 60$  nm were taken into account to ensure that only A2 unfolding events –and not dissociation of the D4-mediated intermonomer interaction (see section 5.2)– are analyzed.

The force dependence of unfolding and refolding rates was described by a single barrier kinetic model:  $k(F) = k_0 \exp(F\Delta x/k_B T)$ , with the rate at zero force  $k_0$  and the distance to the transition state  $\Delta x$  as fit parameters. Fitting was carried out as linear fits to the natural logarithm of the data. Reported error margins for  $k_0$  and  $\Delta x$  correspond to 1 SD.

For bead rupture measurements, lifetimes at different constant forces were determined from the survival fraction vs. time data based on  $> 35$  rupture events for each condition. In the case of 1SA-beads, data were described by a single-exponential decay, and the corresponding lifetime was determined by a linear fit to the natural logarithm of the data. Data obtained for beads functionalized with 3SA or 4SA were piecewise fitted by linear regression as described in section 4.5. In the case of the more complex decay behavior observed for commercial streptavidin-coated beads (section 4.4), lifetimes for the fastest- and slowest-decaying populations were estimated by linear fits to the natural logarithm of the first and last 20 % of data points, respectively. The dependence of estimated lifetimes on force was again described by the single barrier kinetic model introduced above.

For analysis of the three-state "hopping" resulting from transitions within the two D'D3 domains within a VWF dimer, as presented in section 5.4, traces were subjected to 5-frame moving average smoothing. To determine the relative population of the different states, thresholds between the states were determined by locating the local minima in extension histograms. Automatically detected thresholds were manually inspected and adjusted, if necessary. The obtained relative fractions of data points in the three states were fitted under the assumption of two identical, independent underlying transitions that can be described by a simple single-barrier kinetic model. Fitting, including the expressions used for fitting, is described in more detail in section 5.4. For analysis of the kinetics of the transitions, the dwell times in the respective states, *i.e.* the times spent in a state before crossing a threshold, were determined. Pseudo dwell time distributions were then constructed by weighting the dwell times for opening (closing) with the number of closed (open) interactions, in order to obtain opening (closing) times corresponding to a single underlying interaction (cf. [154] and section 5.4). Rates were determined both from binned pseudo dwell time distributions and from un-binned distributions, representing the pseudo dwell times as fraction of events, by exponential fitting. The obtained rates at different forces were again fitted by a single-barrier kinetic model.

## 2.3 Recombinant protein constructs and protein purification

This section gives an overview of all recombinant protein constructs investigated in the experiments that I conducted within the framework of this thesis. A list of all constructs is given in Table 2.1.

### VWF constructs

All VWF constructs investigated in this thesis were engineered and prepared by Tobias Obser and Gesa König from the group of Prof. Dr. Reinhard Schneppenheim and PD Dr. Maria Brehm at the University Medical Center Hamburg-Eppendorf (UKE), Department of Pediatric Hematology and Oncology. I carried out protein purification, with assistance from Thomas Nicolaus (LMU Munich).

Dimeric VWF constructs for AFM imaging and MT force measurements were designed as hetero-bifunctional dimers, consisting of two different types of monomers possessing different N-terminal peptide tags.

The dimers used to investigate VWF's static conformation by AFM imaging, as presented in chapter 3, comprised a monomer equipped with a strep-tag II [155] for high-affinity purification, and a monomer carrying a ybbr-tag [156]. The latter did not serve a specific purpose for AFM imaging, but was introduced to enable immobilization to a CoA-functionalized surface for complementary AFM force spectroscopy experiments conducted by Dr. Jochen Müller, as described in chapter 3.

In the case of the dimeric constructs employed for MT force measurements, one monomer again possessed a ybbr-tag, allowing for covalent conjugation of CoA-biotin. The second monomer was equipped with a strep-tag II for high-affinity purification, followed by a tobacco etch virus (TEV) protease cleavage site [157] and the N-terminal sortase motif GG [158]. The TEV site served two purposes: first, to remove the strep-tag after purification, as it might otherwise interact with streptavidin on the magnetic beads during measurements, and second, to free the sortase motif GG, which must be located terminally for the sortase reaction.

In addition to full-length dimers, comprising all domains present in mature VWF, also several constructs with deletions of certain domains were investigated as controls: *delD4*, with a deletion of the full D4 assembly (D4N-TIL4, aa 1873-2255; both for AFM imaging and MT constructs), *delD'D3*, with a deletion of the full D'D3 assembly (TIL'-E3, aa 764-1273; for MT constructs only), and *delA1*, with a deletion of the A1 domain (aa 1272-1462; for MT constructs only).

Hetero-bifunctional dimers were obtained by co-transfection of HEK-293 cells with two different plasmids so that the two different types of monomers were co-expressed. Multimerization was obstructed by deleting the VWF pro-peptide sequence (domains D1 and D2, aa 26-763). N-terminal tags were inserted after the required N-terminal signal peptide (aa 1-25). Plasmid construction, transfection of HEK-293 cells and protein expression were performed as described in detail in [20]. In brief,  $2 \cdot 10^6$  HEK-293 cells (DSMZ, Germany) were transfected in Dulbecco's modified Eagle's medium (Life Technologies) containing 10 % fetal bovine serum (Life Technologies), 2  $\mu$ g of each of the two plasmids, and 15  $\mu$ l Lipofectamine 2000 (Life Technologies).

Construct	Description	Chapter
VWF wt strep/ybbR	hetero-dimer comprising full-length monomers with N-terminal strep-tag II or ybbR-tag	3
VWF <i>delD4</i> strep/ybbR	hetero-dimer comprising monomers with deletion of D4 and with N-terminal strep-tag II or ybbR-tag	3
VWF wt strep-TEV-GG/ybbR	hetero-dimer comprising full-length monomers with N-term. strep-tag II, TEV site, and GG motif, or ybbR-tag	5
VWF <i>delD4</i> strep-TEV-GG/ybbR	hetero-dimer comprising monomers with deletion of D4 and with N-term. strep-tag II, TEV site, and GG motif, or ybbR-tag	5
VWF <i>delA1</i> strep-TEV-GG/ybbR	hetero-dimer comprising monomers with deletion of A1 and with N-term. strep-tag II, TEV site, and GG motif, or ybbR-tag	5
VWF <i>delD'D3</i> strep-TEV-GG/ybbR	hetero-dimer comprising monomers with deletion of D'D3 and with N-term. strep-tag II, TEV site, and GG motif, or ybbR-tag	5
VWF wt multimer	multimeric wt VWF without tags	6
VWF C1099Y multimer	multimeric VWF variant p.Cys1099Tyr without tags	6
VWF C2771R multimer	multimeric VWF variant p.Cys2771Arg without tags	6
VWF C2773R multimer	multimeric VWF variant p.Cys2773Arg without tags	6
VWF C2811A multimer	multimeric VWF variant p.Cys2811Ala without tags	6
G-ddFLN4-ybbR	ddFLN4 with N-terminal glycine and short linker, and C-term. ybbR-tag	4
4SA-Cys-His	tetravalent streptavidin (SA) with C-term. cysteine and poly-His tag on one subunit	4
3SA-Cys-His	trivalent SA with C-term. cysteine and poly-His tag on non-functional subunit	4
1SA-Cys-His	monovalent SA with C-term. cysteine and poly-His tag on functional subunit	4
0SA-Cys-His	non-functional SA with C-term. cysteine and poly-His tag on one subunit	4
Cys-ELP-LPETGG	Elastin-like polypeptide linker with N-term. cysteine and C-term. LPETGG motif	4, 5

**Table 2.1: List of recombinant protein constructs investigated in the framework of this thesis.** The short notation of each construct is given, along with a short description (for more details, see section 2.3). The last column specifies the chapter(s) in which the experimental results regarding the respective construct are described.

24 h after transfection, cells were transferred into selection medium containing 500 µg/ml G418 (Invivogen) and 250 µg/ml Hygromycin B (Invivogen). After 2–3 weeks, the polyclonal cell culture was seeded for expression. After 72 h of cell growth, the medium was exchanged against OPTIPRO serum-free medium (Life Technologies) for serum-free collection of secreted recombinant VWF. The culture supernatant was collected after 72 h and concentrated using Amicon Ultra-15 MWCO 100 kDa (Merck Millipore).

All dimeric constructs were purified via a HiTrap StrepTrap affinity chromatography column (GE Healthcare) using the AEKTA Explorer system (GE Healthcare). As running buffer, 20 mM Hepes, 150 mM NaCl, 1 mM MgCl<sub>2</sub>, 1 mM CaCl<sub>2</sub>, pH 7.4, was used. Elution buffer additionally contained 2.5 mM d-desthiobiotin. Eluates were buffer exchanged (to the running buffer) and concentrated by centrifuge filtration using Amicon Ultra MWCO 100 kDa (Merck Millipore).

For investigating the multimer size distributions of wildtype (wt) VWF and several variants with C-terminal (p.Cys2771Arg, p.Cys2773Arg, and p.Cys2811Ala) or N-terminal (p.Cys1099Tyr) mutations resulting in defective dimerization and multimerization, multimeric VWF constructs were recombinantly expressed. WtVWF was expressed using the full-length cDNA of human wtVWF within the mammalian expression vector pcDNA3.1 [159]. Single missense mutations p.Cys1099Tyr, p.Cys2771Arg, p.Cys2773Arg and p.Cys2811Ala were inserted into the same vector by site-directed mutagenesis employing the QuikChange kit (Stratagene) and the resulting vectors were sequenced to confirm insertion of the mutations and absence of any additional unwanted mutations. Expression yields VWF constructs without any additional peptide tags. Top10 supercompetent cells (Invitrogen) were transformed with these vectors and plasmid purification was performed using the Endofree Plasmid Maxi Kit (QIAGEN). 4 µg vector DNA were used to transfect HEK-293 cells ( $2 \cdot 10^6$ ) employing Lipofectamine 2000 according to the manufacturer's instructions. The cells were selected for stable expression for 2 weeks by adding 500 µg/ml G418 to the Dulbecco's modified Eagle's medium with 10 % fetal bovine serum. 72 hours before harvesting the VWF-containing medium, the medium was exchanged with serum-free OPTIPRO serum-free medium.

Multimeric VWF constructs in serum-free medium were purified and buffer exchanged by repeated centrifuge filtration using Amicon Ultra MWCO 100 kDa, using buffer adjusted to pH 7.4, containing 20 mM Hepes, 150 mM NaCl, 1 mM MgCl<sub>2</sub>, and 1 mM CaCl<sub>2</sub>. No further steps of purification were performed. I refrained from using VWF constructs equipped with N- or C-terminal peptide tags for high-affinity purification, as such tags might influence VWF's multimerization. I further refrained from purifying the untagged samples via a VWF affinity matrix, as I observed such purification procedures to markedly affect the conformation of VWF's N-terminal portions, possibly due to the required relatively harsh elution conditions.

### Elastin-like polypeptide linkers

Recombinant ELP linkers expressed in *E.coli NiCo21 (DE3)* were a kind gift from Dr. Wolfgang Ott (LMU Munich). The  $\approx 300$  aa ELP linker with a contour length of  $\approx 120$  nm used in the framework of this thesis has the sequence [(VPGEG)-(VPGVG)<sub>4</sub>-(VPGAG)<sub>2</sub>-(VPGGG)<sub>2</sub>-(VPGEG)]<sub>6</sub> and additionally possesses a single N-terminal cysteine and the C-terminal sortase recognition motif LPETGG. Cloning, expression and purification have been described [126, 160], and can be performed using standard procedures for the production of recombinant proteins.

Plasmids are provided at Addgene by Ott et al. (Addgene accession number 90472 for the ELP linker used for the experiments presented in this thesis).

### Streptavidin variants

SA variants were designed, expressed, and purified by Steffen M. Sedlak (LMU Munich). Tetrameric SA constructs of different valencies were designed that consist of a combination of functional subunits and mutant subunits deficient in biotin binding. For controlled site-specific and covalent immobilization, one of the subunits possesses a single C-terminal cysteine residue, followed by a poly-histidine tag for purification. Tetravalent 4SA consists of four functional subunits, one of which carries the cysteine. Trivalent 3SA consists of three functional and one mutant subunits, with the latter possessing the cysteine. Conversely, monovalent 1SA comprises three mutant and one functional subunit, with the functional subunit possessing the cysteine residue. The 0SA construct, consisting of four mutant subunits, serves as control.

Preparation of these constructs was performed as previously described [161, 162]. In brief, functional and mutant subunits with or without the cystidine residue and poly-histidine tag were cloned into pET vectors (Novagen – EMD Millipore, USA) and separately expressed in *E.coli* BL21(DE3)-CodonPlus (Agilent Technologies, USA). Resulting inclusion bodies were solubilized in 6 M guanidine hydrochloride. Prior to refolding, for each SA variant the respective two different subunits were then mixed at a 1:10 ratio, in order to ensure a 1:3 ratio of subunits in the final tetrameric SA construct after purification via the polyhistidine-tag.

### ddFLN4 construct

Recombinant ddFLN4 expressed in *E.coli* (with the internal cysteine at position 18 mutated to serine) was a kind gift from Dr. Lukas F. Milles (LMU Munich). At its C-terminus, the ddFLN4 construct possesses a polyhistidine-tag for purification and a ybbR-tag [156]. At its N-terminus, the construct has a short linker sequence (MGTGSGSGSGSAGTGSG) with the terminal methionine followed by a single glycine. Due to efficient cleavage of the methionine by *E.coli* methionine aminopeptidases, the glycine is expected to be available for sortase-catalyzed ligation to a large extent. The ddFLN4 gene was synthesized codon-optimized for expression in *E.coli* as a linear DNA fragment (GeneArt – ThermoFisher Scientific), and inserted into pET28a Vectors via Gibson assembly [163] (New England Biolabs). Protein expression in *E.coli* NiCo21 (DE3) (New England Biolabs) and purification via the polyhistidine-tag were carried out as previously described in detail [164].

## 2.4 Buffers

For AFM imaging experiments on VWF dimers under varied pH conditions, buffer solutions containing 150 mM NaCl and 20 mM of one of the following buffering agents were used: Na-acetate (pH 5.4), BisTris (pH 6.2, 6.6, and 6.8), Hepes (pH 7.1 and 7.4) or Tris (pH 8.0 and 8.6). The pH was adjusted using HCl and NaOH, respectively. Buffers used for measurements in the presence of divalent ions additionally contained 1 mM CaCl<sub>2</sub> and 1 mM MgCl<sub>2</sub>. Buffers used for measurements in the presence of free Imidazole further contained 200 mM Imidazole in

addition to  $\text{CaCl}_2$  and  $\text{MgCl}_2$ . Prior to measurements in the absence of divalent ions, proteins were incubated with buffer containing 10 mM EDTA for 8 h and subsequently the buffer was exchanged to the measurement buffer. For AFM imaging experiments on multimeric VWF constructs, buffer solution mimicking physiological conditions ("near-physiological"; 20 mM HEPES, 150 mM NaCl, 1 mM  $\text{CaCl}_2$ , 1 mM  $\text{MgCl}_2$ , pH 7.4) was used. All buffer exchanges were performed via centrifuge filtration using Amicon Ultra MWCO 100 kDa centrifugal filters (Merck Millipore).

MT force measurements on ddFLN4 and on VWF dimers under near-physiological conditions were performed in near-physiological buffer supplemented with 0.1 % Tween-20. Measurements in the absence of calcium were performed in EDTA buffer containing 20 mM HEPES, 150 mM NaCl, 10 mM EDTA, 0.1 % Tween-20, at pH 7.4. Before measurements without calcium, the flow cell was incubated with EDTA buffer for 2 h. Measurements at acidic pH were performed in buffer containing 150 mM NaCl, 1 mM  $\text{MgCl}_2$ , 1 mM  $\text{CaCl}_2$ , 0.1 % Tween-20, and either 20 mM BisTris (pH 6.2) or 20 mM Na-acetate (pH 5.5). Buffer exchanges during an MT experiment were conducted by slowly flushing the flow cell with at least 1 ml (approximately 20 flow cell volumes) of the respective buffer.

# Role of pH-dependent interactions in dimers for regulating the mechanics and structure of VWF

In this chapter, a systematic investigation of the influence of the pH and of divalent ions on the conformation of VWF dimers, as well as on their response to (rather high) force, will be presented, based on single-molecule AFM imaging and AFM-based force spectroscopy experiments. Studying the impact of pH and ionic conditions was motivated by the considerations discussed in section 1.5 based on previous work that I was involved in, which showed the importance of interactions within dimers for VWF's force sensing ability [20]. Combining information on the structure and the mechanics of VWF dimers allows to more thoroughly characterize both previously known and newly identified intermonomer interactions, and suggests a mechanism for markedly enhancing VWF's hemostatic activity by even minor pH deviations, which *in vivo* might occur locally at sites of vascular injury.<sup>1</sup>

The work in this chapter was performed in close collaboration with Dr. Jochen P. Müller, with our contributions being equal, and parts of it have been described in his PhD thesis [165]. Dr. Jochen P. Müller collected and analyzed AFM-based single-molecule force spectroscopy data. I collected and analyzed AFM imaging data. We equally contributed to data interpretation.

## 3.1 Force response of VWF dimers under varied pH conditions

For single-molecule force measurements, which were conducted by Dr. Jochen P. Müller, hetero-bifunctional VWF constructs as described in [20] were used, composed of two A1-CK

---

<sup>1</sup>The work presented in this chapter was published in similar form in the *Biophysical Journal*, vol. 111, pp. 312-322, 2016, as *pH-Dependent Interactions in Dimers Govern the Mechanics and Structure of von Willebrand Factor* by Jochen P. Müller\*, Achim Löff\*, Salomé Mielke, Tobias Obser, Linda K. Bruetzel, Willem Vanderlinden, Jan Lipfert, Reinhard Schneppenheim, and Martin Benoit (\*equally contributing first authors).

### 3. Role of pH-dependent interactions in dimers for regulating the mechanics and structure of VWF

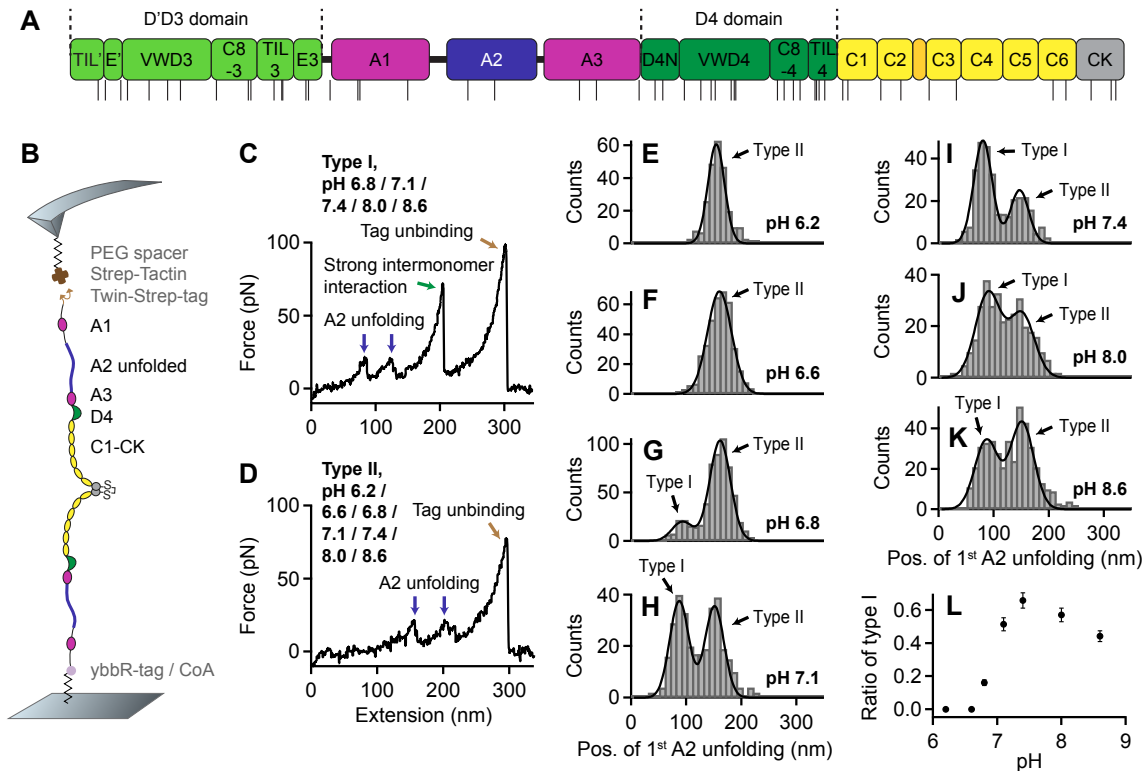


**Figure 3.1: AFM-based single-molecule force measurements on dimeric VWF A1-CK constructs under varied pH conditions.** (A) Domain organization of mature VWF (residues 764-2813), as described in [4, 41]. Positions of histidine residues are indicated by black lines beneath. (B) Schematic of pulling dimeric A1-CK constructs (not drawn to scale). (C-D) Denoised force–extension traces of type I and type II, characterized by A2 unfolding peaks (blue arrows) at low (type I) and at high extension values (type II), respectively. While type II traces were observed throughout the probed pH range, type I traces, showing the force response of dimers that were initially firmly closed via the strong intermonomer interaction [20], were essentially only obtained at pH values of 6.8 and above. At all pH values at which type I traces were observed, dissociation of the strong intermonomer interaction (green arrow) yielded unvaried characteristic length increments. The final peak (brown arrow) corresponds to tag unbinding, *i.e.*, to the dissociation of the specific Twin-Strep-tag/Strep-Tactin interaction and rupture of the probed molecule from the AFM tip [20]. (E-F) Unimodal distributions of the position of the first A2 unfolding peak, obtained for pH 6.2 (E,  $n = 253$ ) and 6.6 (F,  $n = 385$ ). The distributions are well described by fits of Gaussian functions (solid lines). (G-K) Bimodal distributions of the position of the first A2 unfolding peak, obtained for pH values of 6.8 (G,  $n = 586$ ), 7.1 (H,  $n = 329$ ), 7.4 (I,  $n = 317$ ), 8.0 (J,  $n = 336$ ), and 8.6 (K,  $n = 428$ ). To estimate the ratio of type I and type II traces, the distributions were fitted with double Gaussian functions (solid lines). (L) Ratio of type I traces as a function of the pH. Error bars represent Poisson noise (1 SD). AFM-based force measurements were performed by Dr. Jochen P. Müller. Figure as published in [166].

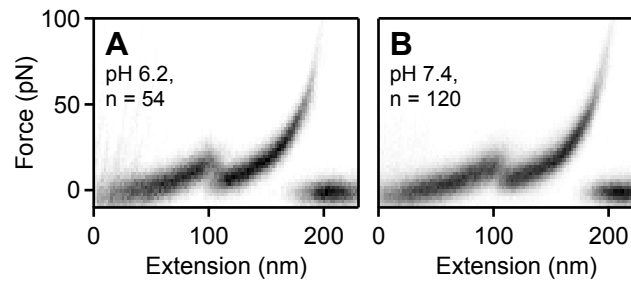


**Figure 3.2: AFM-based single-molecule force measurements on VWF monomers under varied pH conditions.** (A) Overlay of force–extension traces of full-length VWF monomers (D'D3-CK), measured at pH 6.2 ( $n = 54$ ). (B) Overlay of force–extension traces of monomers at pH 7.4 ( $n = 120$ ). Importantly, monomer traces were essentially unaffected by pH. AFM-based force measurements were performed by Dr. Jochen P. Müller. Figure as published as supporting information to [166].

monomers (aa 1238-2813) with different N-terminal tags (Fig. 3.1B). Dimeric A1-CK constructs were preferred over full-length constructs, as they resulted in significantly increased yields of specific pulling events. Higher yields may be a result of better accessible tags when located at the native linker N-terminal of A1 compared to being located directly at the N terminus of D'D3. A ybbR-tag at the N terminus of one of the A1-CK monomers enabled covalent attachment to a coenzyme A functionalized glass surface [156], a Twin-Strep-tag at the N terminus of the other A1-CK monomer allowed for specific pulling via a Strep-Tactin functionalized AFM cantilever [167]. Polyethylene glycol (PEG) spacers were used both at glass surface and cantilever to minimize unspecific protein–surface interactions. Further details on the experimental methods regarding the AFM-based force spectroscopy measurements are given in [20, 166].

Single-molecule force measurements were performed under different pH conditions, ranging from pH 6.2 to pH 8.6, while keeping ionic conditions fixed (150 mM NaCl, 1 mM CaCl<sub>2</sub>, 1 mM MgCl<sub>2</sub>). Different pH values were adjusted by buffer exchange, after attachment of constructs to the functionalized surface at a pH of 7.4. Force–extension traces corresponding to specific pulling events were identified using the appearance of two A2 unfolding peaks as a positive fingerprint [20]. For all probed pH values, traces corresponding to specific pulling events did not exhibit any further characteristic peaks except those of A2 unfolding and –in traces of type I– the high-force peak corresponding to the dissociation of the strong D4-mediated intermonomer interaction in initially firmly closed dimers (*cf.* section 1.4). Traces of type I exhibited A2 unfolding peaks at low extension values, traces of type II –*i.e.* of dimers in which the strong D4-mediated interaction was not formed (*cf.* section 1.4)– at high extension values, with the first A2 unfolding peak being observed at extensions of roughly 80 and 150 nm, respectively [20].

While traces of type I were only observed at pH values of 6.8 and above (Fig. 3.1C), traces of type II were observed for all examined pH values (Fig. 3.1D). In other words, at a pH of 6.2 and 6.6 only type II traces were observed, whereas at pH values of 6.8 and above both type I and type II traces were obtained, yet with markedly varied ratios. Accordingly, quantifying the position of the first A2 unfolding peak in force–extension traces yielded unimodal distributions for pH 6.2 and 6.6 (Fig. 3.1E-F), and characteristic bimodal distributions for pH values of 6.8 and above (Fig. 3.1G-K). These distributions revealed that the mean values of the positions of first A2 unfolding were, both for type I and type II traces, conserved throughout

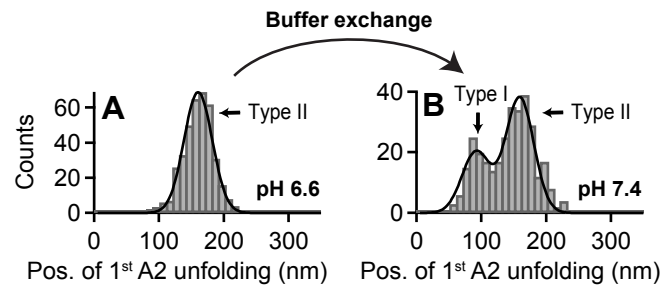


**Figure 3.3: Reversibility of the pH-dependent mechanisms affecting the formation of the strong D4-mediated intermonomer interaction.** (A) Unimodal distribution of the position of the first A2 unfolding peak in force–extension traces of A1-CK dimers measured at pH 6.6 (same histogram as shown in Fig. 3.1F,  $n = 385$ ), indicating that only type II traces were observed. (B) Histogram of the position of the first A2 unfolding peak, obtained after buffer exchanging immobilized proteins to buffer solution of pH 7.4 ( $n = 323$ ) and with the same cantilever that was used at pH 6.6. Bimodality of the distribution indicates that a significant number of type I traces were observed, proving that the molecular mechanisms that critically affect the pH-dependent formation of the strong intermonomer interaction are largely reversible. Fitting a double Gaussian (solid line) yielded a ratio of  $35 \pm 3\%$  type I traces. AFM-based force measurements were performed by Dr. Jochen P. Müller. Figure as published in [166].

the probed pH range within a standard deviation of 5 nm, giving evidence that no domains were significantly destabilized by acidic pH, e.g., due to destabilized disulfide bonds. In line with this, force–extension traces of VWF monomers (full-length, D'D3-CK) at pH 6.2 were essentially identical to the ones obtained at pH 7.4 (Fig. 3.2). The ratios of type I and type II traces for pH 6.8 and above were estimated from double Gaussian fits to the distributions of the first A2 unfolding position. It should be noted that these distributions of the first A2 unfolding position were chosen for determining the ratios –instead of directly determining the ratio of traces exhibiting the peak corresponding to dissociation of the strong D4-mediated intermonomer interaction–, as due to the relatively weak Twin-Strep-tag/Strep-Tactin bond, rupture of the construct from the cantilever frequently occurred before dissociation of the strong intermonomer interaction in type I traces. The ratio of type I traces as a function of the pH exhibited an abrupt increase at approximately pH 7.0 and a maximum value of  $66 \pm 5\%$  at pH 7.4 (Fig. 3.1L), closely matching the ratio previously observed for full-length dimers [20]. Upon further alkalization, the ratio of type I traces slightly decreased, resulting in a value of  $44 \pm 3\%$  at pH 8.6. It should be noted that both at pH 8.0 and 8.6 the yield of specific pulling events, *i.e.* force–extension traces exhibiting two clear A2 unfolding peaks, was lower than at pH 7.4 and below. Overall, these data show that the formation of the strong intermonomer interaction in VWF's dimeric subunits strongly depends on the pH.

In order to test for reversibility of the underlying molecular mechanisms, the buffer of immobilized proteins was exchanged after measurements at pH 6.6 (histogram of first A2 unfolding position shown in Fig. 3.1F and Fig. 3.3A) to buffer solution adjusted to pH 7.4. Importantly, force–extension traces of type I were recovered, indicating that the pH-dependent mechanisms that critically affect the formation of firmly closed dimers are largely reversible. However, the ratio of type I traces was lower ( $35 \pm 3\%$ ) compared to experiments without prior incubation at acidic pH, as inferred from the bimodal distribution of the position of first A2 unfolding (Fig. 3.3B).

## 3.2 Static conformation of VWF dimers under varied pH and ionic conditions

To complement the single-molecule force experiments, I employed AFM imaging to assess the conformational ensemble of dimeric VWF constructs adsorbed onto a poly-L-lysine coated mica substrate under different pH conditions (see sections 2.1 and 2.4 for details on the imaging protocol and employed buffers). Exemplary images are shown in Fig. 3.4A-B. I quantified the ratio of compact dimers by analyzing the conformation of each dimer individually (see Fig. 2.2). Concretely, I analyzed the stem length for each dimer, *i.e.* the distance along the contour from the CK domain to the position at which the two constituent monomers separate from each other. I further measured the distance along the contour between the CK domain and the beginning of higher N-terminal domains for both monomers and used the mean of these distances to normalize the stem length. In general, the distributions of this normalized stem length exhibited two distinct populations, corresponding to dimers with (partially) open stems and fully formed ones, respectively (Fig. 3.5). Dimers corresponding to the latter population, exhibiting a normalized stem length above 1, were assigned as compact [20]. It should be noted that at the (unphysiological) alkaline pH values of 8.0 and 8.6, a non-negligible fraction of molecules –up to approximately 40 % at pH 8.6– had to be discarded from analysis, as apparent self-aggregation repeatedly impeded unequivocal tracing, in line with observations from an earlier TEM study [47].

I determined the ratio of compact full-length dimers (D'D3-CK) as a function of the pH, both in the presence of divalent ions (Fig. 3.4C, blue circles), and in the absence of divalent ions (Fig. 3C, red triangles), *i.e.* under conditions that obstruct the formation of the D4-mediated strong intermonomer interaction [20]. In the latter case, to remove divalent ions from solution, samples were incubated with EDTA prior to buffer exchange to the measurement buffer. In the absence of divalent ions, compactness decreased monotonically with increasing pH and was very well described by the fit of a simple sigmoidal function reaching its half-maximum at a pH of approximately 6.6 (dashed line; sigmoidal fit of the form  $y = y_{\max} / \{1 + \exp((x_{\text{half}} - x) / \text{const.})\}$ ). These findings suggest compactness to be mainly driven by a single process in the absence of divalent ions. In the presence of divalent ions, for pH values of 6.8 and below, I obtained ratios of compact dimers essentially identical to the ones observed in the absence of divalent ions. Above a pH of 6.8, however, a second regime of compactness was observed. Intriguingly, the deviation to the data obtained in the absence of divalent ions was highest at a pH of 7.4, and is fully in line with the pH dependence of the strong intermonomer interaction observed in force measurements.

Furthermore, I studied the compactness of dimers with a deletion of the D4 domain (*delD4* dimers) in the presence of divalent ions (Fig. 3.4C, brown squares). Throughout the whole pH range, compact dimers with fully formed stems were observed only occasionally (Fig. 3.4B-C), strongly suggesting the D4 domain to play a key role not only for the formation of the strong intermonomer interaction [20], but also for promoting compactness of dimers under acidic pH conditions.

I further observed that the pH, in addition to its impact on the strong D4-mediated intermonomer interaction, also affected the formation of C-terminal stems [20, 47]. In order to

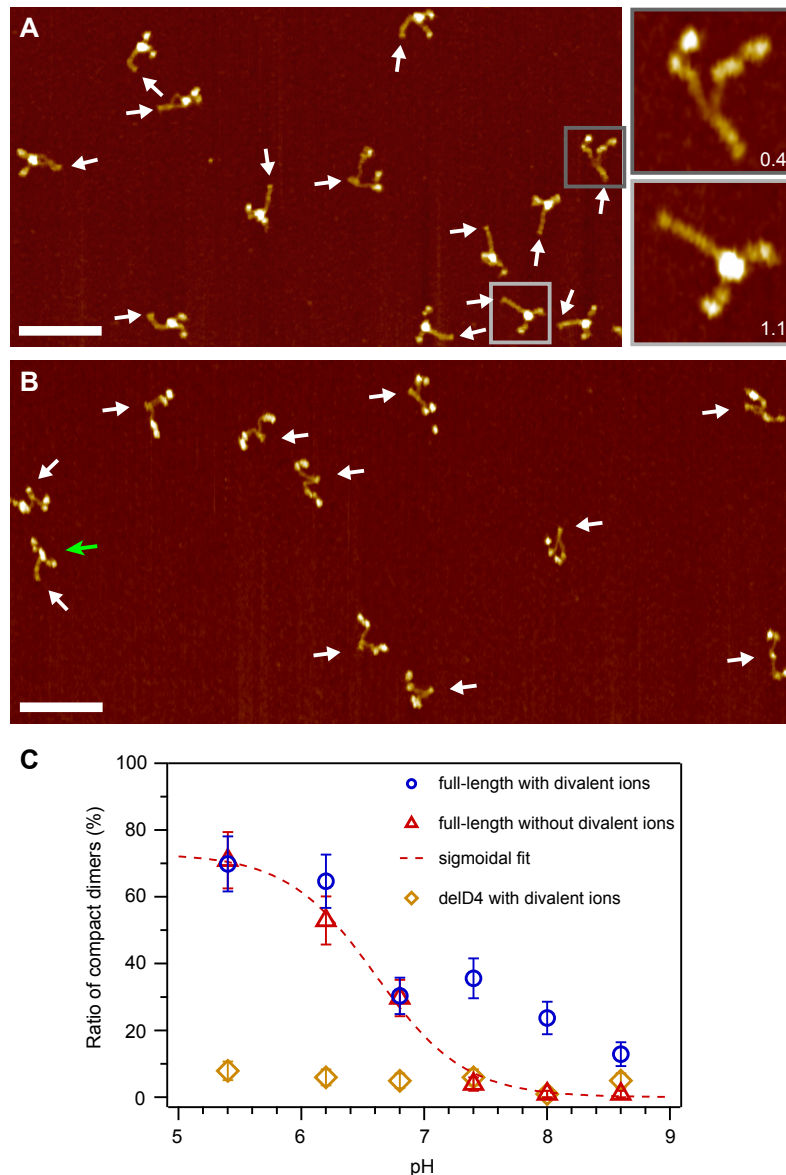


**Figure 3.4: Conformation of dimeric VWF constructs under varied pH and ionic conditions.** (A) Representative AFM image of full-length VWF dimers (D'D3-CK), adsorbed onto a functionalized mica surface from buffer solution without divalent ions and adjusted to pH 6.2. Arrows mark positions of CK domains. A large fraction (> 50%) of dimers exhibited a compact conformation with fully formed C-terminal stems. Insets exemplarily show a flexible dimer possessing a partially formed stem and a compact dimer with a fully formed stem, respectively. Numbers indicate values of the normalized stem length. Scale bar is 100 nm, range of color scale is 2.4 nm. (B) Representative AFM image of VWF dimers with a deletion of the D4 domain (*delD4* dimers), adsorbed onto a functionalized mica substrate from buffer solution adjusted to pH 6.8 and containing divalent ions. White arrows mark positions of CK domains. Throughout the whole probed pH range, nearly all *delD4* dimers exhibited a flexible conformation. The green arrow indicates an occasional compact dimer. Scale bar is 100 nm, range of color scale is 2.4 nm. (C) Ratio of compact VWF dimers as a function of the pH. Only dimers with a normalized stem length above 1 were assigned as compact. Shown are data of full-length dimers in the presence (blue circles) and in the absence (red triangles) of divalent ions, and of *delD4* dimers in the presence of divalent ions (brown squares). The dashed red line is a sigmoidal fit (half-maximum value at pH 6.6) to the data obtained for full-length dimers in the absence of divalent ions, *i.e.* under conditions that obstruct the formation of the strong intermonomer interaction mediated by the D4 domain [20]. Error bars represent Poisson noise (1 SD). For each data point,  $n \geq 100$  dimers were analyzed. Figure adapted from [166].

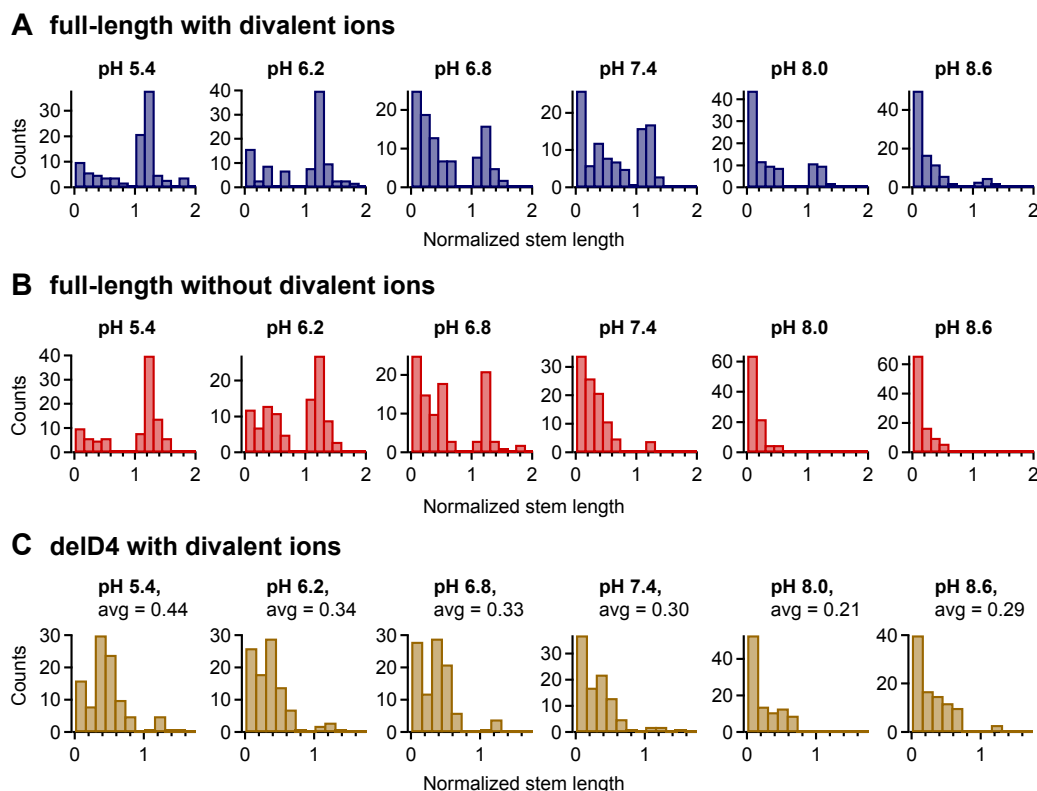


**Figure 3.5: C-terminal stems in VWF dimers under varied pH and ionic conditions.** (A) Distributions of the normalized stem length of full-length dimers in the presence of divalent ions, obtained for pH 5.4, 6.2, 6.8, 7.4, 8.0, and 8.6 by tracing dimers in AFM images individually along their contour. (B) Distributions of the normalized stem length of full-length dimers constructs in the absence of divalent ions. (C) Distributions of the normalized stem length of *delD4* dimers and respective average values, in the presence of divalent ions. The ratios of compact dimers shown in Fig. 3.4C correspond to the fractions of counts with a normalized stem length above 1 in the respective distributions shown here. It should be noted that at the alkaline pH values of 8.0 and especially 8.6, a non-negligible fraction of molecules had to be discarded from analysis due to apparent self-aggregation. Figure adapted from [166].

investigate this effect without the influence of D4-mediated interactions, I analyzed distributions of the normalized stem length for the *delD4* construct (Fig. 3.5C), exhibiting virtually only values of the normalized stem length below 1, corresponding to flexible dimers. In general, higher average stem lengths were favored by low pH, even in the absence of D4-mediated interactions promoting compactness. In particular, also the functional shape of the stem length distributions changed considerably with the pH. While at alkaline pH values the distribution of the normalized stem length exhibited an approximately exponential shape, at lower pH values it revealed a maximum centered at roughly 0.4 that became more prominent with decreasing pH, suggesting that the different C domain interactions involved in stem formation are differently affected by the pH. The maximum centered at approximately 0.4 corresponds to dimers possessing roughly half-formed C-terminal stems, *i.e.* stems that are formed from CK domains up to a region comprising domains C5 to C3, which interestingly exhibit a comparably low density of histidine residues (Fig. 3.4A).

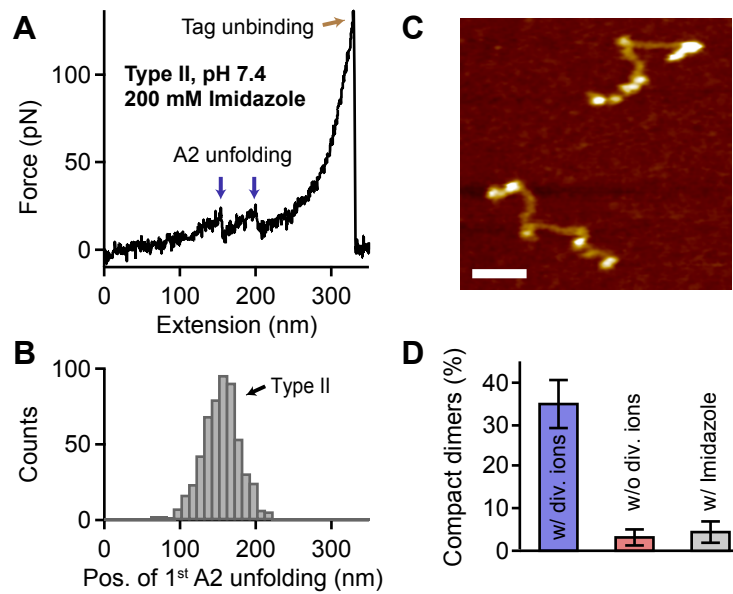


**Figure 3.6: Obstruction of the strong intermonomer interaction by imidazole.** (A–B) Single-molecule force measurements on A1-CK dimers at pH 7.4 in the presence of divalent ions and 200 mM imidazole. Force–extension traces of type II (A) were observed almost exclusively, as inferred from a unimodal distribution of the position of the first A2 unfolding peak (B). AFM-based force measurements were performed by Dr. Jochen P. Müller. (C–D) AFM imaging of full-length VWF dimers adsorbed onto a functionalized mica surface from buffer solution adjusted to pH 7.4 and containing 200 mM imidazole in addition to divalent ions. Nearly all dimers exhibited a flexible conformation (C). Scale bar is 30 nm, range of color scale is 2.4 nm. The ratio of compact dimers was close to zero (D,  $n = 81$ ), similarly to the one obtained in the absence of divalent ions (see Fig. 3.4C). Further co-plotted is the markedly higher ratio observed for dimers adsorbed from buffer containing divalent ions, but no imidazole (see Fig. 3.4C). Error bars represent Poisson noise (1 SD). Figure as published in [166].

### 3.3 Obstruction of the strong D4-mediated intermonomer interaction by imidazole

The data presented above indicate that the strong intermonomer interaction is most favorable at pH 7.4, and only occurs in the presence of divalent ions. To gain further insight into the underlying molecular mechanisms, it was tested whether the role of divalent ions in the strong intermonomer interaction originates from an electrostatic effect or rather involves coordination chemistry, possibly with the histidine residues which are abundant in the D4 domain (Fig. 3.1A). To this end, force experiments on A1-CK dimers at pH 7.4 in buffer solution supplemented with free imidazole (200 mM) in addition to  $\text{MgCl}_2$  and  $\text{CaCl}_2$  were performed. In contrast to EDTA, which has only very low selectivity among the different divalent cations, imidazole has virtually no affinity towards  $\text{Mg}^{2+}$  and  $\text{Ca}^{2+}$ , but is capable of strong coordination bond formation with transition metal ions [168], which might be available during the biosynthesis of VWF. Strikingly, essentially only force–extension traces of type II were obtained (Fig. 3.6A), as inferred from a unimodal distribution of the position of the first A2 unfolding event (Fig. 3.6B). Obstruction of the strong intermonomer interaction by free imidazole was further corroborated by AFM imaging of full-length dimers, adsorbed from the same buffer solution. In the presence of imidazole, nearly all dimers exhibited a flexible conformation (Fig. 3.6C–D), which is in line with a scenario in which divalent (transition) metals are involved in the formation of the strong

intermonomer interaction.

### 3.4 Discussion and Conclusion

In the previous sections, AFM-based single-molecule force measurements and AFM imaging were employed to characterize VWF's force response and conformational ensemble under different pH conditions. It was initially found that the mechanical resistance of VWF's dimeric subunits strongly depends on the pH, as quantified by the ratio of type I force–extension traces, *i.e.* traces corresponding to the force response of dimers that were initially firmly closed via the strong D4-mediated intermonomer interaction [20]. Interestingly, at low pH values of 6.2 and 6.6, virtually no dimers exhibited the strong intermonomer interaction. At first glance, this finding may appear contradictory to imaging data, which revealed that, almost throughout the whole examined pH range, low pH favors a compact conformation of dimers, thereby confirming a previous TEM study [47]. In fact, combining the results from force and imaging experiments leads to the conclusion that compact dimers below pH 6.8 have a low mechanical resistance (Fig. 3.7, top), and accordingly, that the strong intermonomer interaction in VWF dimers is absent at these low pH values. In other words, compactness of dimers under acidic pH conditions is not accomplished by the strong intermonomer interaction, suggesting a second pH-dependent process to promote compactness under acidic pH conditions [47]. Indeed, in the presence of divalent ions, the compactness of dimers as a function of the pH revealed two regimes, strongly suggesting at least two pH-dependent interactions promoting compactness. The process that promotes compactness above pH 6.8 is the formation of the strong intermonomer interaction (Fig. 3.7, bottom), as inferred from two observations: first, the critical pH of 6.8, above which a second regime of compactness was observed, equals the critical pH of the strong intermonomer interaction observed in force experiments, and second, compactness above pH 6.8 can be abolished by taking out divalent ions from solution, in line with a loss of the strong intermonomer interaction observed in force experiments after treating samples with EDTA [20]. In the absence of divalent ions, a monotonic decrease of the compactness of dimers with increasing pH was observed. The fact that this decrease was well described by the fit of a sigmoidal function suggests unidirectional pH-dependent interactions that do not rely on divalent ions. AFM imaging experiments on dimeric *delD4* constructs revealed a crucial role of the D4 domain for promoting compactness at acidic pH. This finding strongly suggests the existence of a second intermonomer interaction mediated by D4, which is mechanically less stable than the strong intermonomer interaction.

Importantly, C-terminal stem formation by itself, based on weak interactions between C domains [20], was also affected by the pH, as revealed by distributions of the normalized stem length obtained for *delD4* dimers under varying pH conditions. While at alkaline pH values the distributions exhibited an approximately exponential shape, decreasing the pH led to the emergence of a maximum corresponding to dimers possessing roughly half-formed stems, suggesting that the different C domain interactions involved in stem formation are differently affected by the pH. Going along with this observation, the average value of the normalized stem length increased by trend with decreasing pH (Fig. 3.5), resulting in a decreased average distance between the two D4 domains within a dimer. As a decreased distance between D4 domains in turn results in a higher effective concentration of these two putative binding partners, one could speculate that the pH dependence of the stem formation might be the

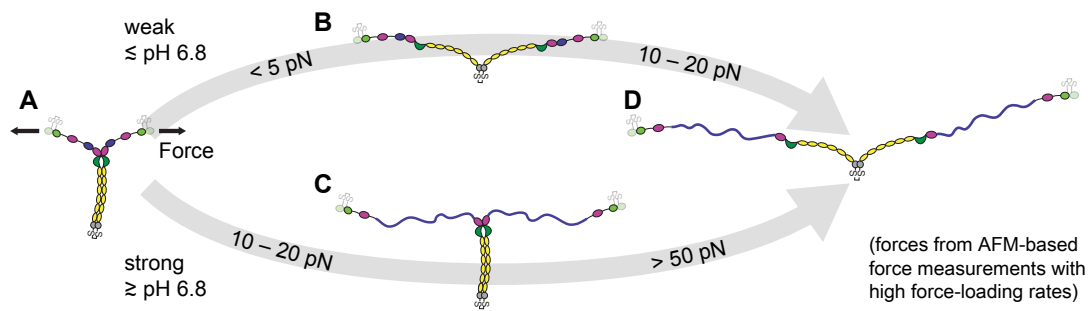


**Figure 3.7: Strong and weak C-terminal stems in VWF's dimeric subunits.** Schematically depicted are force-induced conformational changes (indicated forces correspond to loading rates probed in AFM-based single-molecule force experiments) of VWF dimers that initially possess a fully formed C-terminal stem (C-terminal rod, A). At pH values below approximately 6.8, C-terminal rods are by trend weak and can dissociate at forces clearly below the detection limit of AFM force experiments, *i.e.* dissociation occurs very likely well below 5 pN (B). At forces of roughly 10-20 pN, VWF's A2 domains unfold and add a contour length of approximately 60-70 nm (lengths in schematic are drawn roughly to scale) each to the elongation of dimers [7, 56, 169, 170] (D). At pH values above approximately 6.8 however, C-terminal rods are by trend firmly closed via the strong D4-mediated intermonomer interaction. In this case, unfolding of the A2 domains at 10-20 pN is the first critical step of elongation (C). At forces above 50 pN the strong intermonomer interaction can dissociate and add approximately 80 nm to the elongation of dimers (D). Importantly, forces on VWF result from a positive feedback between elongational flow and length. For a VWF multimer subjected to elongational flow under acidic pH conditions, forces of for instance 10-20 pN, as required for A2 unfolding, can be expected to be reached more readily, compared to near-physiological conditions, due to rapid initial opening of weak rods. Figure adapted from [166].

only pH dependence underlying the increase of compactness of dimers with decreasing pH. A simple estimation, based on the observed distances between the D4 domains in a dimer and the assumption that the effective concentration of D4 scales with the inverse cube of these distances, suggests that the pH-induced changes of the distance between the D4 domains of a dimer may well lead to an increase of their effective concentration by a factor of 4 over the probed pH range. However, the strong pH dependence of the ratios of compact dimers in the absence of divalent ions (Fig. 3.4C, red), suggests that –assuming a constant affinity for the interaction between the two D4 domains– a change of the effective concentration by almost two orders of magnitude would be necessary to explain the observed increase of compactness with decreasing pH. Therefore, it appears very likely that the mechanically weak intermonomer interaction mediated by D4 under acidic conditions possesses an intrinsic pH dependence. Remarkably, the direction of this pH dependence is opposite to the one of the strong intermonomer interaction mediated by the same domain. Both the pH dependence of the weak D4-mediated interaction and of the stem formation may play a pivotal role for orderly multimerization and packing of VWF in the trans-Golgi and WPB [47].

A key finding is the pH dependence of the strong intermonomer interaction in VWF's dimeric subunits. Strikingly, decreasing the pH from 7.4 by less than one unit switches off the strong intermonomer interaction, thereby drastically decreasing the mechanical resistance of dimers. While at pH 6.6 the strong intermonomer interaction was virtually not observed, it could form again after buffer exchange to buffer solution adjusted to pH 7.4. This finding indicates that the molecular mechanisms that underlie the pH dependence of the strong intermonomer interaction are largely reversible. Importantly, the key domain D4 possesses a high density

of histidine residues, whose imidazole sidechains can be protonated, resulting in a change of their net charge, around a pH of approximately 6.5 (the  $pK_a$ -value of free histidines [171]). This value is very close to the pH range over which the strong intermonomer interaction was abruptly switched off. A possible role of histidines was indeed indicated by measurements in the presence of free imidazole, which revealed obstruction of the strong intermonomer interaction. Given that the strong intermonomer interaction crucially depends on divalent ions [20], it appears likely that coordination of metal ions by histidine residues may play a fundamental role for the formation of the strong intermonomer interaction. Indeed, it is well-known that coordination chemistry through imidazole is impeded by protonation. It should be noted that full obstruction of the strong intermonomer interaction by removal of divalent ions was not achieved by a simple buffer exchange to buffer not containing divalent ions, but required addition of a chelating agent such as EDTA (see section 2.4). This implies that also ion species not added to the buffer solutions, for instance ions of transition metals such as zinc, could be involved in the formation of the strong intermonomer interaction. Furthermore, it should be stressed that the effect of imidazole should be taken into account when using it in protein purification procedures for VWF constructs.

Histidine residues might also play a role for mediating the increase in compactness of dimers under acidic conditions, as suggested by the sigmoidal fit to the data obtained in the absence of divalent ions, which reached its half-maximum value at a pH of approximately 6.6, close to the  $pK_a$ -value of histidines. High-resolution structures of the D4 domain and its constituent modules will likely be of great value to elucidate these pH dependencies in the future.

### Potential physiological role of VWF's pH sensitivity

In the vasculature, activation of VWF for hemostasis crucially depends on its ability to sense hydrodynamic forces [4, 5, 172], originating from an interplay of multimer length and elongational flow components [7, 21, 22, 24] (see sections 1.3 and 1.4). Importantly, force sensing by VWF is tuned by the strong intermonomer interaction in its dimeric subunits, as it markedly shortens the effective length of a multimer contributing to force sensing [20]. For the pH values probed in the experiments presented above, the fraction of firmly closed dimers reached a maximum at a pH of 7.4, indicating that VWF's mechanical resistance is maximized with respect to the physiological pH of 7.4 in the blood. Accordingly, critical rates of elongational flow needed to activate VWF for hemostasis, *i.e.* to initiate collagen binding and platelet aggregation, will be highest at physiological pH, assuming that the interactions of VWF with collagen and platelets as such remain unvaried by pH.

It is tempting to speculate on the role of this pH dependence, considering that locally the pH may be disturbed at sites of vascular injury. Indeed, it is widely accepted that local pH variations, especially acidification, occur in connection with injury and inflammation [26, 104–107], although it remains unclear to what extent and on which timescales the blood pH might be affected. Clearly, the data presented here suggest that deviations from physiological pH will lower critical rates of elongational flow to activate VWF for hemostasis. In particular, acidification is expected to very effectively reduce such critical elongational flow rates. Indeed, data obtained from flow experiments and published within the framework of a PhD thesis (Dr. Daniel Steppich, University of Augsburg, Germany) suggest that critical shear rates for elongation of VWF are lowered both upon acidification and alkalization [173]. In principle, the

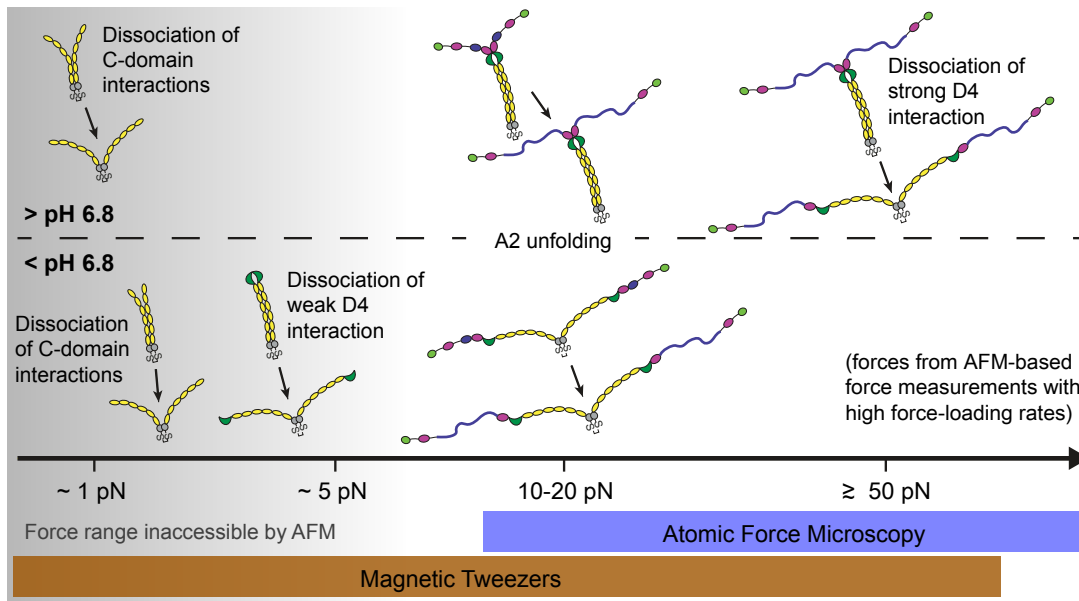


**Figure 3.8: Overview of force-sensitive interactions and transitions within VWF dimers under varied pH conditions.** Schematically depicted are selected intermonomer interactions within VWF dimers and their pH dependencies, as identified by AFM-based force measurements and AFM imaging, and the observed or estimated forces needed for dissociation of the respective interactions. In addition, force-induced unfolding of the A2 domain is depicted. Dissociation of the depicted interactions contributes significantly to elongation of VWF multimers under force. The stated forces correspond to the ones observed in AFM-based force measurements conducted with high loading rates. The blue and brown bars beneath indicate the force range accessible by AFM- and MT-based force spectroscopy, respectively. Importantly, the weak interactions involved in formation of C-terminal stems could not directly be probed by AFM force measurements.

relative impact of the pH on critical elongational flow rates can be estimated based on the ratio of firmly closed dimers in VWF, observed at a given pH [20]. For instance, at a pH of 6.6, at which virtually no dimers exhibit the strong intermonomer interaction, the critical elongational flow may only be roughly half compared to the one at pH 7.4, as in the latter case VWF's effective force sensing length is expected to be decreased by approximately 30 %, assuming approximately half of VWF's dimeric subunits to be firmly closed via the strong intermonomer interaction. On the other hand, under acidic conditions VWF's force sensing length will initially be lower than under physiological conditions, due to compact, yet mechanically relatively unstable dimers. However, as strongly suggested by the force data, most compact dimers below pH 6.8 will open up at comparably very low elongational flow rates and consequently increase VWF's effective force sensing length very rapidly, thereby triggering further elongation, due to the positive feedback between hydrodynamic force and length.

Taken together, decreasing the pH by one unit from physiological pH yields a markedly increased degree of compactness of dimers, yet a considerably lowered mechanical stability. While high compactness at acidic pH can be assumed to be a prerequisite for orderly multimerization in the trans-Golgi and storage in Weibel-Palade bodies, low mechanical resistance at acidic pH may enhance VWF's hemostatic activity at sites of locally lowered pH encountered in the wake of injuries. One could hence speculate that VWF's pH-dependent elongation behavior represents a smart means to favor VWF activation exactly where needed.

**Summary: interactions in VWF dimers and open questions**

An overview of the different intermonomer interactions that were identified and on their pH dependencies is given in Fig. 3.8, along with the observed or estimated forces needed to dissociate the respective interactions. I want to stress that the stated forces are the ones that were observed in AFM-based force measurements conducted with rather high, very likely unphysiological, force-loading rates. It can be expected that dissociation can occur at markedly lower forces in the physiologically likely more relevant case of extended exposure to force, which could be tested in force-clamp measurements at low forces.

Importantly, the weak D4-mediated interaction and in particular the weak C-domain interactions involved in stem formation could not be probed directly in AFM-based force measurements due to the limited force resolution, but were only inferred from AFM imaging results. However, opening of C-terminal stems that are not firmly closed by the strong D4-mediated intermonomer interaction likely constitutes the first step of VWF's elongation under force, and thus the first step in VWF's activation cascade. Consequently, a comprehensive characterization and understanding of the involved low-force interactions would be of outstanding interest.

In order to directly probe VWF at low force, I aimed at employing magnetic tweezers. In the next chapters, the development and validation of a novel approach for protein force spectroscopy in magnetic tweezers is presented, followed by its application to dimeric VWF constructs. The MT measurements indeed allowed to directly observe transitions in the VWF stem, and revealed that the strong D4-mediated intermonomer interaction can dissociate at much lower forces, in the same range as A2 unfolding, when subjected to a constant force, as will be described in sections 5.3 and 5.2, respectively.



# Modular, ultra-stable and highly parallel protein force spectroscopy in MT

In this chapter, I will present a novel, modular approach for protein force spectroscopy in magnetic tweezers, enabling precise and multiplexed force measurements for a wide range of proteins in the physiologically relevant force regime. After a short introduction on the current state of the art of protein force spectroscopy in MT, the novel protein attachment strategy based on Elastin-like polypeptide linkers will be described, followed by a validation of the method using the previously well-described protein domain ddFLN4 as a test system. Furthermore, the lifetime of the biotin–streptavidin bond that links protein and magnetic bead is characterized and optimized by using a recently developed monovalent streptavidin variant. Finally, the impact of different pulling geometries, resulting from the tetravalency of streptavidin, on the lifetimes of biotin unbinding is investigated in detail using streptavidin variants of different valencies.

Application of the presented MT approach for force-clamp measurements on dimeric VWF will be described in the next chapter.<sup>1,2</sup>

The protein attachment protocol was developed in close collaboration with Dr. Philipp U. Walker and was already described in his PhD thesis [138], along with data on ddFLN4. Our contributions to the development of the attachment protocol and to data interpretation were equal. I prepared and conducted all presented MT measurements, with support by Dr. Philipp U. Walker. I analyzed the data, mostly using software written and provided by Dr. Philipp U. Walker (*cf.* section 2.2.3). Dr. Philipp U. Walker was not involved in the work presented in

---

<sup>1</sup>The work presented in the first four sections of this chapter, along with data described in chapter 5, was posted in similar form as a preprint to *bioRxiv* (2018; doi: 10.1101/491977), as *Modular, ultra-stable and highly parallel protein force spectroscopy in magnetic tweezers using peptide linkers* by Achim Löff, Philipp U. Walker, Steffen M. Sedlak, Tobias Obser, Maria A. Brehm, Martin Benoit, and Jan Lipfert, and is currently under review at the *Proceedings of the National Academy of Sciences of the U.S.A.*

<sup>2</sup>The work presented in the last section of this chapter closely follows a manuscript in preparation, entitled *The tetravalency of streptavidin results in distinct lifetimes of biotin unbinding under constant load* by Achim Löff\*, Steffen M. Sedlak\*, Sophia Gruber, Martin Benoit, Jan Lipfert, and Hermann E. Gaub (\*equally contributing first authors).

section 4.5.

The work presented in section 4.5 was performed in close collaboration with Steffen M. Sedlak, with our contributions being equal. Steffen M. Sedlak designed and prepared the different streptavidin variants and performed isothermal titration calorimetry measurements. Functionalization of magnetic beads with streptavidin was conducted jointly. I prepared and conducted the lifetime measurements using MT and performed AFM imaging experiments. We contributed equally to data analysis and interpretation.

## 4.1 Protein force spectroscopy in MT: state of the art and challenges

As mentioned before, mechanical forces acting on proteins or ligand-receptor pairs are an integral part of many biological processes. Often the physiological functions of proteins are critically regulated by force: examples include the mechano-activation of enzymes and the force-regulated exposure of cryptic binding sites [1, 2] – regulatory strategies that are also adopted by von Willebrand factor, as discussed in section 1.4. Another common example is the force-dependent unfolding and refolding of protein domains as “strain absorbers” to dissipate mechanical stress [1, 2]. Most insights into the mechanical properties and regulation of proteins and their complexes at the single-molecule level have been obtained from AFM- or OT-based force spectroscopy experiments. While AFM and OT force spectroscopy measurements have provided unprecedented insights, they also have important shortcomings [121]. AFM measurements cannot resolve forces below  $\approx 10$  pN; OT provide excellent spatio-temporal resolution even for forces down to  $\approx 1$  pN, but are not capable of measuring many molecules in parallel [121]. In addition, both AFM and OT intrinsically control position and not force, such that constant-force measurements – which allow for a much more straight-forward determination of rates as compared to measurements with variable force – require active feedback.

MT have the potential to overcome these shortcomings. In MT, molecules of interest are tethered between a surface and superparamagnetic beads, as described in section 2.2.2 (Fig. 2.4). External magnetic fields exert precisely controlled forces [141] in the range of  $\approx 0.01$  – 100 pN, and MT naturally operate in constant force mode, *i.e.* the applied force is constant during the measurement (to within 0.01 %; *cf.* section 2.2.2 and Fig. 2.5), as long as the external magnetic field is not actively changed, with excellent sensitivity in particular at low forces. Furthermore, previous work has demonstrated camera-based tracking for  $\approx 10$ s – 100s of nucleic acid-tethered beads simultaneously [142–144] in  $(x,y,z)$  with  $\approx$  nm-spatial resolution, and, recently, also up to  $\leq$  ms-temporal resolution [145–147]. In addition, MT do not suffer from heating or photo-damage [121], and thus in principle allow for long-term, stable, and robust measurements on many molecules in parallel.

Despite these advantages, MT so far have mainly been employed to investigate nucleic acid tethers. A key challenge in applying MT to protein force spectroscopy remains to tether  $\approx$  nm-sized proteins between much larger,  $\approx$   $\mu$ m-sized beads and the surface, while avoiding unspecific protein–surface and bead–surface interactions, and ideally with a large number of usable tethers in each field of view. Previous MT studies on proteins, therefore, mostly employed large protein constructs, often polyproteins with repeats of e.g. titin Ig or protein L domains [174–177]. Previous strategies for attaching proteins to the surface in MT were

either non-covalent, based on antibodies [178–182] or His-tag  $\text{Cu}^{2+}$ -NTA chemistry [183, 184], or on covalent linkage, either of Halo-tag fusion proteins to a surface coated with Halo-tag amine ligands [174–176, 185] or using the Spy-tag-SpyCatcher system [177, 186]. Non-covalent attachment has the disadvantage of limited force stability compared to covalent attachment. Attachment via fusion proteins potentially complicates the analysis due to unfolding and refolding transitions of the proteins used for attachment, as for instance in the case of the Halo-tag [174]. In addition, attachment strategies without dedicated linkers can be expected to be prone to unspecific surface interactions. Recent studies have used fusion proteins with titin Ig-domains flanking the protein of interest as spacers, which however may again complicate analysis due to their unfolding and folding transitions [177, 186]. Finally, attachment via fusion proteins appears to suffer from a low number of usable tethers, as so far there have been no reports of multiplexed protein unfolding and refolding measurements.

Taken together, making full use of the promising potential of MT for protein force spectroscopy, in particular for long-term and parallel measurements, will require a more versatile and efficient approach for tethering of a wide range of proteins, without the need for elaborate protein modification.

In the following section, I present a modular protein attachment strategy that uses a dedicated peptide linker, ensuring efficient attachment to the surface while minimizing unspecific interactions, both critical prerequisites for high-throughput parallel measurements. In this approach, the protein of interest requires only short (1 and 11 aa) peptide tags for coupling to the linker and bead, respectively, avoiding the need for large fusion proteins and providing a general attachment strategy that is independent of protein size. I hence anticipate this tethering strategy to be applicable to a wide range of proteins and expect it to be of immediate use also for other parallel force spectroscopy techniques, such as single-molecule centrifugation [122, 123] or acoustic force spectroscopy [124], extending their capabilities towards protein force spectroscopy.

## 4.2 Protein attachment *via* Elastin-like polypeptides

The novel attachment strategy uses an unstructured Elastin-like polypeptide (ELP) linker [126, 160] with a contour length of  $\approx 120$  nm and functional groups at its termini. The ELP linker serves as spacer for site-specifically immobilizing the protein of interest to the bottom glass slide of the flow cell and to reduce unspecific protein–surface [126] and bead–surface interactions (Fig. 4.1A). The ELP linker is attached to a glass slide functionalized with thiol-reactive maleimide groups via an N-terminal cysteine (see section 2.2.3 for details of the coupling protocol). It further carries a C-terminal LPETGG motif that allows for site-specific and covalent ligation to the protein of interest via an N-terminal glycine residue in a reaction catalyzed by the enzyme sortase A [158]. For coupling to the bead, the protein of interest is further engineered to carry an 11-aa ybbR-tag [156] at its C-terminus that is covalently attached to coenzyme A–biotin in the *sfp* phosphopantetheinyl transferase reaction. Finally, the biotin-label forms a high-affinity non-covalent bond to streptavidin-functionalized beads. Importantly, this approach requires only short peptide tags on the protein of interest that can readily be introduced by standard molecular cloning methods and have been shown to be compatible with expression and folding of a large range of proteins [127, 156, 158, 188, 189]. It should further be noted that

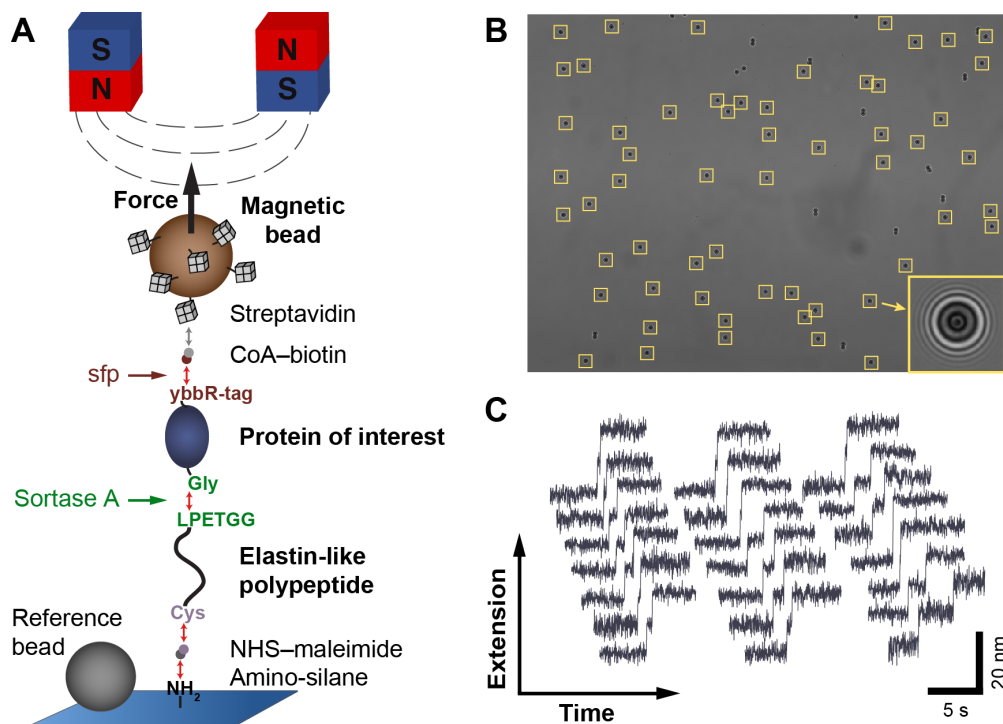


**Figure 4.1: Attachment protocol for highly parallel force spectroscopy on proteins in MT.** (A) Schematic of the strategy for tethering a protein of interest between the bottom glass slide of the flow cell and a magnetic bead (not to scale). An ELP linker with a single cysteine at its N-terminus is coupled to the amino-silane on the glass slide *via* a small-molecule NHS–maleimide cross-linker. After covalent coupling of coenzyme A (CoA)–biotin to the ybbR-tag at the C-terminus of the protein in a bulk reaction catalyzed by sfp phosphopantetheinyl transferase, the protein is covalently ligated to the ELP linker via one (or more) glycines at its N-terminus in a reaction mediated by sortase A, which selectively recognizes the C-terminal LPETGG motif of the ELP linker. Finally, a streptavidin-coated magnetic bead is bound to the biotinylated protein via the high-affinity biotin–streptavidin interaction. Red and grey double arrows indicate covalent and non-covalent bonds, respectively. Forces are exerted on the magnetic bead by permanent magnets positioned above the flow cell. Non-magnetic polystyrene beads baked onto the surface are used as reference beads for drift correction. (B) Representative field of view. Yellow boxes indicate approximately 60 beads marked for tracking. The enlarged image of one bead shows the diffraction ring pattern used for 3D bead tracking. (C) Example tether extension time traces showing the characteristic three-state unfolding pattern of ddFLN4 (see section 4.3). All traces shown were recorded in parallel from different beads within the same field of view at a constant force of 21 pN. Figure as in [187].

the described tethering approach also works for proteins equipped with a C-terminal LPETGG motif in combination with ELP linkers that carry N-terminal glycine residues, thus providing even more flexibility. In this case, the ybbR-tag would be located N-terminally. In principle, the ybbR can also be located within a flexible loop in the protein of interest [156].

I applied the tethering protocol to two very different protein systems: the small, single protein domain ddFLN4 ( $\approx 100$  aa) and large full-length dimeric VWF ( $\approx 4000$  aa), as shown in detail in the next section and in chapter 5, respectively. I obtained comparable and efficient tethering of beads with a large number of specific, single-molecule tethers in both cases. Typically, in a single field of view ( $\approx 440 \times 330 \mu\text{m}^2$ ) of the used MT setup (Fig. 4.1B; see section 2.2.2 and Figs. 2.4 and 2.5 for details on the setup) 50 to 100 tethered beads can be tracked in parallel, of which 30 to 50 tethers exhibit characteristic unfolding and refolding signatures (Fig. 4.1C). The beads that do not show characteristic signatures are likely anchored to the surface by

multiple protein tethers, since in control measurements without the protein of interest added, there is essentially no unspecific binding of beads to the surface (0-1 beads per field of view). The fraction of specific tethers attached via a single protein can be increased by decreasing the density of proteins immobilized on the surface. However, decreasing the protein concentration too much will also result in a decrease of the number of single-tethered beads. Optimizing the conditions, I achieved fractions of up to  $\approx 60\%$  specific, single-protein tethers, while still obtaining a large number of tethered beads at the same time. The most efficient flow cell exhibited 50 specific out of 85 beads within the single field of view measured. Given ongoing improvements in camera technology, I expect that the number of protein tethers that can be measured in parallel will further increase by at least an order of magnitude in the near future.

### 4.3 Three-state unfolding and folding of ddFLN4 at constant force

In order to validate the tethering protocol, I first applied it to the small Ig-fold domain ddFLN4 (Fig. 4.2A), which is the fourth domain of the F-actin crosslinking filamin rod of *Dictyostelium discoideum* and is thought to act as a molecular "strain absorber" by unfolding under tension [153, 192]. Extraordinarily fast refolding is facilitated by an intermediate state along the refolding pathway [153, 192]. This domain is well suited as a test system, as it exhibits a characteristic three-state unfolding pattern that has been extensively studied in AFM experiments [153, 192] and is routinely employed as a molecular fingerprint in AFM force spectroscopy experiments (e.g. [161, 164, 193]).

#### Rates and extensions of ddFLN4 unfolding and folding at different constant forces

To characterize unfolding and (re-)folding in the MT assay, I recorded time traces of tether extension under different, constant forces. In a typical measurement (Fig. 4.2B), the force is increased from an initial low value (0.5 pN) that allows for (re-)folding, to a high value (25 pN in Fig. 4.2B) that promotes unfolding, and subsequently decreased to a moderate value (6.5 and 7.5 pN in Fig. 4.2B) to directly monitor refolding. Subsequently, this cycle is repeated multiple times with variable force levels to collect statistics. Unfolding and refolding of ddFLN4 were observed as clear double-steps in the traces, *i.e.*, as an increase or decrease of the tether extension in two separate steps that I interpret as transition between the native (N) and intermediate (I) and between the intermediate and unfolded (U) states, respectively (Fig. 4.2B, insets).

I analyzed the changes in extension for the transitions  $N \leftrightarrow I$  and  $I \leftrightarrow U$  as well as for the full transition  $N \leftrightarrow U$  for many different clamped forces (Fig. 4.2C). The resulting force-extension profiles are well described by fits of the worm-like chain model with a fixed persistence length of 0.5 nm, chosen in accordance with a previous AFM study [153], yielding contour length values (mean  $\pm$  SD) of  $15.0 \pm 0.1$  nm,  $18.3 \pm 0.1$  nm, and  $31.9 \pm 0.2$  nm, in excellent agreement with values reported from AFM [153, 192].

The data are fully consistent with previous work that found unfolding of the ddFLN4 domain to proceed via a mandatory, short-lived intermediate state: In a first unfolding step, strands A and B (42 aa; blue in Fig. 4.2A) detach and unfold, with strands C-G (58 aa; red in Fig. 4.2A) forming a

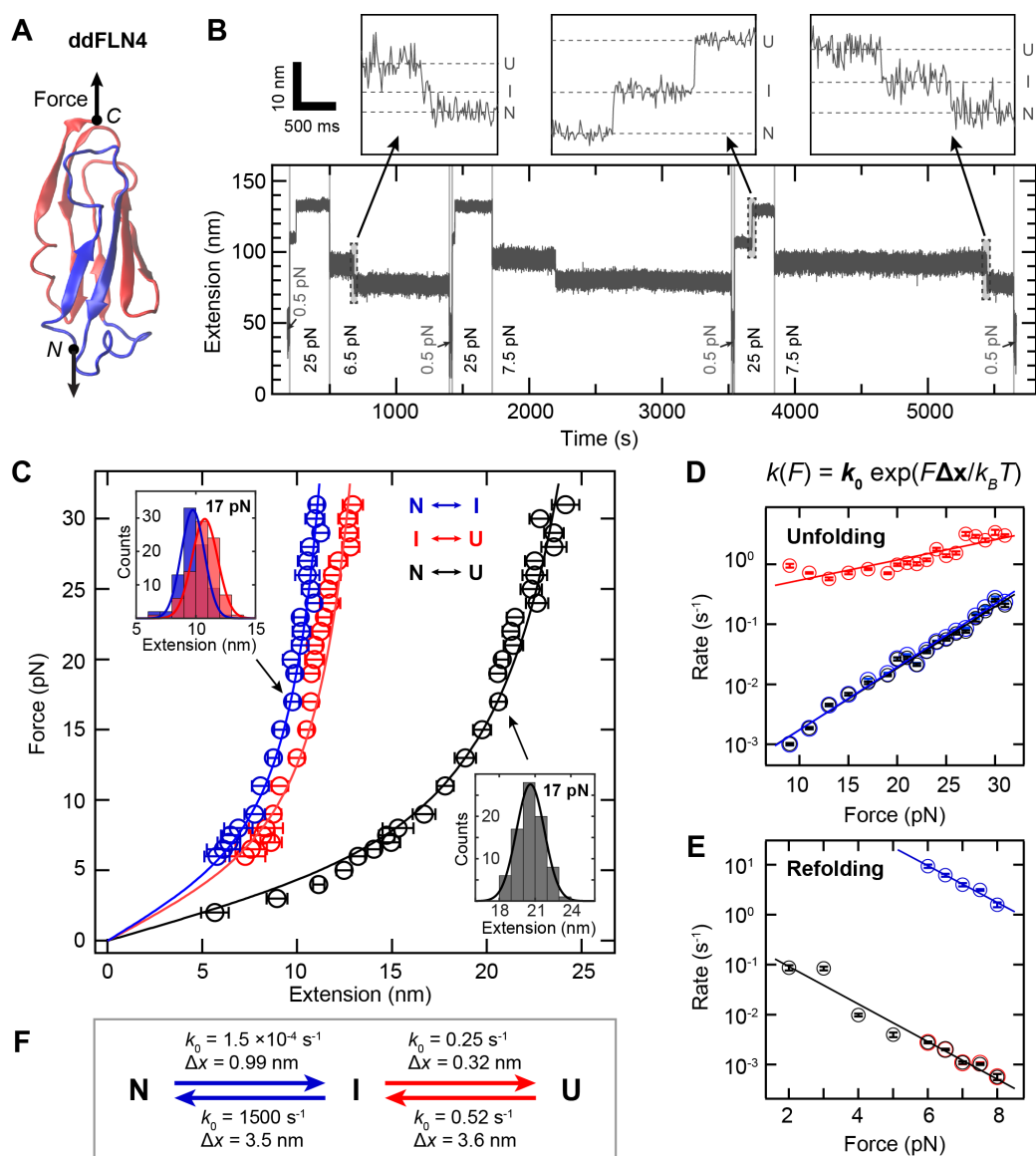


**Figure 4.2: Three-state folding and unfolding of ddFLN4 at constant force.** (A) Structure of ddFLN4 (PDB: 1KSR [190], rendered using VMD [191]), with strands A and B rendered in blue and strands C-G, forming the structured portion of the intermediate state, in red. Arrows indicate the direction of force acting on ddFLN4's termini during MT experiments. (B) Extension vs. time trace of a ddFLN4 tether subjected to alternating intervals of high force (here 25 pN) allowing for ddFLN4 unfolding, intermediate force (here 6.5 or 7.5 pN) allowing for direct observation of refolding, and low force (0.5 pN) to ensure refolding before the next cycle. Unfolding and refolding of ddFLN4 *via* the mandatory intermediate state are observed as upward or downward double-steps in the traces, respectively. Dashed lines in insets indicate extension levels corresponding to the native (N), intermediate (I) and unfolded (U) states, respectively. (C) Force–extension profiles of ddFLN4 for the transitions N↔I (blue) and I↔U (red), and for full (un)folding N↔U (black). Data points are obtained by Gaussian fits to step extension histograms (insets) at each constant force. Data points above 8 pN are from unfolding (based on 68-131 events obtained from 27-36 independent tethers), data points up to 8 pN from refolding (54-159 events from 26-39 independent tethers). Error bars correspond to the FWHM of Gaussian fits, divided by the square root of counts. Lines are fits of the WLC model. (D) Rates of unfolding at different constant forces for the three transitions. Color code as in panel C. Error bars correspond to 95 % confidence intervals of exponential fits to the fraction of observed events as a function of time (see section 2.2.3 and Fig. 4.4). Lines are fits of a single-barrier kinetic model. (E) Rates of refolding at different constant forces. Color code, error bars, and fits analogous to panel D. (F) Fitted rates at zero force  $k_0$  and distances to the transition state  $\Delta x$  for the unfolding and refolding transitions as determined from the fits of a single-barrier kinetic model shown in panels D and E. Figure as in [187].

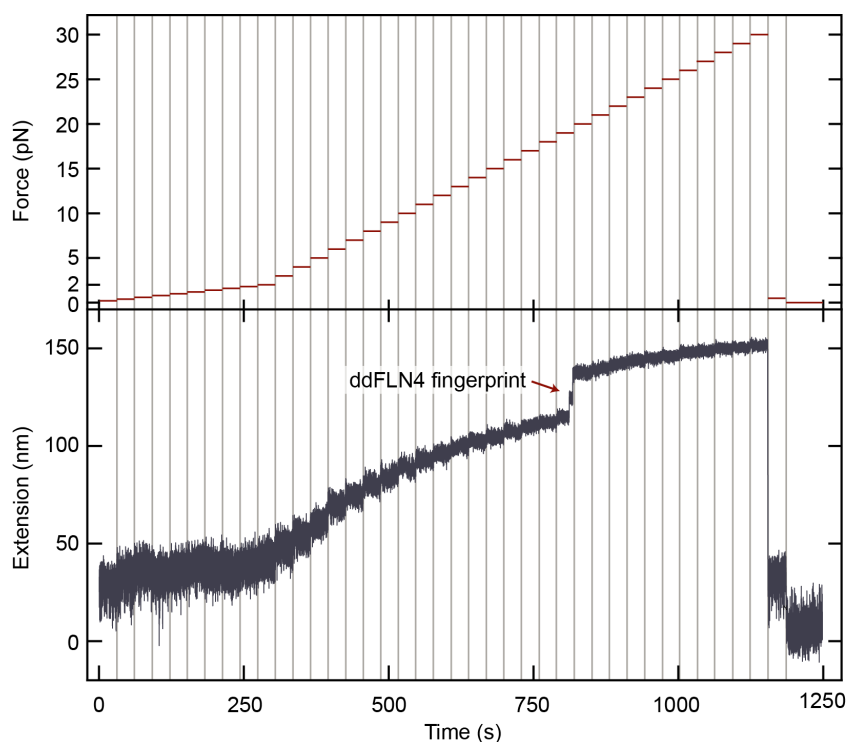


**Figure 4.3: Extension of ELP linker–protein tethers.** Exemplary extension trace (bottom) of a ddFLN4–ELP linker complex tethered between glass surface and magnetic bead as shown in Fig. 4.1, recorded while the force was increased stepwise every 30 s (indicated by red lines; top), in steps of 0.2 pN between 0.2 and 2 pN, and in steps of 1 pN between 2 and 30 pN. Afterwards, the tether was relaxed to 0.5 pN to allow for refolding of ddFLN4 and further relaxed to zero force to determine the zero position of extension. No peculiar features –in particular no steps– were observed over the entire probed force range, with exception of the characteristic ddFLN4 unfolding pattern, which served to identify specific single-tethered beads. This finding shows that the ELP linker does not cause any signals that may interfere with analysis of the specific signals of the measured protein of interest. Figure as in the supporting information to [187].

less stable intermediate state [192], which quickly unfolds in the second unfolding step. Folding of ddFLN4 was also suggested to proceed via an intermediate state that is most likely structurally identical or very similar to the intermediate populated during unfolding [153]. In my data set, data from unfolding (data points  $> 8$  pN) and refolding (data points  $\leq 8$  pN) are well described by a single WLC curve, confirming that the intermediate states populated during unfolding and folding are structurally very similar or identical. Importantly, no other features except the double-steps originating from ddFLN4 were observed in the force range probed (Fig. 4.3), showing that the other components of the tethering strategy do not interfere with the measurements.

The force clamp measurements allowed to directly determine the rates of all transitions (*cf.* section 2.2.3 and Fig. 4.4). For unfolding (Fig. 4.2D), I observed the rate for the first transition,  $N \rightarrow I$ , to increase with increasing force from  $\approx 0.001 \text{ s}^{-1}$  at 9 pN to  $\approx 0.2 \text{ s}^{-1}$  at 31 pN. I fitted the rates to a single-barrier kinetic model, in which the rate is given by  $k(F) = k_0 \exp(F\Delta x/k_B T)$ , where  $F$  is the applied force,  $k_0$  the rate at zero force,  $\Delta x$  the distance to the transition state,  $k_B$  the Boltzmann constant, and  $T$  the absolute temperature [137]. I find  $k_{0,N \rightarrow I} = 1.5 \cdot 10^{-4} \text{ s}^{-1}$  ( $1.3$  to  $1.8 \cdot 10^{-4} \text{ s}^{-1}$ ) and  $\Delta x_{N \rightarrow I} = 0.99 \pm 0.03 \text{ nm}$  (mean  $\pm$  SD for all rates and  $\Delta x$  values). The measured rates for full unfolding  $N \rightarrow U$  are essentially identical to those for the transition  $N \rightarrow I$

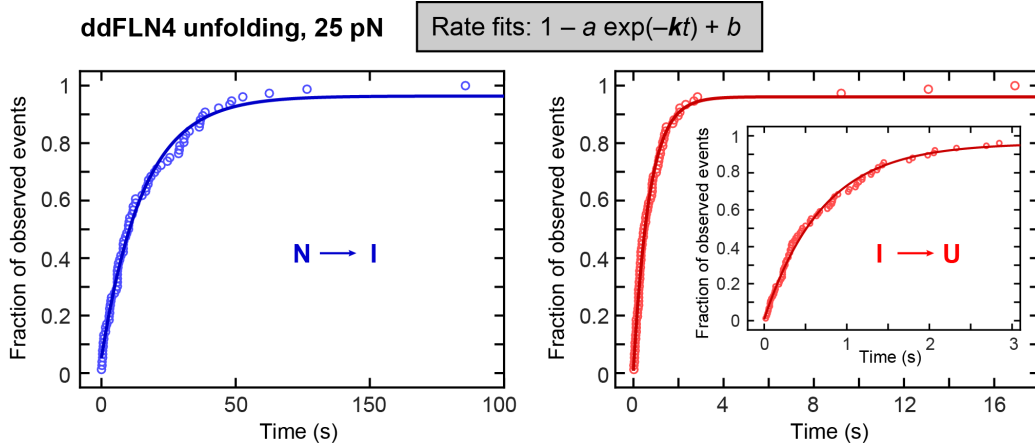


**Figure 4.4: Determination of rates from observed unfolding and refolding events.** Concept of rate determination from the fraction of observed unfolding or refolding events as a function of time. Shown here as an example are the fractions of observed unfolding events vs. time for the two substeps of ddFLN4 unfolding at 25 pN, *i.e.* for the transitions from the native (N) to the intermediate (I) state (left, blue) and from the intermediate to the unfolded (U) state (right, red). To obtain the unfolding rate  $k$  of a transition at constant force  $F$ , the fraction of observed unfolding events as a function of time  $t$  is fit to the expression  $1 - a \exp(-kt) + b$  (lines), where the free parameters  $a$  and  $b$  can compensate for events that were missed due to the finite measurement time or due to the finite time of motor movement when setting the force. As a rule, parameters  $a$  and  $b$  were close to 1 and 0, respectively. Figure as in the supporting information to [187].

(Fig. 4.2D), owing to the fact that the rates for the second transition,  $I \rightarrow U$  ( $k_{0,I \rightarrow U} = 0.25 \text{ s}^{-1}$  [0.19 to  $0.32 \text{ s}^{-1}$ ];  $\Delta x_{I \rightarrow U} = 0.32 \pm 0.04 \text{ nm}$ ), are at least one order of magnitude faster (Fig. 4.2D), implying that the transition  $N \rightarrow I$  is the rate-limiting step for unfolding. The three-fold difference between  $\Delta x_{N \rightarrow I}$  and  $\Delta x_{I \rightarrow U}$  reflects that the difference between the rates  $N \rightarrow I$  and  $I \rightarrow U$  decreases with increasing force.

For refolding in the force range from 2 pN to 8 pN (Fig. 4.2E), the rates for the first substep  $U \rightarrow I$  ( $k_{0,U \rightarrow I} = 0.52 \text{ s}^{-1}$  [0.34 to  $0.79 \text{ s}^{-1}$ ];  $\Delta x_{U \rightarrow I} = 3.6 \pm 0.3 \text{ nm}$ ) are again essentially identical to the rates for full refolding  $U \rightarrow N$  (Fig. 4.2E) and rates for the second transition  $I \rightarrow N$  ( $k_{0,I \rightarrow N} = 1500 \text{ s}^{-1}$  [950 to  $2500 \text{ s}^{-1}$ ];  $\Delta x_{I \rightarrow N} = 3.5 \pm 0.3 \text{ nm}$ ) are at least three orders of magnitude higher compared to the first transition, implying that again the first transition,  $U \rightarrow I$ , is rate-limiting (Fig. 4.2F). For forces below 6 pN, the intermediate state was too short-lived to be reliably detected, so that rates were determined separately only for forces  $\geq 6 \text{ pN}$ .

I compared the force-clamp results (summarized in Fig. 4.2F) to the rates at zero force reported previously from fits of a single barrier kinetic model to constant pulling speed AFM measurements [153]. For unfolding, the rates for the second step  $k_{0,I \rightarrow U}$  are in excellent agreement ( $0.25$  and  $0.33 \text{ s}^{-1}$  in MT and AFM, respectively), yet the zero force rates for the first step  $k_{0,N \rightarrow I}$  appear, in contrast, to differ significantly ( $1.5 \cdot 10^{-4}$  vs.  $0.28 \text{ s}^{-1}$ ). However, in AFM measurements with extremely low pulling speeds of  $1 \text{ nm/s}$  a markedly higher mechanical strength of ddFLN4 has been observed and explained by switching to a second unfolding pathway [194]. The reported zero-force rate (for full unfolding) from AFM of  $1.4 \cdot 10^{-4} \text{ s}^{-1}$  is in excellent agreement with the results obtained in the MT measurements. Thus, the MT data support the existence of a second unfolding pathway and suggest that differences between the two pathways can be largely attributed to the first unfolding step  $N \rightarrow I$ .

For refolding, a direct comparison is less straightforward, as refolding in AFM experiments

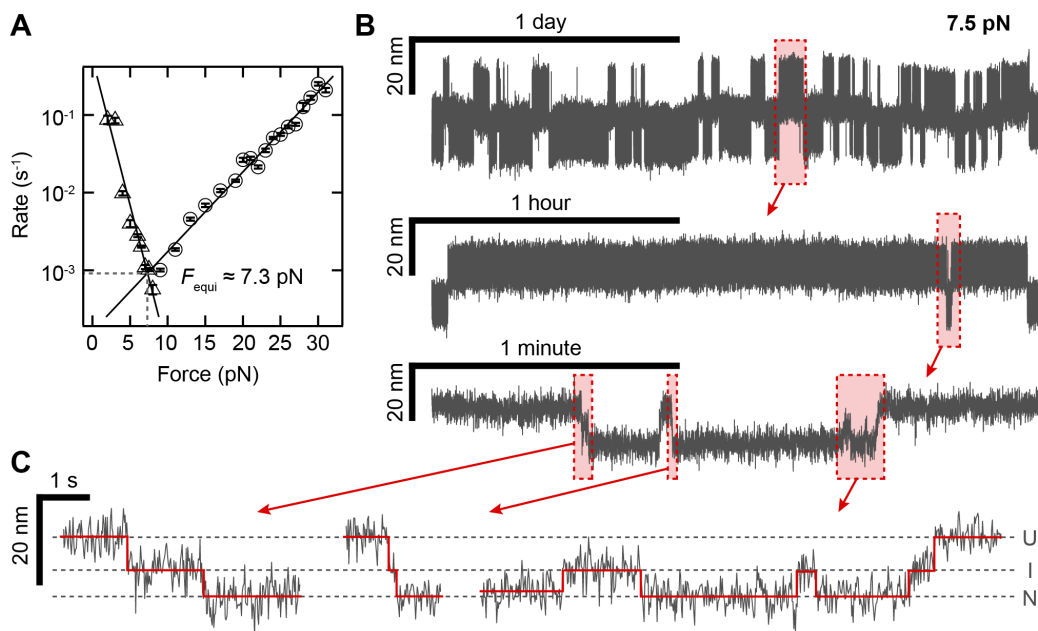


**Figure 4.5: Long-term ddFLN4 folding and unfolding traces close to equilibrium.** (A) Force dependence of the rates for complete unfolding (circles) and refolding (triangles) as determined in Fig. 4.2D-E. The intersection of the linear fits predicts the equilibrium force  $F_{\text{equi}} \approx 7.3$  pN at which the probabilities of ddFLN4 being in the folded and unfolded state are equal. (B) 55 h-long extension vs. time trace of a ddFLN4 tether subjected to a constant force of 7.5 pN and zooms into indicated segments of the trace. (C) Zooms show not only full unfolding and folding transitions, but also transitions from the native to the intermediate state and back. Dashed lines indicate average extension levels corresponding to the native (N), intermediate (I), and unfolded (U) states, respectively. Red lines indicate positions of transitions between states and extension levels in each state, as determined by the step-finding algorithm employed for the analysis. Figure as in [187].

has been measured at zero force and not under load [153]. The rates obtained from MT and AFM differ significantly ( $k_{0,U \rightarrow I}$ : 0.52 vs. 55  $\text{s}^{-1}$ ;  $k_{0,I \rightarrow N}$ : 1500 vs. 179  $\text{s}^{-1}$ ), which might indicate different folding pathways in the presence and absence of force. Intriguingly, however, in both cases the same intermediate state appears to be populated during folding. Whereas the first step of folding –and thereby also full folding– is markedly slowed down by force, the second step of folding is almost 10-fold sped up, suggesting a pre-alignment of the structured portion of the intermediate state by force that allows for faster folding of strands A and B in the second folding step. Since ddFLN4 *in vivo* is positioned within actin-crosslinking filamin and under tensile load, it appears plausible that a force-induced pre-alignment of the intermediate state might play a physiological role.

### Ultra-stable equilibrium measurements of ddFLN4 unfolding and refolding

By determining the force at which the fitted rates for full unfolding and refolding (Fig. 4.2D,E; black lines) intersect, the equilibrium force at which the probabilities of ddFLN4 being in the unfolded and folded states are equal could be predicted to be approximately 7.3 pN (Fig. 4.5A). I tested this prediction by measuring at a constant force of 7.5 pN, close to the predicted equilibrium force. Since the predicted rates at equilibrium are only  $\approx 3 \text{ h}^{-1}$  (Fig. 3A), I performed very long measurements (up to 55 h; Fig. 4.5B), harnessing the excellent force and drift stability of MT. Indeed, repeated transitions between the unfolded and folded states were observed, with



the system spending approximately half of the time in each of the two states, as expected for a measurement close to equilibrium. Examining the traces close to equilibrium in detail, one can observe repeated transitions not only  $N \leftrightarrow U$  via the I state (Fig. 4.5C, left and middle trace), but also from the U and N states into the I state that return to the initial state (Fig. 4.5C, right trace), again strongly suggesting that the same intermediate state is populated during unfolding and folding. Finally, it is noteworthy that even for the very long measurements reported here, no significant change of ddFLN4's force response over time was observed, indicating reliable, correct refolding of the domain without any hysteresis effects, both for the long equilibrium measurement at constant force and for repeated cycles of unfolding and refolding under varying load (Fig. 4.6). Taken together, the long-term stability combined with its very characteristic three-state unfolding signature make ddFLN4 an ideal fingerprint for the identification of single-molecule tethers.

## 4.4 Lifetime of single biotin–streptavidin bonds under constant load

Having established ddFLN4 as an ideal fingerprint for the identification of specific single-molecule tethers and having demonstrated the ability to apply constant forces over extended periods of time to multiple tethers in parallel, I aimed at utilizing the MT assay to investigate not only protein folding and refolding, but also ligand–protein receptor interactions. As a proof-of-concept measurement, and to further validate the tethering approach, I directly probed the stability of the high-affinity, non-covalent biotin–streptavidin interaction under constant force. Since all other linkages in the tethering protocol consist of mechanically stable covalent bonds, I used ddFLN4-tethered beads to apply different high forces (45–65 pN) to the biotin–streptavidin bond and monitored the time until bead rupture. In the analysis, only beads that showed the specific ddFLN4 unfolding signature in two short force plateaus of 65 pN at the beginning of the measurement were taken into account. Importantly, the number of beads that ruptured already during these initial short plateaus was small ( $< 3.5\%$ ).

For the commercially available streptavidin-coated beads used for the measurements presented in the previous sections (Dynabeads M-270 Streptavidin, Invitrogen/Thermo Fisher), I found the survival fraction to decay with time in a complex, multi-exponential fashion (Fig. 4.7A) for all forces probed, suggesting the existence of several populations of the biotin–streptavidin interaction with different lifetimes. To quantify the lifetimes involved, I fit the fastest and slowest decaying populations by linear regression to the logarithm of the first and last 20% of data points, respectively (lines in Fig. 4.7A). Over the studied force range, the lifetime of the fastest decaying population ranged from  $\approx 100$  s at 65 pN to  $\approx 2100$  s at 45 pN, whereas the lifetime of the slowest decaying population was  $\approx 50$ -fold higher, increasing from  $\approx 5000$  s at 65 pN to  $\approx 68\,000$  s at 45 pN (Fig. 4.7C). For both populations, the lifetime was found to increase exponentially with decreasing force (Fig. 4.7C). Already for a force of 20 pN, extrapolated lifetimes are well above a day and off-rates at zero force are in the range of  $10^{-7}$  to  $10^{-8}$   $s^{-1}$ , consistent with the fact that beads remained stably bound for hours or days in the MT force spectroscopy measurements at forces  $\leq 20$  pN (e.g. section 4.3).

I hypothesized that the different populations and multi-exponential lifetimes for commercially available streptavidin-functionalized beads originate from the biotin–streptavidin complex

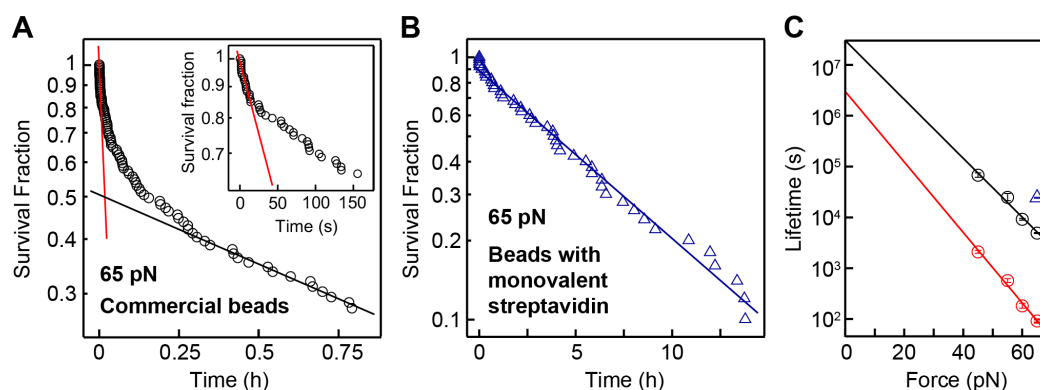


**Figure 4.7: Lifetime of single biotin-streptavidin bonds under constant load.** (A) Survival fraction as a function of time for commercially available beads coated with tetraivalent streptavidin (Dynabeads M-270 Streptavidin), tethered by ddFLN4 and subjected to a constant force of 65 pN. The survival fraction decays in a complex, multi-exponential fashion, suggesting the existence of several populations of biotin-streptavidin interactions with different lifetimes. Red and black lines are linear fits to the logarithm of the first and last 20 % of data points, respectively, to estimate off-rates of the fastest- (inset) and slowest-decaying populations. (B) Survival fraction as a function of time for ddFLN4-tethered beads functionalized with a monovalent streptavidin variant, measured at 65 pN. The blue line is a linear fit to the natural logarithm of all data points. Note the markedly different scale of the time axis. (C) Estimated lifetime of the biotin-streptavidin interaction at different constant forces for the fastest- and slowest-decaying population of commercial beads with tetraivalent streptavidin (red and black circles, respectively), and for beads with monovalent streptavidin (blue triangle). Error bars correspond to 1 SD; lines are fits of a single-barrier kinetic model. The number of measured, specifically tethered beads per condition was between 44 and 118, of which 35 to 86 ruptured during the duration of the measurement. The measurement duration for beads with monovalent streptavidin was 15 h, and for the commercial beads 1 h at 65 pN, 3 h at 55 and 60 pN, and 15 h at 45 pN. Figure as in [187].

being loaded with force in different geometries that result from the tetraivalency of streptavidin [161]. Indeed, for measurements with custom-made beads functionalized with a monovalent version of streptavidin [161] in a well-defined geometry using a C-terminal tag [162], the survival fraction was well described by a single-exponential decay (Fig. 4.7B). Immobilization of the monovalent streptavidin construct via the C-terminus of its functional subunit was chosen because it has recently been demonstrated in AFM force spectroscopy measurements that the monovalent streptavidin-biotin complex can withstand markedly higher forces when loaded with force from the C-terminus as compared to pulling from the N-terminus [162]. Indeed, I found the lifetime of the custom-made monovalent streptavidin beads to be 24 000 s ( $\approx 6.7$  h) at 65 pN (Fig. 4.7B), similar to and even exceeding that of the 20 % longest-lived commercially available beads (Fig. 4.7C).

Summarizing, commercially available, multivalent streptavidin (far) exceeds the requirements of typical constant force force-spectroscopy measurements (with lifetimes  $\geq 1$  day at forces  $\leq 20$  pN), but has a multi-exponential lifetime distribution. Monovalent, site-specifically attached streptavidin, in contrast, exhibits a single-exponential lifetime distribution with extremely high force stability, making it an attractive approach for force spectroscopy on systems that require high forces over extended periods of time.

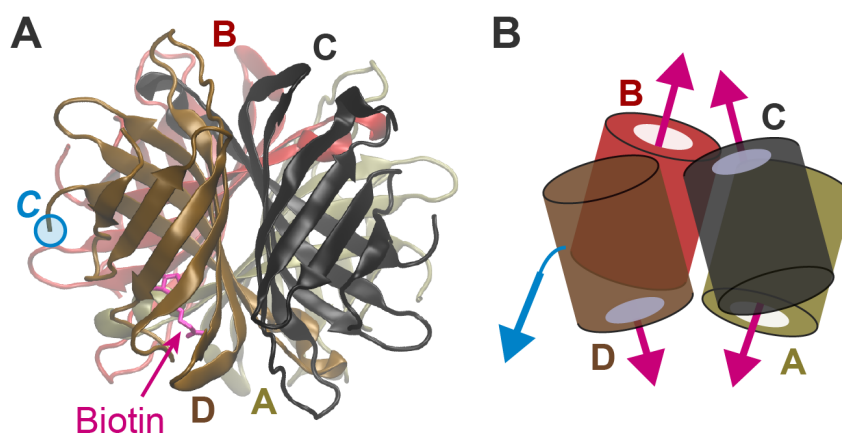


**Figure 4.8: Distinct force loading geometries resulting from the tetravalency of streptavidin.** (A) Crystal structure of the streptavidin tetramer, with the four subunits shown in different colors. Biotin bound to one of the subunits is shown in magenta. The C terminus of the same subunit is marked by the light blue circle. Structure of the tetramer without biotin (PDB: 5TO2 [195]) was rendered using VMD [191]. The biotin was added to subunit D according to the structure of a streptavidin dimer with bound biotin (PDB: 1MK5 [196]) after aligning the structures with STAMP [197] in VMD. (B) Schematic representation of the tetramer structure, with subunits being represented by colored barrels. Arrows mark the positions at which force can be applied to the molecule in the SMFS experiments described here. The light blue arrow marks the C-terminus of subunit D used for site-specific immobilization. Magenta arrows indicate the four possible directions of pulling biotin out of the different binding pockets. Depending on which subunit biotin is bound to, force will propagate differently through the complex.

## 4.5 Distinct lifetimes of biotin unbinding owing to streptavidin's multivalency

As indicated by the results presented in the previous section, the lifetime of the streptavidin–biotin interaction strongly depends on the geometry of force application. Even in the case of site-specific attachment of streptavidin, four different geometries for biotin unbinding under force are possible as a result of the tetravalency of streptavidin (Fig. 4.8), and consequently up to four different populations of lifetimes can be expected. This potential variability in the stability of the interaction is not only of importance for force spectroscopy measurements, but may also affect other assays involving force, e.g. under flow. The non-covalent, high-affinity binding of the small molecule biotin to streptavidin is ubiquitously used in a variety of biological, chemical, biophysical and pharmaceutical applications [198, 199] and thus of general interest.

To facilitate systematic investigation of the influence of the pulling geometry on the stability of the biotin–streptavidin complex, variants of streptavidin with different valencies were engineered by Steffen M. Sedlak. Tetra-, tri-, and monovalent variants of streptavidin with four, three, and one functional subunit(s), respectively, were prepared, with the remaining subunits being incapable of biotin binding (4SA, 3SA, and 1SA, respectively; Fig. 4.9A). In addition, a control variant consisting of four non-functional subunits was prepared (0SA). All variants

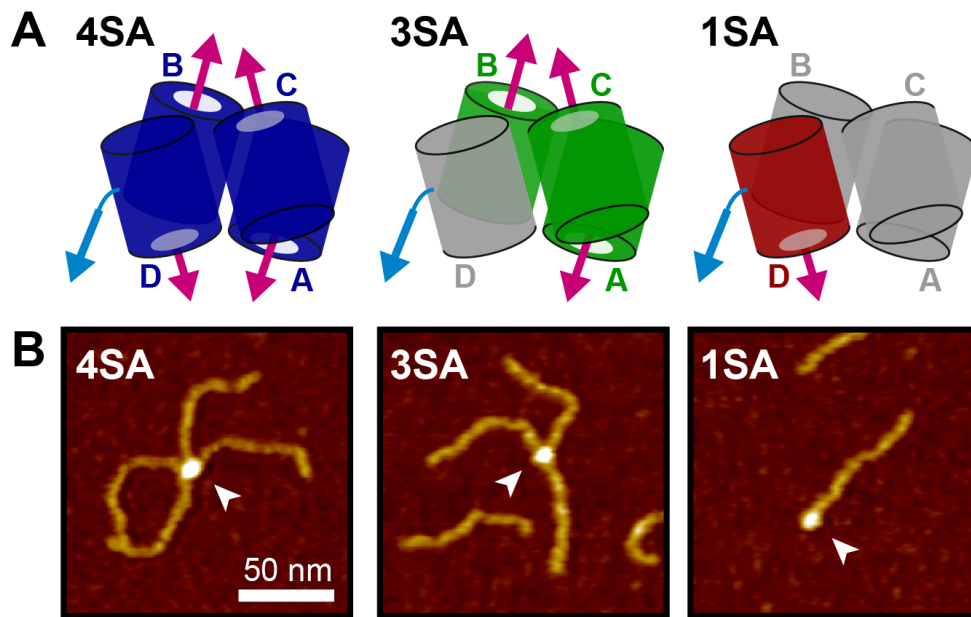


**Figure 4.9: Streptavidin variants with different valencies.** (A) Schematic structure of streptavidin constructs with different valencies. 4SA (left), 3SA (middle), and 1SA (right) possess four, three and one functional subunit(s), respectively (shown in color). The remaining subunits (gray) are incapable of biotin binding. All constructs possess a single C-terminal cysteine at their D subunit – which is nonfunctional for 3SA and functional for 1SA– for site-specific immobilization (light blue line). In the MT experiments, force is applied to the constructs from the immobilization site (light blue arrows) and from the biotin being pulled out of one of the functional subunits (possible directions indicated by magenta arrows). (B) Exemplary AFM images of 4SA (left), 3SA (middle), and 1SA (right) with the highest observed number (four, three, and one, respectively) of biotinylated DNA strands bound. The streptavidin molecules are marked by arrowheads. Height range of color scale is 2 nm.

possess a single cysteine residue at the C-terminus of their D subunit (see Fig. 4.8), allowing for site-specific immobilization. For 3SA, the D subunit is the only non-functional one, whereas for 1SA it is the only functional one (Fig. 4.9A).

To verify the valency of the different variants, they were incubated with biotinylated, short (250 bp) double-stranded DNA strands, and I directly visualized the resulting streptavidin–DNA complexes by AFM imaging (Fig. 4.9B). A large excess of DNA over streptavidin (approximately ten-fold for 4SA and 3SA, and four-fold for 1SA and 0SA) was used to ensure that streptavidin molecules with DNA strands bound to all functional subunits could be observed. Indeed, a maximum of four, three, and one bound DNA strand(s) was observed for 4SA, 3SA and 1SA, respectively, confirming the expected valencies. An exemplary image for the case of 3SA is shown in Fig. 4.10. In the case of 0SA, no streptavidin–DNA complexes were observed. The expected valencies were further confirmed by isothermal titration calorimetry (ITC) measurements conducted by Steffen M. Sedlak, which revealed essentially identical enthalpies of biotin binding to variants 1SA, 3SA and 4SA, with different stoichiometries corresponding to the respective valency. This finding indicates that in the absence of force all subunits are equivalent with regard to biotin binding and no effects of different binding geometries come into play.

To directly measure the lifetime of the biotin–streptavidin interaction under constant force, and in particular to investigate the influence of different pulling geometries, I performed MT measurements using the different streptavidin variants (Fig. 4.11), analogous to the lifetime

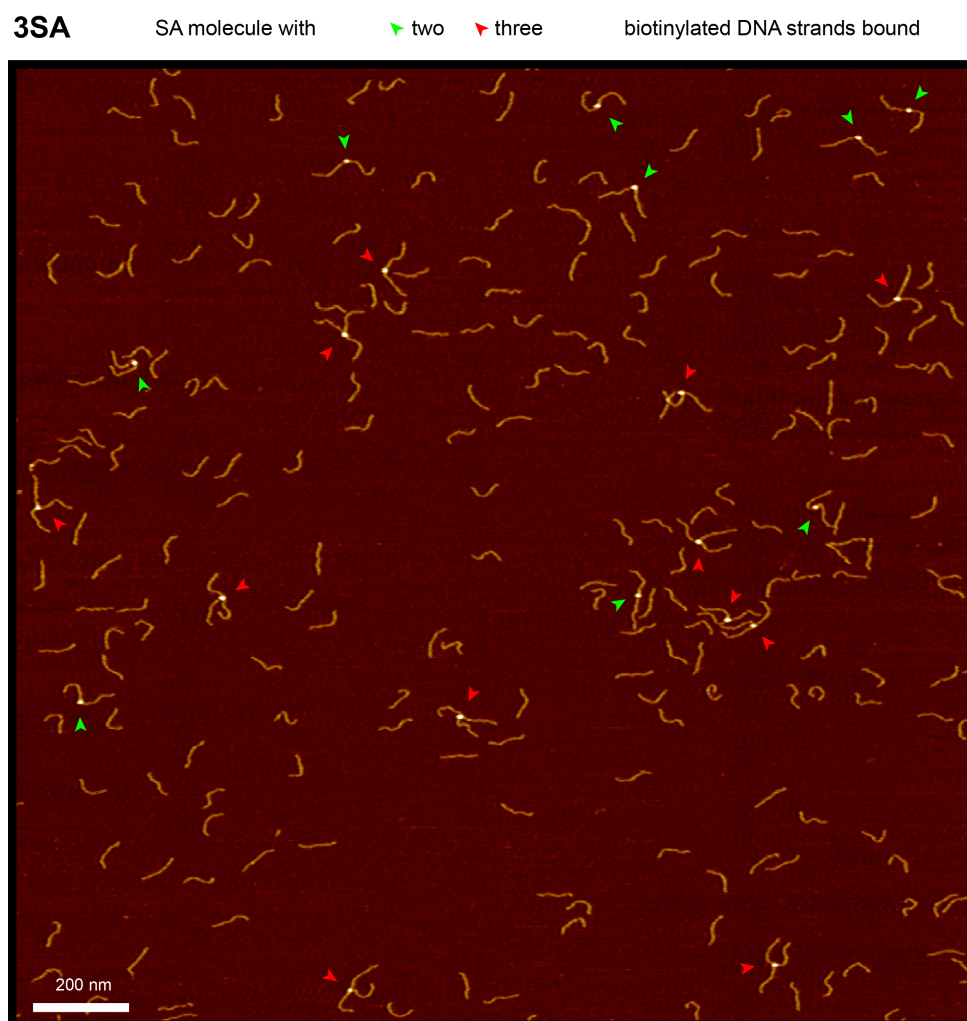


**Figure 4.10: AFM imaging of streptavidin with biotinylated DNA.** AFM imaging of streptavidin in complex with biotinylated 250 bp dsDNA strands is shown here exemplary for 3SA, after incubation in a 1:10 stoichiometry. Arrowheads mark streptavidin molecules, with the color of arrowheads indicating the number of bound DNA strands (green – two, red – three). For 3SA, up to three bound strands were observed. Importantly, no 3SA molecules with four strands were observed. Height range of color scale is 2 nm.

measurements presented in the previous section. For a subset of these measurements, I was supported by Sophia Gruber (LMU Munich). To this end, 4SA, 3SA, and 1SA were –via the single C-terminal cysteine at their D subunits– site-specifically and covalently immobilized on magnetic beads functionalized with polyethylene glycol linkers with a thiol-reactive maleimide group (Fig. 4.11A). The beads were then allowed to bind to biotinylated ddFLN4–ELP tethers (*cf.* Fig. 4.1), and binding occurs *via* one of the functional subunits of the respective streptavidin construct. The ddFLN4 domain again served as fingerprint domain to identify specific, single-tethered beads, *i.e.* beads exhibiting a single biotin–streptavidin interaction (Fig. 4.11B). To measure the lifetime of this interaction, beads were subjected to a constant force of 65 pN and the time until bead rupture –corresponding to unbinding of biotin from streptavidin– was monitored (Fig. 4.11B).

In the case of 1SA, only the subunit that is attached to the bead *via* its C-terminus is capable of biotin binding, and unbinding should hence always occur in the same pulling geometry.

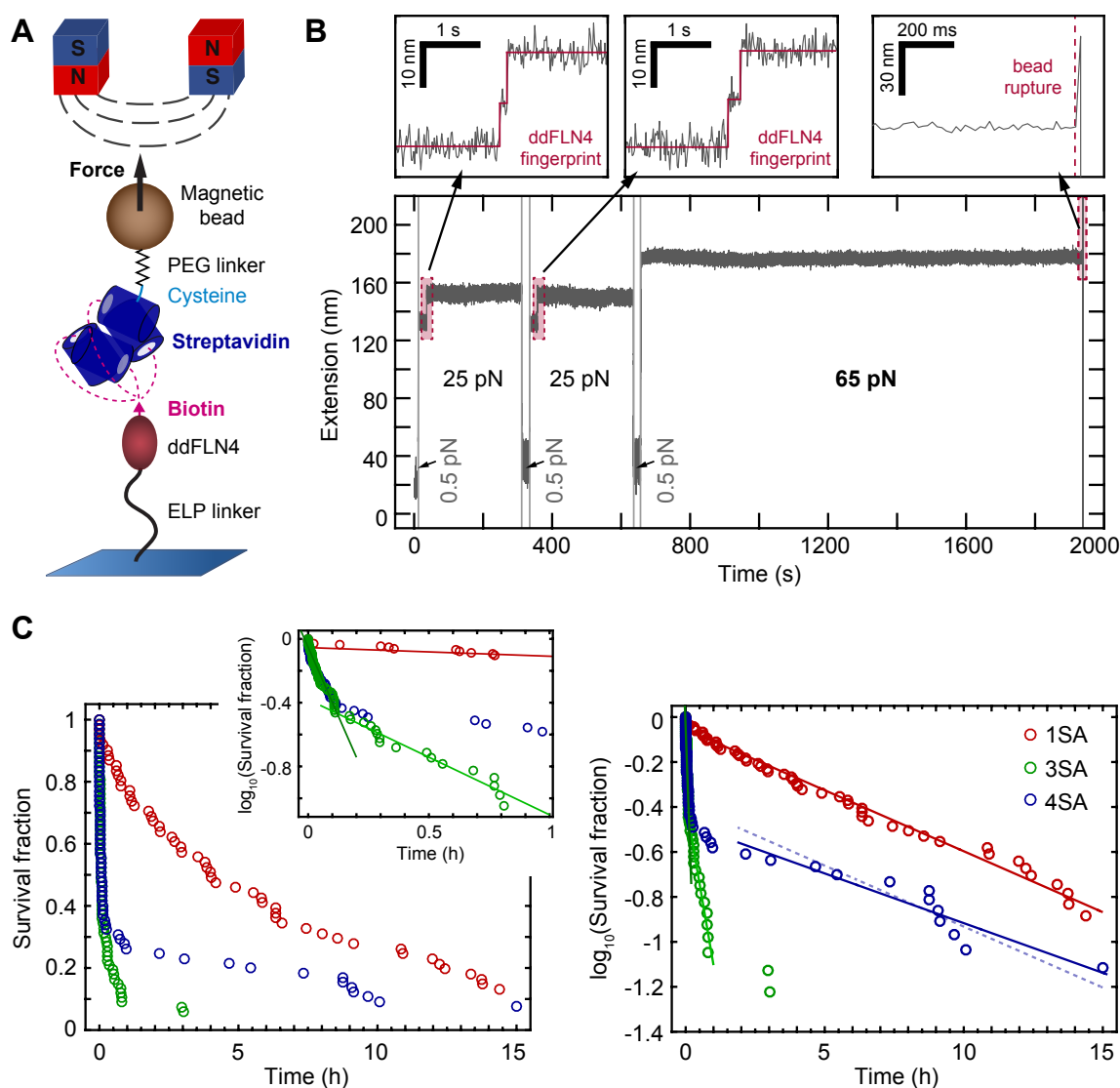


**Figure 4.11: Lifetime of the biotin–streptavidin interaction under constant force.** (A) Schematic of MT experiments (not to scale). Streptavidin (4SA, 3SA or 1SA) is site-specifically and covalently immobilized on magnetic beads via the single C-terminal cysteine at its D subunit and a polyethylene glycol (PEG) linker possessing a thiol-reactive maleimide group. Biotinylated ddFLN4 is covalently immobilized on the bottom slide of the MT flowcell via an ELP linker. Binding of the biotin to one of the functional subunits of the respective streptavidin construct thus tethers the beads by a single biotin–streptavidin interaction. Force is exerted on the magnetic beads by permanent magnets positioned above the flowcell. (B) Exemplary time trace of the tether extension during an MT measurement. At the beginning of the measurement, beads are subjected to two 5-min intervals of a constant force of 25 pN, allowing for unfolding of ddFLN4 in a characteristic three-state manner (left and middle zoom-in), which serves as fingerprint to identify specific, single-tethered beads. Short low force intervals (0.5 pN) allow for ddFLN4 refolding. Tethers are then subjected to a constant force of 65 pN and the time until bead rupture due to unbinding of biotin from streptavidin is monitored (right zoom-in). (C) Survival fractions as a function of time for 1SA (red), 3SA (green), and 4SA (blue). The data are shown both linearly scaled (left) and logarithmically (right and inset). Lines are linear fits to the data in logarithmic space, as explained in the text. The dotted blue line has the same slope as the fit obtained for the 1SA data set (see text).

Indeed, as already shown in the previous section, the monovalent variant exhibited a single-exponential lifetime distribution, indicating a single population with a –remarkably long–lifetime of approximately 8.0 h (28 800 s; 95 % CIs: 27900–29 800 s), as inferred from a linear fit to the data in logarithmic space (Fig. 4.11C, red), in good agreement with the value of 6.7 h obtained in the previous section for a slightly smaller data set.

3SA is inverse to the 1SA variant, in the sense that all but the attached subunit are functional. Consequently, 3SA is expected to exhibit up to three different populations of lifetimes, but to lack the population observed for 1SA. Indeed, in the MT experiments, 3SA only exhibited comparably very fast unbinding events (Fig. 4.11C, green). In the logarithmic representation of the data, two approximately linear regimes are visible, suggesting the existence of two populations with distinct lifetimes (Fig. 4.11C, inset). As the first, *i.e.* shorter-lived, population appears to comprise roughly two thirds of all unbinding events, it appears plausible to assume that this population comprises two of the three different pulling geometries, which however exhibit lifetimes that are too similar to be distinguished in this experiment conducted at 65 pN. Measurements at lower forces might allow to separate these populations.

Linear fits to the two approximately linear regimes in logarithmic space yielded lifetimes of approximately 7.5 min (453 s; 422–488 s) and 36 min (2160 s; 1930–2460 s), respectively. Two data points at  $\approx 3$  h were as outliers not taken into account for fitting. Remarkably, the lifetime of the shortest-lived population at 65 pN is almost two orders of magnitude (64-fold) lower than the one observed for the 1SA construct.

For 4SA, all pulling geometries possible for 3SA and 1SA can be realized. In line with this, both short- and long-lived populations were observed in the MT measurements on the 4SA variant (Fig. 4.11C, blue). After approximately 10 min at 65 pN, unbinding of already roughly 60 % of all initially tethered beads had occurred, in excellent agreement with the shortest-lived population observed for 3SA. Many of the remaining tethers, in contrast, survived for several hours and can be assumed to correspond to the pulling geometry of the 1SA variant. This assumption is corroborated by the fact that the decay of those beads that had survived the first two hours of the measurement closely matches the one observed in the measurements on 1SA, as visualized by the dotted blue line in Fig. 4.11C, which has the same slope as the fit to the 1SA data. A formal fit to the data points at times above 2 h (blue line in Fig. 4.11C) yielded a lifetime of 10.0 h (36 200 s; 28500–49 400 s), agreeing well with the lifetime obtained for 1SA, within the 95 % confidence intervals.

In the intermediate regime of times between approximately 10 min and 2 h, the number of unbinding events is not sufficient for a formal analysis, but the obtained data appear to be consistent with the existence of another population of lifetimes corresponding to the longer-lived one of the two populations observed for 3SA.

Taken together, the data on the 4SA variant are fully in line with the 1SA and 3SA data. Combined, the above findings confirm the hypothesis that the lifetime of biotin unbinding from streptavidin strongly depends on the pulling geometry. They further allowed to identify the pulling geometry that yields the longest lifetime, which corresponds to pulling biotin out of the binding pocket of the subunit that is attached. As the lifetime for this geometry is, at the force probed here, almost two orders of magnitude higher than for the other possible geometries, it would be highly beneficial to utilize this geometry in applications for which high force stability is desirable. Importantly, this can straight-forwardly be realized employing the monovalent streptavidin variant used in the above experiments.

Finally, it should be noted that the lifetimes obtained for the site-specifically attached variants used here were, both for the longest- and for the shortest-lived population, approximately four-fold higher than the respective lifetimes estimated for commercial beads, as described in the previous section (see Fig. 4.7). This difference might be explained by the fact that for the custom streptavidin constructs, force was applied from the C-terminus used for attachment, whereas in the case of commercially available beads the attachment is likely not site-specific, resulting in a variety of pulling geometries. In line with this, it has recently been demonstrated in AFM SMFS experiments that a monovalent streptavidin–biotin complex can withstand markedly higher forces when loaded with force from the C-terminus as compared to pulling from the N-terminus [162].

# Chapter 5

## Single-molecule constant force measurements on VWF dimers

In this chapter, the MT force spectroscopy approach presented in chapter 4 is applied to dimeric VWF constructs, with the aim of characterizing mechano-sensitive, regulatory inter- and intramonomer interactions and transitions within VWF dimers, in particular in the physiologically most relevant low-force regime below  $\approx 10$  pN. These include unfolding and refolding of the A2 domain, which is thoroughly characterized here with special attention to the impact of calcium binding to A2, and dissociation of a previously reported strong intermonomer interaction mediated by the D4 domains. Furthermore, at very low forces of only  $\approx 1$  pN, I could directly observe the opening and closing of the VWF stem in a zipper-like fashion, in line with predictions based on previous work that I was involved in (see section 1.4 and chapter 3). Finally, I found an unexpected new feature characterized by fast, reversible transitions at intermediate forces around  $\approx 8$  pN, that I could trace back to a transition within the D'D3 assembly. Possible physiological implications of the different interactions for regulation of VWF's hemostatic activity are discussed in each section. <sup>1</sup>

### 5.1 Impact of calcium binding on A2 domain unfolding and folding

Having demonstrated the attachment approach on a small well-characterized protein in the previous section, I also applied it to large ( $\approx 500$  kDa) dimeric constructs of full-length VWF. As discussed in section 1.5, dimers are of special interest to study regulatory interactions in VWF, as they are the smallest repeating subunits of VWF multimers, consisting of two multi-domain monomers that are C-terminally linked via disulfide bonds and have a contour length of  $\approx 130$  nm between their N-termini [4, 41] (Fig. 5.1A). Since different peptide tags

---

<sup>1</sup>The work presented in the first three sections of this chapter, along with data described in chapter 4, was posted in similar form as a preprint to *bioRxiv* (2018; doi: 10.1101/491977), as *Modular, ultra-stable and highly parallel protein force spectroscopy in magnetic tweezers using peptide linkers* by Achim Löff, Philipp U. Walker, Steffen M. Sedlak, Tobias Obser, Maria A. Brehm, Martin Benoit, and Jan Lipfert, and is currently under review at the *Proceedings of the National Academy of Sciences of the U.S.A.*

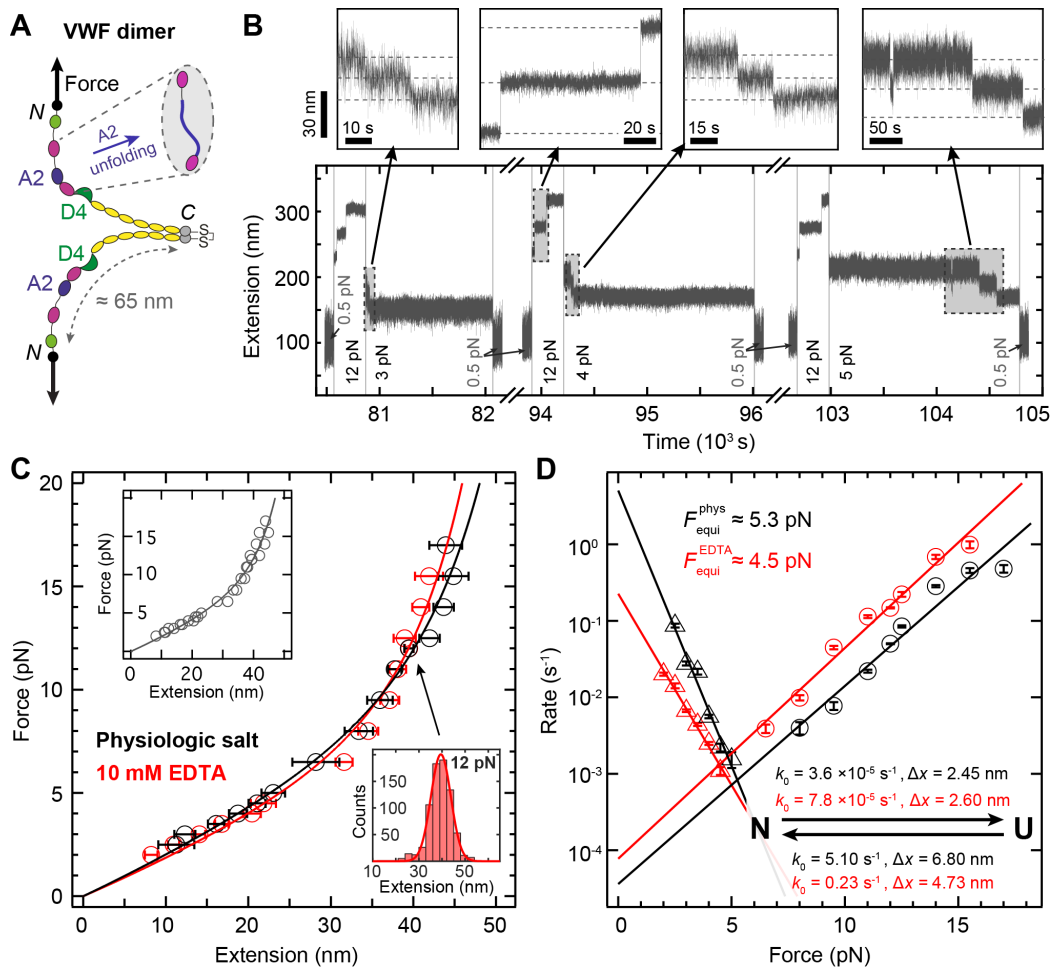


**Figure 5.1: Folding and unfolding of A2 domains within VWF dimers.** (A) Schematic structure of a VWF dimer, consisting of two  $\approx 65$  nm, multi-domain monomers C-terminally connected by disulfide bonds. The two A2 domains, which can unfold under force (inset), are shown in blue. Arrows indicate the direction of force acting on the two N-termini during MT experiments. (B) Segments from a  $\approx 30$ -hour long extension vs. time trace of a VWF dimer tether subjected to alternating intervals of high force (here 12 pN), allowing for A2 unfolding, of intermediate force (here 3, 4 or 5 pN), allowing for direct observation of A2 refolding, and of low force (0.5 pN) to ensure refolding. Unfolding and refolding of the two A2 domains are observed as two independent positive or negative steps in the trace, respectively. Dashed lines in the insets indicate extension levels with none, one, or both of the A2 domains unfolded. (C) Force–extension curves of A2 (un)folding, in near-physiological buffer containing  $Ca^{2+}$  (black) and in buffer without  $Ca^{2+}$  and with 10 mM EDTA (red). Data points are obtained by Gaussian fits to step extension histograms (lower right inset) at each constant force. Data points above 5 pN are from unfolding (based on 62–632 and 40–747 events for the near-physiologic and EDTA case, respectively, obtained from 13–53 independent tethers), data points up to 5 pN are from refolding (41–120 and 49–158 events for the near-physiologic and EDTA case, respectively, obtained from 10–19 independent tethers). Error bars correspond to the FWHM of Gaussian fits, divided by the square root of counts. Lines are fits of the WLC model. Upper left inset shows a global WLC fit to all data points. (D) Rates of unfolding (circles) and refolding (triangles) at different constant forces for near-physiologic (black) and EDTA (red) buffer. Error bars correspond to 95% confidence intervals of exponential fits to the fraction of observed events as a function of time (*cf.* section 2.2.3 and Fig. 4.4). Lines are fits of a single-barrier kinetic model, yielding rates at zero force  $k_0$  and distances to the transition state  $\Delta x$  for unfolding and refolding as indicated. Figure as in [187].

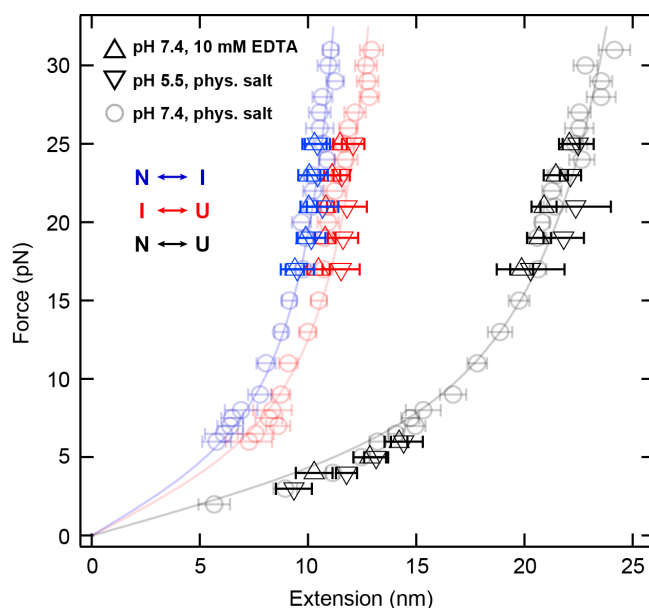


**Figure 5.2: Measurements on ddFLN4 under varied pH and ionic conditions as control.** Extension of ddFLN4 unfolding and refolding steps at different constant forces and under varied buffer conditions. Extensions of the transitions between the native state and the intermediate state (blue) as well as between the intermediate and the unfolded state (red) are shown separately in addition to the full extension between native and unfolded state (black). Data points at forces up to 8 pN are from refolding, data points at forces above 8 pN from unfolding measurements. Co-plotted with lower opacity are the data obtained for near-physiologic buffer conditions (pH 7.4, with divalent ions; circles) as shown in Fig. 4.2C and the respective WLC fits (lines). Force–extension data sets obtained at pH 7.4 in the presence of 10 mM EDTA (upward triangles) and at acidic pH 5.5 in the presence of divalent ions (downward triangles) both are within measurement uncertainty identical to the ones obtained for near-physiologic buffer conditions. Error bars correspond to the FWHM of Gaussian fits, divided by the square root of counts. Figure as in the supporting information to [187].

at the two N-termini are required for attaching dimers in the desired pulling geometry (Fig. 5.1A), heterodimers consisting of two different monomers that are N-terminally modified with a ybbR-tag or a sortase motif GG, respectively, were genetically engineered (see section 2.3). After tethering in the MT, I recorded time traces of VWF dimers with alternating plateaus of high force (Fig. 5.1B, 6-20 pN) and moderate force (Fig. 5.1B, 2-5 pN). In most cases, I observed two unfolding and two refolding steps in the recorded high and moderate force traces, respectively, with extension values matching the expected values for unfolding of the A2 domains ( $\approx 180$  aa each) that were previously probed in isolation in OT [7, 56]. Observation of domain (un-)folding only for the two A2 domains is consistent with the prediction that all domains of VWF except A2 are protected against unfolding by long-range disulfide bonds [41] and with the results of recent AFM studies [20, 166]. Further characteristic features in the traces, caused by inter- and intra-domain interactions, are described in the following sections. For all analyses, also regarding the following sections, only tethers exhibiting the unfolding signal of two A2 domains were taken into account, thus utilizing A2 as an internal fingerprint to identify specific single-molecule tethers.

I first used the MT assay to elucidate the controversial impact of calcium binding to A2's calcium binding loop on A2 stability [51, 56, 170]. Since force-induced unfolding of A2 is

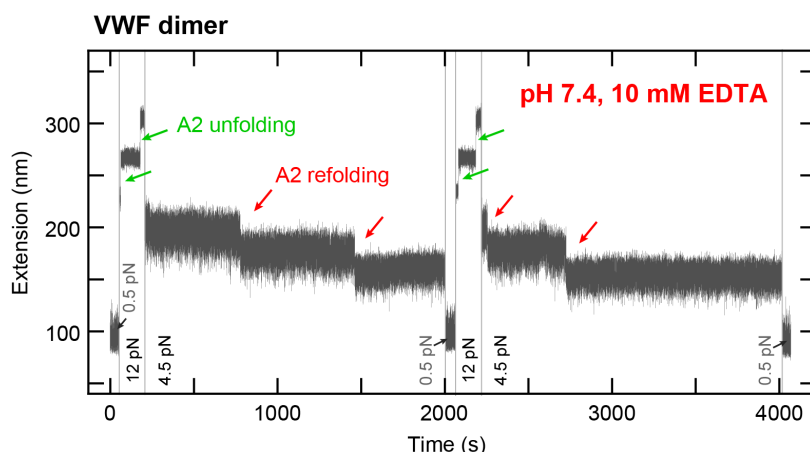


**Figure 5.3: Refolding of VWF A2 domains under mechanical load in the absence of  $\text{Ca}^{2+}$ .** Extension vs. time trace of a VWF dimer tether subjected to alternating intervals of high force (here 12 pN), allowing for A2 unfolding, of intermediate force (here 4.5 pN), allowing for direct observation of A2 refolding, and of low force (0.5 pN) to ensure refolding, in buffer without  $\text{Ca}^{2+}$  and with 10 mM EDTA. Unfolding and refolding of the two A2 domains are observed as two independent positive or negative steps in the trace, respectively. Direct observation of refolding steps (marked by red arrows) shows that A2 can refold under significant mechanical load even in the absence of  $\text{Ca}^{2+}$ . Figure as in the supporting information to [187].

a prerequisite for mechano-enzymatic cleavage of VWF by ADAMTS13 and thus for down-regulation of VWF [7], a comprehensive understanding of the dynamics of A2 unfolding and refolding, as well as how they may be tuned, is of high interest and may help to comprehend certain pathological mutations that cause VWD type 2A by destabilizing the A2 domain (e.g. [82]). To address this issue, I performed measurements both in buffer mimicking the physiological pH and salt concentrations of the vasculature ("near-physiologic"; pH 7.4, 150 mM NaCl, 1 mM  $\text{MgCl}_2$ , and 1 mM  $\text{CaCl}_2$ ) and in buffer lacking divalent ions and supplemented with 10 mM EDTA. First, I analyzed the change in extension upon A2 unfolding and refolding for different constant forces. For both buffer conditions, the resulting force–extension profiles (Fig. 55.1), combining data from unfolding (data points  $\geq 6.5$  pN) and from refolding (data points  $\leq 5$  pN), are well described by a single WLC curve. The WLC fits yielded values for contour length and persistence length of 75.0 nm and 0.42 nm (95 % CI: 70.8–79.2 nm and 0.37–0.46 nm) for near-physiologic buffer, and of 68.5 nm and 0.50 nm (62.7–74.3 nm and 0.41–0.58 nm) for the EDTA buffer, and thus show no significant difference. This finding indicates that calcium has no effect on the extension of the unfolded state, as expected for full unfolding of A2 accompanied by disruption of the calcium binding loop. A WLC fit to the combined data from both buffer conditions (inset in Fig. 5.1C) yielded contour and persistence length values of 71.9 nm and 0.45 nm (68.3–75.4 nm and 0.41–0.50 nm). The contour length increments determined from the MT measurements on full-length dimeric VWF are in excellent agreement with OT unfolding studies on isolated A2 domains [7, 56], suggesting that complete A2 unfolding is not obstructed by the presence of other domains. Control measurements using the same attachment protocol and ddFLN4 tethers under the same buffer conditions found no difference in the force response for the different buffer conditions (Fig. 5.2).

I further studied the kinetics of A2 unfolding and refolding. In the case of unfolding, rates are approximately two- to four-fold higher for the EDTA buffer in the force range probed, 6.5–17 pN (Fig. 5.1D, circles). For both buffer conditions, rates increase exponentially with increasing force,

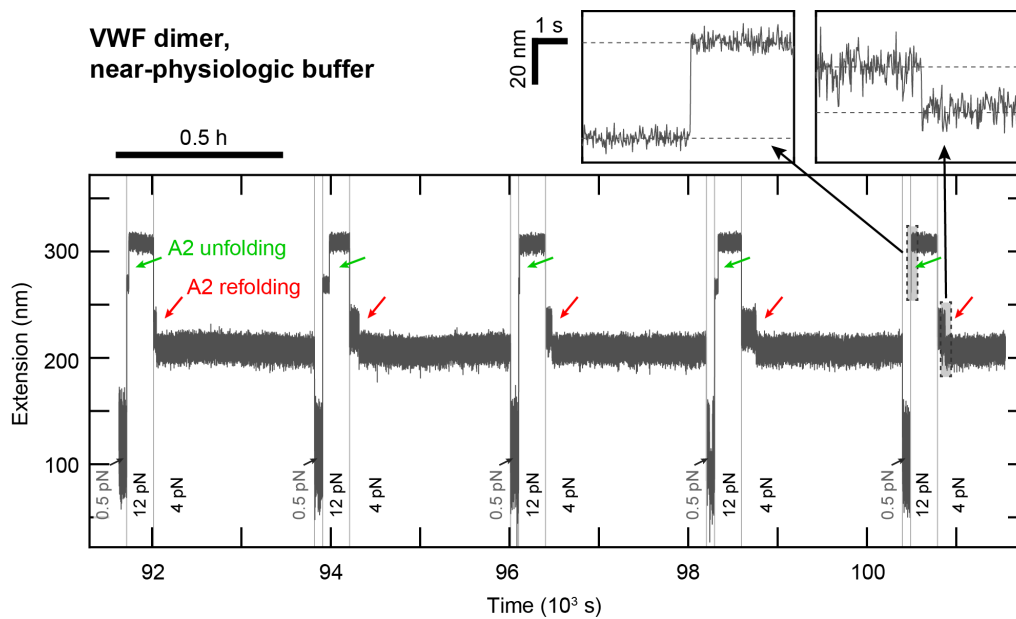


**Figure 5.4: Occasional inhibition of A2 refolding in VWF dimer tethers.** Segment of a  $\approx 30$  h-long extension vs. time trace of a VWF dimer tether subjected to alternating intervals of high force (here 12 pN), allowing for A2 unfolding, and of different intermediate forces (4 pN shown here), allowing for direct observation of A2 refolding, recorded under near-physiologic buffer conditions. The shown tether exhibits the unfolding and refolding signal (marked by arrows) of only one of the two A2 domains. Otherwise, the tether does not show any differences to regular tethers exhibiting signals of both A2 domains. In particular, the observed A2 unfolding and refolding steps were indistinguishable (see insets). In such tethers exhibiting only one A2 signal, which occurred only occasionally, refolding of one of the A2 domains may be inhibited due to cis-trans isomerization of a cis-proline, as reported in a previous OT study [7]. Figure as in the supporting information to [187].

with a slightly stronger dependence on force for the EDTA condition. Fitting a single-barrier kinetic model yielded values for the unfolding rate at zero force  $k_{\text{unf},0} = 3.6 \cdot 10^{-5} \text{s}^{-1}$  ( $1.8$  to  $7.1 \cdot 10^{-5} \text{s}^{-1}$ ) and  $7.8 \cdot 10^{-5} \text{s}^{-1}$  ( $5.1$  to  $12 \cdot 10^{-5} \text{s}^{-1}$ ) and distances to the transition state  $\Delta x_{\text{unf}} = 2.45 \pm 0.22 \text{ nm}$  and  $2.60 \pm 0.15 \text{ nm}$  in the presence and absence of  $\text{Ca}^{2+}$ , respectively. The rates measured in the constant force MT assay are two orders of magnitude slower than the rates determined in near-physiologic buffer in OT measurements on isolated A2 domains. While in principle this difference might indicate stabilization of A2 by neighboring domains, I deem it likely that it at least partially results from the transformation of rupture force distributions measured in the OT using the Dudko-Hummer-Szabo method [200], which is sensitive to the elastic response of employed flexible linkers. In the traces obtained by MT, I did not observe any features that correspond to dissociation of potential interactions of A2 with neighboring domains.

For refolding against external forces of 2-5 pN, rates are approximately two- to sixfold higher in the presence of  $\text{Ca}^{2+}$  (Fig. 5.1D, triangles) and decrease exponentially with force, with a more pronounced force dependence in the presence of  $\text{Ca}^{2+}$ , which is reflected by the higher value of  $\Delta x_{\text{ref}}$  of  $6.80 \pm 0.56 \text{ nm}$  compared to  $4.73 \pm 0.26 \text{ nm}$  in the absence of  $\text{Ca}^{2+}$ . The refolding rate at zero force in the presence of  $\text{Ca}^{2+}$   $k_{\text{ref},0} = 5.1 \text{ s}^{-1}$  ( $2.9$  to  $8.7 \text{ s}^{-1}$ ) is 20-fold higher than in the absence of  $\text{Ca}^{2+}$ ,  $k_{\text{ref},0} = 0.23 \text{ s}^{-1}$  ( $0.18$  to  $0.28 \text{ s}^{-1}$ ), indicating that calcium substantially speeds up folding of A2. The rather pronounced force dependence of A2 refolding implicates that even at relatively low forces below 5 pN, as expected to be readily reached for long multimers in the

bloodstream (*cf.* section 1.3), A2 domains will, once unfolded, stay unfolded for an extended time span, thus allowing for cleavage by ADAMTS13. When force decreases, however, A2 can rapidly refold, preventing excessive cleavage. From the determined rates, furthermore, the equilibrium force at which A2 is equally likely to be in the unfolded and folded state can be predicted to be  $\approx 5.3$  pN under near-physiologic conditions.

Taken together, the obtained results demonstrate that A2 is stabilized by the presence of  $\text{Ca}^{2+}$  both by increasing the refolding rate and stabilizing against unfolding compared to the conditions without  $\text{Ca}^{2+}$ . The observed increases in the refolding rates in my experiments are in quantitative agreement with a previous report using OT on isolated A2 domains [56]. Importantly, I directly observed refolding under mechanical load even in the absence of  $\text{Ca}^{2+}$  (Figs. 5.1C-D and 5.3), in contrast to a previous study that had claimed refolding to only occur in the presence of calcium [170]. The role of  $\text{Ca}^{2+}$  in the stabilization against unfolding is controversial: I observe a modest reduction in the unfolding rate by  $\text{Ca}^{2+}$ , which is consistent with the low-force data found in one OT study [56], which, however, reported no statistically significant change in the unfolding rate with and without  $\text{Ca}^{2+}$  overall, possibly as their assay might have lacked the sensitivity to resolve small differences. In contrast, I find no evidence for a long-lived intermediate in the unfolding pathway in the presence of  $\text{Ca}^{2+}$  that was claimed by one OT study [170], but had not been observed in other OT studies [7, 56]. Finally, it should be noted that I occasionally observed tethers that apparently only showed the unfolding and refolding signal of one A2 domain (Fig. 5.4). In such tethers, refolding of one A2 domain may be inhibited due to cis-trans isomerization of a cis-proline, as reported in a previous OT study [7].

## 5.2 Dissociation of the D4-mediated strong intermonomer interaction

Performing measurements on full-length VWF dimers as described in the previous section, in addition to the steps attributed to A2 unfolding and refolding, I less frequently also observed larger steps of  $\approx 70$ -80 nm (at forces of  $\approx 10$  pN; Fig. 5.5A,C-D). I hypothesized these steps to originate from the dissociation of a strong intermonomer interaction mediated by the D4 domains that has recently been identified in AFM force measurements in approximately one-half of all VWF dimers under near-physiologic conditions [20, 166] (see section 1.4 and chapter 3). A schematic of this intermonomer interaction and its dissociation, which leads to opening of dimers with previously closed C-terminal stems, is shown in Fig. 5.5B. Consistent with their assignment to the D4-mediated intermonomer interaction, the large steps occurred much less frequently in the absence of divalent ions –which have been shown to be critical for the intermonomer interaction [20, 166]–, as tested by measurements in buffer containing 10 mM EDTA (Fig. 5.5A). As a further control, I also conducted force measurements on a mutant construct lacking the entire D4 domain (*delD4*) under near-physiologic buffer conditions (Figs. 5.5A and 5.6). While the A2 domain unfolding and refolding signal remained unchanged for this construct (Fig. 5.6), the larger steps indeed vanished, confirming them to originate from the D4-mediated intermonomer interaction (Fig. 5.5A).

The dissociation of the intermonomer interaction was in some cases –after intermittent relaxation to a low force– observed repeatedly for the same molecule, implying reversibility

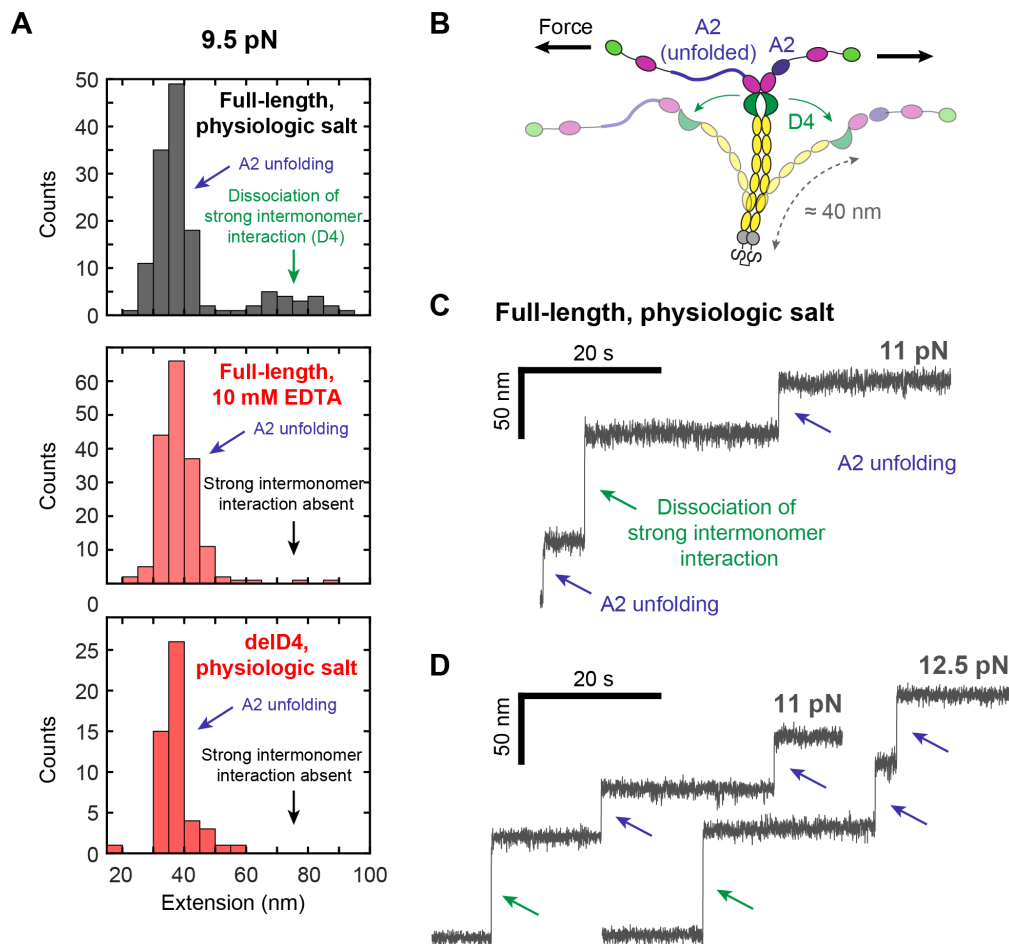


**Figure 5.5: Dissociation of a D4-mediated intermonomer interaction in VWF dimers.** (A) Extension histograms of steps observed in traces of VWF dimers recorded at a force of 9.5 pN, for full-length dimers in the presence of divalent ions (top) or in the presence of 10 mM EDTA (middle), and for dimers with a deletion of the D4 domain (*delD4*, see Fig. 5.6) in the presence of divalent ions (bottom). In the case of the full-length dimers, in the presence of divalent ions a broad peak at extension values of roughly 70-80 nm is observed in addition to the peak associated with A2 unfolding, centered at ca. 36 nm. In the presence of EDTA, or for the *delD4* construct, in contrast, only the peak associated with A2 unfolding is observed. The length increase by 80 nm, the sensitivity to removal of divalent ions by EDTA, and the involvement of the D4 domain are in line with the dissociation of a strong intermonomer interaction mediated by VWF's D4 domain that has recently been identified in AFM force measurements on VWF dimers [20, 166] (*cf.* section 1.4 and chapter 3). (B) Schematic of dimer opening. Dissociation of an intermonomer interaction mediated by the D4 domain (green) leads to the opening of the closed stem region of VWF (yellow) and thus a release of formerly hidden length of approximately 80 nm. Dimer opening occurs independently of A2 (blue) unfolding, since the A2 domains are not shielded from force by the D4-mediated interaction. (C) Exemplary extension trace of a full-length dimer exhibiting unfolding of both A2 domains and dimer opening, recorded at 11 pN. (D) Extension traces from the same VWF dimer tether, probed at different forces and repeatedly exhibiting dimer opening, implying reversibility of the D4-mediated intermonomer interaction. Figure as in the supporting information to [187].

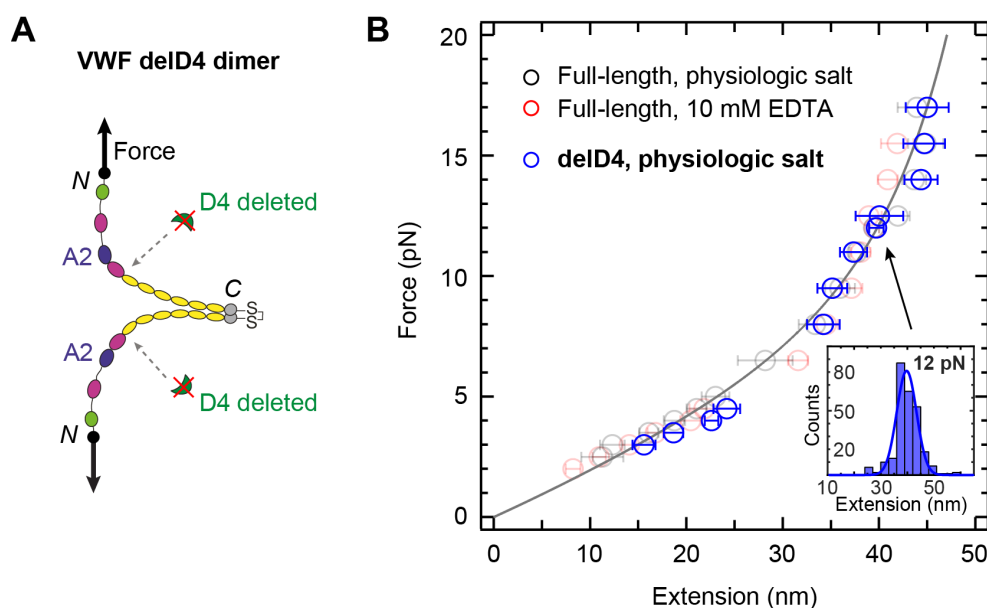


**Figure 5.6: Measurements on VWF dimers with deletion of the D4 domain.** (A) Schematic structure of a VWF dimer with deletion of both D4 domains (*delD4* dimer). The two A2 domains are shown in blue. Arrows indicate the direction of force acting on the two N termini during MT experiments. (B) Force–extension profile of A2 unfolding and refolding, recorded for the *delD4* construct in near-physiologic buffer at pH 7.4 (blue symbols). The force–extension profile closely matches those obtained for the full-length construct in near-physiologic buffer and in buffer with 10 mM EDTA (co-plotted with lower opacity in black and red, respectively), as presented in Fig. 5.1C. The line is the global WLC fit to all data from the full-length construct, as presented in the inset in Fig. 5.1C. Data points are obtained by Gaussian fits to step extension histograms (inset) at each constant force. Data points above 5 pN are from unfolding, data points up to 5 pN from refolding. Error bars correspond to the FWHM of Gaussian fits, divided by the square root of counts. Figure as in the supporting information to [187].

of the interaction (5.5D). Since it has previously been established that formation of the D4-mediated intermonomer interaction crucially requires transition metal ions [166], which are, however, only present in trace amounts in the used buffer, this finding might either indicate a very high affinity of ion binding or that ions can stay bound even upon dissociation of the binding interface of the intermonomer interaction. However, to date no high-resolution structure of the D4 domain is available that could provide more instructive mechanistic insights into this interaction.

Remarkably, whereas in constant pulling speed AFM measurements dissociation of the D4-mediated intermonomer interaction had always occurred at much higher forces than –and therefore after– A2 unfolding [20, 166], in the constant force measurements in MT I observed dissociation of this interaction in the same force range as A2 unfolding, suggesting a pronounced force–loading rate dependence for the intermonomer interaction. In fact, in the constant-force measurements I repeatedly observed dissociation of this interaction even before unfolding of one or both of the A2 domains (5.5C-D). Importantly, this implies that the D4-mediated intermonomer interaction can dissociate at physiologically relevant forces in the bloodstream, suggesting it to play an even more important role for tuning VWF’s sensitivity to hydrodynamic forces –and thus for regulating VWF’s hemostatic activity– than already discussed in chapter 3.

## 5.3 VWF stem zipping and unzipping at low forces

As discussed in detail in section 1.4 and chapter 3, AFM imaging [20, 166] and electron microscopy [47] suggest that the VWF stem consisting of six C-domains can open and close in a zipper-like fashion (Fig. 5.7A-B). However, transitions of the VWF stem have not been observed directly. Forces required to unzip the stem have been estimated to be as low as  $\lesssim 1$  pN [20], far below the resolution limit of previous AFM-based force spectroscopy measurements on VWF dimers, but accessible in my MT experiments.

To probe for interactions in the VWF stem, I subjected dimeric VWF tethers that had shown the characteristic A2 unfolding pattern to low constant forces. At forces of  $\approx 1$  pN, I indeed observed repeated, reversible transitions with a maximum contour length increase of  $\approx 50$ - $60$  nm that is consistent with fully unzipping and re-zipping the VWF stem (Figs. 5.7 and 5.8). Increasing force in the range 0.6-1.4 pN systematically shifted the population towards higher tether extensions, which are interpreted as less compact “unzipped” conformations of the VWF stem. Importantly, such transitions were never observed for ddFLN4-tethered beads. In addition, the large change in extension at very low forces makes it appear highly unlikely that the observed transitions originate from domain unfolding events (for comparison, a tether extension of  $< 5$  nm would be expected for unfolding of an A2 domain at a force of  $\approx 1$  pN, due to the WLC stretching behavior of the unfolded protein chain).

The observed transitions appeared to occur between multiple levels and to feature more than two distinct states, as would be expected from the observation by AFM imaging that multiple C-domain interactions contribute to the opening and closing of the stem. Measurements using high-speed bead tracking (1 kHz; Fig. 5.7D) further confirmed that the transitions are not discrete jumps between only two states, but rather gradual transitions with several intermediate extension levels, and revealed transitions to occur on time scales  $\leq 1$  s.

Taken together, these observations are consistent with the predicted occurrence of unzipping transitions in the VWF stem at forces of  $\approx 1$  pN. Molecular interactions that break and release contour length at such low forces are expected to be particularly relevant for the regulation of VWF’s physiological function as these are likely the first interactions to open under elevated flow and to set off a cascade of increased contour length and increased force, since hydrodynamic peak forces grow as the square of the contour length [4, 7].

However, a reliable assignment of the transitions will require additional analysis and measurements. A more in-depth analysis of traces that exhibit stem (un-)zipping transitions could for instance involve adopting a Hidden Markov Model approach, which may enable a more reliable identification of intermediate states. In order to dissect the contributions of the different C domains, as well as the impact of D4, measurements under a range of solution conditions are of interest. I expect experiments at lower pH values to be particularly insightful, as acidic pH has been shown to promote formation of the C-domain stem, which I expect to be accompanied by an increased mechanical stability of C-domain interactions observable in MT experiments. Furthermore, measurements in the absence of divalent ions, and/or on *delD4* dimers, will allow to study C-domain interactions without the potentially dominating effect of the D4 domain (*cf.* chapter 3). Going along a similar line, constructs with a deletion of certain C domains may allow to establish which C domains are vital for stem formation. Finally, the observed pathological effects of certain clinically relevant mutations located in C domains may be a result

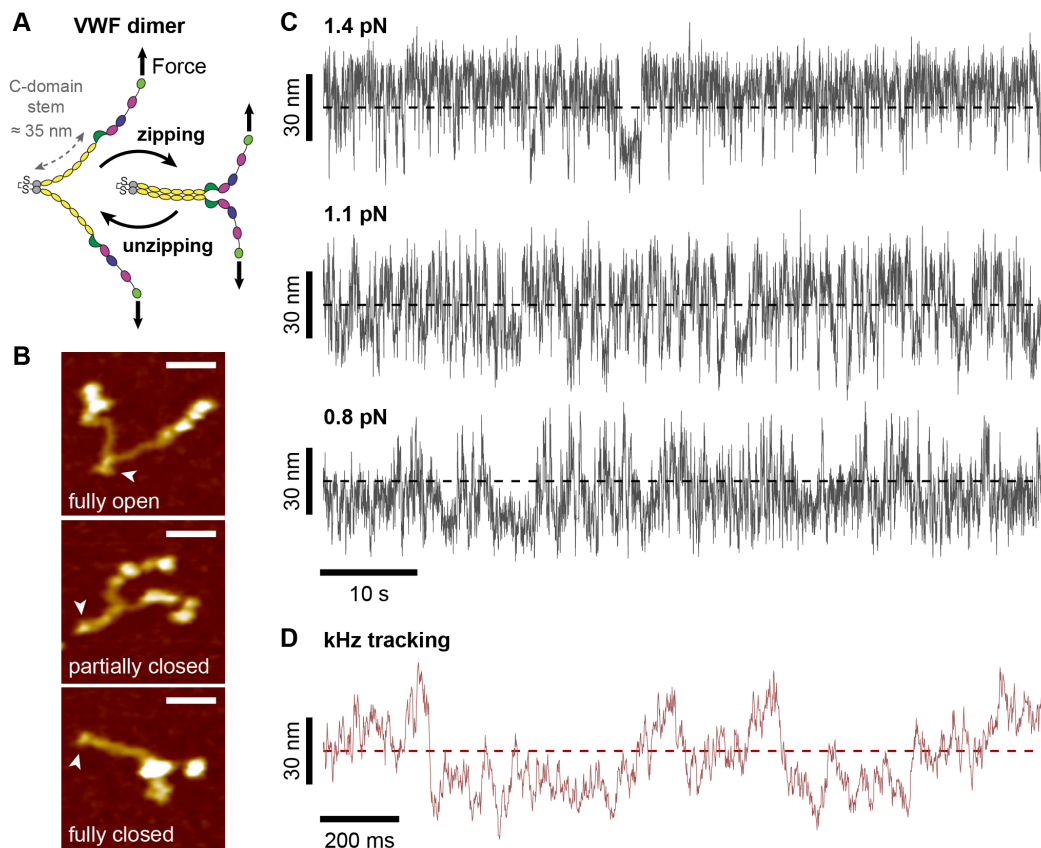


**Figure 5.7: Unzipping and zipping of the C-domain stem in VWF dimers (I).** (A) Schematic of closing and opening of the stem (domains C1-C6, yellow) of VWF dimers in a zipper-like fashion due to interactions between the C-domains. (B) AFM images of single VWF dimers adsorbed onto a surface under near-physiologic buffer conditions. Arrowheads indicate C-terminal ends of dimers, where the two constituting monomers are linked. In thermal equilibrium and in the absence of force, dimer stems exhibit conformations ranging from fully open to fully closed. It should be noted that in approximately one-half of all dimers, the stem region is firmly closed by the D4-mediated intermonomer interaction [20, 166]. Scale bars are 20 nm; height range of color scale is 2.4 nm. (C) Extension vs. time traces of VWF dimer constructs subjected to low forces in MT. Fast reversible transitions between a maximum and minimum value of extension, approximately 60 nm apart, are observed that I attribute to closing and opening of the C-domain stem. Dashed lines indicate the midpoint between the two extreme values of extension. At a force of  $\approx 1.1$  pN, the system spends approximately half of the time above and below the midpoint. Traces are raw data recorded at 58 Hz. (D) Segment of an extension vs. time trace of the same tether shown in panel C, at 1.3 pN, recorded at an acquisition rate of 1 kHz. The measurements with high temporal resolution indicate that the observed transitions are not jumps between two discrete extension levels, but rather gradual transitions with several intermediate extension levels, suggestive of zipper-like closing and opening of the stem with several pairs of interacting C-domains. Figure as in [187].

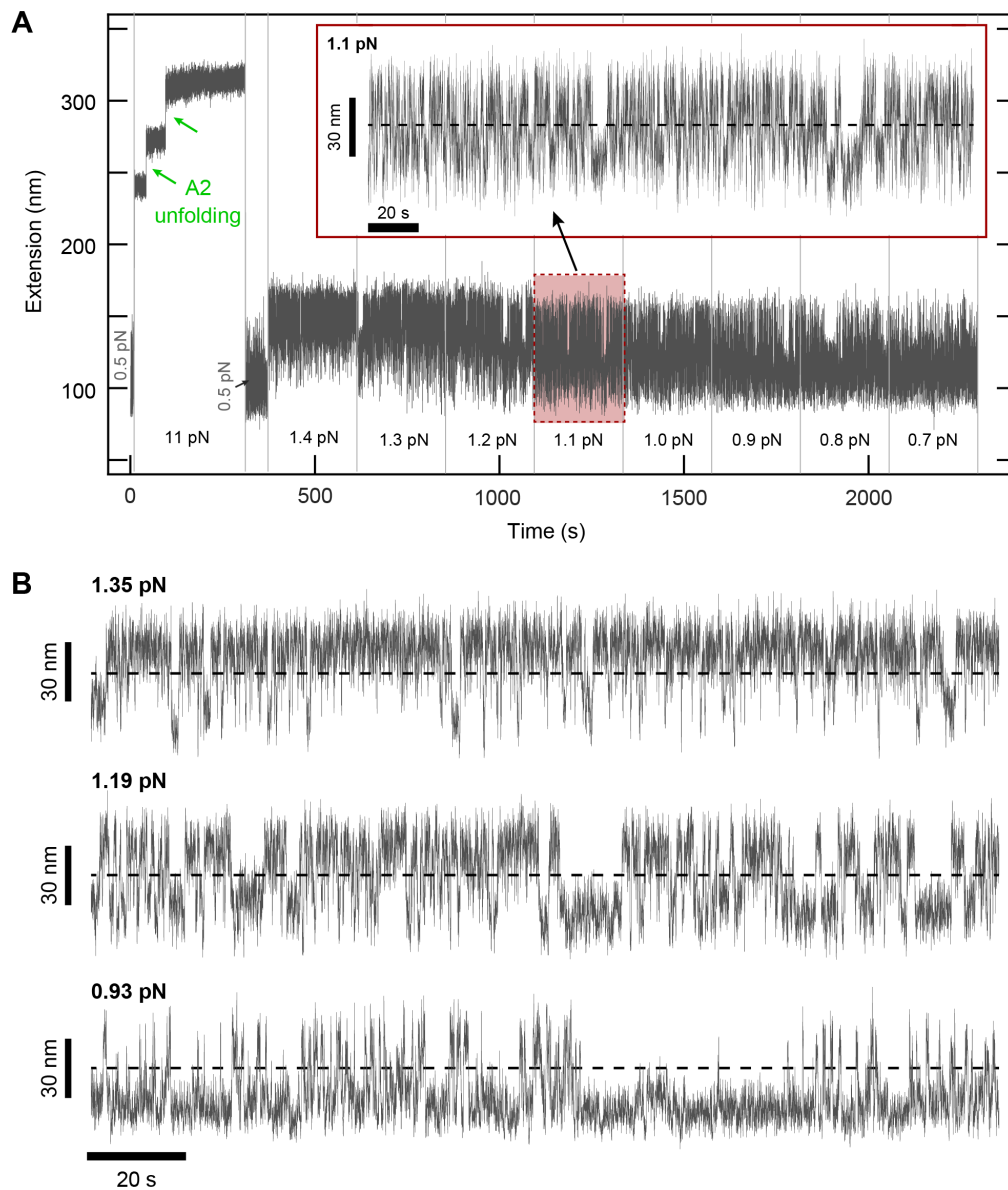


**Figure 5.8: Unzipping and zipping of the C-domain stem in VWF dimers (II).** (A) Full trace of the VWF dimer tether presented in Fig. 5.7. After fingerprint A2 domain unfolding at 11 pN (green arrows) and refolding at 0.5 pN, the tether is subjected to stepwise decreasing low forces between 1.4 and 0.7 pN for 240 s each. Fast reversible transitions to multiple extension levels between a maximum and minimum value of extension, approximately 60 nm apart, are observed that I attribute to closing and opening transitions of the C-domain stem. The inset shows the 240 s-long segment at 1.1 pN. The dashed line indicates the midpoint between the two extreme values of extension. (B) Extension vs. time traces of a VWF tether from a different flow cell, again exhibiting fast transitions at forces of  $\approx 1$  pN, with the population being shifted towards higher tether extensions for higher forces. Dashed lines indicate the midpoint between the two extreme values of extension. Figure as in the supporting information to [187].

of altered dynamics of stem opening and closing. One example might be the rather common variant p.Phe2561Tyr –with a single point mutation in the C4 domain–, which has recently been reported to be associated with an increased risk of myocardial infarction, especially in young female carriers [201]. Remarkably, although both platelet integrin GPIIb/IIIa and platelet receptor GPIb $\alpha$  binding appear to be unaltered for this variant [53, 201], it exhibits markedly increased platelet aggregation under shear flow, and microfluidic assays revealed an approximately two-fold reduction of the critical shear rate for inducing aggregate formation [201]. These findings suggest an increased force-sensitivity of variant p.Phe2561Tyr, possibly due to destabilization and consequently faster opening of the C-domain stem, which might be detectable in the MT assay.

## 5.4 Fast transitions of an intra-domain interaction within the D'D3 assembly

In addition to the force-induced transitions in VWF dimers presented in the previous sections, I further discovered a new, previously not described feature. This feature is characterized by rather fast and reversible transitions between three distinct states of extension (termed "three-state hopping" in the following), with the bottom and middle state, and the middle and top state, each being separated by approximately 7-10 nm, depending on the applied force (Fig. 5.9). Population of all three states was observed at forces of approximately 8 pN. Decreasing or increasing the force over the range of a few pN resulted in progressive depletion of the top and bottom state, respectively, and eventually also of the middle state. A more comprehensive characterization and analysis of the three-state hopping will be given in the following, after assessing the origin of this feature. For a subset of the measurements presented in this section, I was supported by Sophia Gruber (LMU Munich).

### Identifying the origin of the three-state hopping

The existence of three states separated by apparently identical extension increments strongly suggested this hopping to originate from two identical underlying processes that occur independently in the two constituent monomers within the dimer. Regarding the nature of this underlying transition within a monomer, I developed four hypotheses:

- 1) Involvement of the A2 domain, e.g. by partial unfolding. This idea was motivated by the fact that A2 is the only domain in VWF that is not protected against force-induced unfolding. However, this hypothesis would contradict the previous observation of full A2 unfolding without any long-lived intermediate state (see section 5.1).
- 2) Dissociation of an intramonomer interaction involving the A1 domain, especially the A1–D'D3 interaction already described in section 1.4. Due to the flexible linker region between A1 and D'D3, dissociation of this interaction could yield the extension increments observed in the experiment.
- 3) An intra-domain transition within the large D4 domain, which is an assembly of four individual submodules. Although each submodule has been predicted to be protected against unfolding by long-range disulfide bonds [41], submodules might interact with each other. The hopping might thus correspond to the force-induced dissociation of such an interaction.

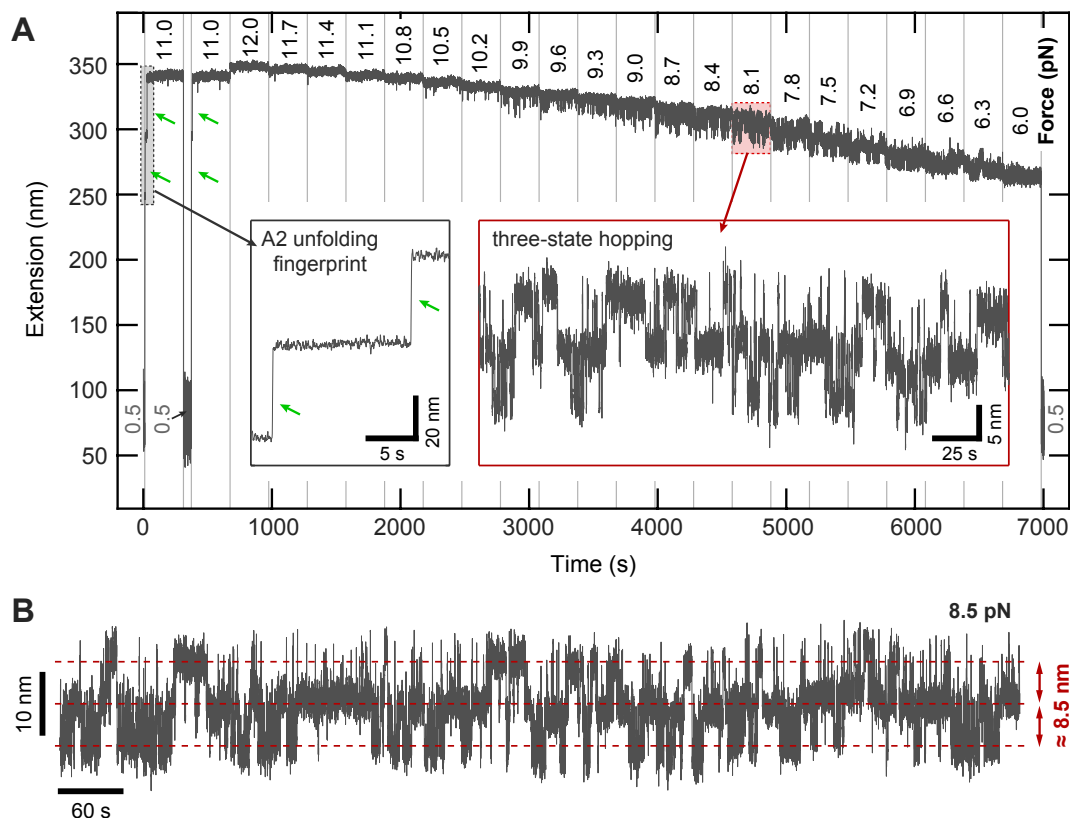


**Figure 5.9: Three-state hopping in full-length VWF dimers. (A)** Extension vs. time trace of a full-length VWF dimer tether exhibiting fast, reversible transitions between three distinct states at forces around 8 pN. After two 5-min plateaus of 11 pN, allowing to observe A2 unfolding as fingerprint to identify specific tethers, the force was stepwise decreased every 5 min from 12 to 6 pN in steps of 0.3 pN. Transitions between three distinct states are visible, with the population of the three states being shifted by force (see Fig. 5.13). At forces around 8 pN, the top and bottom state are approximately equally populated. The extensions of the transitions between bottom and middle state and between middle and top state were observed to be identical, and ranged from approximately 7-10 nm over the studied force range. **(B)** Longer, 16-min trace of a different bead recorded at 8.5 pN, showing three-state hopping with roughly equal population of the top and bottom state, which are both  $\approx 8.5$  nm apart from the middle state. Dashed red lines indicate extension levels corresponding to the three states. The shown traces were subjected to 5-frame moving average smoothing.

However, currently no high-resolution structure of the D4 domain is available.

4) An intra-domain transition within the large D'D3 domain, which also is an assembly of several (six) individual submodules that might interact with each other. A high-resolution crystal structure of D'D3, which indeed revealed interactions between four of the submodules, as will be described below, became only available after the measurements presented in this section had already been completed.

Hypothesis 1) could be ruled out by the observation that three-state hopping occurred independently of the folding state of A2, *i.e.* both before unfolding of the first A2 domain and even after full unfolding of both A2 domains (Fig. 5.10A). This finding also implicates that no interaction of A2 with a different domain is underlying the hopping.

To test hypothesis 2), measurements on *delA1* dimers with a deletion of the A1 domains were conducted (for details on deletion constructs, see section 2.3). Unaltered three-state hopping

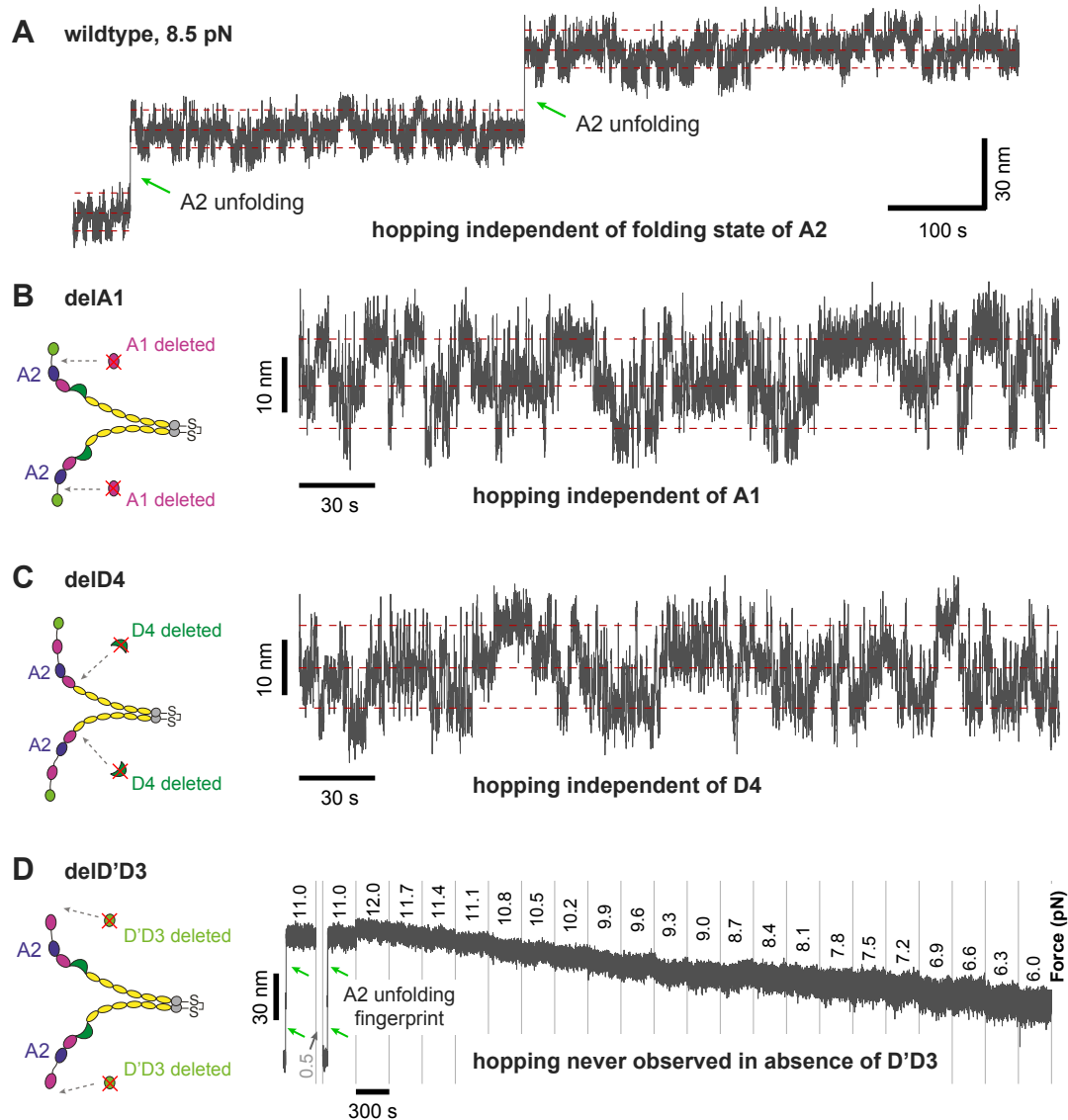


**Figure 5.10: Localization of the three-state hopping to transitions within D'D3 domains.** (A) Extension vs. time trace of a full-length VWF dimer subjected to a force of 8.5 pN, exhibiting three-state hopping independently of the folding state of the two A2 domains. (B) Schematic and exemplary segment of a measurement on *delA1* dimer tethers, showing unaltered three-state hopping. (C) Schematic and exemplary segment of a measurement on *delD4* dimer tethers, again showing unaltered three-state hopping. (D) Exemplary extension vs. time trace of a *delD'D3* dimer tether, not exhibiting hopping. Importantly, in the absence of D'D3 hopping was, for > 50 specific tethers, never observed. All traces were subjected to 5-frame moving average smoothing. Dashed red lines in panels A-C indicate extension levels corresponding to the three states of hopping.

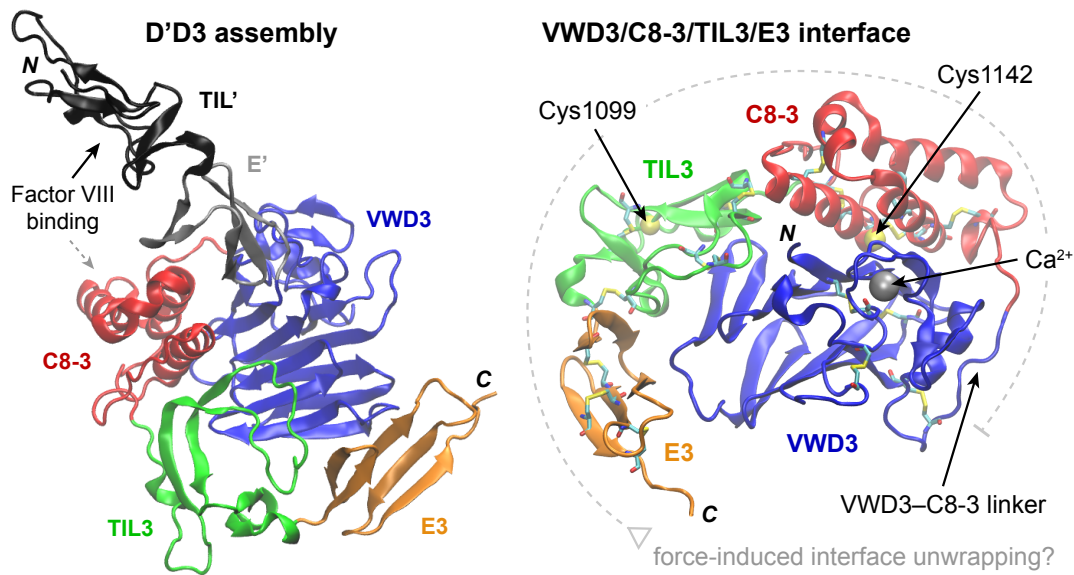


**Figure 5.11: Structure of the D'D3 assembly and its VWD3/C8-3/TIL3/E3 interface.** The crystal structure of the monomeric, full D'D3 assembly (PDB: 6N29 [48]) was rendered using VMD [191], with each submodule shown in a different color (left). While submodules VWD3, C8-3, TIL3 and E3 are packed rather compactly, with submodules C8-3, TIL3 and E3 being wound around the larger VWD3 module, the N-terminal submodules TIL' –containing the binding site for factor VIII– and E' project away from the rest of the assembly and are thus more exposed [48]. The interface between modules VWD3, C8-3, TIL3 and E3 (right) is primarily stabilized by hydrophobic patches and hydrogen bonds and involves several histidine residues [48]. The positions of cysteines Cys1099 and Cys1142 (yellow spheres) are buried in the interface. Cysteines involved in disulfide bonds are shown in licorice representation. The silver sphere represents a calcium ion bound to the VWD3 module. The dashed gray line indicates the length that would be gained by the hypothesized force-induced “unwrapping” of the interface.

was still observed (Fig. 5.10B), showing that A1 is not involved.

Similarly, hypothesis 3) was ruled out by measurements on *delD4* dimers, which also still exhibited three-state hopping (Fig. 5.10C).

In contrast, in experiments on *delD'D3* dimers (Fig. 5.10D), lacking the full D'D3 assemblies, hopping was never observed for > 50 specific tethers measured analogously to the measurement protocol shown in Fig. 5.9. This finding indicates that in line with hypothesis 4) transitions within the two D'D3 domains in a dimer are responsible for the three-state hopping.

Only very recently, a crystal structure of the monomeric D'D3 domain was published by Dong *et al.* [48] (Fig. 5.11). While the N-terminal submodules TIL' –containing the binding site for factor VIII– and E' project away from the rest of the assembly and are thus more exposed, the remaining submodules VWD3, C8-3, TIL3 and E3 were found to be packed rather compactly, with submodules C8-3, TIL3 and E3 being wound around the larger VWD3 module [48]. I hypothesize that force-induced “unwrapping” of this interface between modules VWD3, C8-3, TIL3 and E3 is the process underlying the hopping observed in the MT measurements. Peeling modules E3, TIL3 and C8-3 off the VWD3 module, as indicated schematically by the dashed gray line in Fig. 5.11 (right), would yield a gain in extension that agrees well with the increments observed in experiments, as estimated from the crystal structure. Importantly, all submodules appear to be stabilized against unfolding by disulfide bonds, which are shown

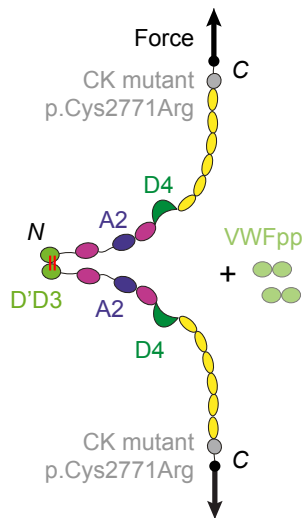


**Figure 5.12: Schematic of an inverted VWF dimer construct.** In order to probe the force response of D'D3 domains in their native conformation as in mature VWF, *i.e.* after dimerization with another D'D3 domain *via* disulfide bonds Cys1099-Cys1099' and Cys1142-Cys1142' (indicated by red lines), "inverted" dimers could be employed. To produce such N-terminally, but not C-terminally linked dimers, monomers with mutation p.Cys2771Arg in the CK domain to impair C-terminal dimerization [45, 202] and with C-terminal tags for site-specific protein attachment can be expressed in the presence of the VWF propeptide (VWFpp) domains D1 and D2, resulting in N-terminal linkage.

in licorice representation in Fig. 5.11. In order to verify the hypothesis, measurements on a construct with insertion of an artificial linker sequence into the flexible linker region between submodules VWD3 and C8-3 are planned. The additional length of this linker would increase the extension of hopping observed in the experiment, if indeed unwrapping of E3, TIL3 and C8-3 from VWD3 is the transition underlying the hopping. In addition, steered molecular dynamics simulations could help to determine the expected extension increments for this unwrapping and to compare them with the experimental observations.

The interface between modules VWD3, C8-3, TIL3 and E3 is primarily stabilized by hydrophobic patches and hydrogen bonds and involves several histidine residues, implicating a likely pH sensitivity, as histidine residues can be protonated at acidic pH [48]. Submodule VWD3 further contains a calcium binding loop, and calcium binding might stabilize VWD3 and potentially also the interface. Importantly, the positions of cysteines Cys1099 and Cys1142, which are involved in N-terminal multimerization of VWF (see Fig. 1.1), are buried in the interface. Dong *et al.* hence proposed that this interface may serve to shield Cys1099 and Cys1142 during the early stages of VWF's biosynthesis, especially in the ER, from disulfide bond formation. Conversely, these two cysteines should be available for multimerization in the trans-Golgi, with the opening of the interface possibly being driven by the acidic pH encountered in the trans-Golgi [48].

It is important to note that the interface as described here is only present in the monomeric D'D3 domain, *i.e.* before multimerization of VWF and its secretion into the bloodstream. This implicates that in the physiological case, the interface may never be loaded with force in the described conformation. In other words, the dissociation of this interface, as probed under force in MT, in the physiological case may not be mechano-regulated. Still, the MT measurements can provide important insights into the stability of the interface under different pH and ionic conditions. It is currently unclear if interactions between the involved submodules may also be relevant after multimerization, *i.e.* after the D'D3 domain has dimerized with a D'D3 domain of the neighboring dimer within a multimer by formation of disulfides Cys1099-Cys1099' and Cys1142-Cys1142'. It can be assumed that in the dimerized D'D3 force would propagate from the C terminus through the E3 module and at least up to the disulfide Cys1099-Cys1099' formed between the two TIL3 domains, but no structure of the dimerized D'D3 is currently available to

assess if potentially still interactions between different submodules may be loaded with force. Such interactions may for instance affect binding or release of factor VIII, since Dong *et al.* speculated that the factor VIII binding site might not be limited to TIL', but extend to C8-3, based on the location of certain mutations in D'D3 that influence factor VIII binding [48]. In order to test if force-induced transitions are still present in the dimerized D'D3 domain, MT force measurements on "inverted" dimers are planned, *i.e.* on dimers that are N-terminally linked, but not C-terminally dimerized (Fig. 5.12). For preparation of such constructs, C-terminal dimerization will be impaired by introducing the mutation p.Cys2771Arg in the CK domain (*cf.* chapter 6), and N-terminal linkage will be facilitated by expressing monomers together with the VWF propeptide.

### Relative populations of the three states of hopping at different forces

In order to characterize the three-state hopping for the wildtype construct and to extract thermodynamic parameters of the underlying transitions, I first analyzed the relative populations of the three states of hopping at different forces. In Fig. 5.13, this is exemplary shown for the tether presented in Fig. 5.9, which had been subjected to forces between 12 and 6 pN, with the force being decreased every 5 min in steps of 0.3 pN. For each measured force, an extension histogram of the respective 5-frame moving average-smoothed trace was obtained, and the three different states could be observed as distinct peaks in the histograms (Fig. 5.13). By using the local minima between the distinct peaks in the histograms as thresholds to separate the different states, the relative fractions of data points in the three states was determined for each force. The obtained relative fractions were then fitted under the assumption of two identical, independent processes underlying the hopping. As a consequence of this assumption, the probability  $P_{\text{top}}$  of the system being in the top state is the probability that both underlying interactions are in their open state. Conversely, the probability  $P_{\text{bottom}}$  of being in the bottom state corresponds to the probability that both underlying interactions are closed. The middle state corresponds to the situation in which one interaction is in the open state and the other one in the closed state. More formally,

$$P_{\text{top}} = p_{\text{open}}^2 \quad (5.1)$$

$$P_{\text{middle}} = 2 \cdot p_{\text{open}} \cdot p_{\text{closed}} \quad (5.2)$$

$$P_{\text{bottom}} = p_{\text{closed}}^2 \quad (5.3)$$

In thermodynamic equilibrium, the probabilities  $p_{\text{open}}$  and  $p_{\text{closed}}$  of one underlying interaction being in its open and closed state, respectively, are given by

$$p_{\text{open}} = \frac{1}{1 + \exp(\Delta G/k_B T)} = \frac{1}{1 + \frac{k_{\text{close}}}{k_{\text{open}}}} \quad (5.4)$$

$$p_{\text{closed}} = \frac{1}{1 + \exp(-\Delta G/k_B T)} = \frac{1}{1 + \frac{k_{\text{open}}}{k_{\text{close}}}}, \quad (5.5)$$

with  $\Delta G$  being the Gibbs free energy difference between the open and the closed state, and  $k_{\text{open}}$  and  $k_{\text{close}}$  being the rates of opening and closing, respectively, at the given force. I further assumed that the underlying interactions can be described by a simple single-barrier kinetic

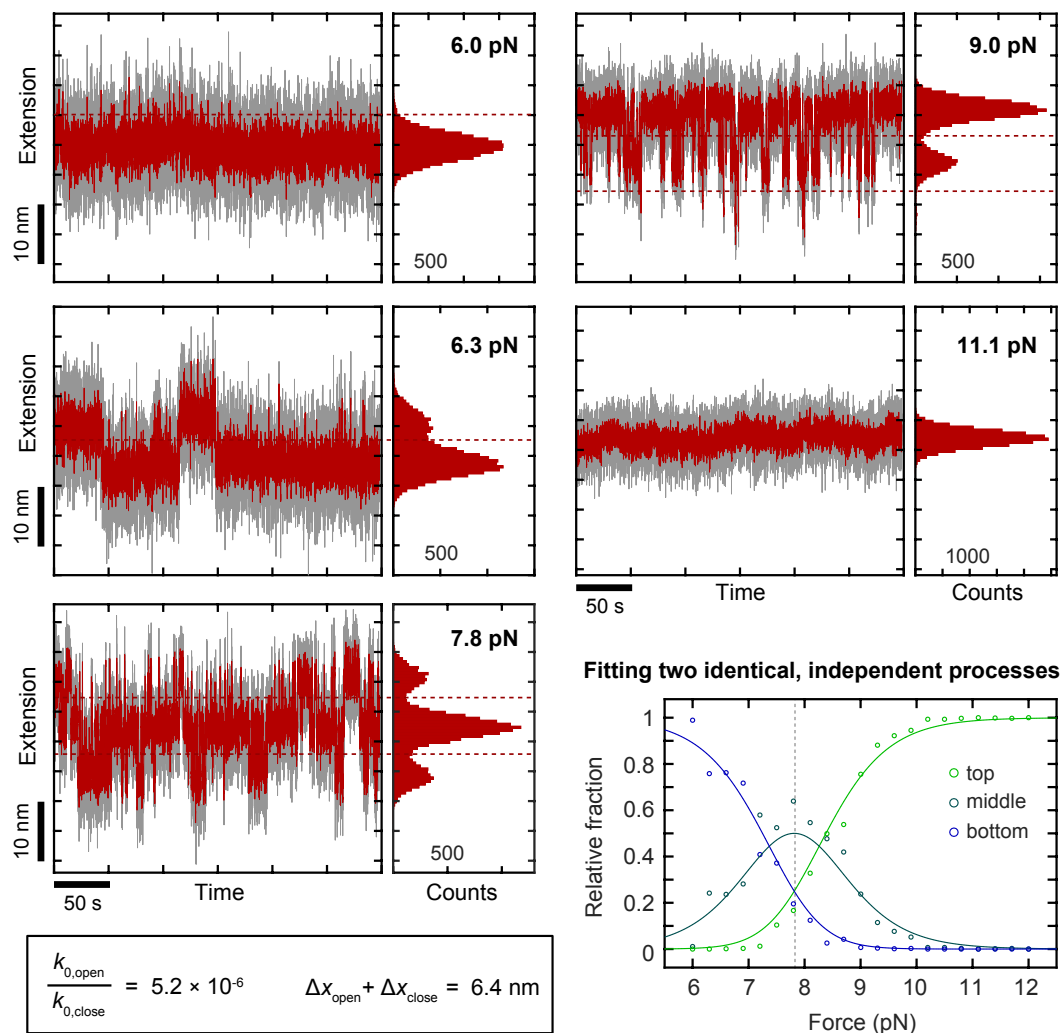


**Figure 5.13: Relative populations of the three states of hopping as a function of force.** As exemplarily shown here for the trace presented in Fig. 5.9, the relative populations of the three states of hopping can be analyzed to extract thermodynamic parameters of the underlying transitions. To this end, for each measured force an extension histogram of the respective 5-frame moving average-smoothed trace is obtained, as exemplarily shown here for five selected forces (upper five panels, red). For comparison, the unsmoothed traces are shown in gray. At forces close to  $\approx 8$  pN, the histograms show three distinct peaks corresponding to the three states of hopping. Decreasing (or increasing) the force progressively depletes the top (or bottom) state, respectively, and eventually also the middle state. By using the local minima between the distinct peaks in the histograms as thresholds (dashed red lines) to separate the different states, the relative fractions of data points in the three states can be determined for each force (lower right panel). The obtained relative fractions were fitted (lines) under the assumption of two identical, independent processes underlying the hopping, as explained in detail in the text, yielding values for the ratio of the zero-force rates of opening and closing, as well as for the sum of the distances to the transition state, as indicated. The dashed gray line indicates the force at which the rates of opening and closing are equal.

model, in which the opening and closing rates scale exponentially with force (*cf.* section 2.2.1), *i.e.*

$$k_{\text{open}}(F) = k_{0,\text{open}} \cdot \exp(F\Delta x_{\text{open}}/k_{\text{B}}T) \quad (5.6)$$

$$k_{\text{close}}(F) = k_{0,\text{close}} \cdot \exp(-F\Delta x_{\text{close}}/k_{\text{B}}T). \quad (5.7)$$

Taken together, the above considerations yield the following expressions for the probabilities to be in the top, middle, and bottom state:

$$P_{\text{top}} = \left( 1 + \frac{2}{A} \cdot e^{-FB/k_{\text{B}}T} + \frac{1}{A^2} \cdot e^{-2FB/k_{\text{B}}T} \right)^{-1} \quad (5.8)$$

$$P_{\text{middle}} = \left( 1 + \frac{A}{2} \cdot e^{FB/k_{\text{B}}T} + \frac{1}{2A} \cdot e^{-FB/k_{\text{B}}T} \right)^{-1} \quad (5.9)$$

$$P_{\text{bottom}} = \left( 1 + 2A \cdot e^{FB/k_{\text{B}}T} + A^2 \cdot e^{2FB/k_{\text{B}}T} \right)^{-1}, \quad (5.10)$$

$$\text{with } A \equiv \frac{k_{0,\text{open}}}{k_{0,\text{close}}} \text{ and } B \equiv (\Delta x_{\text{open}} + \Delta x_{\text{close}}). \quad (5.11)$$

Fitting these expressions to the relative fractions obtained from the measurement thus yielded values for the ratio of the zero-force rates of opening and closing  $A$ , as well as for the sum of the distances to the transition state  $B$ , which were found to be on the order of  $10^{-7}$ - $10^{-6}$  and 6-7.5 nm, respectively. Since analysis was not yet finished at the time of writing this thesis, and has so far only been conducted for individual beads, no standard deviations are reported for the extracted thermodynamic parameters. However, the results obtained for several independent beads from different measurements (see for instance Figs. 5.16 and 5.17) were all comparable, with  $A$  and  $B$  being in the ranges indicated above. The obtained values for  $A$  correspond to a Gibbs free energy difference at zero force between the closed and open state of approximately  $15 k_{\text{B}}T$ , implying a high thermodynamic stability of the underlying interaction under the investigated near-physiological conditions, so that dissociation in the absence of an external force is negligible.

### Kinetics of three-state hopping

The MT data obviously also contain information about the kinetics of hopping. To extract rates of opening and closing of the interactions underlying the three-state hopping, distributions of the observed dwell times, *i.e.* the times the system spends in one of the three states before crossing an extension threshold to a different state, were regarded. Importantly, since two independent interactions are occurring in parallel in the case of three-state hopping, such simple dwell time distributions do not reflect the timescales for opening (or closing) of a single underlying interaction, but of the combination of the two interactions, which are assumed to be identical. For instance, for the transition from the bottom to the middle state, one does not directly observe the timescale for opening of a single interaction, but for opening of one out of two interactions, so that the observed dwell times correspond to  $\frac{1}{2}$  of the timescale for opening of a single interaction. Hence, in order to obtain dwell time distributions corresponding to the timescales of a single underlying interaction, one has to take into account the number of

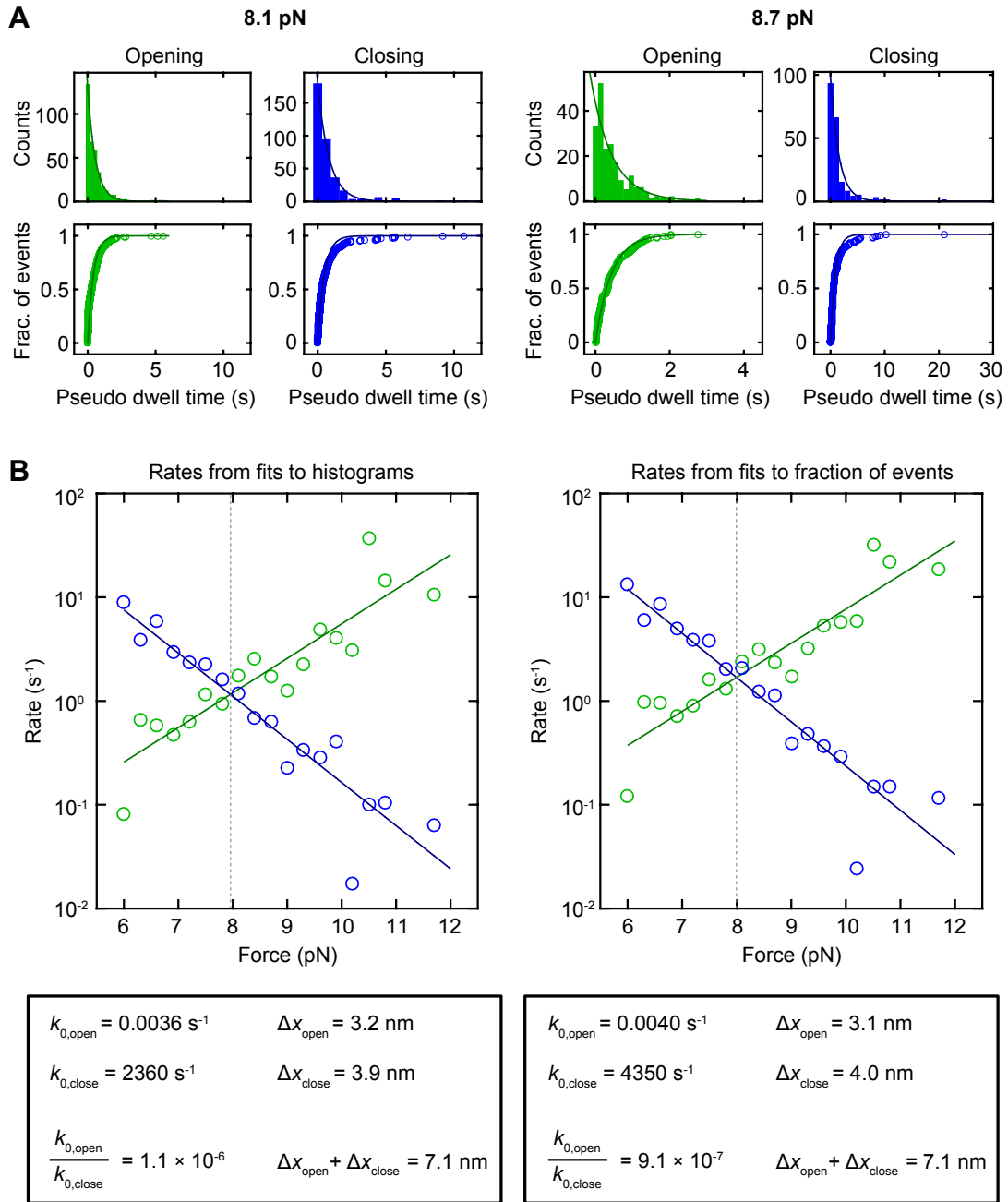


**Figure 5.14: Kinetics of three-state hopping.** (A) Pseudo dwell time analysis. Exemplary shown for the tether presented in Figs. 5.9 and 5.13 are pseudo dwell time distributions (*cf.* main text) for two selected forces, both for opening (*i.e.* transitions from bottom to middle and middle to top state) and closing (*i.e.* transitions from top to middle and middle to bottom state). Implicit is the assumption that the three-state hopping results from two identical, independent processes. While the upper panels show binned distributions, the lower panels represent the same data as fraction of observed events vs. time and thus in an un-binned fashion. Exponential fits to the distributions (lines) yield rates for opening and closing, respectively. (B) Opening and closing rates as a function of force. The left panel shows the rates obtained from fitting the binned distributions, the right panel the rates from fitting the un-binned data. Fits of a single-barrier kinetic model (lines) yielded values for the zero-force opening and closing rates and the respective distances to the transition state as indicated, in reasonable agreement with the values obtained by fitting the relative populations of states (see Fig. 5.13). The dashed gray lines indicate the force at which the rates of opening and closing are equal.

interactions that are still closed (or open) for each transition, and the dwell times observed in the measurement have to be weighted accordingly by this number. Applying the above considerations yields so-called pseudo-dwell time distributions [154], which reflect the kinetics of a single interaction.

Pseudo dwell time distributions for two exemplary forces for the tether already presented in Figs. 5.9 and 5.13 are shown in Fig. 5.14A. The data are shown both as binned distributions and in an un-binned fashion, represented as fraction of observed events *vs.* pseudo dwell time. Exponential fits to the pseudo dwell time distributions yielded rates of opening and closing, respectively (Fig. 5.14B). Rates obtained by fitting to binned and un-binned distributions were found to be very similar, but fitting to un-binned distributions was preferred owing to higher stability of fitting. The dependence of the opening and closing rates on force was further fitted by a simple single-barrier kinetic model (Fig. 5.14B), yielding values for the zero-force rates  $k_{0,\text{open}}$  and  $k_{0,\text{close}}$ , which were found to be on the order of  $10^{-3} - 10^{-4} \text{ s}^{-1}$  and  $10^3 - 10^4 \text{ s}^{-1}$  respectively, and for the distances to the transition state  $\Delta x_{\text{open}}$  and  $\Delta x_{\text{close}}$  ( $\approx 3 \text{ nm}$  and  $4 \text{ nm}$ , respectively). Importantly, these values are in good agreement with those obtained by analyzing the relative populations of the different states. This consistency indicates that the hopping can indeed be well described by three states, with possible intermediate states being negligible.

### Two-state hopping and potential inhibition of interface formation in D'D3

Importantly, not all specific VWF dimer tethers (as identified by the occurrence of two A2 unfolding events as fingerprint) exhibited three-state hopping. The fraction of tethers showing three-state hopping under near-physiologic buffer conditions was found to be roughly 50 %. Roughly 40 % of tethers exhibited hopping-like transitions between only two distinct states (Fig. 5.15A). Two-state hopping was observed in the same force range as three-state hopping, and, furthermore, the two states were separated by extension increments identical to the ones observed for the transitions in three-state hopping, strongly suggesting that in such tethers the underlying transition within the D'D3 domain is inhibited in one of the two monomers. The remaining roughly 10 % of all tethers did not show any hopping, implicating that, overall, the transition may be inhibited in approximately 30 % of all individual D'D3 domains.

To test the assumption that the transitions observed in two-state hopping correspond to one of the two identical interactions underlying the three-state hopping, the relative populations of the two states and the kinetics of opening and closing were analyzed for an exemplary two-state tether (Fig. 5.15B,C), analogously to the analysis of three-state tethers presented above. Indeed, the obtained rates and distances to the transition state were comparable to those found for three-state hopping, corroborating the assumption that in tethers exhibiting two-state hopping the transition within one of the D'D3 domains is unaltered, whereas it is inhibited in the other D'D3 domain.

Currently, it can only be speculated what the reason for such an inhibition might be. Interestingly, occasionally tethers were observed that initially exhibited three-state hopping, but only two-state hopping at later stages of the measurement. This observation suggests that the inhibition of the transition in one D'D3 domain may result from a spontaneously occurring alteration in D'D3 that inhibits closing of the interaction. It is for instance conceivable that upon force-induced opening of the VWD3/C8-3/TIL3/E3 interface, Cys1099 and/or Cys1142 might be able to form non-native disulfide bonds that could disrupt the interface region, thereby

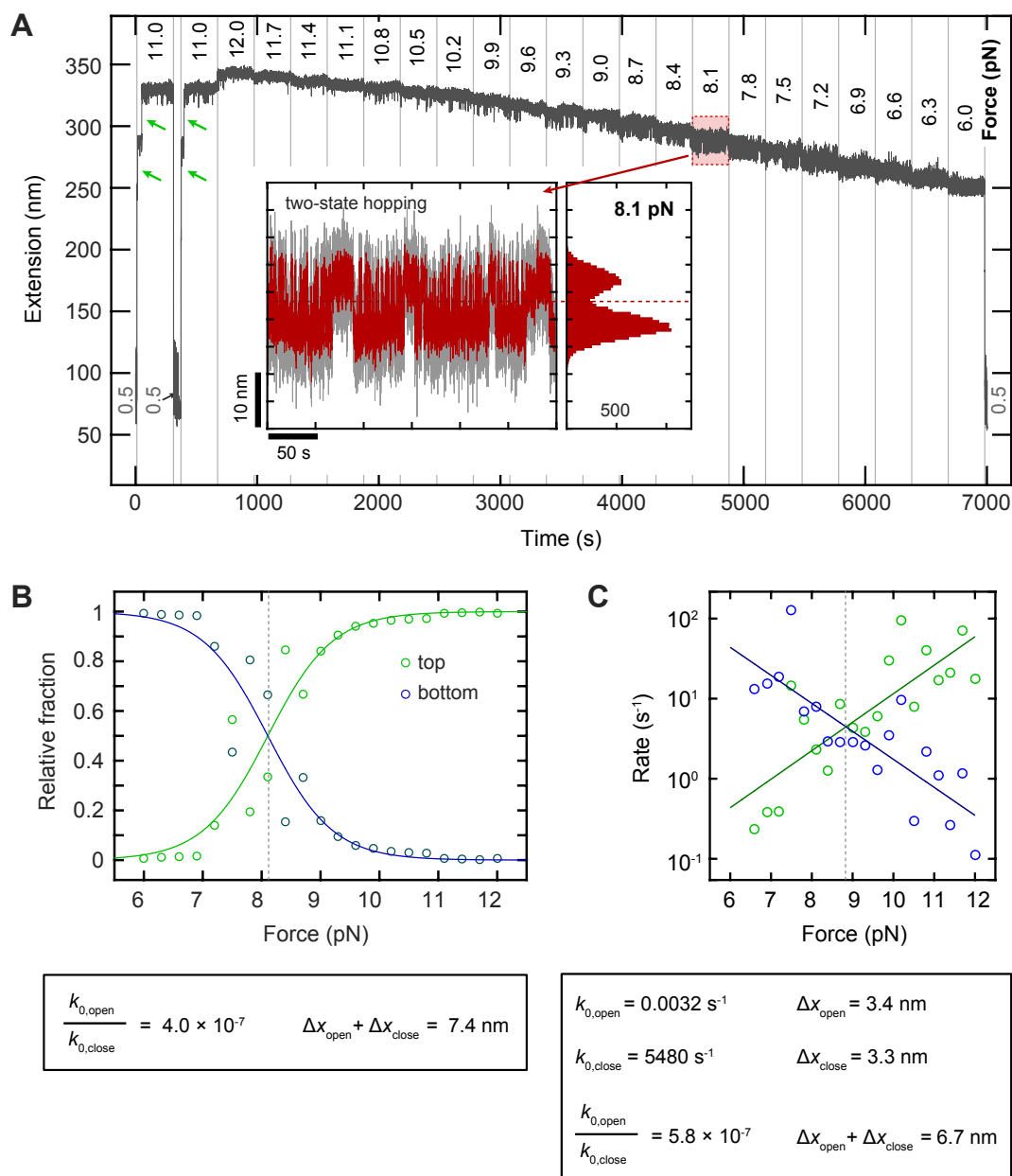


**Figure 5.15: Hopping between only two states.** (A) Extension vs. time trace of a full-length VWF dimer tether, subjected to the same measurement protocol as presented in Fig. 5.9, but exhibiting hopping between only two instead of three states, suggesting that the underlying transition only occurs in one of the two D'D3 domains. The inset shows the bimodal extension histogram obtained for the segment of the trace at 8.1 pN, close to the force at which opening and closing rates are expected to be equal. The dashed red line indicates the threshold between the two states used for analysis. The shown traces were subjected to 5-frame moving average smoothing. (B) Analysis of the relative populations of the two observed states, and fits (lines) under the assumption of a two-state model. (C) Opening and closing rates as a function of force, as determined from un-binned dwell time distributions, and fits (lines) of a single-barrier kinetic model. Importantly, the obtained thermodynamic parameters were found to be comparable to the ones obtained for tethers showing three-state hopping.

impairing its re-association.

### Impact of acidic pH and calcium chelation

The structure of D'D3 strongly suggests the stability of the interface between submodules VWD3, C8-3, TIL3, and E3 to be pH-dependent. The hypothesis that the hopping observed in the MT measurements results from opening and closing of this interface would consequently imply that pH changes are expected to have an impact on the hopping.

Repeated measurements on the same field of view, but under varied pH conditions, allowed to directly assess the effect of the pH. Fig. 5.16 shows the analysis of an exemplary tether that was first measured at the physiologic pH of 7.4 and subsequently, after buffer exchange, at pH 6.2, under identical ionic conditions. At pH 7.4, three-state hopping was observed as described in detail above (see Figs. 5.9, 5.13, and 5.14). At pH 6.2, in contrast, hopping was shifted to markedly lower forces, with the force at which opening and closing of the interaction are equally likely being reduced by  $\approx 25\%$ , as can be seen directly from the measurement trace and from the formal analysis (Fig. 5.16B,C). The observation that acidic pH shifts the hopping to lower forces is in line with the proposed destabilization of the VWD/C8-3/TIL3/E3 interface by loss of hydrogen bonds due to protonation of histidine residues [48]. The analysis based on the relative populations of the states revealed a marked decrease of the Gibbs free energy difference between the closed and open state at zero force from  $\approx 14.9 k_B T$  at pH 7.4 to  $\approx 7.3 k_B T$  at pH 6.2 (Fig. 5.16B).

In addition, at pH 6.2 the transitions between the states appeared to be less clear and to exhibit slightly reduced extension increments, resulting in significant overlapping of the peaks in the respective extension histograms (Fig. 5.16A). As a consequence, for further analysis the thresholds separating the different states had to be assigned manually. For these reasons, the rates obtained from the dwell time analysis are likely not fully confident. Nonetheless, for the sake of completeness it should be mentioned that also the pseudo dwell time analysis indicated a significant decrease of the Gibbs free energy difference between the closed and open state at zero force from  $\approx 14.6 k_B T$  at pH 7.4 to  $\approx 7.6 k_B T$  at pH 6.2 (Fig. 5.16C).

Importantly, I observed the destabilizing effect of acidic pH to be fully reversible, as inferred from a measurement conducted at pH 7.4 after a measurement at a low pH of 5.5. This observation would again be in line with the scenario in which the pH dependence is mediated by histidine residues in the interface.

Similarly, also the potential effect of divalent ions on the hopping can be assessed by performing measurements under different buffer conditions. Divalent ions may in principle be relevant for the hopping, as the crystal structure of D'D3 revealed calcium binding to the VWD3 submodule, which might stabilize VWD3 and thereby the interface. However, measurements in the absence of divalent ions and in the presence of 10 mM EDTA showed hopping at the same forces as in the presence of calcium (Fig. 5.17), contradicting a significant destabilization due to calcium chelation. It should however be noted that it cannot be entirely excluded that even in the presence of such high concentrations of EDTA, calcium might still be bound to VWD3 if its affinity for calcium is very high. Measurements in the presence of EDTA should therefore be repeated with longer incubation times before the measurement.

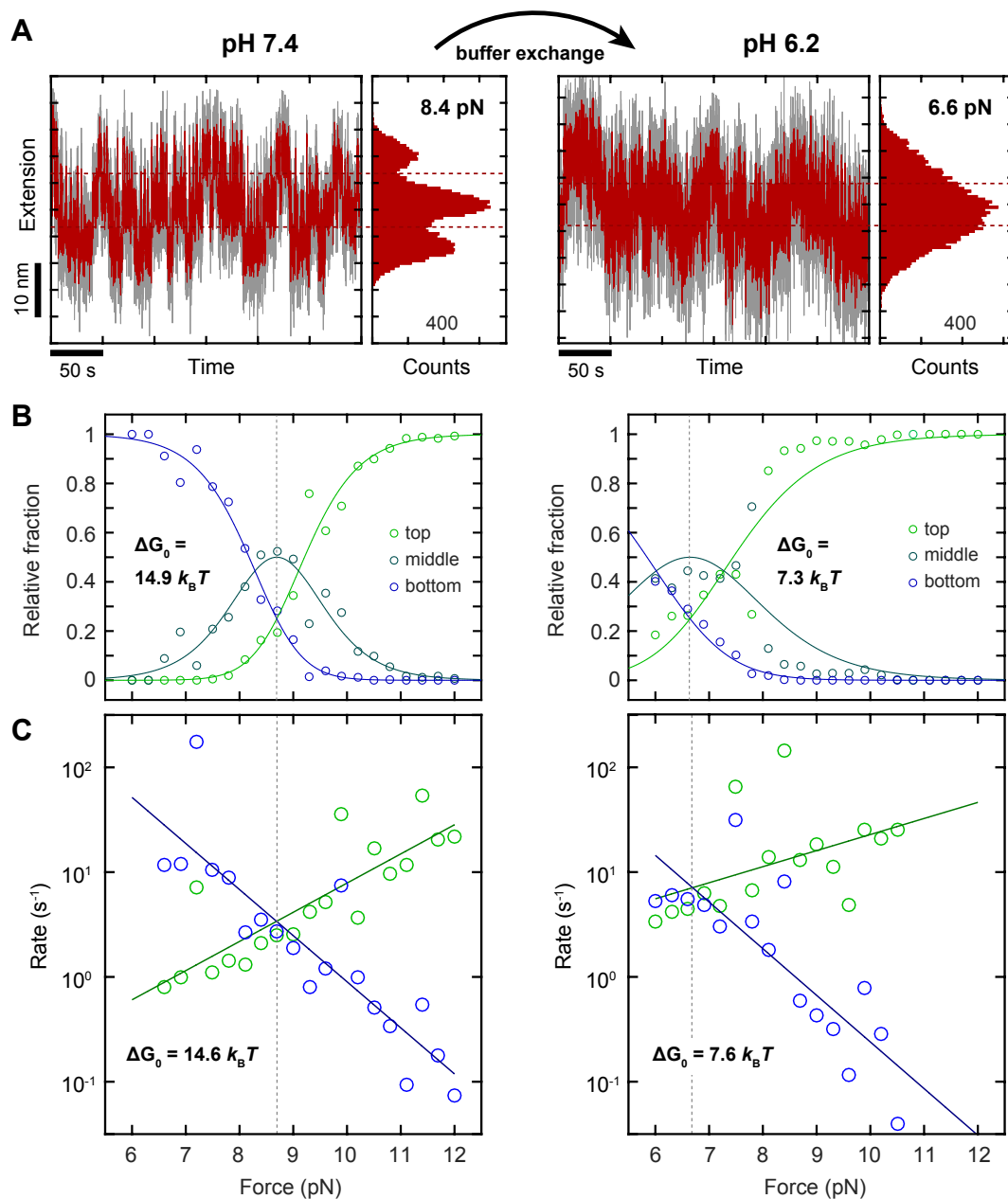


**Figure 5.16: Effect of acidic pH on hopping.** (A) Exemplary segments of a trace with respective extension histograms of the same bead, measured first at the physiologic pH of 7.4 (left) and, after buffer exchange, at pH 6.2 (right), under identical, near-physiologic ionic conditions. Shown is in each case a segment of the trace at a force close to the point at which opening and closing appeared to be equally likely. At pH 6.2, transitions between states appeared much less clearly and with slightly reduced extension, resulting in significant overlapping of the peaks in the histogram. As a consequence, thresholds between the states (dashed red lines) had to be assigned manually for analysis at pH 6.2. (B) Analysis of the relative populations of the three states, and fits (lines) analogous to the procedure presented in Fig. 5.13. (C) Opening and closing rates as a function of force, as determined from un-binned pseudo dwell time distributions, and fits (lines) of a single-barrier kinetic model. For both analyses, the obtained Gibbs free energy difference at zero force between the closed and open state was found to markedly decrease from pH 7.4 to pH 6.2. In line with this, the force at which the rates of opening and closing are equal (dashed gray lines) was considerably lower under acidic pH as compared to physiologic pH.

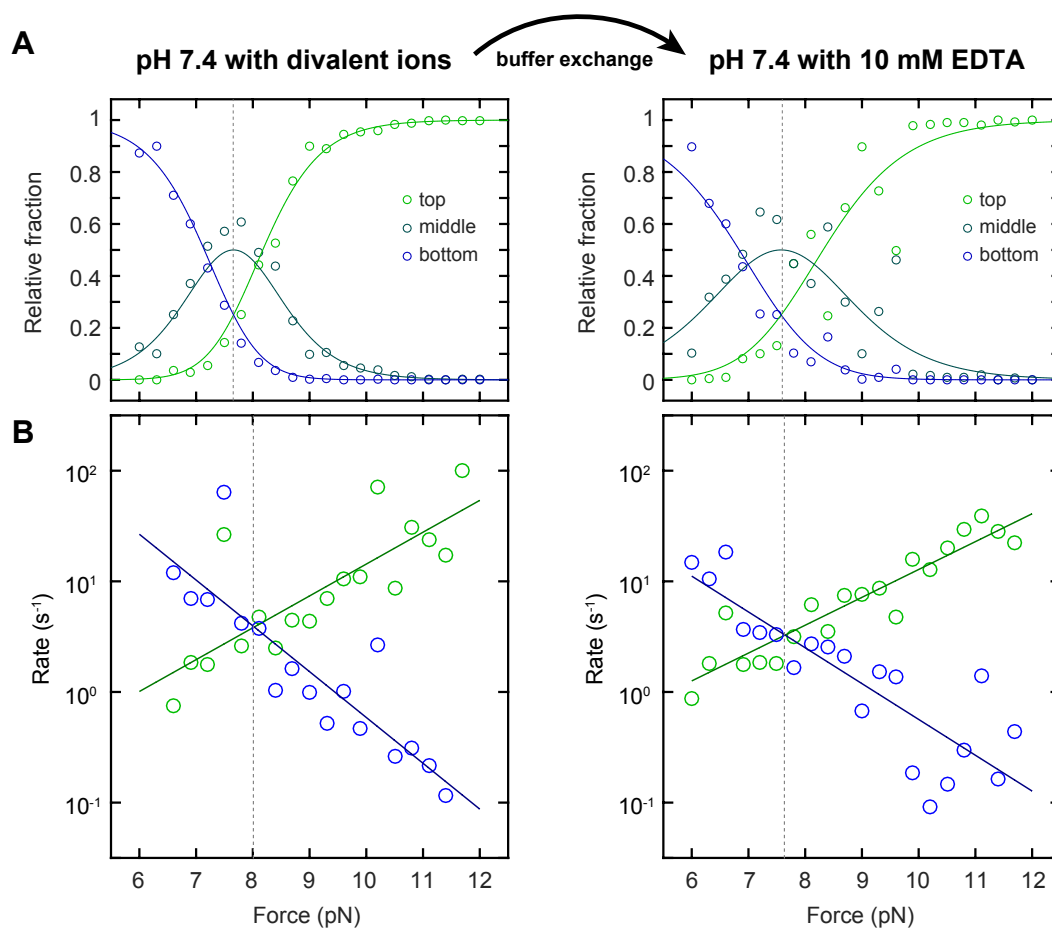


**Figure 5.17: Effect of calcium chelation on hopping.** (A) Analysis of the relative populations of the three states of hopping for the same bead, measured first at near-physiologic ionic conditions, *i.e.* in the presence of calcium (left), and, after buffer exchange, in the absence of calcium and with 10 mM EDTA (right). (B) Opening and closing rates as a function of force, as determined from un-binned pseudo dwell time distributions, and fits (lines) of a single-barrier kinetic model. For both analyses, the force at which the rates of opening and closing are equal (dashed gray lines) was found to be identical, within experimental error, for the two different ionic conditions, suggesting no significant destabilization due to calcium removal.

Taken together, the results presented in this section strongly suggest that the observed three-state hopping results from the opening and closing of a pH-dependent interface between the submodules VWD3, C8-3, TIL3, and E3 in the D'D3 domains that likely plays a regulatory role during VWF's biosynthesis. Experiments on a construct with insertion of an artificial linker between VWD3 and C8-3, as described above, could confirm this assumption in the near future. Furthermore, experiments on "inverted" dimers (Fig. 5.12), to probe D'D3 in its native conformation as present in mature VWF multimers *-i.e.* after dimerization with another D'D3 domain *via* disulfide bonds Cys1099-Cys1099' and Cys1142-Cys1142', will hopefully help to answer the open question if intra-domain interactions within D'D3 still play a regulatory role in mature VWF multimers, *e.g.* for factor VIII binding.



# Chapter 6

## Advancing multimer analysis of VWF by single-molecule AFM imaging

This chapter goes into a somewhat different direction and expands the focus from the level of single VWF dimers to multimers. The research project described in the following, which was performed in collaboration with researchers from the University Clinical Center Hamburg-Eppendorf and from the Asklepios Klinik Altona in Hamburg, aimed at elucidating mechanisms of VWF multimerization and of pathological multimerization defects. To this end, I introduced single-molecule AFM imaging as a tool for analyzing multimer size distributions of recombinant VWF samples and for directly visualizing non-native multimers occurring for VWF variants with disturbed multimerization. <sup>1</sup>

### 6.1 VWF multimer size distribution and multimerization defects

As discussed in chapter 1, large VWF multimers are hemostatically more active than smaller ones, as they experience higher hydrodynamic forces and are capable of multivalent binding [4, 11, 12, 43]. Consequently, a correct multimer size distribution is of utmost importance for ensuring normal function of VWF. For instance, mutations that alter the normal size distribution of VWF and result in reduction of large multimers can lead to the subtype 2A of von Willebrand Disease (VWD) [11, 12]. On the other hand, an excess of very large multimers, e.g. due to deficiency of the VWF-cleaving enzyme ADAMTS13, will result in hyperactivity of VWF and can cause excessive formation of blood clots in the microvasculature, such as in thrombotic thrombocytopenic purpura [83].

Linear multimers are assembled in the trans-Golgi exclusively from dimers –VWF’s smallest repeating subunits– which are linked via the disulfide bonds Cys1099-Cys1099’ and Cys1142-Cys1142’ between their N-terminal D’D3 assemblies [46] (Fig. 1.1), and mutations in this

---

<sup>1</sup>The work described in this chapter was published in similar form in *PLoS ONE*, vol. 14, no. 1, e0210963, 2019, as *Advancing multimer analysis of von Willebrand factor by single-molecule AFM imaging* by Achim Löff, Gesa König, Sonja Schneppenheim, Reinhard Schneppenheim, Martin Benoit, Jochen P. Müller, and Maria A. Brehm.

region can impair multimerization. In a recent study [203], which combined quantitative electrophoretic multimer analysis, fluorescence correlation spectroscopy, and total internal reflection fluorescence microscopy-based photobleaching, it was reported that the size distribution of VWF is exponential and may well result from a simple step-growth polymerization mechanism, where the number  $N$  of multimers of size  $i$  ( $i = 1$  representing a dimer), is given by the expression  $N(i) = N_1 \cdot p^{(i-1)}$ . Here,  $N(i)$  is a constant fitting parameter representing the number of dimers after multimerization, and  $p$  describes the extent of multimerization. Larger values of  $p$  are indicative of samples in which large multimers are more abundant. For mutant p.Cys1099Tyr, which impairs N-terminal linkage of dimers, an exponential size distribution was still observed, albeit with a lower extent of multimerization.

VWF's size distribution can also be affected by mutations in its C-terminal CK domain, as dimers are built in the ER from monomers that are linked in a tail-to-tail fashion via the three disulfide bonds Cys2771-Cys2773', Cys2773-Cys2771', and Cys2811-Cys2811' between their CK domains [44, 45, 202, 204] (Fig. 1.1). This dimerization process crucially involves protein disulfide isomerase A1 (PDIA1), as has been shown in a recent study that I was involved in before my PhD work [45]. An impaired dimerization in the ER results in a more complex multimerization process than the above-mentioned simple step-growth multimerization. When dimerization is disturbed, multimers are assembled from dimers as well as from monomers, giving rise to the occurrence of 'non-native' multimers that comprise monomeric subunits [205, 206]. Importantly, the N-terminal attachment of monomers to the ends of a multimer terminates its growth [11], as the resulting multimer ends on C-termini instead of N-termini. Thus, non-native multimers can be differentiated into 'odd-numbered' and 'even-numbered' ones, having a monomer attached to only one end and both ends, respectively. Odd-numbered multimers –*i.e.* multimers of sizes  $i = 1.5, 2.5, 3.5$ , and so forth– were, *inter alia*, reported for the VWD 2A/IIID mutants p.Cys2771Arg and p.Cys2773Arg [202, 205, 206]. The relevance of the bond Cys2811-Cys2811' was illustrated by the artificial mutation p.Cys2811Ala, which leads to the occurrence of odd-numbered multimers, albeit with an only minor reduction in the number and size of large multimers [45]. In line with the latter observation, this mutation has never been found in a patient with VWD [45]. As suggested by molecular dynamics (MD) simulations, the disulfide bond Cys2811-Cys2811' was predicted not to be structurally essential for dimerization, but to shield and protect the disulfides Cys2771-Cys2773' and Cys2773-Cys2771' from reduction, thus rendering dimerization irreversible [45]. This hypothesis implies that in the absence of the protective disulfide bond partial reopening of the bonds Cys2771-Cys2773' and Cys2773-Cys2771' can occur.

In order to gain deeper insights into the mechanisms of VWF multimerization and multimerization defects, and to overcome certain limitations of established methods of VWF multimer analysis, I aimed at directly visualizing the size distribution of recombinant VWF multimer samples, employing single-molecule AFM imaging. As presented in the following sections, the obtained results show excellent quantitative agreement with electrophoretic multimer analysis, which is the standard technique for multimer size distribution analysis and commonly used in diagnosis of VWD subtypes. Furthermore, investigating several mutants that exhibit disturbed multimerization, it could be demonstrated that AFM imaging can provide detailed insights into VWF processing and pathological defects at the single-molecule level that cannot be gained from electrophoretic multimer analysis alone. AFM imaging could hence aid conventional elec-

trophoretic multimer analysis as a complementary technique and provide a valuable research tool to elucidate the pathological mechanisms of a variety of VWD-related VWF variants.

## 6.2 Quantitative analysis of VWF multimer size distributions by AFM imaging

I first performed proof-of-principle AFM single-molecule imaging experiments with recombinant wtVWF and compared the results with those obtained by electrophoretic multimer analysis. To this end, wtVWF multimers were adsorbed onto a functionalized mica substrate (for details of sample preparation, see section 2.1) and imaged employing AFM (Fig. 6.1). Electrophoresis experiments were conducted by Sonja Schneppenheim and Ulrich Budde at the Asklepios Klinik Altona, and gels were analyzed quantitatively by Jochen P. Müller, LMU Munich (see section 2.1). From the AFM images, I directly determined the size distribution by counting the number  $N$  of molecules of multimer size  $i$ , where  $i = 1$  denotes a dimer,  $i = 2$  a tetramer, and so forth. The analysis of AFM images is described in detail in section 2.1 and in Fig. 6.3. I observed a distribution of multimer sizes that decayed in an approximately exponential fashion (Fig. 6.1Ci), in line with a recent study [203]. Due to the exponential decay and the chosen single-molecule approach, multimers of sizes  $i > 5$  were observed only occasionally in AFM images. I estimated the extent  $p$  of multimerization by fitting the expression  $N(i) = N_1 \cdot p^{(i-1)}$  to the data for multimer sizes up to  $i = 5$ , and obtained a value of  $0.43 \pm 0.11$  ( $\pm 1$  SD). This value is in excellent agreement with the value of  $0.47 \pm 0.03$  that was obtained by quantitative luminescence intensity profiling of wtVWF electrophoretic multimer analyses (Fig. 6.2A-B).

To test the capability of the AFM imaging approach to detect alterations in the size distribution, I further investigated the mutant p.Cys1099Tyr, which exhibits a well-described defect in multimerization [46, 203]. This mutation, which impairs the N-terminal linkage of dimers, had been shown to also result in an exponential size distribution, but with a steeper decay than observed for wtVWF, corresponding to a lower extent of multimerization [203]. I indeed observed an exponential size distribution shifted towards smaller values of  $i$  compared with wtVWF (Fig. 6.1Cii). A significantly lower value for  $p$  of  $0.21 \pm 0.07$  was obtained, again in good agreement with quantitative electrophoretic multimer analysis, which yielded  $p = 0.15 \pm 0.01$  (Fig. 6.2C). These data show that AFM imaging is an adequate method to determine the degree of VWF multimerization in a quantitative fashion.

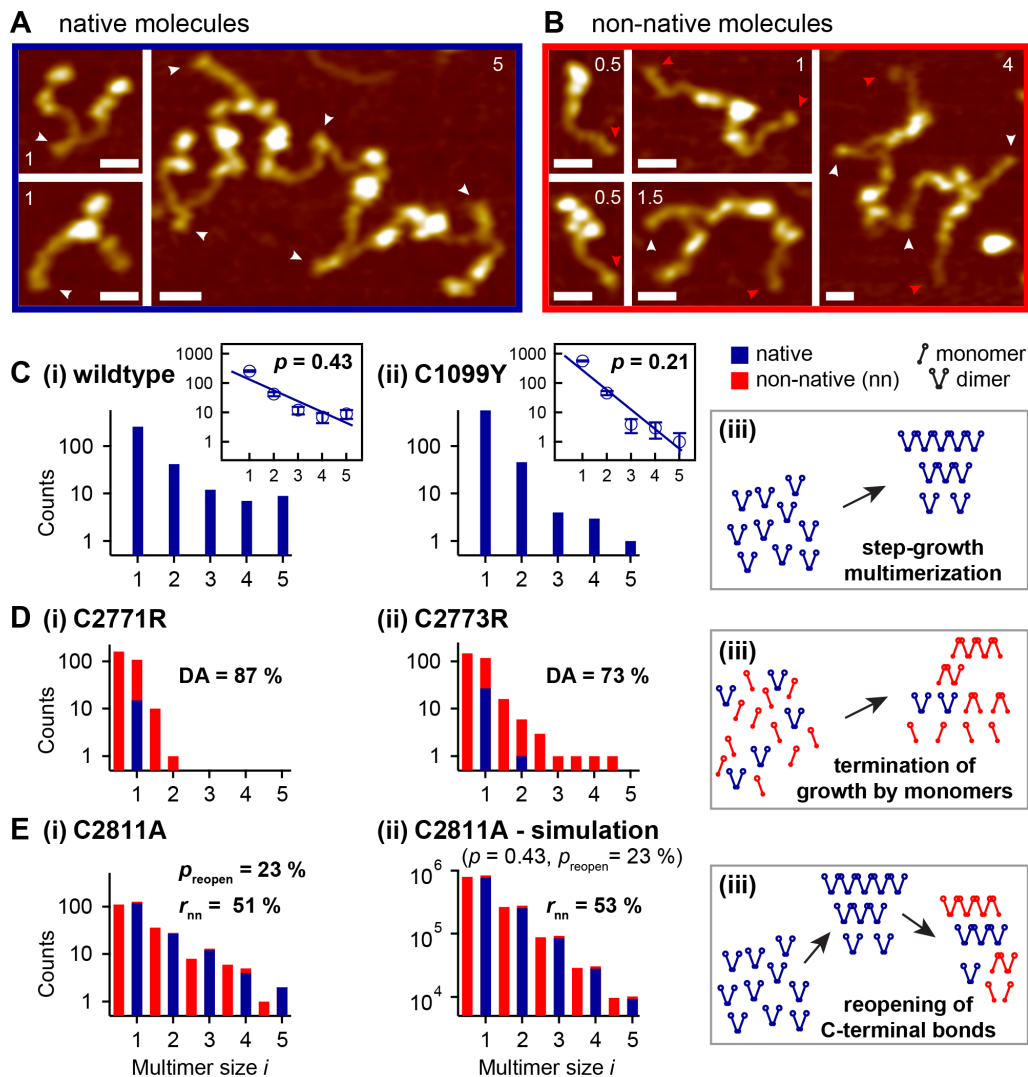


**Figure 6.1: Multimer analysis of wildtype and mutant VWF by AFM imaging of individual molecules.** (A, B) Representative AFM images of individual native (A) and non-native (B) VWF molecules. Numbers in images indicate the multimer size  $i$  ( $i = 1$  corresponds to a dimer). White arrowheads mark paired, red arrowheads unpaired CK domains. For more details on the identification of dimeric and monomeric building blocks within VWF molecules, see section 2.1 and Fig. 6.3. Scale bars represent 20 nm, range of color scale is 2.4 nm. (C) Size distributions of wtVWF (i) and mutant p.Cys1099Tyr (ii), and schematic of step-growth multimerization (iii). Insets in subpanels i and ii show linear fits to the data represented in logarithmic space, yielding values for the extent  $p$  of multimerization of 0.43 and 0.21, respectively. (D) Size distributions of VWF mutants p.Cys2771Arg (i) and p.Cys2773Arg (ii), and schematic of the underlying multimerization process (iii). Native and non-native molecules are depicted in blue and red, respectively. Non-native molecules end on a C-terminal CK domain (small, closed circle) at one or both termini, while native molecules end on N-terminal D'D3 assemblies (open circle). From the observed size distributions, values for the dimerization abolishment of 87 % and 73 % were determined for p.Cys2771Arg and p.Cys2773Arg, respectively. (Ei) Size distribution of VWF mutant p.Cys2811Ala, for which non-native molecules had been hypothesized to result from reopening of disulfide-linked CK domains. The overall ratio of non-native molecules was found to be 51 %. The (apparent) reopening probability was determined to be 23 %. (Eii) Size distribution (shown for  $i \leq 5$ ) obtained from a simulation that assumed multimers to initially follow an exponential size distribution –with  $p = 0.43$  as observed for wtVWF– and to afterwards reopen partially at their CK domains with the experimentally determined probability for p.Cys2811Ala. Simulations yielded, similarly to p.Cys2811Ala, a ratio of 53 % non-native molecules, and very low fractions of even-numbered non-native molecules. (Eiii) Schematic representation of the hypothesized scenario of initial wildtype-like step-growth multimerization and subsequent reopening of C-terminal disulfide bonds within constituent dimers. Figure as published in [42].

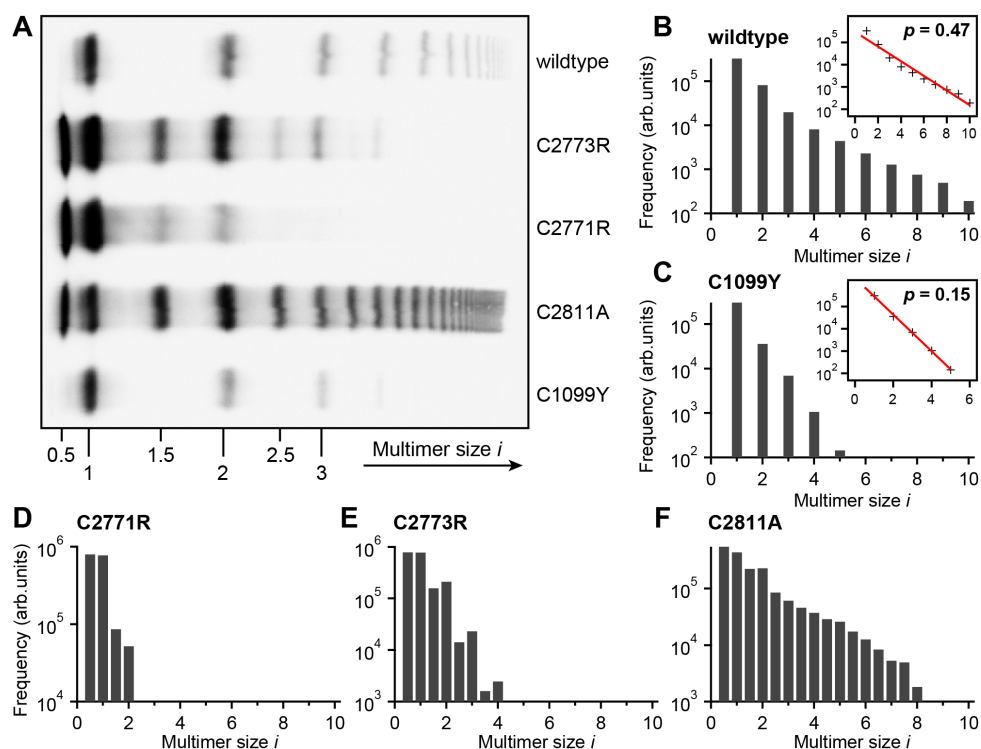


**Figure 6.2: Quantitative electrophoretic multimer analysis of wildtype and mutant VWF.** (A) High-resolution agarose gel of multimer samples. Numbers beneath bands indicate the multimer size  $i$  ( $i = 1$  corresponds to a dimer). (B-F) Frequencies of molecules of size  $i$ , as determined from the gel by quantitative luminescence intensity profiling (for more details, see section 2.1), for wtVWF (B) and mutants p.Cys1099Tyr (C), p.Cys2771Arg (D), p.Cys2773Arg (E), and p.Cys2811Ala (F). Insets in panels B and C show linear fits to the frequency data represented in logarithmic space, yielding values for the extent  $p$  of multimerization of 0.47 and 0.15 for wtVWF and mutant p.Cys1099Tyr, respectively. Figure as published in [42].

## 6.3 Insights into processing defects beyond conventional multimer analysis

### Cys2771 and Cys2773 are crucial for VWF dimerization

It has previously been reported that the mutants p.Cys2771Arg and p.Cys2773Arg exhibit disturbed dimerization [202, 205, 206]. Electrophoretic multimer analysis revealed that both of these mutations lead to the formation of multimers containing odd numbers of monomers ('odd-numbered multimers') and to a deficit of large multimers (Fig. 6.2D-E). While p.Cys2771Arg almost exclusively showed monomers and dimers, for p.Cys2773Arg multimers with sizes of up to  $i = 4$  were observed, including also odd-numbered molecules (*i.e.* molecules with sizes of  $i = 0.5, 1.5, 2.5,$  and  $3.5$ ; Fig. 6.2D-E). These data confirm the ability of p.Cys2773Arg to still form small multimers. I assessed the multimer size distribution of p.Cys2771Arg (Fig. 6.1Di) and p.Cys2773Arg (Fig. 6.1Dii) by AFM imaging and determined the number of both dimeric and monomeric building blocks incorporated into all observed VWF molecules. Fig. 6.3 illustrates the identification of monomers and dimers within multimers. The obtained size distributions were again in excellent agreement with those obtained by conventional, electrophoretic multimer analysis. For the mutant p.Cys2771Arg, I found  $96 \pm 6\%$  monomers ( $i = 0.5$ ) and dimers

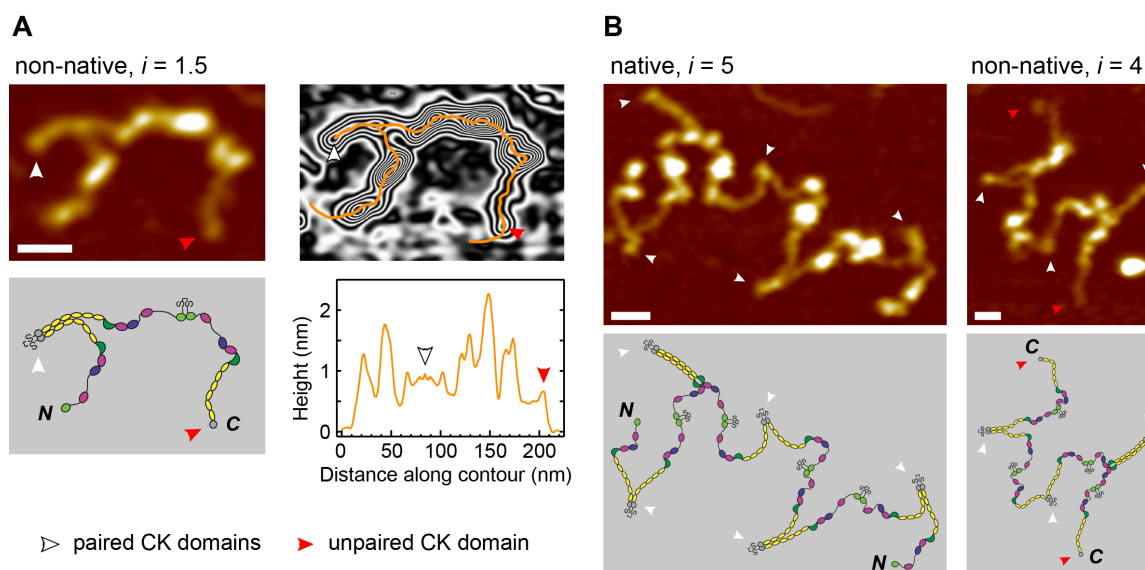


**Figure 6.3: Analysis of VWF multimers in AFM images.** (A) Identification of dimeric and monomeric building blocks within VWF molecules. Left: Exemplary image of an individual non-native VWF molecule of size  $i = 1.5$ , *i.e.* consisting of a dimer and an N-terminally attached monomer, with a schematic representation of the structure below. Scale bar represents 20 nm, range of color scale is 2.4 nm. Right: Height trace along the contour of the molecule (bottom), obtained by tracing the molecule from end to end, following local maxima in height (top). A clear height difference between lower C-terminal portions (C domains, yellow) and higher N-terminal domains is clearly visible. Due to the attachment of a single monomer, the molecule shown here ends on an N- and on a C-terminus, which exhibit markedly different heights. White arrowheads mark the paired –*i.e.* dimerized– CK domains of the dimeric building block, and red arrowheads mark the unpaired CK domain of the monomeric building block. Again, a clear height difference is observed. It should be noted that height tracing of molecules was, for the vast majority of analyzed molecules, not necessary for reliable identification of their dimeric and monomeric building blocks, as the characteristic pattern of alternating higher and lower portions of VWF is also directly visible from the color scale. (B) Further exemplary images of VWF multimers with schematic structures shown below for illustration. Left: native molecule of size  $i = 5$ , *i.e.* consisting of five dimers and thus ending on two N-termini. Right: non-native molecule of size  $i = 4$ , *i.e.* consisting of three dimers and two N-terminally attached monomers, thus ending on two C-termini. White and red arrowheads mark paired and unpaired CK domains, respectively. Scale bars represent 20 nm, range of color scale is 2.4 nm. Figure as published as supporting information to [42].

( $i = 1$ ), and only rarely trimers ( $i = 1.5$ ) and tetramers ( $i = 2$ ). The mutant p.Cys2773Arg exhibited all the multimer sizes that were observed in the electrophoretic multimer analysis. However, in AFM imaging, the observed maximum multimer size was  $i = 4.5$ , *i.e.* one unit larger than in electrophoretic multimer analysis. This finding shows that AFM imaging, as a single-molecule technique, is in principle capable of detecting rare multimer species, which –due to the luminescence intensity detection limit– are not visible in electrophoretic multimer analysis.

A tremendous advantage of AFM imaging over electrophoretic multimer analysis is the possibility to distinguish native multimers from non-native even-numbered ( $i = 1, 2, 3$ , and so forth) multimers of the same size, *i.e.*, from multimers that exhibit a monomeric building block at both ends (Fig. 6.1A-B,Diii). For instance, AFM imaging can resolve the structural difference between C- and N-terminally linked dimers, while in electrophoretic analysis C- and N-terminally linked dimers are hidden in the same band. In other words, AFM imaging

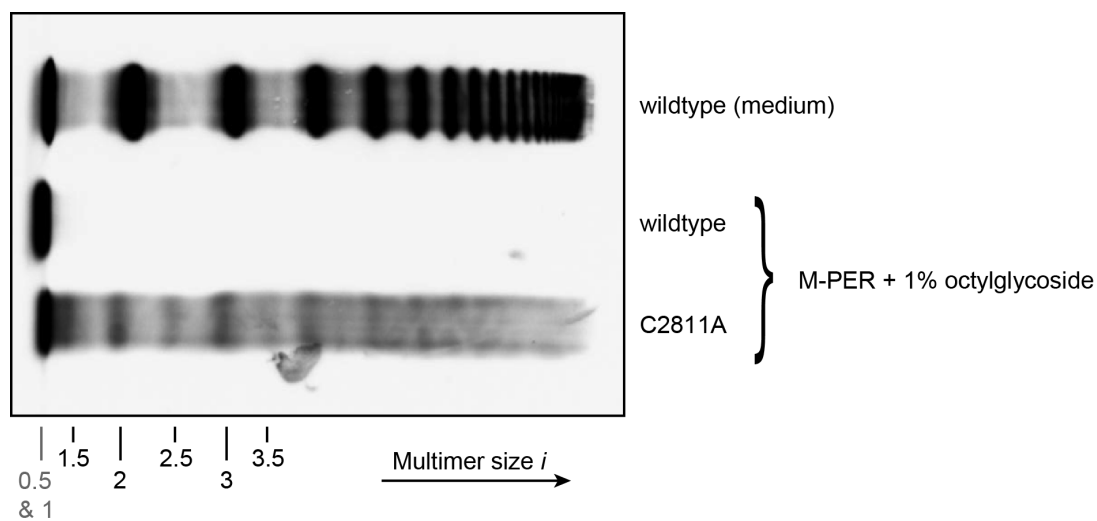


**Figure 6.4: Stability of pseudo-WPBs in HEK-293 cells expressing wtVWF or mutant p.Cys2811Ala.** HEK293 cells stably overexpressing wtVWF (middle lane) or mutant p.Cys2811Ala (bottom lane) were lysed using M-PER lysis buffer containing 1% (w/v) octylglycoside. The lysates were analyzed by electrophoretic multimer analysis. As size reference, wtVWF secreted into the medium is shown (top lane). Cell lysis experiments were conducted by Gesa König (UKE Hamburg). Figure as published in [42].

allows for counting non-native dimers and multimers individually. Analysis showed that for p.Cys2771Arg, only  $14 \pm 4\%$  of the observed dimers are native, *i.e.* linked C-terminally (Fig 6.1Di, note the logarithmic scale). For the mutant p.Cys2773Arg, this ratio was found to be  $23 \pm 5\%$ . The observed difference between the two mutants goes hand in hand with the previous observation that the latter mutant is still able to form small multimers [45, 206], as more native dimers are available for multimer formation. I further quantified the degree of dimerization abolishment (DA) –*i.e.* the fraction of all monomers that are not C-terminally dimerized (*cf.* section 2.1)– and found DA values of  $87 \pm 5\%$  and  $73 \pm 4\%$  for p.Cys2771Arg and p.Cys2773Arg, respectively. Taken together, these data confirm that both cysteines, Cys2771 and Cys2773, are essential for dimerization. Cys2771 appears to be slightly more important, in the sense that the investigated mutation of this cysteine results in a more pronounced loss of dimerization than the mutation of Cys2773, indicating that the absence of Cys2771 cannot be compensated significantly by alternative disulfide bonds. At least partial compensation is however possible in the absence of Cys2773.

In addition, it is noteworthy that the AFM data indicate an approximately equal probability for the N-terminal attachment of dimers and monomers to an assembling VWF molecule during multimerization. I separately determined the fractions of dimeric and monomeric building blocks N-terminally linked to at least one other building block and observed no significant difference between these fractions for p.Cys2771Arg ( $42 \pm 13\%$  and  $55 \pm 4\%$ , respectively), or for p.Cys2773Arg ( $60 \pm 10\%$  and  $60 \pm 4\%$ , respectively).

### Cys2811 plays a secondary role in VWF dimerization

To also investigate the impact of loss of the third cysteine involved in dimerization, Cys2811, I imaged the mutant p.Cys2811Ala, which is unable to form disulfide bond Cys2811-Cys2811' [45] (Fig. 6.1Ei). Approximately one-half of all molecules were observed to be non-native

(rate of non-native molecules:  $r_{\text{nn}} = 51 \pm 4\%$ ), and  $33 \pm 3\%$  of all molecules were isolated monomers. The overall size distribution, however, exhibited an only minor shift towards smaller values of  $i$  compared with wtVWF, in line with observations from electrophoretic multimer analysis (Fig. 6.2F). AFM imaging further revealed a fraction of  $93 \pm 9\%$  native dimers and only  $7 \pm 2\%$  N-terminally linked, non-native dimers (Fig. 6.1Ei), showing that disulfide bond Cys2811-Cys2811' is not crucial for formation of native dimers. Also for larger even-numbered multimers, *i.e.* for tetramers ( $i = 2$ ), hexamers ( $i = 3$ ) and so forth, only a very low fraction of non-native molecules was observed. These findings suggest that Cys2811 is structurally less important than Cys2771 and Cys2773 and plays a secondary role in dimerization.

The observed size distribution can be explained by a scenario in which mutation of Cys2811 directly, but only moderately, impairs dimerization via disulfide bonds Cys2771-Cys2773' and Cys2773-Cys2771' in the ER, *e.g.* by inducing structural changes in the CK domain. In this scenario, multimers would be assembled from both dimeric and monomeric building blocks, entirely analogous to the mechanism of mutants p.Cys2771Arg and p.Cys2773Arg described above, but with a markedly lower degree of DA of  $23 \pm 3\%$ . However, based on MD simulations, it has recently been postulated that disulfide bond Cys2811-Cys2811' is not structurally essential for dimerization, but rather serves to shield and protect the disulfides Cys2771-Cys2773' and Cys2773-Cys2771' from reduction, thus rendering dimerization irreversible [45]. This hypothesis implies that in the absence of the protective disulfide bond Cys2811-Cys2811' the other two bonds (Cys2771-Cys2773' and Cys2773-Cys2771') may undergo partial reopening. To test compatibility of the AFM data with the hypothesis that reopening of C-terminal disulfide bonds can occur, an extreme scenario was assumed in which initially wildtype-like formation of exclusively native, *i.e.* C-terminally linked, dimers takes place, which would then undergo normal multimerization. After multimerization, multimers would break up randomly between CK-domains of constituent monomers, yielding non-native multimers (Fig. 6.1Eiii). In this scenario, all apparent monomeric building blocks observed in the measurements would have originated from the reopening of dimeric building blocks. Under this assumption, I determined the probability  $p_{\text{reopen}}$  for the reopening of a dimeric building block from the data, and obtained a value of  $p_{\text{reopen}} = 23 \pm 3\%$ . Then, simple simulations were performed *in silico* (Fig. 6.1Eii). To this end, an initial exponential size distribution of multimers with an extent of multimerization of  $p = 0.43$ , *i.e.* with the value that was obtained experimentally for wtVWF, and with a large  $N_1$  of  $10^6$ , was constructed. In the next step, each C-terminal dimerization site within multimers, *i.e.* each pair of disulfide-linked CK domains, was broken with an equal probability of  $p_{\text{reopen}} = 23 \pm 3\%$ . The resulting size distribution very closely matched the experimentally observed one. In particular, the overall ratio of non-native molecules was found to be  $r_{\text{nn}} = 53\%$ , agreeing excellently with the ratio of 51% that was determined experimentally. Moreover, the fractions of even-numbered non-native molecules were closely reproduced, *e.g.*, 8% non-native dimers, compared with 7% found in the experiment. The simulations thus show that the experimental data obtained in the absence of disulfide bond Cys2811-Cys2811' are compatible with the proposed scenario involving reopening of C-terminal disulfide bonds after dimerization.

It should further be noted that also a situation combining the two different scenarios described above, *i.e.* a situation in which dimerization of monomers and reopening of dimers occur in parallel already in the ER, could result in the same final size distribution after multimerization. Thus, definite discrimination between these possibilities is not possible by the AFM imaging

data alone and will likely require elaborate *in vivo* measurements. A third scenario, in which C-terminal degradation occurs extracellularly, could be excluded by cell lysis experiments, which were conducted by Gesa König at the University Clinical Center Hamburg-Eppendorf. To investigate if odd-numbered multimers already exist intracellularly, HEK-293 cells stably overexpressing wtVWF or mutant p.Cys2811Ala were lysed using M-PER lysis buffer containing 1 % (w/v) octylglycoside (Fig. 6.4). For cells expressing mutant p.Cys2811Ala, this treatment resulted in lysis of pseudo-Weibel-Palade bodies (pseudo-WPBs), and the cell lysate exhibited all multimer sizes, including non-native multimers, as seen in electrophoretic multimer analysis (bottom lane). Cell lysate of cells expressing wtVWF did not exhibit multimers (middle lane), indicating that pseudo-WPBs containing wtVWF cannot be disrupted under identical conditions.

## 6.4 Discussion and conclusion

In the work described in the previous sections, I introduced the use of single-molecule AFM imaging as a research tool to characterize the size distribution of VWF multimers. I used recombinant VWF expressed in HEK-293 cells, which do not intrinsically possess WPBs, but form pseudo-WPBs induced by expression of VWF. Although WPBs and pseudo-WPBs most likely are not identical in their composition, HEK-293 cells have been shown to produce multimer size distributions that very closely match those found in plasma samples [207], and therefore are a commonly used cell line for recombinant VWF production (*e.g.*: [208–210]). The usage of recombinant protein has a couple of advantages: 1) VWF is secreted into the serum-free medium of choice, making complex purification protocols unnecessary. 2) Absence of ADAMTS13 provides uncleaved VWF samples. 3) Patients are not burdened with voluminous blood draws, which would be necessary for complex purification protocols to yield plasma VWF of high enough purity for imaging. 4) The expression of VWF variants in HEK-293 cells reproduces their homozygous state. Although it is clinically much less common than the heterozygous state, it can be analyzed more straight-forwardly and helped to gain deeper insights into how the different mutations disturb VWF processing. 5) If necessary, reproduction of the heterozygous state is also possible by co-expression of wildtype and variant VWF, and good agreement between the size distribution of heterozygous recombinant multimers and respective patient plasma samples has been reported [207].

Thus, while I do not see immediate application of the presented approach as a diagnostic tool for analysis of patient samples, AFM imaging is an excellent research tool to better comprehend the processing defects of VWD-related VWF variants and the molecular mechanisms underlying certain VWD subtypes.

The utility of this AFM imaging approach was demonstrated by showing that it can provide quantitative insights into VWF processing defects that go beyond the results of conventional multimer analysis. To verify the validity of the imaging approach, I first investigated wtVWF and the mutant p.Cys1099Tyr, which impairs N-terminal disulfide-linkage between dimers [46, 203]. The results obtained from AFM imaging were in very good agreement with data from quantitative electrophoretic multimer analysis and fully consistent with results from an earlier study that had employed a combination of quantitative electrophoretic multimer analysis, fluorescence correlation spectroscopy, and total internal reflection fluorescence microscopy-based photobleaching for investigating multimer size distributions [203]. These findings show

consistency between AFM imaging and the established method of multimer analysis by electrophoresis and prove the capability of AFM imaging to detect multimerization defects of VWF. It should however be pointed out that a quantitative multimer analysis by AFM imaging is limited to rather small multimer sizes due to two different aspects. First, –much like for established methods of multimer analysis– the exponentially decaying size distribution of VWF limits the throughput at high multimer sizes. Since large multimers are much less frequent than smaller ones, reliable statistics can, with reasonable effort, only be collected from AFM images for smaller multimers ( $i \leq 5$  here). However, larger multimers are still fairly commonly observed, which would allow for detection of structural anomalies that might potentiate in larger multimers. For variant p.Cys2811Ala, for instance, nine molecules with sizes of  $i > 5$  were observed, of which four had sizes of  $i > 10$ . Also in these larger multimers I was able to identify processing defects and to distinguish native (five) from non-native (four) multimers. Second, the unambiguous identification of a multimer's dimeric or monomeric subunits becomes increasingly complicated for increasing multimer size due to possible self-overlaps or close colocalization with other molecules.

It is worth noting that the exponential size distributions observed both for wtVWF and mutant p.Cys1099Tyr are fully in line with a step-growth multimerization process with dimers as sole building blocks (Fig. 6.1Ciii). In contrast, for the mutants p.Cys2771Arg and p.Cys2773Arg, which lead to a marked dimerization abolishment [44, 45, 205, 206], multimers are assembled from two different building blocks –dimeric and monomeric ones– by N-terminal linkage [202], implying a compromised multimerization process: the growth of a multimer is terminated by the attachment of monomers via the D'D3 assembly [11], resulting in the formation of non-native multimers and a severe lack of large multimers (Fig. 6.1Diii).

The direct visualization of multimeric VWF samples by AFM imaging proved to be a powerful approach for multimer analysis, complementary to the established method of SDS-agarose gel electrophoresis, where after size separation and blotting multimer bands are typically detected using anti-VWF antibodies and visualization by luminescence [117, 118]. As AFM imaging can directly visualize monomeric and dimeric building blocks of VWF, both individually and as constituents of multimers, the imaging approach chosen in this study is capable of providing additional and quantitative information that cannot be gained from electrophoretic analysis. In particular, AFM imaging does not only allow for identifying odd-numbered non-native molecules, but also for distinguishing between native and even-numbered non-native molecules of the same size  $i$ , for instance between dimers that are linked C-terminally and N-terminally, respectively. The latter discrimination is not directly possible by electrophoretic multimer analysis, as native and non-native molecules of the same size  $i$  are located in the same band in a gel. In principle, information about N- or C-terminal linkage could be obtained by preceding proteolysis of mutant VWF using ADAMTS13, which would result in different proteolytic fragments. However, these fragments would again have to be analyzed by Western blotting, making quantitative analysis difficult. In contrast, AFM imaging allowed to directly quantify how many native dimers can still be formed by the mutants p.Cys2771Arg, p.Cys2773Arg, and p.Cys2811Ala. The data I obtained confirm the severe inhibiting effects on dimerization –and consequently multimerization– of the first two mutations, and show that mutation p.Cys2771Arg affects dimerization more severely than p.Cys2773Arg (Figs. 6.1D and 6.2D-E, and [202]). The fact that 13 % and 27 % of all monomers are still C-terminally dimer-

ized for p.Cys2771Arg and p.Cys2773Arg, respectively, suggests that occasionally alternative disulfide bonds such as Cys2773-Cys2773' or Cys2771-Cys2771' can be formed [45, 202]. The lower rate of C-terminal dimerization of p.Cys2771Arg compared with p.Cys2773Arg may be explained by a higher degree of structural change within the CK domain in case of a mutation of Cys2771 than for a mutation of Cys2773. This assumption is supported by previously published structure modeling and MD simulations [202].

Whereas Cys2771 and Cys2773 were confirmed to be crucial for C-terminal dimerization, significant formation of C-terminally linked, native dimers can still occur in the absence of Cys2811, as observed for mutant p.Cys2811Ala. Consequently, an only minor overall shift to smaller values of  $i$  compared with wtVWF was found for this mutant. The large fraction of C-terminally linked monomers (77 % ; DA = 23 %) indicates that mutation p.Cys2811Ala does not severely inhibit the formation of the dimerizing bonds Cys2771-Cys2773' and Cys2773-Cys2771', indicating that Cys2811 is structurally less important for dimerization, and suggesting a different role for disulfide bond Cys2811-Cys2811'. For instance, it might render dimerization irreversible by shielding the other two disulfides from reduction [45]. As corroborated by simple simulations, the AFM data on p.Cys2811Ala are consistent with such a scenario in which the absence of disulfide bond Cys2811-Cys2811' still allows normal dimerization via disulfide bonds Cys2771-Cys2773' and Cys2773-Cys2771', but results in subsequent partial reopening of these bonds (Fig. 6.1Eiii). It appears plausible that such reopening might already occur in the ER, where VWF monomers are dimerized by PDIA1 [45], an enzyme that is not only able to form but also to reduce disulfide bonds. In other words, lack of disulfide bond Cys2811-Cys2811' would, in this scenario, shift the equilibrium towards increased reduction of disulfides Cys2771-Cys2773' and Cys2773-Cys2771'. Reopening might potentially also occur at the acidic pH values encountered during tubulation of VWF [4, 211], as disulfide reduction has been shown to be possible at the acidic pH of endosomes [212] (pH = 5-5.5) [213]. Since in cell lysis experiments pseudo-WPBs containing p.Cys2811Ala were observed to be less stable than pseudo-WPBs containing wtVWF, it might be possible that Cys2771-Cys2773' and Cys2773-Cys2771' are reduced during tubulation, leading to a less compact packing. However, as described before, the size distribution observed for mutant p.Cys2811Ala could also result from a scenario in which the lack of Cys2811 directly, but only moderately, impairs formation of disulfide bonds Cys2771-Cys2773' and Cys2773-Cys2771' –e.g. due to slight structural changes within the CK domain induced by mutation of Cys2811–, without reopening of formed disulfides. Discrimination between these possibilities may be facilitated in the future by more sophisticated *in vivo* measurements or by new insights from structural studies or MD simulations.

Put succinctly, the AFM imaging data on selected VWF mutants are fully in line with the recently proposed picture of VWF dimerization: Cys2771 and Cys2773 are the essential starting points of dimerization and bonds Cys2771-Cys2773' and Cys2773-Cys2771' are the structural bonds that connect CK domains of monomers. A loss of Cys2771 has a more severe effect than a loss of Cys2773, indicating that an alternative bond Cys2773-Cys2773' is formed less readily than Cys2771-Cys2771'. Cys2811 in contrast appears to play a secondary role in dimerization, as loss of Cys2811 still allows for significant formation of native dimers and consequently larger multimers. From a more methodological point of view, it was shown that AFM imaging is a powerful approach to assess the size distribution of VWF, which can help to gain a quantitative understanding of the processes involved in VWF's multimerization and in multimerization

defects at the single-molecule level. In particular, direct visualization of individual molecules by AFM imaging enables detection of structurally anomalous molecules, even if they are indistinguishable from native molecules in electrophoretic multimer analysis. In the future, AFM imaging may therefore aid electrophoretic multimer analysis as a complementary method to better comprehend the pathological mechanisms of elusive VWF variants, especially in cases where subtle structural differences are expected to play a role.

## Summary, conclusions, and outlook

In the framework of this thesis, different approaches were employed to study the mechanical response and the conformational ensemble of VWF at the single-molecule level, and to thus elucidate and characterize intramolecular interactions and conformational transitions underlying the force-regulation of VWF's hemostatic activity. Investigating the mechanical response of VWF in the physiologically relevant low force regime ( $\lesssim 10$  pN) and, in particular, under constant force was of special interest, as these conditions likely resemble the physiological case of prolonged exposure of a multimer to force when subjected to increased elongational flow at sites of vascular injury [4, 7, 21].

### **Multiplexed protein force spectroscopy at low and constant forces**

In this regard, a key technical achievement in the framework of this thesis was the development and validation of a versatile, modular approach for protein force spectroscopy in MT that enables precise and stable long-term measurements at constant forces and on dozens of single molecules in parallel. In particular, this approach extends protein force spectroscopy into the regime of very low forces down to  $\lesssim 1$  pN. As the employed protein attachment strategy, which makes use of unstructured polypeptide linkers, does not require major protein modification, it can be expected to be applicable to a very wide range of proteins and to also be of use for other parallel single-molecule techniques such as centrifugal or acoustic force spectroscopy. Given ongoing improvements in camera technology, the number of molecules that can be measured in parallel will presumably increase at least one order of magnitude in the near future.

The characteristic three-state folding and unfolding of ddFLN4 served as model system for validation of the MT assay. The MT measurements on ddFLN4 at constant force were in excellent agreement with previous AFM-based constant pulling speed experiments and confirmed the existence of a low-loading rate pathway for unfolding [194]. Also in the context of validation and optimization of the MT assay, it was shown that the lifetime of the biotin–streptavidin interaction, which is ubiquitously used in a variety of biological, chemical, biophysical, and pharmaceutical applications, strongly depends on the pulling geometry. A tested monovalent streptavidin variant was found to provide extremely high force stability, making it an attractive approach for force spectroscopy –or other assays– on systems that are subjected to high forces over extended periods of time. In the future, the force and also chemical stability of the MT

assay could in principle be enhanced even further by replacing the biotin–streptavidin bond between protein of interest and magnetic bead with a covalent linkage.

### Regulatory intramolecular interactions and transitions in VWF dimers

The first project of this thesis, building on previous work conducted before my doctoral studies, aimed at investigating the impact of the pH on the large-scale structure and overall mechanical resistance of VWF dimers by employing a combination of AFM-based single-molecule force spectroscopy and AFM imaging. It could be shown that both the structure and the mechanics of VWF dimers –and thus, in all probability, of multimers– are critically influenced by multiple pH-dependent interactions with opposite trends. Most prominently, the recently discovered strong intermonomer interaction [20], which crucially involves the D4 domain and induces a firmly closed conformation of dimers, was observed with highest frequency at pH 7.4 –being present in approximately one-half of all dimers–, but was essentially absent at pH values below 6.8. However, below pH 6.8, the fraction of compact dimers increased with decreasing pH, in line with a previous transmission electron microscopy study [47]. These findings indicated that the compactness of dimers at pH values below 6.8 is promoted by other interactions in the C-terminal stem region of VWF dimers that possess low mechanical resistance compared with the strong intermonomer interaction. By investigating deletion constructs, it was found that compactness under acidic conditions is primarily mediated by the D4 domain, *i.e.* remarkably by the same domain that also mediates the strong intermonomer interaction. In addition, further mechanically very weak interactions between C domains, occurring not only at acidic, but also at physiologic pH, could be inferred from the AFM imaging data.

Notably, as these findings suggest that VWF has its highest mechanical resistance at physiological pH, local deviations from the physiological pH, which might occur at sites of vascular injury, may represent a means to promote activation of VWF for its hemostatic function exactly where needed. The higher initial compactness at acidic pH can be assumed to be a prerequisite for orderly multimerization of VWF in the trans-Golgi and for storage in Weibel-Palade bodies [47, 54].

More detailed insights into different force-induced conformational transitions within VWF were gained by MT force measurements on VWF dimers. Regarding the strong D4-mediated interaction, the MT experiments at constant force revealed dissociation of this interaction to occur in the same force range as unfolding of A2 domains (at  $\lesssim 10$  pN), in contrast to AFM-based force measurements conducted with (very likely unphysiologically) high force loading rates, which had shown dissociation at considerably higher forces than A2 unfolding. This finding not only suggests a marked force loading rate dependence of the D4-mediated strong interaction, but also implicates a central role of the interaction in VWF's force-induced elongation: its dissociation at physiologically relevant forces will release a considerable length from previously firmly closed dimers and thus, due to the positive feedback between (effective) multimer length and hydrodynamic force, markedly increase the force acting on the multimer.

Unfolding of A2 domains as another force-induced transition that provides a significant length increase was also studied and characterized in detail. Notably, A2 unfolding can not only be expected to represent a central step in VWF's elongation and thus activation, but is also the prerequisite for down-regulation of VWF by enzymatic cleavage. The MT measurements

in particular allowed to resolve the previously controversial impact of  $\text{Ca}^{2+}$  binding to A2 on the kinetics of both unfolding and refolding of A2. While calcium only slightly, but clearly, stabilizes A2 against unfolding, it markedly (up to 20-fold) speeds up refolding. These findings help to better comprehend the remarkable connection between activation and down-regulation of VWF, and to elucidate the pathological mechanisms of mutations in A2 associated with VWD.

The first specific step of VWF's activation cascade likely is the dissociation of weak interactions in the C-terminal stem of dimers that are not firmly closed by the strong D4-mediated interaction. The MT measurements allowed to directly probe such transitions in the stem, which had previously only been inferred indirectly from imaging results, at very low forces of  $\approx 1$  pN. The observed fast and reversible transitions with multiple intermediate states are in line with a zipper-like opening and closing of the stems with several pairs of interacting C domains. However, reliably assigning the interactions and dissecting the contributions of the different C domains will require further measurements, *e.g.* on deletion constructs. Of special interest will be measurements under acidic pH conditions, as these are expected to stabilize C-domain interactions. Moreover, certain clinically relevant variants with mutations in C domains may exhibit altered stem dynamics. Regarding data analysis, a Hidden Markov Model approach may help to more reliably identify the number of intermediate states.

An unexpected finding was the discovery of a previously unknown intradomain transition within VWF's N-terminal D'D3 domains, which manifested in the MT traces as rather fast hopping between distinct states at forces around  $\approx 8$  pN, *i.e.* remarkably also in the physiologically relevant force range of A2 unfolding. A very recent crystal structure of D'D3 [48], which was only published after the measurements presented in this thesis were already finished, suggests the observed transition to originate from dissociation (and re-association) of an interaction between the C-terminal submodules VWD3, C8-3, TIL3, and E3 of the large D'D3 assembly. To verify this hypothesis, measurements on a construct with insertion of an artificial linker, which would increase the observed length increments of the transition in the experiment, are planned. In addition, steered molecular dynamics simulations could help to determine the expected extension increments for the opening of this interaction and to compare them with the experimental observations. As the interaction shields two cysteine residues involved in N-terminal multimerization of VWF, and as it is expected to be pH-dependent, it is thought to play a regulatory role during VWF's pH-guided biosynthesis [48]. The expected pH dependence is in line with a considerable destabilization of the interaction at acidic pH observed in the MT experiments. An important open question is if this interaction is only relevant in the monomeric D'D3 domain during biosynthesis, or if similar force-sensitive interactions are still present in mature VWF after linkage of D'D3 to another D'D3 domain of the neighboring dimer. To address this issue, measurements on "inverted" VWF dimer constructs are planned, in which the two monomers are natively linked between their D'D3 domains and can be pulled from their non-dimerized C termini.

Finally, it is noteworthy that no further prominent features, *e.g.* corresponding to dissociation of autoinhibitory interactions between the A1 domain and neighboring domains, were observed in the MT measurements, suggesting that such interactions likely dissociate already at low forces during early stages of VWF's force-induced elongation.

### VWF multimer size distribution and multimerization defects

Going into a somewhat different direction, one part of this thesis expanded the focus from the level of dimeric subunits of VWF to full multimers and showed the benefit of single-molecule AFM imaging for studying VWF's multimer size distribution and, in particular, pathological multimerization defects. The size distribution of VWF multimers is of utmost importance for VWF's physiological function, since multimers of different sizes significantly differ in their hemostatic activity, both due to the differences in the encountered hydrodynamic forces and due to avidity effects associated with multivalent binding. Results obtained by direct visualization of wtVWF were in excellent quantitative agreement with previous studies and confirmed an exponential size distribution of VWF multimers in line with a simple step-growth multimerization process with dimers as sole building blocks [203]. The strength of the AFM imaging approach lies in its ability to identify structural anomalies arising from certain mutations. For instance, for clinical VWF variants with dimerization defects, the approach allowed to directly identify non-native molecules that also comprise non-dimerized monomers, including multimer species that cannot be distinguished by the established standard method of electrophoretic multimer analysis. Thus, the AFM imaging approach enables thorough quantification of the impact of dimerization or multimerization defects, and could provide a valuable research tool to elucidate the pathological mechanisms of a variety of VWF variants associated with VWD. So far, the imaging approach has only been used on recombinant VWF samples and not on samples acquired from patient blood. While in principle AFM imaging of VWF could in the future also be helpful for diagnostic purposes, this would require improved purification protocols to achieve samples of high enough quality for single-molecule visualization.

### Conclusion

To conclude, molecular mechanisms underlying the remarkable force sensing of VWF –*i.e.* the ability to convert changes in the hydrodynamic flow into a physiological response– were characterized at the single-molecule level, both by directly probing force-induced transitions at physiologically relevant forces and by investigating the conformational ensemble of VWF's dimeric subunits.

Based on the presented data, force-induced elongation of VWF multimers, which is critical for their activation, can be assumed to involve three main transitions. Dissociation of weak interactions in C-terminal stems, which likely tune VWF's initial force sensitivity, already at low forces can be expected to represent the first specific step of elongation. Unfolding of A2 domains and dissociation of the D4-mediated intermonomer interaction presumably occur in the same force range and both provide a considerable length increase. Due to the positive feedback between length and hydrodynamic force, an increased length will result in increased force acting on the multimer. Elongation can hence be expected to proceed rapidly in a cascade-like fashion once sufficient forces for a first significant length increase are reached, provided that the multimer cannot rapidly relax. In this context, elevated elongational flow at sites of vascular injury helps to facilitate activation of VWF where needed by suppressing tumbling and relaxation of the multimer. Vascular injury may further go along with local changes of the pH, which based on the findings of this thesis may represent a second means of promoting activation of VWF precisely where needed, by lowering the mechanical resistance of dimers.

Taken together, the presented results help to comprehend how VWF's extraordinary force response is "built-in" into its molecular architecture, and thus contribute to a better understanding of VWF's physiological function in hemostasis as well as of its pathological dysfunctions.



# Bibliography

- [1] E. M. Puchner and H. E. Gaub, “Single-Molecule Mechanoenzymatics”, *Annual Review of Biophysics*, vol. 41, no. 1, pp. 497–518, 2012.
- [2] V. Vogel, “Mechanotransduction involving multimodular proteins: converting force into biochemical signals.”, *Annual review of biophysics and biomolecular structure*, vol. 35, no. 1, pp. 459–88, 2006.
- [3] T. A. Springer, “Biology and physics of von Willebrand factor concatamers.”, *Journal of thrombosis and haemostasis*, vol. 9 Suppl 1, pp. 130–143, 2011.
- [4] T. A. Springer, “Von Willebrand factor, Jedi knight of the bloodstream”, *Blood*, vol. 124, no. 9, pp. 1412–1426, 2014.
- [5] S. W. Schneider, S Nuschele, A Wixforth, *et al.*, “Shear-induced unfolding triggers adhesion of von Willebrand factor fibers.”, *Proceedings of the National Academy of Sciences*, vol. 104, no. 19, pp. 7899–7903, 2007.
- [6] J. A. Odell and A. Keller, “Flow-induced chain fracture of isolated linear macromolecules in solution”, *Journal of Polymer Science Part B: Polymer Physics*, vol. 24, no. 9, pp. 1889–1916, 1986.
- [7] X. Zhang, K. Halvorsen, C.-Z. Zhang, *et al.*, “Mechanoenzymatic Cleavage of the Ultralarge Vascular Protein von Willebrand Factor”, *Science*, vol. 324, pp. 1330–1334, 2009.
- [8] Z. M. Ruggeri and G. L. Mendolicchio, “Adhesion mechanisms in platelet function”, *Circulation Research*, vol. 100, no. 12, pp. 1673–1685, 2007.
- [9] S. P. Jackson, “The growing complexity of platelet aggregation”, *Blood*, vol. 109, no. 12, pp. 5087–5095, 2008.
- [10] W. S. Nesbitt, E. Westein, F. J. Tovar-Lopez, *et al.*, “A shear gradient–dependent platelet aggregation mechanism drives thrombus formation”, *Nature Medicine*, vol. 15, no. 6, pp. 665–673, 2009.
- [11] J. E. Sadler, U Budde, J. C. J. Eikenboom, *et al.*, “Update on the pathophysiology and classification of von Willebrand disease: a report of the Subcommittee on von Willebrand Factor.”, *Journal of thrombosis and haemostasis : JTH*, vol. 4, no. 10, pp. 2103–14, 2006.
- [12] J. E. Sadler, “Biochemistry and Genetics of Von Willebrand Factor”, *Biochemistry*, vol. 67, pp. 395–424, 1998.
- [13] J. E. Sadler, “New Concepts in Von Willebrand Disease”, *Annual Review of Medicine*, vol. 56, no. 1, pp. 173–191, 2005.
- [14] M. Takahashi, A. Yamashita, S. Moriguchi-Goto, *et al.*, “Critical role of von Willebrand factor and platelet interaction in venous thromboembolism.”, *Histology and histopathology*, vol. 24, no. 11, pp. 1391–8, 2009.

- [15] C. Kleinschnitz, S. F. De Meyer, T. Schwarz, *et al.*, “Deficiency of von Willebrand factor protects mice from ischemic stroke.”, *Blood*, vol. 113, no. 15, pp. 3600–3, 2009.
- [16] B. Nieswandt and G. Stoll, “The smaller, the better: VWF in stroke.”, *Blood*, vol. 115, no. 8, pp. 1477–8, 2010.
- [17] H. Fu, Y. Jiang, D. Yang, *et al.*, “Flow-induced elongation of von Willebrand factor precedes tension-dependent activation”, *Nature Communications*, vol. 8, p. 324, 2017.
- [18] J. Kim, C.-Z. Zhang, X. Zhang, *et al.*, “A mechanically stabilized receptor–ligand flex-bond important in the vasculature”, *Nature*, vol. 466, no. 7309, pp. 992–995, 2010.
- [19] J. Kim, N. E. Hudson, and T. A. Springer, “Force-induced on-rate switching and modulation by mutations in gain-of-function von Willebrand diseases”, *Proceedings of the National Academy of Sciences*, vol. 112, no. 15, pp. 4648–4653, 2015.
- [20] J. Müller, S. Mielke, A. Löf, *et al.*, “Force Sensing by the Vascular Protein von Willebrand Factor is Tuned by a Strong Intermonomer Interaction”, *Proceedings of the National Academy of Sciences*, vol. 113, no. 5, pp. 1208–1213, 2016.
- [21] C. E. Sing and A. Alexander-Katz, “Elongational flow induces the unfolding of von Willebrand factor at physiological flow rates”, *Biophysical Journal*, vol. 98, no. 9, pp. L35–L37, 2010.
- [22] T. T. Perkins, D. E. Smith, and S. Chu, “Single polymer dynamics in an elongational flow.”, *Science*, vol. 276, no. 5321, pp. 2016–21, 1997.
- [23] D. N. Ku, “Blood Flow in Arteries”, *Annual Review of Fluid Mechanics*, vol. 29, pp. 399–434, 1997.
- [24] D. E. Smith, H. P. Babcock, and S. Chu, “Single Polymer Dynamics in steady shear flow”, *Science*, vol. 283, pp. 1724–1727, 1999.
- [25] V. Huck, M. F. Schneider, C. Gorzelanny, *et al.*, “The various states of von Willebrand factor and their function in physiology and pathophysiology”, *Thrombosis and Haemostasis*, vol. 111, no. 4, pp. 598–609, 2014.
- [26] V. Babich, L. Knipe, L. Hewlett, *et al.*, “Differential effect of extracellular acidosis on the release and dispersal of soluble and membrane proteins secreted from the Weibel-Palade body.”, *The Journal of biological chemistry*, vol. 284, no. 18, pp. 12 459–68, 2009.
- [27] Z. M. Ruggeri, J. N. Orje, R. Habermann, *et al.*, “Activation-Independent Platelet Adhesion and Aggregation under Elevated Shear Stress”, *Blood*, vol. 108, no. 6, pp. 1903–1911, 2006.
- [28] B. Bennett, O. D. Ratnoff, and J. Levin, “Immunologic studies in von Willebrand’s disease. Evidence that the antihemophilic factor (AHF) produced after transfusions lacks an antigen associated with normal AHF and the inactive material produced by patients with classic hemophilia.”, *The Journal of clinical investigation*, vol. 51, no. 10, pp. 2597–601, 1972.
- [29] R. D. Starke, F. Ferraro, K. E. Paschalaki, *et al.*, “Endothelial von Willebrand factor regulates angiogenesis.”, *Blood*, vol. 117, no. 3, pp. 1071–80, 2011.

- [30] J. M. Bosmans, M. M. Kockx, C. J. Vrints, *et al.*, “Fibrin(ogen) and von Willebrand Factor Deposition Are Associated With Intimal Thickening After Balloon Angioplasty of the Rabbit Carotid Artery”, *Arteriosclerosis, Thrombosis, and Vascular Biology*, vol. 17, no. 4, pp. 634–645, 1997.
- [31] F. Qin, T. Impeduglia, P. Schaffer, *et al.*, “Overexpression of von Willebrand factor is an independent risk factor for pathogenesis of intimal hyperplasia: Preliminary studies”, *Journal of Vascular Surgery*, vol. 37, no. 2, pp. 433–439, 2003.
- [32] M. Baud’huin, L. Duplomb, S. Téletchéa, *et al.*, “Factor VIII-von Willebrand factor complex inhibits osteoclastogenesis and controls cell survival.”, *The Journal of biological chemistry*, vol. 284, no. 46, pp. 31 704–13, 2009.
- [33] A. Bernardo, C. Ball, L. Nolasco, *et al.*, “Platelets adhered to endothelial cell-bound ultra-large von Willebrand factor strings support leukocyte tethering and rolling under high shear stress”, *Journal of Thrombosis and Haemostasis*, vol. 3, no. 3, pp. 562–570, 2005.
- [34] C. V. Denis, P. André, S. Saffaripour, *et al.*, “Defect in regulated secretion of P-selectin affects leukocyte recruitment in von Willebrand factor-deficient mice.”, *Proceedings of the National Academy of Sciences*, vol. 98, no. 7, pp. 4072–7, 2001.
- [35] B. Petri, A. Broermann, H. Li, *et al.*, “von Willebrand factor promotes leukocyte extravasation.”, *Blood*, vol. 116, no. 22, pp. 4712–9, 2010.
- [36] S. Grassle, V. Huck, K. I. Pappelbaum, *et al.*, “von Willebrand Factor Directly Interacts With DNA From Neutrophil Extracellular Traps”, *Arteriosclerosis, Thrombosis, and Vascular Biology*, vol. 34, no. 7, pp. 1382–1389, 2014.
- [37] S. Shahbazi, P. J. Lenting, C. Fribourg, *et al.*, “Characterization of the interaction between von Willebrand factor and osteoprotegerin”, *Journal of Thrombosis and Haemostasis*, vol. 5, no. 9, pp. 1956–1962, 2007.
- [38] R. Schneppenheim and U. Budde, “von Willebrand factor: the complex molecular genetics of a multidomain and multifunctional protein”, *Journal of Thrombosis and Haemostasis*, vol. 9, pp. 209–215, 2011.
- [39] A. O. Spiel, J. C. Gilbert, and B. Jilma, “Von Willebrand Factor in Cardiovascular Disease”, *Circulation*, vol. 117, no. 11, pp. 1449–1459, 2008.
- [40] B.-Q. Zhao, A. K. Chauhan, M. Canault, *et al.*, “von Willebrand factor-cleaving protease ADAMTS13 reduces ischemic brain injury in experimental stroke.”, *Blood*, vol. 114, no. 15, pp. 3329–34, 2009.
- [41] Y. F. Zhou, E. T. Eng, J. Zhu, *et al.*, “Sequence and structure relationships within von Willebrand factor”, *Blood*, vol. 120, no. 2, pp. 449–458, 2012.
- [42] A. Löf, G. König, S. Schneppenheim, *et al.*, “Advancing multimer analysis of von Willebrand factor by single-molecule AFM imaging”, *PLOS ONE*, vol. 14, no. 1, e0210963, 2019.
- [43] D. D. Wagner, “Cell Biology of Von Willebrand Factor”, *Annu. Rev. Cell Biol.*, vol. 6, pp. 217–246, 1990.

- [44] Y. F. Zhou and T. A. Springer, “Highly reinforced structure of a C-terminal dimerization domain in von Willebrand factor”, *Blood*, vol. 123, no. 12, pp. 1785–1793, 2014.
- [45] S. Lippok, K. Kolšek, A. Löf, *et al.*, “von Willebrand factor is dimerized by protein disulfide isomerase”, *Blood*, vol. 127, no. 9, pp. 1183–1191, 2016.
- [46] A. R. Purvis, J. Gross, L. T. Dang, *et al.*, “Two Cys residues essential for von Willebrand factor multimer assembly in the Golgi.”, *Proceedings of the National Academy of Sciences*, vol. 104, no. 40, pp. 15 647–15 652, 2007.
- [47] Y.-F. Zhou, E. T. Eng, N. Nishida, *et al.*, “A pH-regulated dimeric bouquet in the structure of von Willebrand factor.”, *The EMBO journal*, vol. 30, no. 19, pp. 4098–111, 2011.
- [48] X. Dong, N. C. Leksa, E. S. Chhabra, *et al.*, “The von Willebrand factor D’D3 assembly and structural principles for factor VIII binding and concatemer biogenesis.”, *Blood*, blood–2018–10–876300, 2019.
- [49] J. Emsley, M. Cruz, R. Handin, *et al.*, “Crystal structure of the von Willebrand Factor A1 domain and implications for the binding of platelet glycoprotein Ib.”, *The Journal of biological chemistry*, vol. 273, no. 17, pp. 10 396–401, 1998.
- [50] Q. Zhang, Y.-F. Zhou, C.-Z. Zhang, *et al.*, “Structural specializations of A2, a force-sensing domain in the ultralarge vascular protein von Willebrand factor”, *Proceedings of the National Academy of Sciences*, vol. 106, no. 23, pp. 9226–9231, 2009.
- [51] M. Zhou, X. Dong, C. Baldauf, *et al.*, “A novel calcium-binding site of von Willebrand factor A2 domain regulates its cleavage by ADAMTS13.”, *Blood*, vol. 117, no. 17, pp. 4623–31, 2011.
- [52] J. Bienkowska, M. Cruz, A. Atiemo, *et al.*, “The von Willebrand factor A3 domain does not contain a metal ion-dependent adhesion site motif”, *J Biol Chem*, vol. 272, no. 40, pp. 25 162–25 167, 1997.
- [53] E.-R. Xu, S. von Bülow, P.-C. Chen, *et al.*, “Structure and dynamics of the platelet integrin-binding C4 domain of von Willebrand factor.”, *Blood*, vol. 133, no. 4, pp. 366–376, 2019.
- [54] R.-H. Huang, Y. Wang, R. Roth, *et al.*, “Assembly of Weibel-Palade body-like tubules from N-terminal domains of von Willebrand factor.”, *Proceedings of the National Academy of Sciences*, vol. 105, no. 2, pp. 482–7, 2008.
- [55] N. Shiltagh, J. Kirkpatrick, L. D. Cabrita, *et al.*, “Solution structure of the major factor VIII binding region on von Willebrand factor.”, *Blood*, vol. 123, no. 26, pp. 4143–51, 2014.
- [56] A. J. Xu and T. A. Springer, “Calcium stabilizes the von Willebrand factor A2 domain by promoting refolding”, *Proceedings of the National Academy of Sciences*, vol. 109, no. 10, pp. 3742–3747, 2012.
- [57] H. M. Tsai, “Physiologic cleavage of von Willebrand factor by a plasma protease is dependent on its conformation and requires calcium ion.”, *Blood*, vol. 87, no. 10, pp. 4235–44, 1996.
- [58] C. Baldauf, R. Schneppenheim, W. Stacklies, *et al.*, “Shear-induced unfolding activates von Willebrand factor A2 domain for proteolysis”, *Journal of Thrombosis and Haemostasis*, vol. 7, no. 12, pp. 2096–2105, 2009.

- [59] R. a. Romijn, B Bouma, W Wuyster, *et al.*, “Identification of the collagen-binding site of the von Willebrand factor A3-domain.”, *The Journal of biological chemistry*, vol. 276, no. 13, pp. 9985–91, 2001.
- [60] R. A. Romijn, E. Westein, B. Bouma, *et al.*, “Mapping the Collagen-binding Site in the von Willebrand Factor-A3 Domain”, *Journal of Biological Chemistry*, vol. 278, no. 17, pp. 15 035–15 039, 2003.
- [61] E. G. Huizinga, R Martijn van der Plas, J Kroon, *et al.*, “Crystal structure of the A3 domain of human von Willebrand factor: implications for collagen binding.”, *Structure*, vol. 5, pp. 1147–1156, 1997.
- [62] M. Erent, A. Meli, N. Moiso, *et al.*, “Rate, extent and concentration dependence of histamine-evoked Weibel-Palade body exocytosis determined from individual fusion events in human endothelial cells”, *The Journal of Physiology*, vol. 583, no. 1, pp. 195–212, 2007.
- [63] L. T. Dang, A. R. Purvis, R.-H. Huang, *et al.*, “Phylogenetic and Functional Analysis of Histidine Residues Essential for pH-dependent Multimerization of von Willebrand Factor”, *Journal of Biological Chemistry*, vol. 286, no. 29, pp. 25 763–25 769, 2011.
- [64] A. Fulcher, Z. Ruggeri, and T. Zimmermann, “Isoelectric focusing of human von Willebrand factor in urea-agarose gels”, *Blood*, vol. 61, no. 2, pp. 304–310, 1983.
- [65] M. Lopes da Silva and D. F. Cutler, “Von Willebrand factor multimerization and the polarity of secretory pathways in endothelial cells”, *Blood*, vol. 128, no. 2, pp. 277–285, 2016.
- [66] W. E. Fowler, L. J. Fretto, K. K. Hamilton, *et al.*, “Substructure of human von Willebrand factor.”, *The Journal of clinical investigation*, vol. 76, no. 4, pp. 1491–500, 1985.
- [67] D. Katanov, G. Gompper, and D. A. Fedosov, “Microvascular blood flow resistance: Role of red blood cell migration and dispersion”, *Microvascular Research*, vol. 99, pp. 57–66, 2015.
- [68] L. Lanotte, J. Mauer, S. Mendez, *et al.*, “Red cells’ dynamic morphologies govern blood shear thinning under microcirculatory flow conditions”, *Proceedings of the National Academy of Sciences*, vol. 113, no. 47, pp. 13 289–13 294, 2016.
- [69] K. Rack, V. Huck, M. Hoore, *et al.*, “Margination and stretching of von Willebrand factor in the blood stream enable adhesion”, *Scientific Reports*, vol. 7, no. 1, p. 14 278, 2017.
- [70] T. W. Liu, “Flexible polymer chain dynamics and rheological properties in steady flows”, *The Journal of Chemical Physics*, vol. 90, no. 10, pp. 5826–5842, 1989.
- [71] H. Shankaran and S. Neelamegham, “Hydrodynamic Forces Applied on Intercellular Bonds, Soluble Molecules, and Cell-Surface Receptors”, *Biophysical Journal*, vol. 86, no. 1, pp. 576–588, 2004.
- [72] A. Alexander-Katz, M. F. Schneider, S. W. Schneider, *et al.*, “Shear-flow-induced unfolding of polymeric globules”, *Physical Review Letters*, vol. 97, no. 13, p. 138 101, 2006.
- [73] P. J. Lenting, C. Casari, O. D. Christophe, *et al.*, “von Willebrand factor: the old, the new and the unknown”, *Journal of Thrombosis and Haemostasis*, vol. 10, no. 12, pp. 2428–2437, 2012.

- [74] V. Vicente, P. J. Kostel, and Z. M. Ruggeri, "Isolation and functional characterization of the von Willebrand factor-binding domain located between residues His1-Arg293 of the alpha-chain of glycoprotein Ib.", *The Journal of biological chemistry*, vol. 263, no. 34, pp. 18 473–9, 1988.
- [75] Y. Fujimura, K. Titani, L. Z. Holland, *et al.*, "von Willebrand factor. A reduced and alkylated 52/48-kDa fragment beginning at amino acid residue 449 contains the domain interacting with platelet glycoprotein Ib.", *The Journal of biological chemistry*, vol. 261, no. 1, pp. 381–5, 1986.
- [76] E. F. Plow, M. D. Pierschbacher, E Ruoslahti, *et al.*, "The effect of Arg-Gly-Asp-containing peptides on fibrinogen and von Willebrand factor binding to platelets.", *Proceedings of the National Academy of Sciences*, vol. 82, no. 23, pp. 8057–61, 1985.
- [77] W. G. Owen and R. H. Wagner, "Antihemophilic factor: separation of an active fragment following dissociation by salts or detergents.", *Thrombosis et diathesis haemorrhagica*, vol. 27, no. 3, pp. 502–15, 1972.
- [78] B. Savage, E. Saldívar, and Z. M. Ruggeri, "Initiation of Platelet Adhesion by Arrest onto Fibrinogen or Translocation on von Willebrand Factor", *Cell*, vol. 84, no. 2, pp. 289–297, 1996.
- [79] J.-F. Dong, J. L. Moake, L. Nolasco, *et al.*, "ADAMTS-13 rapidly cleaves newly secreted ultralarge von Willebrand factor multimers on the endothelial surface under flowing conditions", *Blood*, vol. 100, no. 12, pp. 4033–9, 2002.
- [80] M. J. Mourik, J. A. Valentijn, J. Voorberg, *et al.*, "von Willebrand factor remodeling during exocytosis from vascular endothelial cells", *Journal of Thrombosis and Haemostasis*, vol. 11, no. 11, pp. 2009–2019, 2013.
- [81] J. W. Wang, J. A. Valentijn, K. M. Valentijn, *et al.*, "Formation of platelet-binding von Willebrand factor strings on non-endothelial cells", *Journal of Thrombosis and Haemostasis*, vol. 10, no. 10, pp. 2168–2178, 2012.
- [82] A. J. Xu and T. A. Springer, "Mechanisms by which von Willebrand Disease Mutations Destabilize the A2 Domain", *Journal of Biological Chemistry*, vol. 288, no. 9, pp. 6317–6324, 2013.
- [83] J. L. Moake, C. K. Rudy, J. H. Troll, *et al.*, "Unusually Large Plasma Factor VIII: von Willebrand Factor Multimers in Chronic Relapsing Thrombotic Thrombocytopenic Purpura", *New England Journal of Medicine*, vol. 307, no. 23, pp. 1432–1435, 1982.
- [84] A. Löf, J. P. Müller, and M. A. Brehm, "A biophysical view on von Willebrand factor activation", *Journal of Cellular Physiology*, vol. 233, pp. 799–810, 2018.
- [85] M. De Luca, D. A. Facey, E. J. Favaloro, *et al.*, "Structure and function of the von Willebrand factor A1 domain: analysis with monoclonal antibodies reveals distinct binding sites involved in recognition of the platelet membrane glycoprotein Ib-IX-V complex and ristocetin-dependent activation.", *Blood*, vol. 95, no. 1, pp. 164–172, 2000.
- [86] J. F. Dong, M. C. Berndt, A. Schade, *et al.*, "Ristocetin-dependent, but not botrocetin-dependent, binding of von Willebrand factor to the platelet glycoprotein Ib-IX-V complex correlates with shear-dependent interactions", *Blood*, vol. 97, no. 1, pp. 162–168, 2001.

- [87] M. A. Howard and B. G. Firkin, "Ristocetin – a new tool in the investigation of platelet aggregation.", *Thrombosis et diathesis haemorrhagica*, vol. 26, no. 2, pp. 362–9, 1971.
- [88] K. Fukuda, T. Doggett, I. J. Laurenzi, *et al.*, "The snake venom protein botrocetin acts as a biological brace to promote dysfunctional platelet aggregation.", *Nature structural & molecular biology*, vol. 12, no. 2, pp. 152–159, 2005.
- [89] M. S. Read, R. W. Shermer, and K. M. Brinkhous, "Venom coagglutinin: an activator of platelet aggregation dependent on von Willebrand factor.", *Proceedings of the National Academy of Sciences*, vol. 75, no. 9, pp. 4514–8, 1978.
- [90] H. Mohri, Y. Fujimura, M. Shima, *et al.*, "Structure of the von Willebrand factor domain interacting with glycoprotein Ib.", *The Journal of biological chemistry*, vol. 263, no. 34, pp. 17 901–4, 1988.
- [91] M. Sugimoto, J. Dent, R. McClintock, *et al.*, "Analysis of structure-function relationships in the platelet membrane glycoprotein Ib-binding domain of von Willebrand's factor by expression of deletion mutants.", *The Journal of biological chemistry*, vol. 268, no. 16, pp. 12 185–92, 1993.
- [92] M. Auton, K. E. Sowa, M. Behymer, *et al.*, "N-terminal flanking region of A1 domain in von Willebrand factor stabilizes structure of A1A2A3 complex and modulates platelet activation under shear stress.", *The Journal of biological chemistry*, vol. 287, no. 18, pp. 14 579–85, 2012.
- [93] L. Ju, J.-F. Dong, M. A. Cruz, *et al.*, "The N-terminal flanking region of the A1 domain regulates the force-dependent binding of von Willebrand factor to platelet glycoprotein Iba.", *The Journal of biological chemistry*, vol. 288, no. 45, pp. 32 289–301, 2013.
- [94] S. R. Madabhushi, C. Zhang, A. Kelkar, *et al.*, "Platelet GpIba binding to von Willebrand Factor under fluid shear: contributions of the DD3-domain, A1-domain flanking peptide and O-linked glycans.", *Journal of the American Heart Association*, vol. 3, e001420, 2014.
- [95] H. Ulrichs, M. Udvardy, P. J. Lenting, *et al.*, "Shielding of the A1 domain by the D'D3 domains of von Willebrand factor modulates its interaction with platelet glycoprotein Ib-IX-V.", *J Biol Chem*, vol. 281, no. 8, pp. 4699–4707, 2006.
- [96] K. Nishio, P. J. Anderson, X. L. Zheng, *et al.*, "Binding of platelet glycoprotein Ib to von Willebrand factor domain A1 stimulates the cleavage of the adjacent domain A2 by ADAMTS13", *Proceedings of the National Academy of Sciences*, vol. 101, no. 29, pp. 10 578–10 583, 2004.
- [97] H. Lankhof, C. Damas, M. E. Schiphorst, *et al.*, "von Willebrand factor without the A2 domain is resistant to proteolysis.", *Thrombosis and haemostasis*, vol. 77, no. 5, pp. 1008–13, 1997.
- [98] C. Martin, L. D. Morales, and M. A. Cruz, "Purified A2 domain of von Willebrand factor binds to the active conformation of von Willebrand factor and blocks the interaction with platelet glycoprotein Iba.", *Journal of thrombosis and haemostasis*, vol. 5, no. 7, pp. 1363–70, 2007.
- [99] C. Aponte-Santamaría, V. Huck, S. Posch, *et al.*, "Force-sensitive autoinhibition of the von Willebrand factor is mediated by interdomain interactions.", *Biophysical Journal*, vol. 108, no. 9, pp. 2312–21, 2015.

- [100] D. Butera, F. Passam, L. Ju, *et al.*, “Autoregulation of von Willebrand factor function by a disulfide bond switch”, *Science Advances*, vol. 4, no. 2, eaaq1477, 2018.
- [101] S. Miyata and Z. M. Ruggeri, “Distinct structural attributes regulating von Willebrand factor A1 domain interaction with platelet glycoprotein Ib $\alpha$  under flow.”, *The Journal of biological chemistry*, vol. 274, no. 10, pp. 6586–93, 1999.
- [102] S. Miyata, S. Goto, A. B. Federici, *et al.*, “Conformational Changes in the A1 Domain of von Willebrand Factor Modulating the Interaction with Platelet Glycoprotein Ib”, *Journal of Biological Chemistry*, vol. 271, no. 15, pp. 9046–9053, 1996.
- [103] M. Hoore, K. Rack, D. A. Fedosov, *et al.*, “Flow-induced adhesion of shear-activated polymers to a substrate”, *Journal of Physics: Condensed Matter*, vol. 30, no. 6, p. 064 001, 2018.
- [104] H. Christou, N. Bailey, M. S. Kluger, *et al.*, “Extracellular acidosis induces heme oxygenase-1 expression in vascular smooth muscle cells”, *Am J Physiol Heart Circ Physiol*, vol. 288, no. 6, H2647–52, 2005.
- [105] C. V. Serrano, A. Fraticelli, R. Paniccia, *et al.*, “pH dependence of neutrophil-endothelial cell adhesion and adhesion molecule expression.”, *The American journal of physiology*, vol. 271, no. 3, pp. C962–C970, 1996.
- [106] N. S. Ihrcke, W. Parker, K. J. Reissner, *et al.*, “Regulation of platelet heparanase during inflammation: Role of pH and proteinases”, *Journal of Cellular Physiology*, vol. 175, no. 3, pp. 255–267, 1998.
- [107] D. De Backer, “Lactic acidosis”, *Minerva Anestesiologica*, vol. 69, no. 4, pp. 281–284, 2003.
- [108] Bhushan, Ed., *Handbook of Nanotechnology*, 2nd ed. Springer Berlin/Heidelberg, 2007.
- [109] G. Binnig, C. F. Quate, and C. Gerber, “Atomic force microscope”, *Physical review letters*, vol. 56, no. 9, p. 930, 1986.
- [110] G. Binnig, C. Gerber, E. Stoll, *et al.*, “Atomic resolution with atomic force microscope”, *Europhysics Letters*, vol. 3, no. 12, p. 1281, 1987.
- [111] D. Müller, F. Schabert, G. Büldt, *et al.*, “Imaging purple membranes in aqueous solutions at sub-nanometer resolution by atomic force microscopy”, *Biophysical Journal*, vol. 68, no. 5, pp. 1681–1686, 1995.
- [112] S. Scheuring, D. Fotiadis, C. Möller, *et al.*, “Single Proteins Observed by Atomic Force Microscopy”, *Single Molecules*, vol. 2, no. 2, pp. 59–67, 2001.
- [113] D. J. Müller, M. Amrein, and A. Engel, “Adsorption of biological molecules to a solid support for scanning probe microscopy.”, *J Struct Biol*, vol. 119, no. 2, pp. 172–188, 1997.
- [114] Y. Martin, C. Williams, and H. K. Wickramasinghe, “Atomic force microscope–force mapping and profiling on a sub 100-Å scale”, *Journal of Applied Physics*, vol. 61, no. 10, pp. 4723–4729, 1987.
- [115] M. Radmacher, R. Tillmann, M. Fritz, *et al.*, “From molecules to cells: Imaging soft samples with the atomic force microscope”, *Science*, vol. 257, no. 5078, pp. 1900–1905, 1992.

- [116] P. Maivald, H. Butt, S. Gould, *et al.*, “Using force modulation to image surface elasticities with the atomic force microscope”, *Nanotechnology*, vol. 2, no. 2, p. 103, 1991.
- [117] R. Schneppenheim, H. Plendl, and U. Budde, “Luminography—an alternative assay for detection of von Willebrand factor multimers.”, *Thrombosis and haemostasis*, vol. 60, no. 2, pp. 133–6, 1988.
- [118] U. Budde, R. Schneppenheim, H. Plendl, *et al.*, “Luminographic detection of von Willebrand factor multimers in agarose gels and on nitrocellulose membranes.”, *Thrombosis and haemostasis*, vol. 63, no. 2, pp. 312–5, 1990.
- [119] U. Budde, R. Schneppenheim, J. Eikenboom, *et al.*, “Detailed von Willebrand factor multimer analysis in patients with von Willebrand disease in the European study, molecular and clinical markers for the diagnosis and management of type 1 von Willebrand disease (MCMDM-1VWD).”, *Journal of thrombosis and haemostasis*, vol. 6, no. 5, pp. 762–71, 2008.
- [120] V. Moy, E. Florin, and H. Gaub, “Intermolecular forces and energies between ligands and receptors”, *Science*, vol. 266, no. 5183, pp. 257–259, 1994.
- [121] K. C. Neuman and A. Nagy, “Single-molecule force spectroscopy: optical tweezers, magnetic tweezers and atomic force microscopy”, *Nature Methods*, vol. 5, no. 6, pp. 491–505, 2008.
- [122] K. Halvorsen and W. P. Wong, “Massively parallel single-molecule manipulation using centrifugal force.”, *Biophysical Journal*, vol. 98, no. 11, pp. L53–5, 2010.
- [123] D. Yang, A. Ward, K. Halvorsen, *et al.*, “Multiplexed single-molecule force spectroscopy using a centrifuge”, *Nature Communications*, vol. 7, p. 11 026, 2016.
- [124] G. Sitters, D. Kamsma, G. Thalhammer, *et al.*, “Acoustic force spectroscopy”, *Nature Methods*, vol. 12, no. 1, pp. 47–50, 2015.
- [125] W. Ott, M. A. Jobst, C. Schoeler, *et al.*, “Single-molecule force spectroscopy on polyproteins and receptor–ligand complexes: The current toolbox”, *Journal of Structural Biology*, vol. in press, 2016.
- [126] W. Ott, M. A. Jobst, M. S. Bauer, *et al.*, “Elastin-like Polypeptide Linkers for Single-Molecule Force Spectroscopy”, *ACS Nano*, vol. 11, no. 6, pp. 6346–6354, 2017.
- [127] E. Durner, W. Ott, M. A. Nash, *et al.*, “Post-Translational Sortase-Mediated Attachment of High-Strength Force Spectroscopy Handles”, *ACS Omega*, vol. 2, no. 6, pp. 3064–3069, 2017.
- [128] C. Bustamante, J. F. Marko, E. D. Siggia, *et al.*, *Entropic elasticity of  $\lambda$ -phage dna*, 1994.
- [129] J. F. Marko and E. D. Siggia, “Statistical mechanics of supercoiled DNA”, *Physical Review E*, vol. 52, no. 3, pp. 2912–2938, 1995.
- [130] J. F. Marko and E. D. Siggia, “Stretching DNA”, *Macromolecules*, vol. 28, no. 26, pp. 8759–8770, 1995.
- [131] R. Petrosyan, “Improved approximations for some polymer extension models”, *Rheologica Acta*, vol. 56, no. 1, pp. 21–26, 2017.

- [132] T. Odijk, “Stiff Chains and Filaments under Tension”, *Macromolecules*, vol. 28, no. 20, pp. 7016–7018, 1995.
- [133] P. H. Verdier, “Relaxation Behavior of the Freely Jointed Chain”, *The Journal of Chemical Physics*, vol. 52, no. 11, pp. 5512–5517, 1970.
- [134] S. B. Smith, L Finzi, and C Bustamante, “Direct mechanical measurements of the elasticity of single DNA molecules by using magnetic beads.”, *Science*, vol. 258, no. 5085, pp. 1122–6, 1992.
- [135] A. Perico, S. Bisio, and C. Cuniberti, “Polymer dynamics in dilute solutions. The freely rotating chain”, *Macromolecules*, vol. 17, no. 12, pp. 2686–2689, 1984.
- [136] G. I. Bell, “Models for the specific adhesion of cells to cells.”, *Science*, vol. 200, no. 4342, pp. 618–27, 1978.
- [137] E. Evans and K. Ritchie, “Dynamic strength of molecular adhesion bonds”, *Biophysical Journal*, vol. 72, no. 4, pp. 1541–1555, 1997.
- [138] P. U. Walker, “Fast Dynamics of Biological Systems Investigated with Magnetic Tweezers and Small-Angle X-Ray Scattering”, PhD thesis, LMU Munich, Faculty of Physics, 2018.
- [139] T. R. Strick, J. F. Allemand, D Bensimon, *et al.*, “The elasticity of a single supercoiled DNA molecule.”, *Science*, vol. 271, no. 5257, pp. 1835–7, 1996.
- [140] F. Kriegel, N. Ermann, and J. Lipfert, “Probing the mechanical properties, conformational changes, and interactions of nucleic acids with magnetic tweezers”, *Journal of Structural Biology*, 2016.
- [141] J. Lipfert, X. Hao, and N. H. Dekker, “Quantitative modeling and optimization of magnetic tweezers.”, *Biophysical Journal*, vol. 96, no. 12, pp. 5040–9, 2009.
- [142] J. P. Cnossen, D. Dulin, and N. H. Dekker, “An optimized software framework for real-time, high-throughput tracking of spherical beads”, *Review of Scientific Instruments*, vol. 85, no. 10, p. 103 712, 2014.
- [143] N. Ribeck and O. A. Saleh, “Multiplexed single-molecule measurements with magnetic tweezers”, *Review of Scientific Instruments*, vol. 79, no. 9, p. 094 301, 2008.
- [144] I. De Vlaminck, T. Henighan, M. T. van Loenhout, *et al.*, “Highly Parallel Magnetic Tweezers by Targeted DNA Tethering”, *Nano Letters*, vol. 11, no. 12, pp. 5489–5493, 2011.
- [145] B. M. Lansdorp, S. J. Tabrizi, A. Dittmore, *et al.*, “A high-speed magnetic tweezer beyond 10,000 frames per second”, *Review of Scientific Instruments*, vol. 84, no. 4, p. 044 301, 2013.
- [146] D. Dulin, T. J. Cui, J. Cnossen, *et al.*, “High Spatiotemporal-Resolution Magnetic Tweezers: Calibration and Applications for DNA Dynamics.”, *Biophysical Journal*, vol. 109, no. 10, pp. 2113–25, 2015.
- [147] A. Huhle, D. Klaue, H. Brutzer, *et al.*, “Camera-based three-dimensional real-time particle tracking at kHz rates and Ångström accuracy”, *Nature Communications*, vol. 6, no. 1, p. 5885, 2015.

- [148] A. J. W. Te Velthuis, J. W. J. Kerssemakers, J. Lipfert, *et al.*, “Quantitative guidelines for force calibration through spectral analysis of magnetic tweezers data.”, *Biophysical Journal*, vol. 99, no. 4, pp. 1292–302, 2010.
- [149] J. Lipfert, X. Hao, and N. H. Dekker, “Quantitative Modeling and Optimization of Magnetic Tweezers”, *Biophysical Journal*, vol. 96, no. 12, pp. 5040–5049, 2009.
- [150] I. De Vlaminck, T. Henighan, M. T. J. van Loenhout, *et al.*, “Magnetic Forces and DNA Mechanics in Multiplexed Magnetic Tweezers”, *PLOS ONE*, vol. 7, no. 8, e41432, 2012.
- [151] E. Ostrofet, F. S. Papini, and D. Dulin, “Correction-free force calibration for magnetic tweezers experiments.”, *Scientific Reports*, vol. 8, no. 1, p. 15 920, 2018.
- [152] J. W. J. Kerssemakers, E. Laura Munteanu, L. Laan, *et al.*, “Assembly dynamics of microtubules at molecular resolution”, *Nature*, vol. 442, no. 7103, pp. 709–712, 2006.
- [153] I. Schwaiger, M. Schleicher, A. A. Noegel, *et al.*, “The folding pathway of a fast-folding immunoglobulin domain revealed by single-molecule mechanical experiments.”, *EMBO reports*, vol. 6, no. 1, pp. 46–51, 2005.
- [154] Y. Cao, R. Kuske, and H. Li, “Direct observation of Markovian behavior of the mechanical unfolding of individual proteins”, *Biophysical Journal*, vol. 95, no. 2, pp. 782–788, 2008.
- [155] T. G. Schmidt and A. Skerra, “The Strep-tag system for one-step purification and high-affinity detection or capturing of proteins”, *Nature Protocols*, vol. 2, no. 6, pp. 1528–1535, 2007.
- [156] J. Yin, P. D. Straight, S. M. McLoughlin, *et al.*, “Genetically encoded short peptide tag for versatile protein labeling by Sfp phosphopantetheinyl transferase.”, *Proceedings of the National Academy of Sciences*, vol. 102, no. 44, pp. 15 815–15 820, 2005.
- [157] J. Phan, A. Zdanov, A. G. Evdokimov, *et al.*, “Structural basis for the substrate specificity of tobacco etch virus protease.”, *The Journal of biological chemistry*, vol. 277, no. 52, pp. 50 564–72, 2002.
- [158] C. S. Theile, M. D. Witte, A. E. M. Blom, *et al.*, “Site-specific N-terminal labeling of proteins using sortase-mediated reactions.”, *Nature protocols*, vol. 8, no. 9, pp. 1800–7, 2013.
- [159] R. Schneppenheim, J. J. Michiels, T. Obser, *et al.*, “A cluster of mutations in the D3 domain of von Willebrand factor correlates with a distinct subgroup of von Willebrand disease: type 2A/III”, *Blood*, vol. 115, no. 23, pp. 4894–4901, 2010.
- [160] W. Ott, T. Nicolaus, H. E. Gaub, *et al.*, “Sequence-Independent Cloning and Post-Translational Modification of Repetitive Protein Polymers through Sortase and Sfp-Mediated Enzymatic Ligation”, *Biomacromolecules*, vol. 17, no. 4, pp. 1330–1338, 2016.
- [161] S. M. Sedlak, M. S. Bauer, C. Kluger, *et al.*, “Monodisperse measurement of the biotin-streptavidin interaction strength in a well-defined pulling geometry”, *PLOS ONE*, vol. 12, no. 12, e0188722, 2017.
- [162] S. M. Sedlak, L. C. Schendel, M. C. R. Melo, *et al.*, “Direction Matters: Monovalent Streptavidin/Biotin Complex under Load”, *Nano Letters*, acs.nanolett.8b04045, 2018.
- [163] D. G. Gibson, L. Young, R.-Y. Chuang, *et al.*, “Enzymatic assembly of DNA molecules up to several hundred kilobases”, *Nature Methods*, vol. 6, no. 5, pp. 343–345, 2009.

- [164] L. F. Milles, E. A. Bayer, M. A. Nash, *et al.*, “Mechanical Stability of a High-Affinity Toxin Anchor from the Pathogen *Clostridium perfringens*”, *The Journal of Physical Chemistry B*, vol. 121, no. 15, pp. 3620–3625, 2017.
- [165] J. P. Müller, “Force sensing by the vascular protein von Willebrand factor dissected at the single-molecule level”, PhD thesis, LMU Munich, Faculty of Physics, 2016.
- [166] J. P. Müller, A. Löff, S. Mielke, *et al.*, “pH-dependent interactions in dimers govern the mechanics and structure of von Willebrand Factor”, *Biophysical Journal*, vol. 111, no. 2, pp. 312–322, 2016.
- [167] T. G. M. Schmidt, L. Batz, L. Bonet, *et al.*, “Development of the Twin-Strep-tag and its application for purification of recombinant proteins from cell culture supernatants”, *Protein Expression and Purification*, vol. 92, no. 1, pp. 54–61, 2013.
- [168] L. Schmitt, M. Ludwig, G. H.E., *et al.*, “A metal-chelating microscopy tip as a new toolbox for single-molecule experiments by atomic force microscopy”, *Biophysical Journal*, vol. 78, pp. 3275–3285, 2000.
- [169] J. Ying, Y. Ling, L. A. Westfield, *et al.*, “Unfolding the A2 domain of von Willebrand factor with the optical trap.”, *Biophysical Journal*, vol. 98, no. 8, pp. 1685–93, 2010.
- [170] A. J. Jakobi, A. Mashaghi, S. J. Tans, *et al.*, “Calcium modulates force sensing by the von Willebrand factor A2 domain.”, *Nature Communications*, vol. 2, p. 385, 2011.
- [171] J. Srivastava, D. L. Barber, and M. P. Jacobson, “Intracellular pH sensors: design principles and functional significance.”, *Physiology*, vol. 22, pp. 30–39, 2007.
- [172] Z. Ruggeri, “von Willebrand factor”, *J Clin Invest*, vol. 99, pp. 559–564, 1997.
- [173] D. M. Steppich, “The Physics of Von Willebrand Factor”, PhD thesis, University of Augsburg, Germany, 2009.
- [174] H. Chen, G. Yuan, R. S. Winardhi, *et al.*, “Dynamics of Equilibrium Folding and Unfolding Transitions of Titin Immunoglobulin Domain under Constant Forces”, *Journal of the American Chemical Society*, vol. 137, no. 10, pp. 3540–3546, 2015.
- [175] S. Halder, R. Tapia-Rojo, E. C. Eckels, *et al.*, “Trigger factor chaperone acts as a mechanical foldase”, *Nature Communications*, vol. 8, no. 1, p. 668, 2017.
- [176] I. Popa, J. A. Rivas-Pardo, E. C. Eckels, *et al.*, “A HaloTag Anchored Ruler for Week-Long Studies of Protein Dynamics”, *Journal of the American Chemical Society*, vol. 138, no. 33, pp. 10 546–10 553, 2016.
- [177] D. Spadaro, S. Le, T. Laroche, *et al.*, “Tension-Dependent Stretching Activates ZO-1 to Control the Junctional Localization of Its Interactors”, *Current Biology*, vol. 27, no. 24, 3783–3795.e8, 2017.
- [178] A. S. Adhikari, E. Glassey, and A. R. Dunn, “Conformational dynamics accompanying the proteolytic degradation of trimeric collagen I by collagenases.”, *Journal of the American Chemical Society*, vol. 134, no. 32, pp. 13 259–65, 2012.
- [179] X. J. A. Janssen, J. M. van Noorloos, A. Jacob, *et al.*, “Torsion stiffness of a protein pair determined by magnetic particles.”, *Biophysical Journal*, vol. 100, no. 9, pp. 2262–7, 2011.

- [180] E. Pérez-Ruiz, M. Kemper, D. Spasic, *et al.*, “Probing the Force-Induced Dissociation of Aptamer-Protein Complexes”, *Analytical Chemistry*, vol. 86, no. 6, pp. 3084–3091, 2014.
- [181] A. S. Adhikari, J. Chai, and A. R. Dunn, “Mechanical Load Induces a 100-Fold Increase in the Rate of Collagen Proteolysis by MMP-1”, *Journal of the American Chemical Society*, vol. 133, no. 6, pp. 1686–1689, 2011.
- [182] A. van Reenen, F. Gutiérrez-Mejía, L. van IJzendoorn, *et al.*, “Torsion Profiling of Proteins Using Magnetic Particles”, *Biophysical Journal*, vol. 104, no. 5, pp. 1073–1080, 2013.
- [183] H. Chen, S. Chandrasekar, M. P. Sheetz, *et al.*, “Mechanical perturbation of filamin A immunoglobulin repeats 20-21 reveals potential non-equilibrium mechanochemical partner binding function”, *Scientific Reports*, vol. 3, no. 1, p. 1642, 2013.
- [184] M. Yao, W. Qiu, R. Liu, *et al.*, “Force-dependent conformational switch of  $\alpha$ -catenin controls vinculin binding”, *Nature Communications*, vol. 5, no. 1, p. 4525, 2014.
- [185] M. Yao, B. T. B. Goult, B. Klapholz, *et al.*, “The mechanical response of talin”, *Nature Communications*, vol. 7, no. May, p. 11 966, 2016.
- [186] S. Le, X. Hu, M. Yao, *et al.*, “Mechanotransmission and Mechanosensing of Human alpha-Actinin 1”, *Cell Reports*, vol. 21, no. 10, pp. 2714–2723, 2017.
- [187] A. Löff, P. U. Walker, S. M. Sedlak, *et al.*, “Modular, ultra-stable, and highly parallel protein force spectroscopy in magnetic tweezers using peptide linkers”, *bioRxiv*, doi:10.1101/491977, 2018.
- [188] M. W.-L. Popp and H. L. Ploegh, “Making and Breaking Peptide Bonds: Protein Engineering Using Sortase”, *Angewandte Chemie International Edition*, vol. 50, no. 22, pp. 5024–5032, 2011.
- [189] W. Ott, M. A. Jobst, C. Schoeler, *et al.*, “Single-molecule force spectroscopy on polyproteins and receptor–ligand complexes: The current toolbox”, *Journal of Structural Biology*, vol. 197, no. 1, pp. 3–12, 2017.
- [190] P. Fucini, C. Renner, C. Herberhold, *et al.*, “The repeating segments of the F-actin cross-linking gelation factor (ABP-120) have an immunoglobulin-like fold.”, *Nature structural biology*, vol. 4, no. 3, pp. 223–30, 1997.
- [191] W. Humphrey, A. Dalke, and K. Schulten, “VMD: visual molecular dynamics.”, *Journal of molecular graphics*, vol. 14, no. 1, pp. 33–8, 27–8, 1996.
- [192] I. Schwaiger, A. Kardinal, M. Schleicher, *et al.*, “A mechanical unfolding intermediate in an actin-crosslinking protein.”, *Nature structural & molecular biology*, vol. 11, no. 1, pp. 81–5, 2004.
- [193] L. F. Milles, K. Schulten, H. E. Gaub, *et al.*, “Molecular mechanism of extreme mechanostability in a pathogen adhesin.”, *Science*, vol. 359, no. 6383, pp. 1527–1533, 2018.
- [194] Z. T. Yew, M. Schlierf, M. Rief, *et al.*, “Direct evidence of the multidimensionality of the free-energy landscapes of proteins revealed by mechanical probes”, *Physical Review E*, vol. 81, no. 3, p. 031 923, 2010.
- [195] M. Zhang, S. Biswas, W. Deng, *et al.*, “Crystal structure of streptavidin with one wild type subunit and three mutated subunits (N23A/S27D/S45A)”, *To be published*, PDB 2017.

- [196] D. Hyre, I. Le Trong, E. Merritt, *et al.*, “Cooperative hydrogen bond interactions in the streptavidin-biotin system”, *Protein Sci.*, vol. 15, pp. 459–467, 2006.
- [197] R. B. Russell and G. J. Barton, “Multiple protein sequence alignment from tertiary structure comparison: Assignment of global and residue confidence levels”, *Proteins: Structure, Function, and Genetics*, vol. 14, no. 2, pp. 309–323, 1992.
- [198] O. H. Laitinen, V. P. Hytönen, H. R. Nordlund, *et al.*, “Genetically engineered avidins and streptavidins”, *Cellular and Molecular Life Sciences*, vol. 63, no. 24, pp. 2992–3017, 2006.
- [199] C. M. Dundas, D. Demonte, and S. Park, “Streptavidin–biotin technology: improvements and innovations in chemical and biological applications”, *Applied Microbiology and Biotechnology*, vol. 97, no. 21, pp. 9343–9353, 2013.
- [200] O. K. Dudko, G. Hummer, and A. Szabo, “Theory, analysis, and interpretation of single-molecule force spectroscopy experiments”, *Proceedings of the National Academy of Sciences*, vol. 105, no. 41, pp. 15 755–15 760, 2008.
- [201] R. Schneppenheim, N. Hellermann, M. A. Brehm, *et al.*, “The von Willebrand factor Tyr2561 allele is a gain-of-function variant and a risk factor for early myocardial infarction.”, *Blood*, vol. 133, no. 4, pp. 356–365, 2019.
- [202] M. A. Brehm, V. Huck, C. Aponte-Santamaría, *et al.*, “von Willebrand disease type 2A phenotypes IIC, IID and IIE: A day in the life of shear-stressed mutant von Willebrand factor”, *Thrombosis and Haemostasis*, vol. 112, no. 1, pp. 96–108, 2014.
- [203] S. Lippok, T. Obser, J. P. Müller, *et al.*, “Exponential Size Distribution of von Willebrand Factor”, *Biophysical Journal*, vol. 105, no. 5, pp. 1208–1216, 2013.
- [204] A. Katsumi, E. A. Tuley, I. Bodo, *et al.*, “Localization of Disulfide Bonds in the Cystine Knot Domain of Human von Willebrand Factor”, *Journal of Biological Chemistry*, vol. 275, no. 33, pp. 25 585–25 594, 2000.
- [205] R. Schneppenheim, J. Brassard, S. Krey, *et al.*, “Defective dimerization of von Willebrand factor subunits due to a Cys→Arg mutation in type IID von Willebrand disease”, *Proceedings of the National Academy of Sciences*, vol. 93, no. 8, pp. 3581–6, 1996.
- [206] R. Schneppenheim, U. Budde, T. Obser, *et al.*, “Expression and characterization of von Willebrand factor dimerization defects in different types of von Willebrand disease.”, *Blood*, vol. 97, no. 7, pp. 2059–66, 2001.
- [207] G. Castaman, S. H. Giacomelli, P. M. Jacobi, *et al.*, “Reduced von Willebrand factor secretion is associated with loss of Weibel-Palade body formation”, *Journal of Thrombosis and Haemostasis*, vol. 10, no. 5, pp. 951–958, 2012.
- [208] D. J. Groeneveld, J.-W. Wang, M. J. Mourik, *et al.*, “Storage and secretion of naturally occurring von Willebrand factor A domain variants”, *British Journal of Haematology*, vol. 167, no. 4, pp. 529–540, 2014.
- [209] T. C. White-Adams, C. J. Ng, P. M. Jacobi, *et al.*, “Mutations in the DD3 region of VWF traditionally associated with type 1 VWD lead to quantitative and qualitative deficiencies of VWF”, *Thrombosis Research*, vol. 145, pp. 112–118, 2016.

- [210] G. Michaux, L. J. Hewlett, S. L. Messenger, *et al.*, “Analysis of intracellular storage and regulated secretion of 3 von Willebrand disease-causing variants of von Willebrand factor.”, *Blood*, vol. 102, no. 7, pp. 2452–8, 2003.
- [211] G. Michaux, K. B. Abbitt, L. M. Collinson, *et al.*, “The Physiological Function of von Willebrand’s Factor Depends on Its Tubular Storage in Endothelial Weibel-Palade Bodies”, *Developmental Cell*, vol. 10, no. 2, pp. 223–232, 2006.
- [212] J. Yang, H. Chen, I. R. Vlahov, *et al.*, “Evaluation of disulfide reduction during receptor-mediated endocytosis by using FRET imaging”, *Proceedings of the National Academy of Sciences*, vol. 103, no. 37, pp. 13 872–13 877, 2006.
- [213] M. J. Geisow and W. Evans, “pH in the endosome: Measurements during pinocytosis and receptor-mediated endocytosis”, *Experimental Cell Research*, vol. 150, no. 1, pp. 36–46, 1984.



# List of Figures

1.1	Structure and domain organization of VWF . . . . .	7
1.2	Biosynthesis of VWF . . . . .	9
1.3	VWF as a linear polymer in shear and elongational flow . . . . .	12
1.4	Force-induced transitions during elongation and activation of VWF . . . . .	21
2.1	Schematic of AFM imaging in tapping mode . . . . .	24
2.2	Height profiling of VWF dimers in AFM images . . . . .	26
2.3	Two-state, single-barrier kinetic model . . . . .	30
2.4	Schematic of a conventional MT setup . . . . .	32
2.5	Force calibration of the custom MT setup . . . . .	34
3.1	AFM-based force measurements on VWF dimers under varied pH conditions .	44
3.2	AFM-based force measurements on VWF monomers under varied pH conditions	45
3.3	Reversibility of the pH-dependent mechanisms affecting the formation of the strong D4-mediated intermonomer interaction . . . . .	46
3.4	Conformation of dimeric VWF constructs under varied pH and ionic conditions	48
3.5	C-terminal stems in VWF dimers under varied pH and ionic conditions . . . .	49
3.6	Obstruction of the strong intermonomer interaction by imidazole . . . . .	50
3.7	Strong and weak C-terminal stems in VWF's dimeric subunits . . . . .	52
3.8	Overview of force-sensitive interactions and transitions within VWF dimers under varied pH conditions . . . . .	54
4.1	Attachment protocol for highly parallel force spectroscopy on proteins in MT	60
4.2	Three-state folding and unfolding of ddFLN4 at constant force . . . . .	62
4.3	Extension of ELP linker–protein tethers . . . . .	63
4.4	Determination of rates from observed unfolding and refolding events . . . . .	64
4.5	Long-term ddFLN4 folding and unfolding traces close to equilibrium . . . . .	65
4.6	Repeated cycles of unfolding and refolding of ddFLN4 without hysteresis . . .	66
4.7	Lifetime of single biotin–streptavidin bonds under constant load . . . . .	68
4.8	Distinct force loading geometries resulting from the tetravalency of streptavidin	69
4.9	Streptavidin variants with different valencies . . . . .	70
4.10	AFM imaging of streptavidin with biotinylated DNA . . . . .	71
4.11	Lifetime of the biotin–streptavidin interaction under constant force . . . . .	72
5.1	Folding and unfolding of A2 domains within VWF dimers . . . . .	76
5.2	Measurements on ddFLN4 under varied pH and ionic conditions as control . .	77
5.3	Refolding of VWF A2 domains under mechanical load in the absence of Ca <sup>2+</sup> .	78
5.4	Occasional inhibition of A2 refolding in VWF dimer tethers . . . . .	79
5.5	Dissociation of a D4-mediated intermonomer interaction in VWF dimers . . .	81
5.6	Measurements on VWF dimers with deletion of the D4 domain . . . . .	82

---

5.7	Unzipping and zipping of the C-domain stem in VWF dimers (I) . . . . .	84
5.8	Unzipping and zipping of the C-domain stem in VWF dimers (II) . . . . .	85
5.9	Three-state hopping in full-length VWF dimers . . . . .	87
5.10	Localization of the three-state hopping to transitions within D'D3 domains . .	88
5.11	Structure of the D'D3 assembly and its VWD3/C8-3/TIL3/E3 interface . . . . .	89
5.12	Schematic of an inverted VWF dimer construct . . . . .	90
5.13	Relative populations of the three states of hopping as a function of force . . .	92
5.14	Kinetics of three-state hopping . . . . .	94
5.15	Hopping between only two states . . . . .	96
5.16	Effect of acidic pH on hopping . . . . .	98
5.17	Effect of calcium chelation on hopping . . . . .	99
6.1	VWF multimer analysis by AFM imaging of individual molecules . . . . .	104
6.2	Quantitative electrophoretic VWF multimer analysis . . . . .	105
6.3	Analysis of VWF multimers in AFM images . . . . .	106
6.4	Cell lysis of HEK-293 cells expressing wildtype VWF or mutant p.Cys2811Ala	107

# List of Tables

2.1	List of recombinant protein constructs . . . . .	39
-----	--------------------------------------------------	----



# List of Publications

## Publications and manuscripts in preparation included in this thesis

1. Jochen P. Müller\*, Achim Löff\*, Salomé Mielke, Tobias Obser, Linda K. Bruetzel, Willem Vanderlinden, Jan Lipfert, Reinhard Schneppenheim, and Martin Benoit;  
**pH-Dependent Interactions in Dimers Govern the Mechanics and Structure of von Willebrand Factor.** *Biophysical Journal*, vol. 111, pp. 312-322, 2016.  
\* J.P.M. and A.L. contributed equally.
2. Achim Löff, Jochen P. Müller, Martin Benoit, and Maria A. Brehm;  
**Biophysical approaches promote advances in the understanding of von Willebrand factor processing and function.** *Advances in Biological Regulation*, vol. 63, pp. 81-91, 2017.
3. Achim Löff, Jochen P. Müller, and Maria A. Brehm;  
**A biophysical view on von Willebrand factor activation.** *Journal of Cellular Physiology*, vol. 233, pp. 799-810, 2018.
4. Achim Löff, Gesa König, Sonja Schneppenheim, Reinhard Schneppenheim, Martin Benoit, Jochen P. Müller, and Maria A. Brehm;  
**Advancing multimer analysis of von Willebrand factor by single-molecule AFM imaging.** *PLoS ONE*, vol. 14, no. 1, e0210963, 2019.
5. Achim Löff, Philipp U. Walker, Steffen M. Sedlak, Tobias Obser, Maria A. Brehm, Martin Benoit, and Jan Lipfert;  
**Modular, ultra-stable and highly parallel protein force spectroscopy in magnetic tweezers using peptide linkers.** Preprint on *bioRxiv*, doi: 10.1101/491977, 2018, and under review at the *Proceedings of the National Academy of Sciences of the U.S.A.*.
6. Achim Löff\*, Steffen M. Sedlak\*, Sophia Gruber, Martin Benoit, Jan Lipfert, and Hermann E. Gaub;  
**The tetravalency of streptavidin results in distinct lifetimes of biotin unbinding under constant load.** In preparation.  
\* A.L. and S.M.S. contributed equally.

## Further publications that are not part of this thesis

1. Jochen P. Müller, Salomé Mielke, Achim Löff, Tobias Obser, Christof Beer, Linda K. Bruetzel, Diana A. Pippig, Willem Vanderlinden, Jan Lipfert, Reinhard Schneppenheim, and Martin Benoit;  
**Force Sensing by the Vascular Protein von Willebrand Factor is Tuned by a Strong Intermonomer Interaction.** *Proceedings of the National Academy of Sciences of the U.S.A.*, vol. 113, no. 5 pp. 1208-1213, 2016.

2. Svenja Lippok, Katra Kolšek, Achim Löf, Dennis Eggert, Willem Vanderlinden, Jochen P. Müller, Gesa König, Tobias Obser, Karoline Röhrs, Sonja Schneppenheim, Ulrich Budde, Carsten Baldauf, Camilo Aponte-Santamaría, Frauke Gräter, Reinhard Schneppenheim, Joachim O. Rädler, and Maria A. Brehm;  
**Von Willebrand factor is dimerized by protein disulfide isomerase.** *Blood*, vol. 127, no. 9, pp. 1183-1191, 2016.
3. Florian Ehrat, Santanu Bhattacharyya, Julian Schneider, Achim Löf, Regina Wyrwich, Andrey L. Rogach, Jacek K. Stolarczyk, Alexander S. Urban, and Jochen Feldmann;  
**Tracking the Source of Carbon Dot Photoluminescence: Aromatic Domains versus Molecular Fluorophores.** *Nano Letters*, vol. 17, no. 12, pp. 7710-7716, 2017.

# Acknowledgements

I sincerely want to thank all the people who supported me during my doctoral studies, be it with advice, motivation, or friendship beyond work. Special thanks go to...

## ...my supervisors and colleagues in Munich:

**Prof Dr. Hermann E. Gaub** for the opportunity to perform my research in his lab and for providing an always fruitful working environment. I have enjoyed being part of the Gaub lab together with so many knowledgeable and interesting people to learn from.

**Dr. Martin Benoit** for giving me the opportunity to continue my research on von Willebrand factor after my Master's thesis. I am particularly grateful for the freedom to develop and follow my own ideas and strategies without restraints.

**Prof Dr. Jan Lipfert** for his support and fruitful discussions regarding my work with magnetic tweezers, and for accepting me as an inofficial member of the Lipfert lab.

**Dr. Jochen Müller** for recruiting me for research on von Willebrand factor in the first place and for the great teamwork on our joint projects, but especially for becoming a good friend. I enjoyed our discussions on VWF as much as our many events outside the lab. Jochen, thank you for your dedication, your constant support, and your advice, and for always being positive (except maybe when the Club is playing...)!

**Philipp Walker** for the long –sometimes frustrating, but in the end very successful– joint work of pulling proteins in magnetic tweezers, and for vital coffee breaks. Even more important, thank you for lots of fun in and outside the lab, playing kicker, tasting gin, watching sophisticated movies or going on hiking trips. And for *Machst du das immer so??*

**Steffen Sedlak** for the great cooperation on our streptavidin–biotin project and many scientific discussions, but in particular also for a lot of fun events outside the lab.

**Sophia Gruber** for her dedication and the good teamwork during the last months of my doctoral studies. I am glad that I can pass on my open projects into very good hands.

**Dr. Wolfgang Ott** for providing the ELP linkers that made my work with magnetic tweezers possible, and for helpful discussions and advice.

**Dr. Lukas Milles** for providing the ddFLN4 construct I used for my tweezers measurements, and for many interesting discussions.

**Dr. Willem Vanderlinden** for sharing his AFM imaging protocol and helpful discussions, and for important background information on Belgian fries.

**Magnus Bauer** for the good cooperation regarding measurements of focal adhesion kinase in the magnetic tweezers, and for general discussions.

**Ellis Durner** for helpful discussions and advice, especially regarding sortase chemistry.

**Dr. Linda Brützel** for the good teamwork concerning the sample preparation for small-angle X-ray scattering measurements on VWF.

**Thomas Nicolaus** for support (and music) in the chemistry lab, and –this cannot be stressed

enough– for the endless supply of amino-silanized glass slides.

**Angelika Kardinal** for support in the chemistry lab.

**Sylvia Kreuzer** for general support regarding all kinds of paperwork, and for all the sweets.

**All members of the LS Gaub**, for the pleasant working environment and for help and advice whenever needed.

**...collaborating researchers, especially at the UKE in Hamburg:**

**All SHENC members** for the inspiring and fruitful atmosphere in our multidisciplinary research group, and for all the input I got during our SHENC meetings.

**PD Dr. Maria A. Brehm** for the great collaboration on several projects, and for memorable evenings during meetings of our SHENC research group – which were always fun even when they involved playing pool.

**Prof. Dr. Reinhard Schneppenheim** for having made the SHENC research group possible by his enthusiasm for VWF, and for many helpful discussions especially on the clinical aspects of VWF.

**Tobias Obser** for engineering lots and lots of VWF constructs, no matter how complicated. Without his work, my research would not have been possible.

**Gesa König** for all her work on the VWF constructs –delivered in the most beautifully labeled tubes our lab has ever seen–, and for the great teamwork on our joint research projects. However, I am most grateful for the even better teamwork on our personal project. Gesa, thank you for continuously supporting me, being there for me, and making me happy.

Finally, I would also like to thank **my parents** for their interest in my work and their constant support on everything I do. I am very grateful for always having my family to count on.